Instability and acoustics of compressible exponential boundary layer flows

Based on the new solution to the Pridmore-Brown equation with an exponential velocity profile

Zur Erlangung des akademischen Grades Doktor-Ingenieur (Dr.-Ing.)
Genehmigte Dissertation von Yi Zhang aus Beijing, China
Tag der Einreichung: 25. April 2022, Tag der Prüfung: 12. Juli 2022

Erstreferent: Prof. Dr.-Ing. Martin Oberlack
Korreferent: Prof. Dr. rer. nat. Amsini Sadiki
Darmstadt, Technische Universität Darmstadt

TECHNISCHE UNIVERSITÄT DARMSTADT

Fachbereich Maschinenbau
Fachgebiet für Strömungsdynamik

Instability and acoustics of compressible exponential boundary layer flows
Based on the new solution to the Pridmore-Brown equation with an exponential velocity profile

Genehmigte Dissertation von Yi Zhang

Erstreferent: Prof. Dr.-Ing. Martin Oberlack
Korreferent: Prof. Dr. rer. nat. Amsini Sadiki

Tag der Einreichung: 25. April 2022
Tag der Prüfung: 12. Juli 2022

Darmstadt, Technische Universität Darmstadt

Für meine Frau und Familie

Erklärungen laut Promotionsordnung

§8 Abs. 1 lit. c PromO

Ich versichere hiermit, dass die elektronische Version meiner Dissertation mit der schriftlichen Version übereinstimmt.

§8 Abs. 1 lit. d PromO

Ich versichere hiermit, dass zu einem vorherigen Zeitpunkt noch keine Promotion versucht wurde. In diesem Fall sind nähere Angaben über Zeitpunkt, Hochschule, Dissertationsthema und Ergebnis dieses Versuchs mitzuteilen.

§9 Abs. 1 PromO

Ich versichere hiermit, dass die vorliegende Dissertation selbstständig und nur unter Verwendung der angegebenen Quellen verfasst wurde.

§9 Abs. 2 PromO

Die Arbeit hat bisher noch nicht zu Prüfungszwecken gedient.

Darmstadt, 25. April 2022

Y. Zhang

Abstract

In this thesis, inviscid instability and acoustics of compressible exponential boundary layer flows are investigated. Based on the linearised Euler equations (LEEs) and the normal-mode approach, the acoustic wave equation of parallel shear flows, the generalised Pridmore-Brown equation (PBE), is derived. For a boundary layer flow mimicked by an exponential velocity profile, an exact solution to the corresponding PBE is given in terms of the confluent Heun function (CHF). In the stability analyses, the eigenvalue equation for the stability problem based on the exact solution to the PBE is derived, and temporal stability and spatial stability are investigated respectively. For this, asymptotic analyses of the eigenvalue equation are first performed, and analytical solutions for limiting cases are obtained. Then, solutions to the eigenvalue equation are computed, which allow a comprehensive picture of the stability behaviour of the exponential boundary layer. In particular, the first three acoustic modes are computed as a function of the Mach number, the streamwise wavenumber, and the frequency. Unstable modes are found, where the first acoustic mode is always the most unstable one of all acoustic modes. Besides, an acoustic boundary layer thickness (ABLT) is defined, which essentially quantifies how far eigenfunctions reach into the area afar from the boundary layer. Meanwhile, wave angles, which describe the direction of the phase velocity, and eigenfunctions of acoustic modes are displayed. In the end, links between eigenvalues in the temporal stability and spatial stability problems are established. In the study of acoustics of boundary layer flows, the exact solution to the PBE is again employed to derive the reflection coefficient as a function of the Mach number, the streamwise wavenumber, and the incident angle of acoustic waves, and it is computed in wide parameter ranges. It is shown that the over-reflection of acoustic waves arises in boundary layer flows, i.e. the reflected amplitude of acoustic waves is greater than that of incident waves. The phenomenon is validated to be closely related to the critical layer, at which there is an optimal energy exchange from the base flow through the critical layer into the acoustic wave. Meanwhile, a special acoustic phenomenon, the resonant over-reflection, is observed and proved to be caused by the resonant frequency of unstable modes in the temporal stability problem. In addition, the resonant over-reflection also appears at resonant frequencies caused by higher unstable modes, but their over-reflection coefficients are always smaller than that caused by the first unstable mode. In the last part of the present work, the over-reflection of acoustic waves in a supersonic inviscid compressible boundary layer flow is validated by direct numerical simulations (DNS). A wave packet containing plane waves with constant wavelengths and amplitudes is superimposed with the free stream, and the incidence and reflection processes of the wave packet are simulated. In the simulations, the dispersion of the wave packet is observed due to strong shear effects near the wall. Amplification of the amplitude of the reflected waves is determined when the reflected wave eventually returns to the free stream. In particular, there is an exceptionally large over-reflection coefficient when the frequency of the incident wave is close to the resonant frequency, which indicates an occurrence of the resonant over-reflection.

Zusammenfassung

In dieser Dissertation werden die reibungsfreie Instabilität und Akustik von kompressiblen exponentiellen Grenzschichtströmungen untersucht. Auf Grundlage der linearisierten Euler-Gleichungen (LEEs) und des Normal-Mode Ansatzes wird die akustische Wellengleichung für parallele Scherströmungen, die verallgemeinerte Pridmore-Brown-Gleichung (PBE), hergeleitet. Für eine Grenzschichtströmung, die durch ein exponentielles Geschwindigkeitsprofil modelliert wird, wird die exakte Lösung der entsprechenden PBE in Form der konfluenten Heun-Funktion (CHF) hergeleitet. Mittels einer Stabilitätsanalyse wird die Eigenwertgleichung für das Stabilitätsproblem auf Grundlage der exakten Lösung der PBE hergeleitet und die zeitliche und räumliche Stabilität untersucht. Zunächst werden asymptotische Analysen der Eigenwertgleichung durchgeführt und analytische Lösungen für die betrachteten Grenzfälle erhalten. Anschließend werden Lösungen der Eigenwertgleichung berechnet, die ein umfassendes Bild des Stabilitätsverhaltens der exponentiellen Grenzschicht ermöglichen. Insbesondere werden die ersten drei akustischen Moden als Funktion der Machzahl, der Wellenzahl und der Frequenz berechnet. Es werden instabile Moden gefunden, wobei die erste akustische Mode immer die instabilste aller akustischen Moden ist. Außerdem wird eine akustische Grenzschichtdicke (ABLT) definiert, die im Wesentlichen quantifiziert, wie weit Eigenfunktionen in den Bereich fern der Grenzschicht reichen. Weiterhin werden ein Wellenwinkel, der die Richtung der Phasengeschwindigkeit beschreibt, sowie die Eigenfunktionen der akustischen Moden dargestellt. Schließlich werden Zusammenhänge zwischen den Eigenwerten der zeitlichen und der räumlichen Stabilitätsanalyse hergestellt. Zur Untersuchung der Akustik von Grenzschichtströmungen wird erneut die exakte Lösung des PBE genutzt, um den Reflexionskoeffizienten als Funktion von der Machzahl, der Wellenzahl und dem Einfallswinkel der akustischen Wellen abzuleiten und in weiten Parameterbereichen zu berechnen. Es wird gezeigt, dass eine Überreflexion akustischer Wellen in Grenzschichtströmungen auftreten kann, d. h. die Amplitude der reflektierten akustischen Wellen größer ist als die der einfallenden Wellen. Es wird nachgewiesen, dass dieses Phänomen eng mit der kritischen Schicht zusammenhängt, bei der ein optimaler Energieaustausch von der Grundströmung in die akustische Welle stattfindet. Gleichzeitig wird ein spezielles akustisches Phänomen, die resonante Überreflexion, beobachtet und nachgewiesen, dass dieses durch die Resonanzfrequenz zeitlicher instabiler Moden verursacht wird. Darüber hinaus tritt die resonante Überreflexion auch bei Resonanzfrequenzen höherer instabiler Moden auf, deren Überreflexionskoeffizienten jedoch immer kleiner sind als die durch die erste instabile Mode verursachten Überreflexionskoeffizienten. Im letzten Teil dieser Arbeit wird die Überreflexion akustischer Wellen in einer reibungsfreien, kompressiblen Überschall-Grenzschichtströmung durch direkte numerische Simulationen (DNS) verifiziert. Ein Wellenpaket, das ebene Wellen mit konstanten Wellenlängen und Amplituden enthält, wird mit der freien Strömung überlagert, und die Einfalls- und Reflexionsprozesse des Wellenpakets werden simuliert. In den Simulationen ist in Wandnähe die Dispersion des Wellenpakets aufgrund starker Scherungseffekte deutlich zu beobachten. Wenn die reflektierte Welle schließlich

in die freie Strömung zurückkehrt, wird eine Verstärkung der Amplitude der reflektierten Wellen festgestellt. Ein außergewöhnlicher Überreflextionskoeffizient tritt insbesondere dann auf, wenn die Frequenz der einfallenden Welle in der Nähe der Resonanzfrequenz liegt, was auf das Auftreten der resonanten Überreflexion hinweist und die Ergebnisse aus der theoretischen Analyse bestätigt.

Acknowledgements

The present thesis contains the results of all my research over the past four years. It is my great honour to contribute in a small part to the stability problem and acoustics of compressible boundary layers. This thesis owes its completion to many people's guidance, support, and assistance.

First of all, I would like to express my deepest gratitude to my supervisor, Prof. Dr. Martin Oberlack, who provided me with the opportunity to work on this PhD thesis at the Chair of Fluid Dynamics (FDY), TU Darmstadt. He gave me unlimited support and encouragement despite my hesitations and doubts. I still vividly remember his comments when reviewing my first manuscript, each line demonstrating his professionalism and dedication to his PhD students. All the work I have done would not have been possible without his guidance and valuable advice. In addition, I would like to thank Prof. Dr. Sadiki sincerely. I want to express my boundless gratitude for his time and effort in being my reviewer and for all his valuable feedback.

In terms of the specifics of this thesis, I am grateful to Simon for his contribution to the complicated branch cut issues, the in-depth discussions on critical layers, and his many times' revision of our paper. I would also like to thank Lara for her thorough summaries of acoustics and for supporting me at every moment during the writing phase of the thesis. Felician built the BoSSS code for an exponential compressible boundary layer and spent a lot of time and effort discussing related issues with me, which is crucial for the last part of this thesis. I want to thank Jan for his work on the spatial stability problem. I would like to express my sincere gratitude (in alphabetical order) to Dario, Felician, Jens, Juan, Lara, and Simon for the careful proofreading of this thesis and the valuable comments.

I would like to thank all my colleagues in the Turbulence Group for their impressive presentations at the weekly group meetings, whether they were on the other side of the video or sitting next to me as before. The pressure of the weekly meetings is undoubtedly very high, but everyone always manages to show amazing ideas under such pressure, allowing me to grow quickly with the inspiration of my peers as well. I would like to especially thank Dario, my former office mate, who is very reliable and hard-working. We always had in-depth communication and shared ideas about work and life. In addition, my former colleagues, Alpa and Tim, were always there to respond promptly to my questions and share their knowledge, skills, and experiences. I am also grateful to Dominik for providing numerous mathematical support and to Benjamin for sharing experiences in software and writing papers.

The help I received from my colleagues in the Numerical Group cannot be underestimated. They are always very patient in answering my questions as a beginner. Special gratitude is owed to Florian, who put in a lot of time to help me, including solving many IT problems. I would also like to thank Juan. He introduced me to BoSSS code and spent considerable time helping me step by step, even after working hours. Further, I am grateful to Matthias and Jens, who provided me with help countless times to solve problems that I could not have solved on my own.

Moreover, I am thankful to Ruth for all her work on organisational matters. She was always in the background and organised everything so that my work at FDY could be frictionless.

I am pretty much obliged to Prof. Dr. Wang for his help over the past four years. He was the one who read my first manuscript and gave me valuable advice and encouragement, who guided my project application in detail, and who constantly cared for me. I would also like to thank my two Chinese colleagues, Liu Jie and Sun Weihang, for always being there to offer help. Having a similar background allows us to interact in more ways, and I'm sure the friendship will not stop.

Finally, but most importantly, I am extremely grateful to my wife and family. I am deeply thankful to my parents, who believed in and supported all my choices from a young age. They have never pressured me but have always supported me in my PhD research despite the persistence of the pandemic that has exacerbated our geographical separation. I am extremely grateful to my wife, who has always been by my side, communicating thoroughly with me and analysing rationally so that I can always make confident decisions. I could never have finished this thesis without their tremendous support during my PhD.

Parts of this work were funded by the Deutsche Forschungsgemeinschaft (DFG, German Research Foundation) – OB 96/55-1 – 456793479. Some numerical simulations were conducted on the Lichtenberg high-performance computer at the Technical University of Darmstadt.

Contents

List of Figures

List of Tables

List of Abbreviations

1-D	one-dimensional
2-D	two-dimensional
3-D	three-dimensional
AA	acoustic analogy
ABLT	acoustic boundary layer thickness
APU	Auxiliary Power Unit
BLAS	Basic Linear Algebra Subprograms
BoSSS	Bounded Support Spectral Solver
CAA	Computational Aeroacoustics
CFD	Computational Fluid Dynamics
CFL	Courant-Friedrichs-Lewy
CHE	confluent Heun equation
CHF	confluent Heun function
CNS	compressible Navier-Stokes
CRE	compressible Rayleigh equation
DFLD	Deutsche Fluglärmdienst e.V.
DG	discontinuous Galerkin
DG IBM	discontinuous Galerkin immersed boundary method
DNS	direct numerical simulation
EOS	equation of state
FDM	Finite Difference Method
FEM	Finite Element Method
FVM	Finite Volume Method
GFD	geophysical fluid dynamics
GHE	general Heun equation
GHF	general Heun function
GPU	graphics processing unit
HHLR	Hessischer Hochleistungsrechner
HLLC	Harten-Lax-van Leer-Compact
HPC	High-Performance Computing

IBVP	initial-boundary-value problem
LAPACK	Linear Algebra Package
LEE	linearised Euler equation
LES	large eddy simulations
LHS	left-hand side
LTS	local time-stepping
MPI	Message Passing Interface
NRBC	non-reflecting boundary condition
ODE	ordinary differential equation
PBE	Pridmore-Brown equation
PDE	partial differential equation
RHS	right-hand side
RK	Runge-Kutta
TBL	turbulent boundary layer
XDG	extended discontinuous Galerkin

List of Symbols

A	Constant in the Fuchs-Frobenius series
a_1	The first coefficient function of asymptotic analysis for small α
a_2	The second coefficient function of asymptotic analysis for small α
a_3	The third coefficient function of asymptotic analysis for small α
α	Wavenumber in x-direction
α_i	Imaginary part of the wavenumber α
α_r	Real part of the wavenumber α
α_*	The second parameter of the CHF
α_{**}	The second parameter of the CHF, alternative form
α^*	Non-dimensional wavenumber in x-direction
$\bar{\alpha}$	Non-dimensional wavenumber in x-direction scaling by c_0
$\tilde{\alpha}$	Dimensional wavenumber in x-direction
$\tilde{\alpha}_i$	Imaginary part of the dimensional wavenumber $\tilde{\alpha}$
$\tilde{\alpha}_r$	Real part of the dimensional wavenumber $\tilde{\alpha}$
$\tilde{\alpha}_*$	The second parameter of the CHF defined in (2.38)
B	Constant in the Fuchs-Frobenius series
b_1	The first coefficient function of asymptotic analysis for large α
b_2	The second coefficient function of asymptotic analysis for large α
b_3	The third coefficient function of asymptotic analysis for large α
β	Wavenumber in y-direction
β_i	Imaginary part of the wavenumber β
β_r	Real part of the wavenumber β
C_1	The first free parameter of the solution to the PBE (2.35)
C_2	The second free parameter of the solution to the PBE (2.35)
C_{1*}	The first free parameter of the solution to the CHE (A.8)
C_{2*}	The second free parameter of the solution to the CHE (A.8)
C_1'	The first free parameter of the solution to the degenerate PBE (3.35)
C_2'	The second free parameter of the solution to the degenerate PBE (3.35)
$\mathbb{C}$	Complex number
c	Speed of sound
c_0	Constant speed of sound
c_1	The first coefficient function of asymptotic analysis for small ω
c_2	The second coefficient function of asymptotic analysis for small ω
c_3	The third coefficient function of asymptotic analysis for small ω
c_∞	Speed of sound of the free stream
c_k	Coefficient of a three-term recurrence relation

c_r	Resonant phase velocity
c_*	Constant
χ	Transformation of the independent variable y
d_1	The first coefficient function of asymptotic analysis for large ω
d_2	The second coefficient function of asymptotic analysis for large ω
d_3	The third coefficient function of asymptotic analysis for large ω
Δ	Step size
δ	Boundary layer thickness
δ_a	acoustic boundary layer thickness (ABLT)
δ_{ij}	Kronecker delta
δ_*	The fourth parameter of the CHF
δ_{**}	The fourth parameter of the CHF, alternative form
$\tilde{\delta}_*$	The fourth parameter of the CHF defined in (2.38)
e	Euler's number
ϵ	Infinitesimal
ϵ_1	The first function of T_w, T_∞ and T_{aw}
ϵ_2	The second function of T_w, T_∞ and T_{aw}
ϵ_{**}	The fifth parameter of the CHF, alternative form
f	Frequency
Γ	Gamma function
γ	Heat capacity ratio
γ_*	The third parameter of the CHF
γ_{**}	The third parameter of the CHF, alternative form
$\tilde{\gamma}_*$	The third parameter of the CHF defined in (2.38)
I	Quasi-invariant
$\Im$	Imaginary part of a complex number
i	Imaginary unit
J_ν	Bessel function of the first kind
k	Wavenumber
k_1	The first coefficient of asymptotic expansion of ω for small α
k_2	The second coefficient of asymptotic expansion of ω for small α
k_3	The third coefficient of asymptotic expansion of ω for small α
$\boldsymbol{k}$	Wavenumber vector
L_p	Sound pressure level
L_x	Horizontal length of the computational domain
L_y	Vertical length of the computational domain
l_0	Mean free path
l_1	The first coefficient of asymptotic expansion of ω for large α
l_2	The second coefficient of asymptotic expansion of ω for large α

l_3	The third coefficient of asymptotic expansion of ω for large α
l_∞	Characteristic length
λ	Wavelength
M	Mach number
M_0	Mach number of the base flow
M_c	Critical Mach number of instability
m_1	The first coefficient of asymptotic expansion of α for small ω
m_2	The second coefficient of asymptotic expansion of α for small ω
m_3	The third coefficient of asymptotic expansion of α for small ω
$\mathbb{N}$	Natural number
n_1	The first coefficient of asymptotic expansion of α for large ω
n_2	The second coefficient of asymptotic expansion of α for large ω
n_3	The third coefficient of asymptotic expansion of α for large ω
$\boldsymbol{n}$	Normal vector
$\boldsymbol{\nabla}$	Nabla operator
ν	Parameter of Bessel functions
ν_0	Kinematic viscosity
$\mathcal{O}$	Landau notation
ω	(angular) Frequency
ω_i	Imaginary part of the frequncy ω
ω_r	Real part of the frequncy ω
ω^*	Non-dimensional (angular) frequency
$\bar{\omega}$	Non-dimensional (angular) frequency scaling by c_0
$\tilde{\omega}$	Dimensional (angular) frequency
$\tilde{\omega}_i$	Imaginary part of the dimensional frequency $\tilde{\omega}$
$\tilde{\omega}_r$	Real part of the dimensional frequency $\tilde{\omega}$
PV	Cauchy's principal value
p	Pressure
p_0	Pressure of the base flow
p_{ref}	Standarlised reference pressure
p_*	The first parameter of the CHF
p'	Pressure perturbation
p^*	Non-dimensional pressure
$\hat{p}$	Amplitude of pressure perturbation
$\tilde{p}$	Root mean square value of the sound pressure
$\tilde{p}_*$	The first parameter of the CHF defined in (2.38)
ϕ	Angle between $\boldsymbol{k}$ and x-direction
ϕ_c	Critical angle for the presence of a critical layer
ϕ_s	Angle of zone of silence
ϕ_{s_0}	Lower border of zone of silence for $M \leq 2$
ϕ_{s_1}	Upper border of zone of silence
ϕ_{s_2}	Lower border of zone of silence for $M > 2$
ψ	Propagation angle

q_{**}	The first parameter of the CHF, alternative form
R	Reflection coefficient
$\mathbb{R}$	Real number
$\mathcal{R}$	Specific gas constant
$\Re$	Real part of a complex number
r	Parameter of indicial equation
r_1	The first root of indicial equation
r_2	The second root of indicial equation
ρ	Density
ρ_0	Density of the base flow
ρ_∞	Density of the free stream
ρ'	Density perturbation
$\hat{\rho}$	Amplitude of density perturbation
$\hat{\rho}^*$	Conjugate solution of $\hat{\rho}$
s	Entropy
s_0	Entropy of the base flow
σ_*	The fifth parameter of the CHF
$\tilde{\sigma}_*$	The fifth parameter of the CHF defined in (2.38)
T	Tempearture
T_0	Temperature of the base flow
T_{aw}	Adiabatic wall temperature
T_{ij}	Lighthill stress tensor
T_∞	Free stream temperature
T_w	Wall temperature
T^*	Non-dimensional temperature
t	Time
τ_{ij}	Stress tensor, with $i, j \in \mathbb{N}$
Θ	Angle between the phase velocity and x-direction
θ	Parameter defined by (2.36) for the sake of simplicity
θ_i	Imaginary part of the parameter θ
θ_{i_s}	Imaginary part of the parameter θ for the spatial stability problem
θ_{i_t}	Imaginary part of the parameter θ for the temporal stability problem
θ_r	Real part of the parameter θ
θ_{r_s}	Real part of the parameter θ for the spatial stability problem
θ_{r_t}	Real part of the parameter θ for the temporal stability problem
U_∞	Velocity of the free stream in x-direction
u	Velocity in x-direction
u_0	Velocity of the base flow in x-direction
u_i	Velocity in i-direction
u'	Velocity perturbation in x-direction
$\hat{u}$	Amplitude of velocity perturbation in x-direction

V	Volume
v	Velocity in y-direction
v_0	Velocity of the base flow in y-direction
v_g	Group velocity
v'	Velocity perturbation in y-direction
$\hat{v}$	Amplitude of velocity perturbation in y-direction
$\boldsymbol{v}$	Velocity vector
$\boldsymbol{v_0}$	Velocity vector of the base flow
$\boldsymbol{v'}$	Velocity perturbation vector
$\hat{\boldsymbol{v}}$	Amplitude of velocity perturbation vector
w	Solution to the CHE
x	Horizontal direction
$\boldsymbol{x}$	Space vector
ξ	Transformed coordinate defined in (A.29)
Y_ν	Bessel function of the second kind
y	Vertical direction
y_c	Location of the critical layer
y^*	Non-dimensional distance in y-direction
$\tilde{y}$	Transformation of the independent variable y
Z	Acoustic impedance
$\mathbb{Z}$	Integer
z	Argument of hypergeometric functions

1 Introduction

The present thesis summarises my work over the past four years at the Chair of Fluid Dynamics (FDY) at the Technical University of Darmstadt. It is noted that it contains contents of the following papers in slightly modified forms. All these papers result from my work as a research assistant:

- Zhang, Y. & Oberlack, M., 2021 Inviscid instability of compressible exponential boundary layer flows. *AIP Advances*, *11*(10), 105308.
- Zhang, Y., Görtz, S. & Oberlack, M., 2022 Over-reflection of acoustic waves by supersonic exponential boundary layer flows. *Journal of Fluid Mechanics*, *945*.
- Baumgärtener, J-B., Zhang, Y. & Oberlack, M., 2022 Spatial acoustic instabilities in boundary layer flows. Considering for the publication of *Physics of Fluids*.

Unsteady flows of compressible fluids, e.g. turbulence, or vortex separations, are a major cause of noise generation in numerous technical applications. Therefore, the understanding and prediction of flow-induced noises are of great technical relevance and, at the same time, imply an interesting and complex problem of compressible fluid dynamics. Of particular importance is the acoustics of shear flows such as jets, wakes, and boundary layer flows, which play central roles in the noise emission of air traffic. Especially in high-speed shear flows, flow-induced noise exceeds the other noise levels and dominates. For example, jets exhaust by air engines of civil airliners on take-off constitute the most dominant noise source, whose noise level exceeds those of other sources like fans, combustion, and airframe noise (Brun et al., 2008). However, to date, both the problems of sound generation and propagation in modelled engineered shear flows are not fully understood. Although in recent years, the theory of compressible linear shear flows has been gradually improved, there is still a considerable lack of theories for other more complex types of shear flows, e.g. boundary layer flows. This situation motivated us to investigate the stability problem and acoustics in compressible boundary layer flows, which shed some light on understanding laminar-turbulent transition, and sound generation and propagation in such compressible shear flow.

The problems in flow acoustics were classified by Möhring et al. (1983) into three categories: (i) generation of sound with essential participation of the flow; (ii) propagation of sound through flow fields; (iii) generation of flow by sound. In the present work, we only focus on the first two issues.

1.1 Acoustics

Before we begin with flow acoustics, let us revisit some of the knowledge about acoustics. The essence of sound is mechanical deformation fluctuations that propagate in the form of acoustic waves through an elastic transmission medium such as a gas, liquid, and solid. When we talk about acoustic waves, this points to a broader concept. They can be waves that are perceptible to the human ear (sound waves), or they can be waves that are outside the threshold of the human ear (infrasonic or ultrasonic waves). When we refer to the terms sound and noise, they both stand for sounds that can be perceived by the human ear. The former is generally a neutral term, while the latter is associated with a negative attitude, indicating a sound that is subjectively unwanted and considered disturbing.

1.1.1 Generation and propagation of acoustic waves

Since acoustic waves are mechanical waves, we first give some elementary properties of mechanical waves before talking about acoustic waves more specifically. Mechanical waves can be classified into transverse and longitudinal waves. A transverse wave is a wave whose direction of vibration is perpendicular to the direction of wave propagation, while a longitudinal wave is a wave whose direction of vibration coincides with the direction of wave propagation. A pulse on a rope is a typical example of transverse waves. The rope moves up and down as the wave pulse travels from the start to the end of the rope, but the rope itself does not experience any net motion. A mechanical vibration caused by the compression and elongation of the spring creates typical longitudinal waves. The propagation of mechanical waves must require a medium because the essence of mechanical wave propagation is a propagation of the vibrating state of the medium, i.e. propagation of the disturbance rather than individual particles in the medium.

The propagation of sound is in the form of acoustic waves. Like other mechanical waves, the propagation of acoustic waves presupposes a transmission medium with moving particles. It is pointless to talk about sound in the absence of a medium because a sole source, such as a vibrating structure, does not produce sound. This fact enables the study of acoustic waves to be divided based on different media in which acoustic waves propagate. Therefore, depending on the transmission medium, a classification is made between structure-borne sound and fluid-borne sound (De Broeck, 2021).

Structure-borne sound is the most common sound source and the way of sound propagation. The dynamic interaction of solid bodies leads to structure-borne sound. The cause of the acoustic oscillations and their propagation in solid bodies are the coupling forces between the particles of the solid. When a particle is displaced relative to neighbouring molecules, such as an impact-induced displacement, they act as restoring forces, resulting in oscillatory motion of the particle. Due to coupling effects, the oscillation is transferred to the neighbouring molecules, leading to a spatial propagation of the deformation in the form of acoustic waves. As a result, structure-borne sound can occur as a variety of wave types, e.g. as longitudinal, transverse, or Rayleigh waves (Kuttruff, 2007).

Fluid-borne sound is the counterpart of structure-borne sound. Compared to solids, the coupling forces between the particles of liquids and gases are negligible. Therefore, the particles can move freely between each other. For this reason, the oscillatory motion of fluid particles and the transmission of such oscillations to neighbouring molecules are caused exclusively by collisions between the fluid particles (De Broeck, 2021). Hence, fluid-borne sound propagates only in the form of longitudinal waves since fluids are not able to sustain tensile forces. Therefore, as acoustic waves travel in fluids, the medium expands and contracts in the propagation direction.

As carriers of sound, acoustic waves are an expression of energy transfer. Therefore, in addition to the classification in terms of the type of transmission media, the generation of acoustic waves can be classified according to the sources of energy, including mechanical source, electromagnetic source, chemical source, and heat source (Müller & Möser, 2012).

1.1.2 Phase velocity, group velocity and signal velocity

An important concept involved in sound propagation is the velocity at which acoustic waves travel. In real physics, wave propagation involves a wave packet containing a finite number of wave cycles. The information in a wave can only be delivered by starting, stopping, or modulating the amplitude of the wave train, which equivalents a formation of a wave packet. The propagation of a wave packet can occur at up to three velocities, which are the phase velocity, the group velocity, and the signal velocity. The phase velocity is the velocity of each wavelet. The group velocity is the velocity of the instantaneous points on the shape of the envelope, i.e. the velocity of the shape of the envelope. Since the shape of the wave packet may change with time, leading to a change in the energy distribution, the third velocity appears. The signal velocity, also known as the energy velocity, is generally regarded as the actual velocity of the wave packet. More precisely, the signal velocity is defined as the velocity of the leading edge of the energy distribution of the wave packet and the corresponding information content (Cline, 2017).

In a system where the shape of the wave packet is time-independent, the group velocity and the signal velocity are equal. It is therefore always assumed in some literature that the group velocity is the true velocity at which the energy propagates, which is true for most linear systems. However, this assumption is not valid if the shape of the wave packet is time-dependent because the group velocity and the signal velocity can differ. It is worth noting that even if the phase velocity of the waves within the wave packet is faster than the group velocity of the shape or faster than the signal velocity of the energy content of the wave packet envelope, the information contained in the wave packet only manifests itself when the wave packet envelope completely reaches the detector. The energy and information can only propagate at a signal velocity (Cline, 2017).

In a dispersive system, the group velocity and signal velocity can differ. A dispersive system is defined as a system where the phase velocity as the velocity of each wavelet is related to the wave frequency or wavelength, which is the counterpart to the non-dispersive system. Thus, the wavelets contained within a wave packet will have different phase velocities due to their different frequencies or wavelengths. Based on this fact, some of them propagate faster and some slower, thus creating dispersion in the wave packet, i.e. the packet becomes flattened with increasing time during the propagation. The group velocity at this point is the instantaneous velocity of the points on the wave packet envelope, i.e. the velocity at a particular relative position defined by the shape of the wave packet envelope, and therefore is not the signal velocity of the wave packet.

For an acoustic wave packet propagating in an idealised stationary medium, the group velocity and signal velocity are the same. Acoustic waves generated by different frequencies propagate at different wavelengths but with the same velocity, i.e. the speed of sound, and therefore have no dispersion. In a moving medium, due to the velocity of the medium, acoustic waves could propagate at different velocities. In particular, a shear flow with a velocity gradient can be regarded as a dispersive medium.

In the present work, acoustic waves in three different scenarios are considered, namely radiative dispersive waves in stability problems, propagating waves in acoustics problems, and the propagation of wave packets in numerical simulations. In all scenarios, acoustic waves with different phase velocities are observed. This is due to the superposition of the speed of sound and the base flow velocity of the shear layer flow. In the stability problem, we obtain the phase velocity of the perturbation of acoustic modes, which can be subsonic and supersonic. Due to the decay of the amplitude of the perturbation in the positive y-direction, we know that the energy is transmitted, which indicates that the direction of energy propagation should be concerned. We therefore consider the group velocity in the free stream, which is derived from the dispersion relation. The direction of the group velocity is regarded as the real propagation direction of acoustic waves. We refer to such waves with decaying amplitudes in the y-direction in the stability problems as dispersive waves. Note that in the system of the stability problems, there is no signal velocity because the modes and eigenfunctions are not specific to a wave packet. Therefore, it is reasonable to consider the group velocity as the velocity of energy propagation. In contrast to the stability problem, in the acoustic problem, the waveform does not vary with time in the free stream. We do not consider the energy transfer, i.e. the group velocity. The phase velocity is therefore regarded as the velocity of the wave propagation. In numerical simulations, we consider the effects of the dispersion of a wave packet. This is evident when the speed gradient is large. In addition to this, dispersion exists even in the free stream. This is due to the presence of wavelets with different wavelengths in the wave packet, which leads to the dispersion of the wave packet according to the dispersion relation in the free stream. Consequently, the signal velocity is inconsistent with the group velocity in the numerical simulation of the wave packet.

1.2 Aeroacoustic noise

If you live in Frankfurt am Main, you may have noticed the loud noise of aeroplanes flying overhead. Frankfurt has the busiest airport in Germany, which is located just twelve kilometres from the city centre. At this airport, aeroplanes take off and land every minute. No matter where you live in Frankfurt, you cannot avoid the air traffic noise because the flight routes may be temporarily rescheduled due to weather, air traffic jams, etc. With the growing volume of air traffic, increasingly stricter regulations on noise emissions have been enforced, with the aim of limiting the total noise emission. This has become the main restriction on airport operations.

According to the report *Frankfurt Airport Air Traffic Statistics 2019*, the number of aircraft take-offs and landings has increased from $439,093$ to $513,912$ in the 20 years from 1999 to 2019. Meanwhile, the number of passengers has increased from 45 million to 70 million. Air traffic in Frankfurt was growing steadily at a rate of around 2 % per year from 1999 to 2019. At the same time, data obtained from Deutsche Fluglärmdienst e.V. (DFLD) indicate that noise near the airport is increasing every year. This has led the authorities to adopt stricter restrictions to reduce aircraft noise. However, the restrictive measures are limited to curfews, reduced entry speeds, reduced cruising speeds, and other sacrifices to efficiency, which may not only affect the economy and travel times but also increase fuel consumption and pollutant emissions. Therefore, the development of quieter aircraft is an important objective for the next generation of civil aeroplanes in the following two decades (Airbus, 2020). This requires significant progress in noise reduction by the aircraft themselves since flight noise causes damage not only to the ground but also to pilots and passengers.

One of the main sources of civil aircraft noise is from jet engines of aeroplanes. Noise from jet engines is mainly caused by three aspects (Filippone, 2014): (i) jet engine ducts including inlets and nozzles (Tack & Lambert 1965 Mariano 1971; Ishii & Kakutani 1987; Pagneux & Froelich 2001; Khamis & Brambley 2016); (ii) jet exhaust and jet mixing (Balsa 1976; Gutmark et al. 1995; Tam 1995b; Tam et al. 2008; Karabasov 2010); (iii) the boundary layer (Goldstein 1982; Myers & Chuang 1984; Almgren 1986; Nash et al. 1999; Liu 2008; Brambley 2011a). All these three aspects include flows that invariably point to one type of flow model, shear flows. To understand the mechanism of noise generation by these three aspects, we need first to go back to over 70 years ago. Since the 1950s, the mechanism of jet engine noise generation and consequent noise reduction has been rapidly developed. This was thanks to a young interdisciplinary discipline, aeroacoustics[1], which mainly involves the fields of fluid dynamics and acoustics. Aeroacoustics focuses on the sound generated by the unsteady motion of fluids, such as propeller noise or jet engine noise. The main difference between aeroacoustics and classic acoustics mentioned in §1.1 is that the fluid medium in motion has a non-negligible influence on both the generation and propagation of sound, which is the most important topic in aeroacoustics.

Howe (1978) classified theoretical approaches to aeroacoustics into three categories: (i) acoustic analogy methods; (ii) methods based on linearised wave equations; (iii) empirical/semi-empirical methods. In this context, it is inevitably to first mention the milestone work by Lighthill and his famous acoustic analogies, which made a significant contribution to the mechanism of aerodynamic noise generation.

1.2.1 Acoustic analogies

Based on the background of high-speed development of jet aircraft engineering, Lighthill first came up with the idea of an acoustic analogy (AA) in his pioneering papers (Lighthill, 1952, 1954), regarded as the foundation for aeroacoustics. Since then, a new discipline has been opened. The basic framework of acoustic analogies is essentially about the re-arrangement of the Navier-Stokes equations for a compressible flow to an equation for an acoustic variable of interest, e.g. density. The subtlety of Lighthill's equation is that it is exact, and it characterises as a wave equation with source terms. Lighthill's equation reads

$$\frac{\partial^2 \rho'}{\partial t^2} - c^2 \frac{\partial^2 \rho'}{\partial x_i \partial x_i} = \frac{\partial^2 T_{ij}}{\partial x_i \partial x_j}, \tag{1.1}$$

[1] The term aero-acoustics appeared around the 1970s and thereafter was simplified to aeroacoustics and included in the Oxford English Dictionary. If underwater applications are considered, the more general terminology would be flow-induced noise.

where $T_{ij} = \rho u_i u_j + \left(p' - c^2 \rho\right) \delta_{ij} - \tau_{ij}$ is the Lighthill stress tensor, including Reynolds' stress tensor, pressure forcing, and viscous stress tensor in sequence. In this way, the left-hand side (LHS) of the equation resolves into the form of a d'Alembert operator similar to that of classical acoustics, i.e. an acoustic wave equation, while the right-hand side (RHS) is all sound sources. Hence, the essence of this equation is the separation of the aerodynamic sound source term from the acoustic field. These sources can be decomposed into monopole, dipole, and quadrupole. It should be noted that the RHS of this equation still contain the correlation term on the LHS so that it is much more complicated than a classical wave equation and hence difficult to solve. However, Lighthill still provided solutions to the equations through models, which are similar to the various turbulence models that solve the Navier-Stokes equations.

The key of Lighthill's AA is to assume that the sound source generated by the fluid is known and then to use experimental or numerical methods to obtain the solution of the flow field and the sound field. Such an approach brings great convenience for practical applications and explains the most prominent features of aeroacoustic sound generation while inevitably leading to some new issues. The original AA concerned only sound generated by turbulent flow in a region of unbounded medium, which is not realistic. In addition, by artificially separating the flow field from the sound field, it is not possible to investigate how acoustic waves are generated and propagate in fluids. For these reasons, to improve Lighthill's AA theory, many subsequent studies on flow-induced noise were inspired: (i) effects of solid boundaries at rest (Curle 1955); (ii) theory of vortex sound (Powell 1964; Howe 1975); (iii) the effects of moving objects on the sound field (Ffowcs Williams & Hawkings, 1969); (iv) the duality of jet noise (Michalke & Fuchs, 1975; Michalke, 1977); (v) flow-acoustic interactions (Phillips 1960; Doak 1972; Lilley 1974; Mani 1976).

Based on these extensions of Lighthill's AA theory, Goldstein (1984) further developed Lilley's equation into the generalised AA. He started from the Navier-Stokes equations, divided the flow variable into its mean and fluctuating components, and then subtracted the mean flow components from the equation. Next, he collected all linear terms in the governing equation on one side of the equation as the part that describes sound propagation while placing all non-linear terms as known sources on the other side of the equation. Since then, the idea of linearisation has gradually developed, combining classical acoustics with aeroacoustics. Goldstein's generalised AA allows a detailed investigation of the acoustic sources associated with flows and therefore is considered to be particularly suitable for predicting sound generated by perturbations in parallel shear flows. However, Goldstein's equation can only be solved by numerical methods or expensive volume integration. In addition, it completely ignores sound generated by linear sources, which is a serious drawback. In fact, no AA theory has so far succeeded in completely isolating the source terms from the linear term in the acoustic perturbation for a shear flow (Colonius et al., 1997). Nevertheless, linear mechanisms are validated to play a key role in sound generation related to shear flow dynamics (Michalke & Fuchs 1975; Chagelishvili et al. 1997b; Goldstein 2003; Goldstein 2005).

The AA method gives aeroacoustic sources, such as pressure fluctuations on wall surfaces, which create dipole sources. However, it does not answer how pressure fluctuations generate sound (Zhong & Huang, 2018). For example, do the pressure fluctuations compress the wall surface like a drum membrane? Or does the turbulent structure in the boundary layer near the wall stretch, twist and finally break to generate sound? To answer questions like these, it is necessary to consider the approach based on the linearised wave equation summarised by

Howe (1978). More importantly, such methods reveal the linear mechanism of aeroacoustic noise generation.

1.2.2 Linear acoustics

To begin with, it is necessary to understand why the linearisation approach is applicable to acoustic studies. The fundamental of linear acoustics is based on the linearised Euler equations (LEEs). The LEEs are the classical equations for the study of acoustics for long, and the wave equation derived from the LEEs well describes the propagation of sound (Bergmann, 1946). The plausibility of the LEEs as the governing equations for acoustic waves arises from two aspects: (i) neglectability of viscous effects, reducing the Navier-Stokes equations to the Euler equations, and (ii) small perturbations, allowing linearisation in terms of small perturbations.

The fact that viscous effects can be neglected in acoustics can be pointed out with the help of the so-called acoustic Knudsen number. For a general gas, there is the relation $\nu_0 \sim cl_0$, where ν_0 is the kinematic viscosity, c stands for the speed of sound, and l_0 represents the mean free path of the molecules (Rienstra & Hirschberg, 2020). According to this relationship, the ratio of the wavelength of an acoustic wave ($\lambda = c/f$) to the mean free path of molecules l_0 reads

$$\frac{\lambda}{l_0} = \frac{\lambda c}{\nu_0} = \frac{\lambda^2 f}{\nu_0}, \tag{1.2}$$

known as the acoustic Knudsen number, where $\sqrt{\nu_0/f}$ is the diffusion scale and is successfully linked to the wavelength λ. For example, for air with $\nu_0 = 1.5 \times 10^{-5}$ m^2/s and a wave with $f = 1$ kHz, there is $\lambda^2 f/\nu_0 \sim 10^7$. This result means that the viscous effect will only become apparent after the acoustic wave has travelled a distance of approximately 10^7 times the wavelength, i.e. $3 \cdot 10^6$ m. Kinematic viscosity is therefore a rather unimportant effect, and it is reasonable to be neglected.

To explain why the assumption of small perturbations and thus linearisation is appropriate, the sound level can be used. Sound levels are measured in decibels. A common indicator is the sound pressure level, which is defined as

$$L_p = 20\text{lg}\left(\frac{\tilde{p}}{p_{\text{ref}}}\right), \tag{1.3}$$

where $p_{\text{ref}} = 2 \times 10^{-5}$ Pa is the standardised reference pressure and $\tilde{p} = \sqrt{\overline{(p')^2}}$ is the root mean square value of the sound pressure. For example, for a weed whacker operating at full capacity, its maximum sound pressure level is approximately 88 dB, which corresponds to 0.5 Pa. This is also roughly equivalent to the noise level of a Boeing 787-8 taking off and landing (Heathrow-Airport, 2014). Even a very loud noise of 120 dB corresponds to 20 Pa, which is to be compared with the standard atmosphere, 10^5 Pa. By comparing 20 Pa with the 10^5 Pa one can see that threshold of acoustic perturbations can be considered small compared to the mean values of the flow variables.

Therefore, with the two reasons above, the governing equation for acoustic waves can be derived by the linearisation of the inviscid Euler equations, i.e. LEEs. However, the validity of the two assumptions made is limited to the level of daily sound. Normally, above 120 dB sound waves appear non-linear while below that waves can be considered as basically linear in propagation.

The shortcomings of AA are essentially related to the oversimplified flow-acoustic interactions (Sinayoko et al., 2011), which are highly coupled and not easily decoupled (Goldstein, 2005). Faced with this scenario, some researchers in the aeroacoustic community returned to classical linear acoustics based on the LEEs.

Modal analysis is a classical approach to studying linear acoustics. It originates from the study of the dynamic properties of systems. In modal analysis, the crucial step is to determine the resonant frequencies as well as the modes. These results describe the basic dynamical behaviour of a system and indicate how the system will react to the loading of the dynamics. Resonant frequencies (also called eigenfrequencies) are the frequencies that a system naturally tends to have when it is disturbed. For example, each string on a piano is tuned to vibrate at a specific frequency and integer multiples of its frequency. The function describing the oscillation at each resonant frequency is called the eigenfunction. The resonant frequency and the eigenfunction are functions of the properties and boundary conditions of a system. In addition, the terminology, mode, is used to describe a state of dynamic systems to the excitation. Instability is an important terminology to describe the state of the system after disturbances, meaning that an infinitesimal perturbation is amplified and grows to a finite or infinite size. The growth of the perturbation can be exponential or algebraic. Based on these basic concepts, an unstable mode is a mode that leads to the occurrence of instability.

The most common modes in the modal analysis are normal modes that are orthogonal to each other. The method of employing normal modes is also called the normal-mode approach. The underlying idea of the normal-mode approach is that instead of solving a specific physical initial-boundary-value problem (IBVP), we consider normal modes of a system and expect that a solution for the IBVP of the partial differential equations (PDEs) can be represented as a sum of the normal modes. If there is an unstable mode, it is expected that this mode will be present in the solution of a specific physical problem (realised experimentally or solved numerically) and that this unstable mode can be dominant after sufficient amplification in space and/or time (Fedorov & Tumin, 2011).

In hydrodynamic stability analysis and linear acoustics, based on the normal-mode approach, linear mechanisms of sound generation, i.e. sound generated by unstable perturbations originally present in flows, were investigated and well explained in Marcus & Press (1977), Tam & Morris (1980), Criminale & Drazin (1990), and Goldstein (2005). Such a linear sound generation mechanism by a normal-mode dominant growth can be readily identified since the most unstable waves have a nominally supersonic phase velocity and are able to radiate sound efficiently. These linear mechanisms are particularly effective in flows with relatively high Mach numbers. Furthermore, both the analysis and experimental results show that linear terms can be an effective source of sound if the flow is sheared at high rates. Several studies employing the normal-mode approach for different shear flow models can be found in Crighton & Gaster (1976), Tam & Burton (1984a, 1984b), and Wu (2005) for supersonic jets, and in Avital et al. (1998a, 1998b) for mixing layers. In their studies, the linear mechanism of sound generation is proved to be highly related to shear effects of the flows. In addition to the study of the linear sound generation mechanism in shear flows, the phenomenon of radiation of sound by shear flows, known as spontaneous radiation of sound, has been well predicted by the normal-mode approach. This phenomenon was demonstrated by means of DNS. It was first discussed in detail in Landau & Lifshitz (1987) and was observed by numerical simulations in supersonic boundary layer flows (Wagnild, 2012), in highly cooled hypersonic boundary layer flows (Chuvakhov & Fedorov, 2016), and in hypersonic blunt cone boundary layers (Knisely & Zhong, 2019a, 2019b).

Another approach to studying linear acoustics is the so-called non-normal mode approach, which originated from the hydrodynamic stability community. This approach was established in the 1990s when the non-normal nature of shear flow systems was considered (Reddy & Henningson, 1993; Schmid, 2007) and soon applied to the realm of acoustics to study linear mechanisms of sound generation. In Chagelishvili et al. (1997a), an abrupt emergence of acoustic waves from vortices to spontaneous imbalance was found. Farrell & Ioannou (2000) extended the analysis to viscous high Mach number flows. Bakas (2009) showed that the spontaneous generation could be analysed as an instance of a Stokes phenomenon in which the wave solution is switched on by the vortex perturbation when time crosses a Stokes line. A wealth of research based on the non-normal approach explicitly indicates a mechanism of transient growth in sound generation.

In Nold & Oberlack (2013), they noticed a correlation between normal and non-normal modes through symmetry analysis and explained the correlation well using symmetry theory. Based on this, special base flows, such as a parabolic Poiseuille type flow or a linear shear flow, were found to have an extended set of symmetries, which have been used to derive more generalised stability modes. It was further shown in Hau et al. (2017) that the normal mode, as well as the non-normal (Kelvin) mode are subsumed under a common umbrella by a third new mode, which represents the most general approach. Based on this, they investigated the transient growth of perturbations in linear shear flows and further refined the theory of sound generation in linear compressible shear flows.

1.3 Numerical aeroacoustics

Over the last 60 years, the capabilities of Computational Fluid Dynamics (CFD) have constantly increased, and impressive progress has been made (Tam, 1995a; Wang et al., 2006). Utilising these capabilities of CFD is a major factor in ensuring the possibilities of the numerical study of aeroacoustic phenomena nowadays. Computational methods such direct numerical simulation (DNS) or large eddy simulations (LES) are particularly suitable tools for calculations of sound fields (Colonius & Lele, 2004; Wang et al., 2006). These tools facilitate the investigations being able to obtain all the flow quantities in space and time. The obtained high-fidelity numerical simulation results allow a post-process from different perspectives.

In spite of this, the major challenges of Computational Aeroacoustics (CAA) still remain and are summarised in (Tam, 2004) involving the following issues: (i) sufficient numerical resolution of short wavelengths with a minimal amount of grid points; (ii) low numerical noise to ensure that the sound waves, usually having amplitudes five to six orders smaller than the base flow field, are computed accurately; (iii) suitable boundary conditions, as sound waves are able to travel over long distances, contrary to ordinary flow disturbances, which might lead to spurious reflections at the outflow boundary conditions and hence contaminate the solution inside the computation domain; (iv) the existence of multiple scales varying over a wide range, demanding the code to be able to resolve a wide band of wavenumbers; (v) requirement for highly accurate algorithms to be able to simulate the nature of low dissipation and low dispersion of acoustic waves (Delorme et al., 2005).

In the past decades, facing these difficulties, higher-order discontinuous Galerkin (DG) methods (Cockburn et al., 2000) have achieved fruitful developments in the fluid dynamics community. Their advantages are (i) cell-locality, (ii) applicability to arbitrary geometries on unstructured grids, (iii) efficient parallelisation, (iv) suitable for a high order of degrees. These make them attractive to High-Performance Computing (HPC) applications (Altmann et al., 2013). Using DG methods, acoustic wave propagation can be simulated over long distances with low numerical dissipation and low numerical dispersion. Moreover, unstructured meshes are smoothly employed, which makes automatic mesh makers or mesh refinement techniques possible.

1.4 Objective and outline of this thesis

The objective of this work is to investigate the stability problems and acoustics of boundary layer flows. To achieve this, a velocity profile in exponential form is applied to mimic the boundary layer, and the governing equation, also known as the Pridmore-Brown equation (PBE), is derived. Of particular importance is that a new solution to the PBE in terms of the confluent Heun function (CHF) is found. A feature of the PBE is that it not only describes the stability of shear flow but is also an acoustic equation. The newly discovered solution motivates us to explore both of these aspects in detail.

In the aspect of the stability problem, the new exact solution allows a search for all eigenvalues in the complex domain, leading to precise physical results. These results correspond to unstable acoustic modes present in supersonic compressible shear flows. They could become dominant for laminar-turbulent transition in supersonic as well as hypersonic flows. In addition to instability, the unstable mode also exhibits outward radiation of acoustic waves. Therefore, it has important implications both for stability and noise generation. Especially in the context of the current rapid development of supersonic as well as hypersonic vehicles. The research in this thesis contributes to a deeper understanding of the stability of boundary layer flows.

In the aspect of acoustics, a particular wave reflection phenomenon, over-reflection of waves by shear flows, has attracted our attention. This phenomenon has been extensively studied in other fields. But there is still a gap in the field of acoustics, especially in boundary layer flows. The study of over-reflections often requires a deep understanding of stability problems because the mechanisms that trigger over-reflections of waves have been shown to be associated with instability, which in turn can affect the stability of the waves. Based on the facilities we obtain in the study of the stability problems, the over-reflection of acoustic waves in a boundary layer flow can be explored in depth.

The approaches to achieve these objectives include an asymptotic analysis of the solutions to the eigenvalue equation and theoretical analysis of the critical layer. The numerical approaches include the numerical evaluation of the CHF, the solution of the eigenvalue equation, and direct numerical simulations.

The outline of this thesis is as follows:

In chapter 2, based on the LEEs and the normal-mode approach, the generalised PBE for acoustics and the stability of parallel shear flows is derived. Different forms of the generalised PBE containing (i) a velocity profile, a density profile, and a speed of sound profile, (ii) a velocity profile and a temperature profile are summarised. Next, the key equation of this thesis, the PBE with an exponential velocity profile mimicking a boundary layer flow, is derived under the homentropic assumption. Its new exact solution is derived in terms of the confluent Heun function (CHF).

Chapter 3 is dedicated to the in-depth study of boundary layer instability and unstable acoustic modes. Applying the boundary conditions of vanishing disturbances at infinity and zero wall-normal velocity, the boundary value problem is converted to an algebraic eigenvalue problem. Solutions to the eigenvalue problem allow a comprehensive picture of both the temporal and spatial stability behaviours of compressible boundary layers. Therefore, the complex eigenvalues ω are calculated as a function of the streamwise wavenumber α and the Mach number M for the temporal stability problem, while for the spatial stability problem, the complex eigenvalues α are determined depending on the frequency ω and the Mach number M. A series of derived quantities and eigenfunctions are presented with high precision. Among them, the spatial decay rate in positive y-direction is determined by defining an acoustic boundary layer thickness (ABLT) δ_a, which indicates how far outside modes are still audible. Lastly, the results for temporal and spatial stability are compared. The association between eigenvalues in both problems is established as a strong argument for temporal-spatial instability.

In chapter 4, acoustics of boundary layer flows is studied based on the exact solution to the PBE with an exponential velocity profile in terms of the CHF. The reflection and over-reflection of acoustic waves are investigated based on this exact solution. For this purpose, the reflection coefficient R, which is the ratio of the amplitude of the reflected to the incoming acoustic wave, is determined as a function of the streamwise wavenumber α, the Mach number M and the incident angle of the acoustic waves ϕ. Over-reflection refers to $R > 1$, i.e. the reflected wave has a larger amplitude than the incident wave. We prove that in the supersonic context, energy is always transferred from the base flow to the reflected wave, meaning that the case $R < 1$ does not occur. This fact is intimately linked to the critical layer. We show that the presence of the critical layer leads to an optimal energy exchange from the base flow into the acoustic wave, i.e. the critical layer ensures $R > 1$. A special phenomenon, the resonant over-reflection, is observed and proven to be closely related to resonant frequencies ω_r of temporally unstable modes of the boundary layer flow.

By means of DNS the over-reflection of acoustic waves in supersonic inviscid boundary layer flows is investigated in chapter 5. We construct a wave packet consisting of plane waves and superimpose it outside the boundary layer. The whole processes of incidence and reflection of the wave packet in the exponential boundary layer flows are simulated. From the results of the DNS, strong dispersion of the wave packets can be observed due to shear effects near the walls, and in the free stream the dispersion could persist. Despite the effects of dispersion, amplification of the amplitude of the reflected wave can be seen when the reflected wave eventually returns to the free stream. In addition, simulations have been carried out for the acoustic wave with a resonant frequency. The results of the simulations show an over-reflection coefficient that is abnormally higher than the normal over-reflection. In the final part, we further state the limitations of the wave packet model and the reasons for errors in comparison with the theory.

Lastly, a conclusion of this thesis and potential further developments are provided in chapter 6.

2 The Pridmore-Brown equation

2.1 State of the art

The study of acoustic waves in unidirectional shear flows first appeared in the 1930s (Haurwitz, 1931; Küchemann, 1938) after the boundary layer theory was established by Prandtl. Thereafter, Pridmore-Brown (1958) employed the normal-mode ansatz to derive an ordinary differential equation (ODE) for acoustic waves in plane parallel shear flows based on the linearised Euler equations (LEEs), known as the Pridmore-Brown equation (PBE). This equation can also be derived by extending the classic Rayleigh equation (Rayleigh, 1887), which predicts the stability of inviscid incompressible shear flows, to compressible flows, known as the compressible Rayleigh equation (CRE). The CRE was initially used by Lees & Lin (1946) to study inviscid instability and therefore, is subsequently more common in stability theory. In fact, the PBE can be applied both to study the stability problem of shear flows and to describe the propagation of acoustic waves. The essential difference is that for acoustic waves the frequency and wavenumber are considered to be real, whereas for unstable waves they are complex. Normally, for most of the base flows the PBE has no exact solution unless specific assumptions and specific profiles of shear flows are considered. A specific shear flow profile implemented into the PBE still gives rise to the mathematical complexity of the PBE such that analytical solutions are scarce. Due to this, Pridmore-Brown (1958) only gave asymptotic solutions to the PBE for the simplest case, a linear velocity profile, in the limit of small velocity gradients.

It was not until more than a decade later that the PBE with a linear velocity profile was solved for the first time by Goldstein & Rice (1973), who wrote the exact solution in terms of combinations of parabolic cylinder functions. They used this closed-form solution for the understanding of the so-called effective acoustic wall impedance, which includes both wall impedance and boundary layer effects. Applying the effective acoustic impedance, the study of sound propagation could be carried out under a much simpler scenario by superposing a uniform flow with an effective acoustic impedance. However, due to the fact that the solution was written in terms of a complex combination of cylinder functions of different orders, it has not been widely applied analytically to draw further physical conclusions. Numerically, the evaluation by using this analytical solution also appears problematic due to the subtraction of exponentially large terms of the constituting parts. An alternative more practical form of the solution to the PBE for a linear shear flow is based on Whittaker's functions and was given by Jones (1977) to investigate a shear layer matching two uniform streams. Based on this PBE solution, he gave solutions for reflected and transmitted waves and studied how they behave across the linear shear layer by setting an acoustic line source and varying its distance to the shear layer. By examining limiting cases of the layer thickness, i.e. thin and thick shear layers, he concluded that the solution of a thin shear layer approximates that of the vortex sheet. Further, for a thick layer, he gave transmission and reflection coefficients to describe the scattering of sound through the shear layer. The third form of the solution to the PBE with linear shear flow is given by confluent hypergeometric functions (Scott 1979; Koutsoyannis et al. 1979; Koutsoyannis 1980). It is worth mentioning that Koutsoyannis (1980) investigated not only the propagation of acoustic waves but also the stability problem under large wavelength conditions and obtained a critical threshold for instability of $M = 2\sqrt{2}$. In a more recent study of the PBE, Campos (1999) suggested the fourth form, a Fuchs-Frobenius series, for the solution to the PBE with a linear velocity profile, which is derived by the Frobenius method. The original intention of his research was to gain an understanding of the effects of the critical layer in a boundary layer profile composed of a linear and a constant part. In this velocity profile, the critical layer, where the phase velocity of the perturbation equals the local base flow velocity, is the only regular singularity of the PBE except for the point at infinity. Therefore, in the vicinity of the critical layer the series expansion has an infinite convergence radius, and Campos used this facility to study sound propagation near the critical layer. From his observation that the amplitude of the oscillation of acoustic waves decreases near the critical layer, he reasoned that this layer is able to attenuate the sound in its vicinity. In addition, Campos et al. (2014) studied the case of a linear velocity profile superimposed a uniform cross flow. In this case, a third order ODE was obtain rather than the (second order) PBE, which, however, has the advantage that the singularity of the PBE at the critical layer is removed by the cross flow. The exact solution was written as a linear combination of three independent MacLaurin power series.

For a linear velocity profile, it is always necessary to encounter a finite free-stream velocity to ensure that the velocity does not increase indefinitely, enabling to model a boundary layer flow or a mixed layer flow. However, such a velocity profile inevitably introduces an artificial kink between the linear and constant parts of the velocity profile, which in turn leads to non-physical reflections or refractions. To avoid this, researchers shifted their attention to more physical non-linear velocity profiles. In Campos & Serrão (1998), an exponential function was considered to mimic a boundary layer flow, while in Campos & Kobayashi (2000), a hyperbolic tangent function was employed for a free shear layer, and in Campos & Oliveira (2011), a parabolic function was utilised to model a duct flow. For these profiles, likewise the Fuchs-Frobenius series solutions to the PBE could be derived and acoustic effects as well as the influences of the critical layer on the sound propagation were studied. Similar behaviours of sound near the critical layer were testified for these non-linear velocity profiles. However, for more complex velocity profiles, due to the appearance of more than one regular singularity and even irregular singularities in the PBE, the convergence radius of the Fuchs-Frobenius series solution is restricted to the domain between two singularities having a finite distance. Hence, the whole complex domain can not always be overlapped by a single series solution, thus leading to complicated connections between different series solutions. Due to these restrictions of the Fuchs-Frobenius series solution of such complex flows, Campos & Serrão (1998) and Campos & Kobayashi (2000) only studied acoustics of the flows, but not stability, i.e only the non-resonant acoustic spectrums (real-valued frequencies and wavenumbers) were considered by them. Note that all their solutions to the PBE are restricted to homentropic unidirectional shear flows.

In addition to the studies of the PBE based on the above-mentioned exact solutions, the PBE was also investigated in detail by means of analytical and numerical methods, which do not involve the prior determination of an exact solution in the form of standard functions. A well-known analytical method to study the PBE is the WKB method giving dispersion relations for limiting cases. The obtained analytical solutions were used to compare with numerical results. Another analytical method is the asymptotic analysis. We recommend the book of Bender & Orszag (1999) for a detailed introduction to these two analytical methods. Typical numerical methods to obtain the eigenvalues of the PBE are the shooting method (Brown et al., 1954) and the spectral method (Gallagher & Mercer, 1965). The former is intensively employed by Mack (1965, 1969, 1984, 1990). The latter was improved by Gottlieb & Orszag (1977) using Chebyshev polynomials and further developed by Fabre & Jacquin (2004) and Macaraeg et al. (1988) to compressible flows. However, both of these numerical methods generate spurious modes (Gottlieb & Orszag, 1977), which can always not be easily distinguished from the physical modes. This problem does not arise in the present work since the derived analytic solution only delivers the physical results inherently casted into the PBE. In a recent study for a non-isothermal flow, which allows non-uniform speed of sound, WKB approximations were given for high frequencies and asymptotic methods were applied for low frequencies (Rienstra, 2020). These analytical solutions were compared with numerical solutions for acoustic modes in two-dimensional (2-D) and three-dimensional (3-D) lined ducts constructed by the Galerkin projection-based spectral method.

This chapter is structured as follows. In §2.2, the generalised PBE is derived under the assumption of an isentropic but non-homentropic flow, which allows for the presence of transverse temperature gradients associated with the non-uniform speed of sound. Two different forms of the generalised PBE are shown, one of which is given by a non-dimensional form. In §2.3, by further assuming that the flow is homentropic and considering an exponential velocity profile, we derive the key equation of this thesis, i.e. the PBE for exponential boundary layer flows. In addition, two interchangeable non-dimensional forms of this PBE are compared, which are non-dimensionalised by two different common approaches in stability theory and acoustics. Lastly, in §2.4, we give the exact solution to the derived PBE with the exponential velocity profile. The exact solution is given in terms of the confluent Heun function (CHF).

2.2 Governing equations

We consider an inviscid compressible flow without heat conduction, modelled by the Euler equations (Landau & Lifshitz, 2013)

$$\frac{D\rho}{Dt} = -\rho \boldsymbol{\nabla} \cdot \boldsymbol{v}, \tag{2.1a}$$

$$\rho \frac{D\boldsymbol{v}}{Dt} = -\boldsymbol{\nabla} p, \tag{2.1b}$$

$$\frac{Ds}{Dt} = 0, \tag{2.1c}$$

where ρ is the density, $\boldsymbol{v}$ is the velocity vector, p is the pressure, s is the entropy, and

$$\frac{D}{Dt} = \frac{\partial}{\partial t} + \boldsymbol{v} \cdot \boldsymbol{\nabla} \tag{2.2}$$

is the total derivative. Equation (2.1c) is derived from the isentropic assumption of the flow and from that we know the entropy of fluid particles remaining constant as they move in the space, i.e. an adiabatic motion happens. The system of equations (2.1) ignores viscous- and heat-conductive effects. This is reasonable in the framework of the study of acoustic waves and the corresponding effects since the variation of acoustic waves is much faster than these two effects (Rienstra & Hirschberg, 2020).

To obtain a closed system of equations, the equation of state (EOS) is considered, which reads

$$p = p(\rho, s). \tag{2.3}$$

This equation implies

$$\frac{Dp}{Dt} = \left(\frac{\partial p}{\partial \rho}\right)_s \frac{D\rho}{Dt} + \left(\frac{\partial p}{\partial s}\right)_\rho \frac{Ds}{Dt}, \tag{2.4}$$

where the subscripts denote the derivation in the case where s or ρ is regarded as constant. Taking the isentropic condition (2.1c) in (2.4), the EOS is simplified as

$$\frac{Dp}{Dt} = c^2 \frac{D\rho}{Dt}, \tag{2.5}$$

where

$$c = \sqrt{\left(\frac{\partial p}{\partial \rho}\right)_s} \tag{2.6}$$

is the (adiabatic) speed of sound. Since (2.1c) is incorporated and results in (2.5), it is allowed to use (2.5) to replace (2.1c) and thereby obtain a closed system of equations for variables ρ, $\boldsymbol{v}$ and p.

For linear acoustics, we suppose the variables ρ, $\boldsymbol{v}$ and p to be composed of the steady base flow quantities ρ_0, $\boldsymbol{v_0}$, p_0 and small unsteady perturbations ρ', $\boldsymbol{v'}$ and p'

$$(\rho, \boldsymbol{v}, p) = (\rho_0 + \rho', \boldsymbol{v_0} + \boldsymbol{v'}, p_0 + p'), \tag{2.7}$$

where the perturbations are functions of temporal and spatial independent variables in a Cartesian coordinate , i.e. t, x, y, and z. Substituting (2.7) into the equations (2.1a), (2.1b) and (2.5) and neglecting non-linear terms of the small perturbations yields the linearised Euler equations (LEEs) system

$$\frac{\partial \rho'}{\partial t} + \boldsymbol{v_0} \cdot \boldsymbol{\nabla} \rho' + \rho_0 \boldsymbol{\nabla} \cdot \boldsymbol{v'} + \boldsymbol{v'} \cdot \boldsymbol{\nabla} \rho_0 + \rho' \boldsymbol{\nabla} \cdot \boldsymbol{v_0} = 0, \tag{2.8a}$$

$$\rho_0 \left(\frac{\partial \boldsymbol{v'}}{\partial t} + \boldsymbol{v_0} \cdot \boldsymbol{\nabla} \boldsymbol{v'}\right) + \boldsymbol{\nabla} p' + \rho_0 \boldsymbol{v'} \cdot \boldsymbol{\nabla} \boldsymbol{v_0} + \rho' \boldsymbol{v_0} \cdot \boldsymbol{\nabla} \boldsymbol{v_0} = 0, \tag{2.8b}$$

$$\frac{\partial p'}{\partial t} + \boldsymbol{v_0} \cdot \boldsymbol{\nabla} p' + \boldsymbol{v'} \cdot \boldsymbol{\nabla} p_0 = c^2 \left(\frac{\partial \rho'}{\partial t} + \boldsymbol{v_0} \cdot \boldsymbol{\nabla} \rho' + \boldsymbol{v'} \cdot \boldsymbol{\nabla} \rho_0\right). \tag{2.8c}$$

For a proposed unidirectional 2-D parallel shear flow, the base flow velocity is assumed to be in the x-direction and to vary in the y-direction. Hence, the base flow vector reads

$$\boldsymbol{v_0} = (u_0(y), 0)\,. \tag{2.9}$$

This condition indicates two facts. First, $p_0 =$ const, as can be verified by taking (2.9) into (2.1b). Second, by substituting (2.9) into (2.1a) and (2.5) and considering (2.6), it is noticed that $\rho_0(y)$ and $c(y)$ are allowed to vary in the y-direction. The latter means that the entropy is not a constant, which may vary from one streamline to another in the y-direction.

According to the above implications, the LEE system (2.8) can be simplified as

$$\frac{\partial \rho'}{\partial t} + u_0(y)\frac{\partial \rho'}{\partial x} + \rho_0(y)\left(\frac{\partial u'}{\partial x} + \frac{\partial v'}{\partial y}\right) + v'\frac{\partial \rho_0(y)}{\partial y} = 0, \tag{2.10a}$$

$$\rho_0(y)\left(\frac{\partial u'}{\partial t} + u_0(y)\frac{\partial u'}{\partial x}\right) + \rho_0(y)v'\frac{\partial u_0(y)}{\partial y} + \frac{\partial p'}{\partial x} = 0, \tag{2.10b}$$

$$\rho_0(y)\left(\frac{\partial v'}{\partial t} + u_0(y)\frac{\partial v'}{\partial x}\right) + \frac{\partial p'}{\partial y} = 0, \tag{2.10c}$$

$$\frac{\partial p'}{\partial t} + u_0(y)\frac{\partial p'}{\partial x} = c(y)^2\left(\frac{\partial \rho'}{\partial t} + u_0(y)\frac{\partial \rho'}{\partial x} + v'\frac{\partial \rho_0(y)}{\partial y}\right), \tag{2.10d}$$

where (2.10b) and (2.10c) are the first two components of the momentum equation. Alternative, combining (2.10a) and (2.10d) will give

$$\frac{\partial p'}{\partial t} + u_0(y)\frac{\partial p'}{\partial x} + \rho_0(y)c(y)^2\left(\frac{\partial u'}{\partial x} + \frac{\partial v'}{\partial y}\right) = 0, \tag{2.10e}$$

as the linearised adiabatic equation of continuity.

Considering 2-D perturbations, a normal-mode approach for velocity, density, and pressure perturbations is applied. Similar to the classical stability theory, which involves Fourier decomposition in x and t, we introduce a normal-mode ansatz

$$q'(x,y,t) = \hat{q}(y)e^{i(\alpha x - \omega t)}, \tag{2.11}$$

with $q' \in (u', v', \rho', p')$, where the quantities $\hat{u}(y)$, $\hat{v}(y)$, $\hat{\rho}(y)$ and $\hat{p}(y)$ represent the amplitudes of the perturbations, α denotes the streamwise wavenumber, and ω stands for the frequency. Substituting the normal-mode ansatz (2.11) into the system of partial differential equations (PDEs) (2.10a)-(2.10c) and(2.10e) results in a system of ODEs

$$\rho_0(y)\frac{d\hat{v}}{dy} + i\left[\alpha\rho_0(y)\hat{u} - (\omega - \alpha u_0(y))\,\hat{\rho}\right] + \hat{v}\frac{d\rho_0(y)}{dy} = 0, \tag{2.12a}$$

$$\rho_0(y)\hat{v}\frac{du_0(y)}{dy} + i\left[\alpha\hat{p} - (\omega - \alpha u_0(y))\,\hat{u}\right] = 0, \tag{2.12b}$$

$$\frac{d\hat{p}}{dy} - i\,(\omega - \alpha u_0(y))\,\rho_0(y)\hat{v} = 0, \tag{2.12c}$$

$$\rho_0(y)c(y)^2\frac{d\hat{v}}{dy} + i\left[\alpha\rho_0(y)c(y)^2\hat{u} - (\omega - \alpha u_0(y))\,\hat{p}\right] = 0. \tag{2.12d}$$

We rewrite (2.12) into an equivalent second order differential equation with a single dependent variable $\hat{p}$. For this, we first express $\hat{v}$ by $d\hat{p}/dy$ through (2.12c), then substitute the result for $\hat{v}$ in (2.12b) and thereafter express $\hat{u}$ in terms of $\hat{p}$ and $d\hat{p}/dy$. Finally we substitute these results for $\hat{u}$ and $\hat{v}$ into (2.12d) to get a second order ODE for $\hat{p}$, which reads

$$\frac{d^2\hat{p}}{dy^2} + \left(\frac{2\alpha}{\omega - \alpha u_0(y)}\frac{du_0(y)}{dy} - \frac{1}{\rho_0(y)}\frac{d\rho_0(y)}{dy}\right)\frac{d\hat{p}}{dy} + \left[\frac{(\omega - \alpha u_0(y))^2}{c(y)^2} - \alpha^2\right]\hat{p} = 0. \tag{2.13}$$

We refer to (2.13) in the present thesis as the generalised PBE because it differs from the classical PBE by having other profiles, i.e. density and speed of sound profiles or temperature profile, in addition to the velocity profile. To the author's knowledge, there is no exact solution to (2.13), unless the profiles for the base flow velocity $u_0(y)$, density $\rho_0(y)$, and the speed of sound $c(y)$ are specified. If a solution $\hat{p}$ is obtained, $\hat{u}$, $\hat{v}$ and $\hat{\rho}$ can be expressed by $\hat{p}$

$$\hat{u} = -\frac{1}{\rho_0(y)\,(\omega - \alpha u_0(y))^2}\frac{du_0}{dy}\frac{d\hat{p}}{dy} + \frac{\alpha}{\rho_0(y)\,(\omega - \alpha u_0(y))}\hat{p}, \tag{2.14}$$

$$\hat{v} = -\frac{i}{\rho_0(y)\,(\omega - \alpha u_0(y))}\frac{d\hat{p}}{dy}, \tag{2.15}$$

$$\hat{\rho} = -\frac{1}{(\omega - \alpha u_0(y))^2}\frac{d^2\hat{p}}{dy^2} - \frac{2\alpha}{(\omega - \alpha u_0(y))^3}\frac{du_0(y)}{dy}\frac{d\hat{p}}{dy} + \frac{\alpha^2}{(\omega - \alpha u_0(y))^2}\hat{p}. \tag{2.16}$$

Another form of the generalised PBE, using a base temperature profile $T_0(y)$ instead of $\rho_0(y)$ and $c_0(y)$, is more common in studies of stability problems. For this, we consider an ideal gas with the ideal gas law

$$p = \rho \mathcal{R} T, \tag{2.17}$$

where $\mathcal{R}$ is the specific gas constant and $T \in \mathbb{R}^+$ is the temperature. An isentropic process for an ideal gas is an idealized thermodynamic process that is both adiabatic and reversible. Mathematically, it can be represented by the polytropic process equation, which reads

$$pV^\gamma = p\left(\frac{1}{\rho}\right)^\gamma = \text{const.}, \tag{2.18}$$

where V stands for volume of the gas, and γ is the heat capacity ratio. Taking the logarithm of (2.18) we get

$$\ln(p) - \gamma \ln(\rho) = \ln(\text{const.})\,. \tag{2.19}$$

Differentiating (2.19) on ρ

$$\frac{\partial p}{\partial \rho} = \gamma \frac{p}{\rho}, \tag{2.20}$$

and considering the definition of the (adiabatic) speed of sound (2.6), we end up with an alternative expression for the speed of sound (Spurk & Aksel, 2007), which is given by

$$c = \sqrt{\gamma \frac{p}{\rho}}. \tag{2.21}$$

Taking (2.17) into (2.21) yields

$$c = \sqrt{\gamma \mathcal{R} T}. \tag{2.22}$$

Considering (2.17) and (2.22), and substituting the temperature profile $T_0(y)$ into (2.13), an alternative form of the generalised PBE reads

$$\frac{d^2\hat{p}}{dy^2} + \left(\frac{2\alpha}{\omega - \alpha u_0(y)}\frac{du_0(y)}{dy} + \frac{1}{T_0(y)}\frac{dT_0(y)}{dy}\right)\frac{d\hat{p}}{dy} + \left[\frac{(\omega - \alpha u_0(y))^2}{\gamma \mathcal{R} T_0(y)} - \alpha^2\right]\hat{p} = 0. \tag{2.23}$$

In order to transfer results between different scales, it is common to derive the non-dimensional form of an equation. To non-dimensionalise the generalised PBE (2.23), we first introduce the reference values, i.e. characteristic length l_∞, base flow density ρ_∞ and temperature T_∞ that implies the implicit reference, i.e. the speed of sound $c_\infty = \sqrt{\gamma \mathcal{R} T_\infty}$. Accordingly, the non-dimensional variables read

$$p^* = \frac{\hat{p}}{\rho_\infty {c_\infty}^2}, \quad T^* = \frac{T_0}{T_\infty}, \quad y^* = \frac{y}{l_\infty}, \quad M_0 = \frac{u_0}{c_\infty}, \quad \omega^* = \frac{\omega l_\infty}{c_\infty}, \quad \alpha^* = \alpha l_\infty. \tag{2.24}$$

The non-dimensional form of the generalised PBE reads (star omitted)

$$\frac{d^2\hat{p}}{dy^2} + \left(\frac{2\alpha}{\omega - \alpha M_0(y)} \frac{dM_0(y)}{dy} + \frac{1}{T_0(y)} \frac{dT_0(y)}{dy} \right) \frac{d\hat{p}}{dy} + \left[\frac{(\omega - \alpha M_0(y))^2}{T_0(y)} - \alpha^2 \right] \hat{p} = 0. \tag{2.25}$$

As the generalised PBE can be used to study both the stability of shear flows and acoustic modes as well as the propagation of acoustic waves, it was often given different names in separate fields. The generalised PBE (2.25) was studied in Lees & Lin (1946), Lees & Reshotko (1962), Mack (1969), and Bitter & Shepherd (2015) for boundary layer instability in Cartesian coordinates and named as the CRE. In Nayfeh (1973) and Oppeneer et al. (2011), it was derived in a cylindrical coordinate system and studied for acoustic modes in ducts, named the PBE. In Campos (2007) and Campos & Kobayashi (2009), the same equation was derived and studied for the propagation of acoustic waves and therefore named the acoustic wave equation. To avoid ambiguity, we refer to (2.13), (2.23) and (2.25) as the generalised PBE in the following work.

Although the generalised PBE (2.25) is only a second order ODE, very few analytical solutions are known. Even for the simplest case, a linear velocity profile and a linear temperature profile, there is no exact solution. But this situation is being improved with the development of the Heun class equations.

2.3 Exponential boundary layer flows

In the following, we focus on the main topic of the present work, an exponential boundary layer flow of an ideal gas. We first simplify the generalised PBE by the homentropic-flow assumption, which means that the entropy is a constant, i.e. $s_0 = \text{const}$. Considering (2.9) and the fact $p_0 = \text{const}$ derived thereafter, and combining the the EOS $\rho(p_0, s_0)$, it is concluded that the density is a constant, i.e. $\rho_0 = \text{const}$. A Taylor series expansion of the pressure about the reference thermodynamic state denoted by the subscript 0 (neglecting higher-order derivatives) gives

$$p = p_0 + p' = p(\rho_0 + \rho', s_0) \approx p(\rho_0, s_0) + \left[\frac{\partial p}{\partial \rho}(\rho, s_0) \right]_s \rho' = p_0 + {c_0}^2 \rho', \tag{2.26}$$

where $c_0 = \sqrt{(\partial p / \partial \rho)_s}$ is a constant speed of sound. For an ideal gas, the mean flow is isothermal and thus $T_0 = \text{const}$. Equation (2.26) indicates an important condition, namely

$$p' = {c_0}^2 \rho'. \tag{2.27}$$

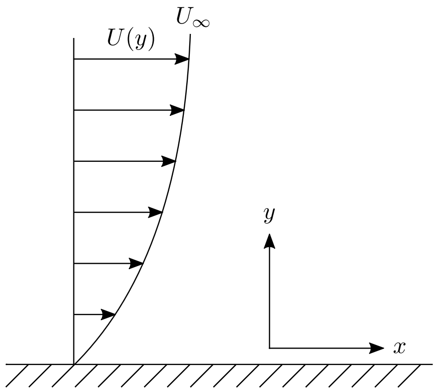

Figure 2.1: Sketch of an exponential boundary layer flow.

In this way, we could omit (2.10d) or (2.10e) and apply the linearised relation for the speed of sound (2.27) to close the LEE system (2.10).

We further specify the velocity profile to an exponential velocity profile, which is employed to mimic a boundary layer flow. The velcotiy velocitiy components $u_0(y)$ and $v_0(y)$ read

$$u_0(y) = U_\infty \left(1 - e^{-\frac{y}{\delta}}\right), \tag{2.28a}$$

$$v_0(y) = 0, \tag{2.28b}$$

where U_∞ is the free-stream velocity and δ is the shear layer thickness, which is a multiplier of the hydrodynamic boundary layer thickness, e.g. 99% boundary layer thickness, displacement thickness and momentum thickness. A sketch of the exponential boundary layer flow is shown in figure 2.1. Inserting (2.28) into (2.10a)-(2.10c) and eliminating p' through (2.27), we get a PDE system, which, non-dimensionalised by U_∞, δ and ρ_0, reads

$$\frac{\partial \rho'}{\partial t} + \left(1 - e^{-y}\right)\frac{\partial \rho'}{\partial x} + \left(\frac{\partial u'}{\partial x} + \frac{\partial v'}{\partial y}\right) = 0, \tag{2.29a}$$

$$\frac{\partial u'}{\partial t} + \left(1 - e^{-y}\right)\frac{\partial u'}{\partial x} + e^{-y}\, v' + \frac{1}{M^2}\frac{\partial \rho'}{\partial x} = 0, \tag{2.29b}$$

$$\frac{\partial v'}{\partial t} + \left(1 - e^{-y}\right)\frac{\partial v'}{\partial x} + \frac{1}{M^2}\frac{\partial \rho'}{\partial y} = 0, \tag{2.29c}$$

where $M = U_\infty / c$ is the global or free-stream Mach number.

It is worth noting that we adopte a different non-dimensional approach here than the approach in (2.24) that is typical in the field of acoustics, i.e. instead of the speed of sound c_0, we use the free-stream velocity U_∞ to non-dimensionalise, as it is common in the study of boundary layer stability problems. Later, for acoustic problems, we keep the same descaling approach to facilitate establishing links between the stability theory and acoustics. Apparently, the parameters and results obtained by different non-dimensional approaches are interchangeable. For details see the last part of this section.

Substituting the normal-mode ansatz (2.11) into the system of PDEs (2.29) results

$$\frac{d\hat{v}}{dy} + i\left[-\left(\omega - \alpha + \alpha e^{-y}\right)\hat{\rho} + \alpha\hat{u}\right] = 0, \tag{2.30a}$$

$$e^{-y}\hat{v} + i\left[\frac{\alpha}{M^2}\hat{\rho} - \left(\omega - \alpha + \alpha e^{-y}\right)\hat{u}\right] = 0, \tag{2.30b}$$

$$\frac{1}{M^2}\frac{d\hat{\rho}}{dy} - i\left(\omega - \alpha + \alpha e^{-y}\right)\hat{v} = 0. \tag{2.30c}$$

We further rewrite (2.30) into an equivalent second order differential equation with the single dependent variable $\hat{\rho}$. For this, we express $\hat{v}$ by $d\hat{\rho}/dy$ through (2.30c), substitute the result for $\hat{v}$ in (2.30b) and thereafter express $\hat{u}$ in terms of $\hat{\rho}$ and $d\hat{\rho}/dy$. Finally we substitute these results for $\hat{u}$ and $\hat{v}$ in (2.30a) to get the second order ODE for $\hat{\rho}$

$$\frac{d^2\hat{\rho}}{dy^2} + \frac{2\alpha e^{-y}}{\omega - \alpha + \alpha e^{-y}}\frac{d\hat{\rho}}{dy} + \left[M^2\left(\omega - \alpha + \alpha e^{-y}\right)^2 - \alpha^2\right]\hat{\rho} = 0, \tag{2.31}$$

known as the PBE (Pridmore-Brown, 1958). If a solution $\hat{\rho}$ to (2.31) is obtained, $\hat{u}$ and $\hat{v}$ can be expressed in terms of $\hat{\rho}$

$$\hat{u} = -\frac{e^{-y}}{M^2\left(\omega - \alpha + \alpha e^{-y}\right)^2}\frac{d\hat{\rho}}{dy} + \frac{\alpha}{M^2\left(\omega - \alpha + \alpha e^{-y}\right)}\hat{\rho}, \tag{2.32}$$

$$\hat{v} = \frac{1}{iM^2\left(\omega - \alpha + \alpha e^{-y}\right)}\frac{d\hat{\rho}}{dy}. \tag{2.33}$$

The PBE (2.31) not only allows an eigenvalue equation to be derived for the stability investigation but also describes the propagation of acoustic waves in the boundary layer flow. On the basis of the stability eigenvalue problem, a resonant spectrum for modes is determined, while a non-resonant spectrum is mainly considered within the framework of the acoustic problem.

In the literature, an alternative form of the non-dimensional PBE with non-dimensional approach by the speed of sound c_0 reads

$$\frac{d^2\hat{\rho}}{dy^2} + \frac{2\bar{\alpha}Me^{-y}}{\bar{\omega} - \bar{\alpha}M + \bar{\alpha}Me^{-y}}\frac{d\hat{\rho}}{dy} + \left[\left(\bar{\omega} - \bar{\alpha}M + \bar{\alpha}Me^{-y}\right)^2 - \bar{\alpha}^2\right]\hat{\rho} = 0, \tag{2.34}$$

where the non-dimensional frequency $\bar{\omega}$ is scaling on c_0, i.e. $\bar{\omega} = \tilde{\omega}\delta/c_0$. This alternative form can be obtained by substituting $\omega = \bar{\omega}/M$ and $\alpha = \bar{\alpha}$ into (2.31) or by simplification of (2.25) with $M_0(y) = M(1 - e^{-y})$ and $T_0(y) = 1$. Note that the dependent variables are $\hat{p}$ and $\hat{\rho}$ in (2.25) and (2.31), respectively. But due to the fact $p' = {c_0}^2\rho'$, $\hat{\rho}$ in (2.31) can be replaced by $\hat{p}$ with no changes of the ODE's form.

2.4 Solution to the Pridmore-Brown equation with an exponential velocity profile

We notice that (2.31) is closely linked to the confluent Heun equation (CHE) introduced by Heun (1888) as a generalisation of the hypergeometric equation. Its solution is given by the confluent Heun function (CHF) denoted with $H\text{c}\left(p_*, \alpha_*, \gamma_*, \delta_*, \sigma_*; z\right)$, where $p_*, \alpha_*, \gamma_*, \delta_*, \sigma_*$

stand for five parameters and z is the independent variable (Ronveaux & Arscott, 1995). The PBE (2.31) can be solved in terms of the CHF (for a detailed derivation and notation see Appendix A.1) and thus, the exact solution is given by

$$\begin{aligned}\hat{\rho}(y) = C_1 e^{iM\alpha e^{-y}+\sqrt{\theta}y} H\mathrm{c}\left(p_*, \alpha_*, \gamma_*, \delta_*, \sigma_*; \frac{\alpha e^{-y}}{\alpha-\omega}\right) \\ + C_2 e^{iM\alpha e^{-y}-\sqrt{\theta}y} H\mathrm{c}\left(\tilde{p}_*, \tilde{\alpha}_*, \tilde{\gamma}_*, \tilde{\delta}_*, \tilde{\sigma}_*; \frac{\alpha e^{-y}}{\alpha-\omega}\right),\end{aligned} \tag{2.35}$$

where

$$\theta = -M^2(\alpha-\omega)^2 + \alpha^2, \tag{2.36}$$

and the parameters are defined as follows

$$\begin{aligned}p_* = \frac{iM(\alpha-\omega)}{2}, \quad \alpha_* = iM(\alpha-\omega) - \frac{1}{2} - \sqrt{\theta}, \quad \gamma_* = 1 - 2\sqrt{\theta}, \quad \delta_* = -2, \\ \sigma_* = iM(\alpha-\omega) - 2M^2(\alpha-\omega)^2 - 2\sqrt{\theta}\left[iM(\alpha-\omega)+1\right],\end{aligned} \tag{2.37}$$

$$\begin{aligned}\tilde{p}_* = \frac{iM(\alpha-\omega)}{2}, \quad \tilde{\alpha}_* = iM(\alpha-\omega) - \frac{1}{2} + \sqrt{\theta}, \quad \tilde{\gamma}_* = 1 + 2\sqrt{\theta}, \quad \tilde{\delta}_* = -2, \\ \tilde{\sigma}_* = iM(\alpha-\omega) - 2M^2(\alpha-\omega)^2 + 2\sqrt{\theta}\left[iM(\alpha-\omega)+1\right].\end{aligned} \tag{2.38}$$

In the following, for the sake of brevity, we omit the parameters of the Hc function and express the Hc function simply as $H\mathrm{c}(;z)$ and $\widetilde{H\mathrm{c}}(;z)$ with their respective parameters according to (2.37) and (2.38), and with $z = \alpha e^{-y}/(\alpha-\omega)$.

In the present work, we investigate both the stability problems and boundary layer acoustics. For the temporal stability problem, there is $\omega \in \mathbb{C}$ and $\alpha \in \mathbb{R}$, while for the spatial stability problem, there is $\alpha \in \mathbb{C}$ and $\omega \in \mathbb{R}$. The case $\alpha \in \mathbb{C}$ and $\omega \in \mathbb{C}$ described in §3.5 is referred to as temporal-spatial instability. For the acoustic problem, only $\alpha \in \mathbb{R}$ and $\omega \in \mathbb{R}$ will be considered.

3 Boundary layer instability

3.1 State of the art

Studies of boundary layer stability originated from the exploration of laminar-turbulent transition mechanisms. An initial idea using small perturbations was limited to incompressible flows in hydrodynamics (Tietjens, 1925). Superposing small perturbations onto the undisturbed base flow to figure out whether the perturbations grow or decay is actually the key idea of the linear stability theory. The most well-known exploration of boundary layer stability was led by Tollmien (1930) and Schlichting (1933), who established a stability theory of viscous incompressible boundary layer flows, thereby explaining the mechanism of instability due to viscosity through energy methods. The related unstable waves were later named after their explorers as T-S waves. Their results were first experimentally verified by Dryden (1947) and Schubauer & Skramstad (1947).

Küchemann (1938) was the first to extend the boundary layer stability theory to a compressible regime but without considering the viscosity, temperature gradient and curvature of the velocity profile. Lees & Lin (1946) further developed the stability theory based on infinitesimal disturbances to a compressible inviscid boundary layer. They found an inviscid mechanism of compressible boundary layer instability, which originates from the extension of the Rayleigh inflection criterion for a density or temperature gradient and is completely different to the viscous instability mechanism for T-S waves. Another milestone work was done by Mack (1965), who first numerically found additional multiple linear unstable modes in a supersonic compressible adiabatic boundary layer flow and explained their occurrence by an inviscid instability. These unstable higher modes are associated with wave radiation and have a mechanism different from both mechanisms mentioned above. Among all unstable modes, the mode with the lowest frequency was considered to be an extension of the T-S waves to compressible flows for low Mach numbers (Dunn, 1955; Lees & Reshotko, 1962). However, when the Mach number exceeds three, the viscous mechanism vanishes, but this mode persists. Therefore, it is not appropriate to further call it T-S mode. For this reason, this mode is named the first mode[2]. Higher unstable modes are named in order of the frequencies, the second mode[3], third mode and etc. These higher unstable modes were first verified experimentally by Demetriades (1974). Mack (1990) introduced the terminology "acoustic mode", referring to the second and all other higher modes, while he named the first mode "vorticity mode"[4]. He further expanded this concept to unstable modes, which are usually only observed for supersonic flows. These unstable acoustic modes were also found numerically, respectively, in a confined supersonic mixing layer (Tam & Hu, 1989a), a two-dimensional jet flow (Mack,

[2] In the literature, this mode is always referred to as the first Mack mode.
[3] The second mode is always referred to as the second Mack mode.
[4] In some literature, it is termed hydrodynamic mode.

1990), a supersonic round jet flow (Lindzen & Barker, 1985; Luo & Sandham, 1997; Parras & Le Dizès, 2010), and, more recently, a hypersonic blunt cone boundary layer (Knisely & Zhong, 2019a, 2019b).

The study of boundary layer stability has important implications for the understanding of the occurrence of laminar-turbulent transition. As a semi-free shear layer, the boundary layer stability is largely influenced by the free stream and the wall surface. When a disturbance, such as an acoustic wave or vorticity, enters the boundary layer from the free stream, the growth of the disturbance is triggered by a linear eigenmode which leads to a non-linear breakdown to turbulence. This process of converting external disturbances entering the boundary layer into waves within the boundary layer and providing initial amplitude, frequency, and phase is defined as receptivity by Morkovin (1969). The eigenmodes that determine the linear growth are obtained by solving the eigenvalue problem of the homogeneous linearised stability equation. As for the final step, the breakdown to turbulence is mainly caused by non-linear secondary instabilities when the amplitude of the perturbation reaches a certain level. This three-step process is the most classical path of transition with weak disturbances. Besides, if the amplitude of the disturbances is not small, transient growth as the second path of transition, which is based on the non-orthogonal nature of eigenfunctions, becomes important (Schmid & Henningson, 2001). If the disturbances are large enough to completely bypass their linear growth, a direct breakdown to turbulence occurs, which is the mechanism of the third path of transition (Morkovin, 1985). A graphical summary of the transition paths leading to turbulence can be found in Morkovin et al. (1994), which includes another two paths in addition to the three main paths, laying between transient growth and eigenmode growth and between transient growth and the bypass mechanisms.

With the development of computer science and numerical computing, the study of the stability of compressible boundary layers has become increasingly complex and has been extended to the hypersonic regime (Zhong & Wang, 2012). More factors are considered, including temperature gradient, roughness, temperature of flat plate, etc. But the analytical solution to these problems is scarce. In the present work, we make full use of the analytical solution (2.35) to the Pridmore-Brown equation (PBE) (2.31) to focus on the temporal and spatial stability problems. The goal of the present study in this chapter is to find unstable modes using analytical solutions and characterise different modes to study their behaviours. It is worth mentioning that the same exponential boundary layer model was suggested by Oberlack (2001) for a turbulent boundary layer (TBL) flow using symmetry methods. Using TBL data at a very high Reynolds number from the experiments of Saddoughi & Veeravalli (1994), he concluded that the largest part of a TBL, i.e. the deficit region, is covered by an exponential profile. The conclusion was later validated by the experiments by Lindgren et al. (2004). Different to the analysis of the exponential boundary layer in Campos & Serrão (1998), we study the entire spectrum, including both the real and imaginary part of the eigenvalues, where the imaginary part refers to stability problems. All results in this chapter are founded on our new solution to the PBE with an exponential profile (2.31) in terms of the confluent Heun function (CHF), from which we derive the corresponding eigenvalue problem and completely solve for the eigenvalues using a numerical root-finding algorithm. Based on these eigenvalues, we comprehensively analyse the stability of both sub- and supersonic flows and induced acoustic phenomena based on the eigenvalues and eigenfunctions.

This chapter is structured as follows. In §3.2, with the appropriate boundary conditions for the stability problem, the boundary value problem is converted to an algebraic eigenvalue problem.

Asymptotic solutions of the eigenvalue problem for both temporal and spatial stability are derived in the limiting parameter cases as functions of the Mach number M and the streamwise wavenumber α for the former, and the Mach number M and the frequency ω for the latter. In §3.3 and §3.4, numerical results are provided separately for the temporal and the spatial stability problem to validate the analytical results and to compare them with previous theories. In addition, features of the acoustic modes are thoroughly discussed. In §3.5, we summarise the similarities between the results for temporal and spatial stability, analyse their differences and, most importantly, further establish the links between them. In the last part, §3.6, we state the main conclusions of this chapter and discuss some valuable potential subjects. Parts of the analysis and numerics in the present paper were aided by `Maple 2020` (Maplesoft, 2020) and `MATLAB 2020b` (Mathworks, 2020).

In this chapter, the parts of general analysis and temporal stability (§3.2 and §3.3) are based on the peer-reviewed publication Zhang & Oberlack (2021). Essential parts of spatial stability (§3.4), and the association between temporal and spatial stability (§3.5) are completed according to the work in Baumgärtener, Zhang and Oberlack (2022), which is going to be submitted.

3.2 Eigenvalue problem

3.2.1 Eigenvalue equation

In this section, with the exact solution (2.35) to the PBE (2.31) and appropriate boundary conditions, we derive the eigenvalue problem for the boundary layer stability. We first assume that the energy is bounded. This means that the amplitude of the density perturbation vanishes at $y \to \infty$, which induces the first boundary condition

$$\lim_{y \to \infty} \hat{\rho}(y) = 0. \tag{3.1}$$

We should note that presently we explicitly exclude neutrally stable supersonic modes, i.e. we do not consider a finite $\hat{\rho}$ because we are mainly interested in unstable modes (see e.g. Blumen et al., 1975).

The spectrum of eigenvalues obtained by employing (3.1) is not continuous but discrete. The difference between the discrete and continuous spectrum is closely linked to the eigenfunctions in the asymptotic limit $y \to \infty$. The discrete spectrum is linked to a vanishing $\hat{\rho}$ as $y \to \infty$, while the continuous spectrum corresponds to a bounded value of $\hat{\rho}$ (Fedorov & Tumin, 2011).

The second boundary condition is obtained through the impermeability condition at the wall. We adopt here the simplest case, i.e. an inelastic rigid wall. Thus, the normal component of the velocity perturbation at the wall vanishes, i.e.

$$\hat{v}(0) = 0. \tag{3.2}$$

Employing equation (3.2) into (2.30c), we obtain for $y = 0$ that

$$\frac{d\hat{\rho}}{dy}(0) = 0, \tag{3.3}$$

which is the second boundary condition for $\hat{\rho}$.

Inserting the solution (2.35) into the first boundary condition (3.1), yields

$$\lim_{y\to\infty} \hat{\rho}(y) = \lim_{y\to\infty} \left(C_1 e^{\sqrt{\theta}y} + C_2 e^{-\sqrt{\theta}y} \right) = 0, \tag{3.4}$$

where $Hc(;0) = 1$ (Olver et al., 2010) has been employed.

As in general ω or α is complex, according to (2.36) this renders θ also to be complex. Hence, we decompose θ as follows

$$\theta = \theta_r + i\theta_i. \tag{3.5}$$

Temporal stability We first consider the temporal stability problem, i.e. $\alpha \in \mathbb{R}$ and $\omega \in \mathbb{C}$, which gives

$$\omega = \omega_r + i\omega_i, \tag{3.6}$$

where $\omega_r = \Re(\omega)$ is the frequency and $\omega_i = \Im(\omega)$ is a growth rate in time. If we consider the normal-mode ansatz (2.11), it shows

$$\rho'(x, y, t) = \hat{\rho}(y) e^{i(\alpha x - \omega_r t)} e^{\omega_i t}, \tag{3.7}$$

which indicates a rate of decay for $\omega_i < 0$ and a rate of growth for $\omega_i > 0$. In this case, θ_r and θ_i are given by

$$\theta_{r_t} = \alpha^2 - M^2 \left[(\alpha - \omega_r)^2 - {\omega_i}^2 \right], \tag{3.8a}$$
$$\theta_{i_t} = 2M^2(\alpha - \omega_r)\omega_i. \tag{3.8b}$$

Spatial stability Next, for the spatial stability problem with $\omega \in \mathbb{R}$ and $\alpha \in \mathbb{C}$ we have

$$\alpha = \alpha_r + i\alpha_i, \tag{3.9}$$

where $\alpha_r = \Re(\alpha)$ is the wavenumber and $\alpha_i = \Im(\alpha)$ is a growth rate in space. Taking (3.9) into the normal-mode ansatz (2.11) results in

$$\rho'(x, y, t) = \hat{\rho}(y) e^{i(\alpha_r x - \omega t)} e^{-\alpha_i x}, \tag{3.10}$$

which means a rate of growth for $\alpha_i < 0$ and a rate of decay for $\alpha_i > 0$. In this case, θ_r and θ_i read

$$\theta_{r_s} = {\alpha_r}^2 - {\alpha_i}^2 - M^2 \left[(\alpha_r - \omega)^2 - {\alpha_i}^2 \right], \tag{3.11a}$$
$$\theta_{i_s} = 2\alpha_r\alpha_i - 2M^2(\alpha_r - \omega)\alpha_i. \tag{3.11b}$$

With (3.5), the square root of θ reads (Mostowski & Stark, 2014)

$$\sqrt{\theta_r + i\theta_i} = \frac{\sqrt{2}}{2} \left[\sqrt{\sqrt{{\theta_r}^2 + {\theta_i}^2} + \theta_r} + \mathrm{sign}(\theta_i) i \left(\sqrt{\sqrt{{\theta_r}^2 + {\theta_i}^2} - \theta_r} \right) \right], \tag{3.12}$$

where the principal value is taken, and the branch cut is along the negative real axis. Other choices of the square root are equally possible and independent of physics.

Employing (3.12) into (3.1) indicates that the boundary condition can only be satisfied when $C_1 = 0$. Therefore, the solution (2.35) reduces to

$$\hat{\rho}(y) = C_2 e^{iM\alpha e^{-y} - \sqrt{\theta} y} \widetilde{H\mathrm{c}} \left(; \frac{\alpha e^{-y}}{\alpha - \omega} \right), \tag{3.13}$$

where the omitted set of parameters is to be taken from (2.38).

Inserting the second boundary condition (3.3) into the solution (3.13) yields

$$\left(-iM\alpha - \sqrt{\theta} \right) \widetilde{H\mathrm{c}} \left(; \frac{\alpha}{\alpha - \omega} \right) - \frac{\alpha}{\alpha - \omega} \widetilde{H\mathrm{c}}' \left(; \frac{\alpha}{\alpha - \omega} \right) = 0. \tag{3.14}$$

where $\widetilde{H\mathrm{c}}'$ denotes the derivative of the $\widetilde{H\mathrm{c}}$ function with respect to the independent variable, which is the final argument of $\widetilde{H\mathrm{c}}$. As a result, the boundary value problem (2.35), (3.1) and (3.3) is converted to the algebraic eigenvalue problem (3.14), where M and α are free parameters and ω is the sought eigenvalue in the complex domain for the temporal stability problem, and M and ω are free parameters and α is the sought eigenvalue in the complex domain for the spatial stability problem.

Equation (3.14) is the basic equation for the key results presented in the following sections in §3.3 and §3.4, and describes both acoustic phenomena and stability aspects. The central distinction between these two processes is made by non-resonant ($\omega_i = 0$ and $\alpha_i = 0$) and resonant ($\omega_i \neq 0$ or $\alpha_i \neq 0$) spectra, in which the former describes mainly the propagation of the acoustic waves, while the latter quantifies stability.

In the rest sections of this thesis, when we refer to the temporal stability problem, we mean that $\alpha \in \mathbb{R}$ is the parameter, and $\omega \in \mathbb{C}$ is the sought eigenvalue. When we refer to the spatial stability problem, we mean that $\omega \in \mathbb{R}$ is the parameter, and $\alpha \in \mathbb{C}$ is the sought eigenvalue. If we only mention the stability problems, we are referring to both. A special case occurs in §3.5, where $\omega \in \mathbb{C}$ and $\alpha \in \mathbb{C}$ happen simultaneously, and we call it temporal-spatial stability.

It is to note that the PBE (2.31) admits the following discrete symmetry in parameter space, i.e.

$$\alpha \to -\alpha, \quad \omega \to -\omega. \tag{3.15}$$

For the temporal stability problem we employ $\alpha \in \mathbb{R}$ and $\omega \in \mathbb{C}$, the symmetry (3.15) maps neutrally stable modes to neutrally stable modes ($\omega_i = 0$), while unstable modes ($\omega_i > 0$) generate stable modes ($\omega_i < 0$). As we are presently interested in neutrally stable and unstable modes, we subsequently limit ourselves to $\alpha \in \mathbb{R}^+$ for the temporal stability problem. Similarly, for the same reason of symmetry between stable and unstable modes, we restrict the parameter $\omega \in \mathbb{R}^+$ for the spatial stability problem.

3.2.2 Asymptotic analysis for the eigenvalue equation

Due to the transcendental behaviour of the CHF, an exact analysis of the eigenvalue equation (3.14) turned out to be impossible, and an explicit solution for eigenvalues is not accessible. Still, also a numerical solution turned out to be difficult (see §3.3 and §3.4). In fact, compared to other hypergeometric equations and functions little is known about the family of Heun equations and Heun functions. Against this background, an asymptotic analysis of the eigenvalues for the small and large parameters will be performed in a preliminary step, which will then also serve to validate the computational results. For details of the expansion of the Hc function and the eigenvalue equation (3.14) see Appendix A.2.

3.2.2.1 Temporal stability for small and large α

We first consider the asymptotic solution of the eigenvalue problem for the small wavenumber, i.e. $\alpha \to 0$. From theoretical considerations and results to be shown in §3.3, a power-series expansion of ω as a function of α is suggested, i.e.

$$\omega = k_1\alpha + k_2\alpha^2 + k_3\alpha^3 + \mathcal{O}(\alpha^4). \tag{3.16}$$

Substituting the above relation into (3.14), expanding the Hc function by power series (Ronveaux & Arscott, 1995) and collecting the coefficients of the powers of α, the eigenvalue equation (3.14) can be rewritten as

$$a_1(k_1; M)\alpha + a_2(k_1, k_2; M)\alpha^2 + a_3(k_1, k_2, k_3; M)\alpha^3 + \mathcal{O}(\alpha^4) = 0, \tag{3.17}$$

where each of the coefficient functions a_1, a_2 and a_3 have to be zero separately. Its solution provides the values of k_1, k_2 and k_3 in (3.16) (see Appendix A.2), which in turn give the leading order terms of ω for $\alpha \to 0$

$$\omega(M,\alpha) = \frac{M+1}{M}\alpha - \frac{M\left(2M^2+15M+12\right)^2}{72(M+1)^4}\alpha^3 + \mathcal{O}(\alpha^4). \tag{3.18}$$

Equation (3.18) implies that there are only real ω eigenvalues for small α, and the eigenvalue is unique. This asymptotic solution of the eigenvalues is validated by solutions of (3.14) in §3.3.1.

Next, we consider the asymptotic behaviour of (3.14) for the large wavenumber, i.e. $\alpha \to \infty$. A Laurant series in α beginning with a linear dependence proved to be successful, where the leading terms read

$$\omega = l_1\alpha + l_2 + l_3\alpha^{-1} + \mathcal{O}(\alpha^{-2}). \tag{3.19}$$

Employing the above relation to (3.14), expanding the Hc function and its derivative in the limit $\alpha \to \infty$ and collecting the leading order terms, we obtain

$$b_1(l_1; M)\alpha^2 + b_2(l_1, l_2; M)\alpha^1 + b_3(l_1, l_2, l_3; M)\alpha^0 + \mathcal{O}(\alpha^{-1}) = 0, \tag{3.20}$$

where each coefficient function b_1, b_2 and b_3 has to vanish separately, which in turn determines l_1-l_3 (see Appendix A.2). Together with (3.19) we obtain

$$\omega(M,\alpha) = \frac{M+\sqrt{M^2+4}}{2M}\alpha + l_2(M) + l_3(M)\alpha^{-1} + \mathcal{O}(\alpha^{-2}), \tag{3.21}$$

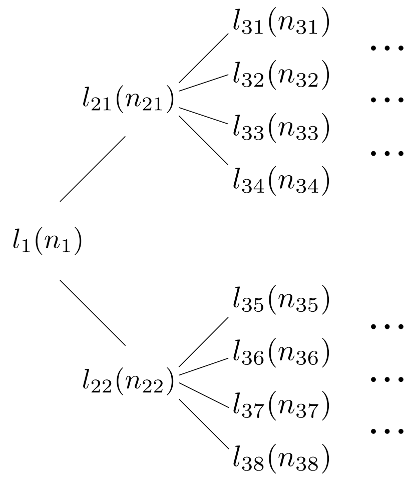

Figure 3.1: A tree diagram to illustrate (3.21)/(3.22) and (3.28)/(3.29).

where $l_1 = \left(M - \sqrt{M^2+4}\right)/2M$ has been excluded (see Appendix A.2) and

$$l_2(M) = \pm \frac{M^3 - M^2\sqrt{M^2+4} + M + \sqrt{M^2+4}}{\left(M^3 - M^2\sqrt{M^2+4} + 4M - 2\sqrt{M^2+4}\right)\sqrt{-2M^2 + 2M\sqrt{M^2+4}}}, \tag{3.22}$$

i.e. we obtain two real values of l_2, while the values of l_3 have been omitted due to the limitation of space. Without giving details we observe that for l_3 we get four values corresponding to one value of l_2, i.e. we have eight values of l_3 in total. An illustration of multiple values of l_i is shown in figure 3.1. We observe that this branching process continues for higher l_i, and further for each value α, i.e. multiple numbers are obtained, which leads to an infinite multi- and real-valued behaviour of ω as $\alpha \to \infty$.

It should be emphasised that the above analytical solutions (3.18) and (3.21) are only valid for $M \leq 1$ and $M \leq \sqrt{2}/2$, respectively, due to the limitation of the radius of convergence of the series expansion of the *H*c function. Since for $M > 1$ (for small α) and $M > \sqrt{2}/2$ (for large α), the argument $\alpha/(\omega - \alpha)$ of the *H*c function is located outside the radius of convergence of its series expansion, which equals one, the power-series expansion employed in (A.13) fails. This can be checked by substituting the leading order term from (3.18) and (3.21) into the argument of the *H*c function. However, it is still possible to obtain the value of the *H*c function by numerical methods. The numerical method to extend the evaluation of the *H*c function outside the circle of convergence of the series is the analytic continuation (Motygin, 2018).

3.2.2.2 Spatial stability for small and large ω

The asymptotic analysis of the eigenvalue equation (3.14) for spatial stability starts with a power series to expand α as a function of ω, which reads

$$\alpha\left(M, \omega\right) = m_1\omega + m_2\omega^2 + m_3\omega^3. \tag{3.23}$$

Similar to the asymptotic analysis for temporal stability, taking (3.23) into (3.14), expanding the Hc function by power series (Ronveaux & Arscott, 1995) and collecting the coefficients to the powers of ω, the eigenvalue equation (3.14) can be expressed as

$$c_1(m_1;M)\omega + c_2(m_1,m_2;M)\omega^2 + c_3(m_1,m_2,m_3;M)\omega^3 + \mathcal{O}(\omega^4) = 0, \tag{3.24}$$

where each coefficient function c_1, c_2 and c_3 has to be zero separately. From this, the leading order term of α for $\omega \to 0$ reads (for details to functions c_1, c_2 and c_3 see Appendix A.3)

$$\alpha\left(M,\omega\right) = \frac{M}{M+1}\omega, \tag{3.25}$$

where from functions c_2 and c_3 the coefficients $m_2 = 0$ and $m_3 = 0$ are determined. The asymptotic solution (3.25) indicates an unique real eigenvalue α for $\omega \to 0$. This result can be clearly observed in §3.4.1.

To consider the asymptotic behaviour of (3.14) for the large frequency, i.e. $\omega \to \infty$, a Laurent series in α is employed

$$\alpha\left(M,\omega\right) = n_1\omega + n_2 + n_3\omega^{-1}. \tag{3.26}$$

Substituting the above relation into (3.14), expanding the Hc function and its derivative in the limit $\omega \to \infty$ and collecting the leading order terms, we obtain

$$d_1(n_1;M)\omega^2 + d_2(n_1,n_2;M)\omega + d_3(n_1,n_2,n_3;M)\omega^0 + \mathcal{O}(\omega^{-1}) = 0, \tag{3.27}$$

where each coefficient function d_1, d_2 and d_3 has to vanish separately, which in turn determines n_1-n_3 (see Appendix A.3).

The asymptotic solution for $\omega \to \infty$ reads

$$\alpha(M,\omega) = \frac{2M}{M+\sqrt{M^2+4}}\omega + n_2(M) + n_3(M)\omega^{-1} + \mathcal{O}(\omega^{-2}), \tag{3.28}$$

where $n_1 = 2M/\left(M-\sqrt{M^2+4}\right)$ has been excluded (see Appendix A.3) and

$$\begin{aligned} n_2(M) = \pm\, & \frac{M\sqrt{2}\left[M^8+6M^6+8M^4-2M^2-2-M\left(M^6+4M^4+2M^2-2\right)\sqrt{M^2+4}\right]}{\sqrt{\left(M-1\right)\left(M^2+M+1\right)\sqrt{M^2+4}-M^2\left(M^2+3\right)}}\times \\ & \times\frac{1}{2\left(M^2+4\right)\left(M^4+3M^2+1\right)-2M\left(M^4+5M^2+5\right)\sqrt{M^2+4}}. \end{aligned} \tag{3.29}$$

At this point, we obtain two real values of n_2, while the values of n_3 have been omitted due to the limitation of space. By saving details we observe four values for n_3 corresponding to one value of n_2, i.e. we have eight values of n_3 in total. A similar principle of multiple values for the large ω is thereby confirmed and shown in figure 3.1. We testify that this branching process continues for higher n_i, i.e. multiple values are obtained, which leads to an infinite multi- and real-valued behaviour of α as $\omega \to \infty$.

It should be emphasised again that the above analytical solutions (3.25) and (3.28) are only valid for $M \leq 1$ and $M \leq \sqrt{2}/2$, respectively, due to the limitation of the radius of convergence of the series expansion of the Hc function.

The results of asymptotic analysis for spatial stability are very similar to that of temporal stability. By only taking the first leading order term in (3.18) and (3.25), or (3.21) and (3.28), we find that ω and α are inverse functions of each other, i.e. the coefficients of the first leading order terms of $\omega(\alpha, M)$ and $\alpha(\omega, M)$ are reciprocal of each other.

3.2.3 α-ω-plane analysis and physical bounds

To understand the intrinsic character of the eigenvalue spectrum $\omega = \omega(\alpha, M)$ for temporal stability and $\alpha = \alpha(\omega, M)$ for spatial stability, we will first derive physical bounds in the α-ω-plane.

We start from the temporal stability problem and consider the dimensional value of $\tilde{\omega} = \tilde{\omega}_r + i\tilde{\omega}_i$, where $\tilde{\omega}_r$ stands for the frequency and $\tilde{\omega}_i$ is the temporal damping/amplification. From (2.11) we observe that the dimensional value of $\tilde{\omega}_r/\tilde{\alpha}$ represents the phase velocity of the acoustic wave in the x-direction. In the present work, under the homentropic assumption, only acoustic modes are expected to appear. This means that the phase velocity should be greater than or equal to the speed of sound c, which leads to a lower bound to the acoustic eigenvalues.

Normally, for subsonic flows and considering for a moment a continuous spectrum, there are two branches (Tumin 2011; Chuvakhov & Fedorov 2016). One of the branches is the upper bound $U_\infty + c$, which stands for an acoustic wave to propagate downstream, and the other is the lower bound $U_\infty - c$, which represents an acoustic wave to propagate upstream. However, the latter does not appear in the present study because we only focus on the discrete spectrum. Further, through asymptotic analysis, we exclude the possibility of discrete modes arising from the branch $U_\infty - c$, which in the non-dimensional case is equivalent to $\omega/\alpha = 1 - 1/M$ of $\sqrt{\theta}$. A detailed explanation of this can be found in Appendix A.2.

From our results observed in both sub-and supersonic cases in §3.3.1, the phase velocity of the perturbation is always greater than the speed of sound. The upper bound for the frequency $\tilde{\omega}_r$ emerges from the fact that the phase velocity of the perturbation cannot exceed the sum of the speed of sound c and free-stream velocity U_∞. Thus, for the acoustic modes, the phase velocity of the perturbation in this paper satisfies the following condition

$$c \leq \frac{\tilde{\omega}_r}{\tilde{\alpha}} \leq c + U_\infty, \tag{3.30}$$

where the dimensional values are given by $\tilde{\omega} = U_\infty \omega/\delta$ and $\tilde{\alpha} = \alpha/\delta$. It yields further its non-dimensional form

$$\frac{1}{M} \leq \frac{\omega_r}{\alpha} \leq 1 + \frac{1}{M}, \tag{3.31}$$

which can be observed in all the following results in §3.3.1.

For supersonic flows and $M > 2$, special modes appear in $1/M \leq \omega_r/\alpha \leq 1 - 1/M$. This occurs only when the Mach number is greater than two. Otherwise, the lower bound of the acoustic mode $1/M$ will constrain the eigenvalues. Those modes are the supersonic modes. The category of sub- and supersonic modes was first discussed by Lees & Lin (1946). In the present thesis, it is defined from the perspective of temporal stability as follows.

i) Subsonic modes, $\omega_r/\alpha \in [1 - 1/M, 1 + 1/M]$: They correspond to non-radiating acoustic waves. The perturbation of subsonic modes is normally confined to the boundary layer. The

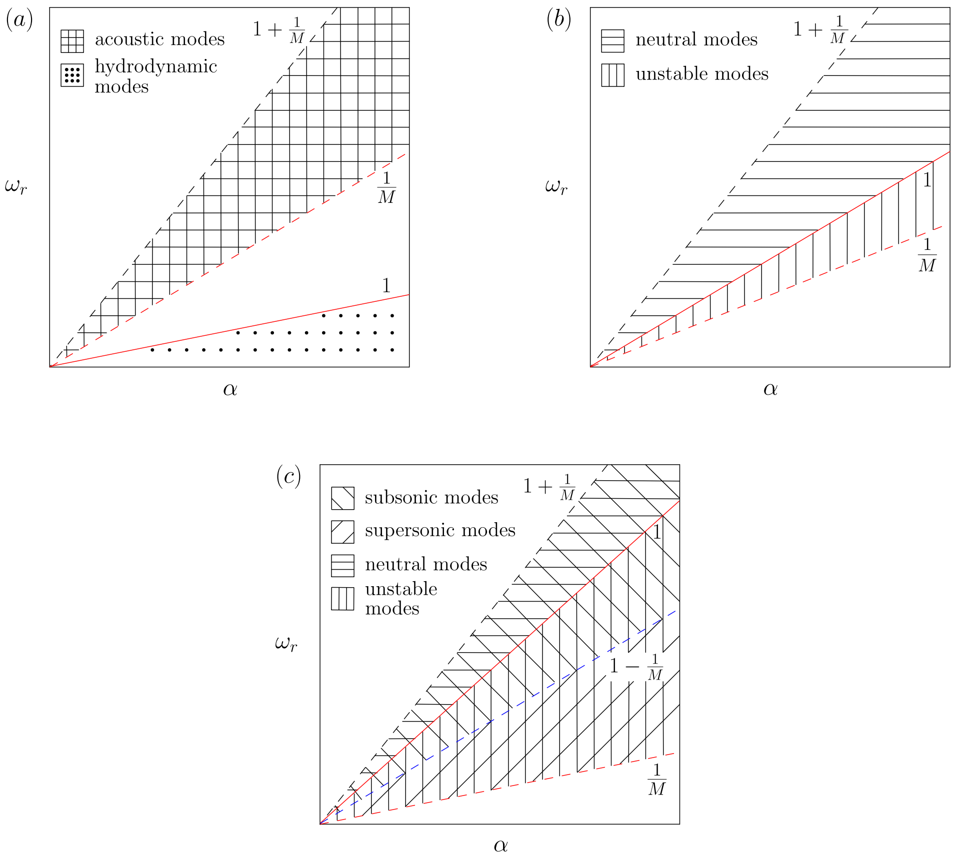

Figure 3.2: Scheme of temporal modes in terms of different intervals of Mach numbers: (a) $M \leq 1$, (b) $1 < M \leq 2$, and (c) $M > 2$, where different line types with slope equal to $1 - 1/M$ - - -, $1/M$ - - -, 1 —— and $1 + 1/M$ - - - correspond to the phase velocity ω_r/α.

eigenfunctions correspond either to spatial exponential decay $(\omega_i = 0)$ or spatial exponential decay superposed by weak oscillations $(\omega_i \neq 0)$, in y-direction.

ii) Supersonic modes, $\omega_r/\alpha \in [1/M, 1 - 1/M]$: They correspond to radiating acoustic waves and exist for $M > 2$ only. The eigenfunctions of supersonic modes mainly spatially oscillate to the far-field $y \to \infty$ but with weak damping for $\omega_i \neq 0$.

Figure 3.2 intuitively summarises the schematic of the different modes, which can be observed in the results in §3.3 below. For a subsonic flow as displayed in figure 3.2(a), the acoustic and hydrodynamic modes are distinguished by the phase velocity of the perturbation. The hydrodynamic mode has an obviously small phase velocity, which is rather different from the speed of sound c (Mancinelli et al., 2018). For a supersonic flow, two cases are distinguished, i.e. $1 < M \leq 2$ and $M > 2$. In figure 3.2(b) for $1 < M \leq 2$, unstable acoustic modes appear. The regions of neutral and unstable modes are separated by a transonic line $\omega_r = \alpha$, at which the phase velocity of the perturbation is equal to the free-stream velocity and marked by a dash-dotted line. In figure 3.2(c) for $M > 2$, supersonic modes appear, which are always unstable.

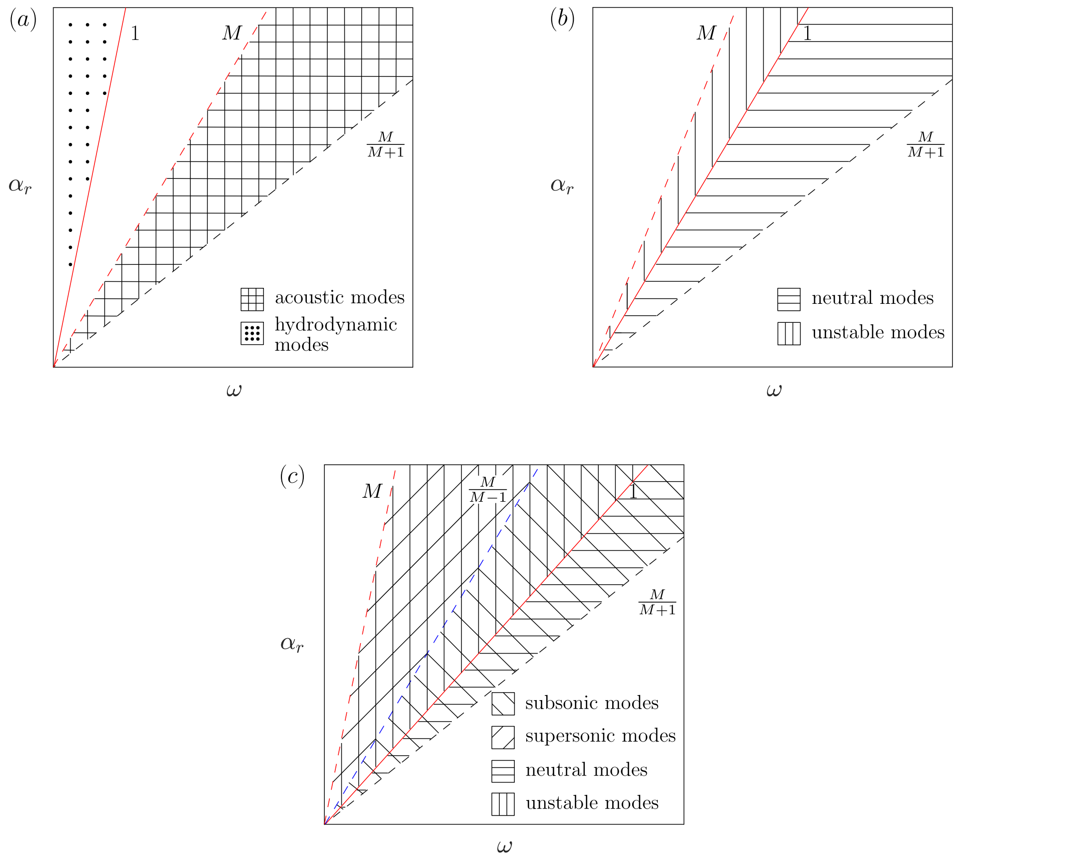

Figure 3.3: Scheme of spatial modes in terms of different intervals of Mach numbers: (a) $M \leq 1$, (b) $1 < M \leq 2$, and (c) $M > 2$, where different line types with slope equal to $M/(M-1)$, M, 1 and $M/(M+1)$ correspond to the reciprocal of the phase velocity α_r/ω.

In the case of the spatial stability problem, physical bounds remain, i.e.

$$c \leq \frac{\tilde{\omega}}{\tilde{\alpha}_r} \leq c + U_\infty. \tag{3.32}$$

Thus, the classification of subsonic and supersonic modes is as the same as that of temporal stability. For the spatial stability problem where the eigenvalue spectrum $\alpha = \alpha_r + i\alpha_i$ is sought, It yields further its non-dimensional form

$$\frac{M}{M+1} \leq \frac{\alpha_r}{\omega} \leq M, \tag{3.33}$$

The classification of subsonic and supersonic modes also follows the classification under physical bounds (3.30).

i) Subsonic modes, $\alpha_r/\omega \in [M/(M+1), M/(M-1)]$.

ii) Supersonic modes, $\alpha_r/\omega \in [M/(M-1), M]$.

Figure 3.3 shows the scheme of spatial stability modes for different Mach numbers.

Note that here we classify the modes by the phase velocity in the x-direction. This should not be confused with the velocity of the base flow. When we refer to subsonic, transonic, and supersonic flow (case), we are referring to the Mach number of the free stream, $M < 1$, $M = 1$, and $M > 1$ respectively.

3.2.4 The neutral-unstable mode border

It was already noted above that the line of neutral stability is separated by the transonic line, at which phase velocity and free-stream velocity are equal. In the present notation, this means $\omega = \alpha$ (same applies for $\alpha = \omega$), which, being employed in the PBE (2.31), simplifies the latter to

$$\frac{d^2\hat{\rho}}{dy^2} + 2\frac{d\hat{\rho}}{dy} + \left(\alpha^2 M^2 e^{-2y} - \alpha^2\right)\hat{\rho} = 0. \tag{3.34}$$

The exact solution of (3.34) can be expressed in terms of Bessel functions, i.e.

$$\hat{\rho}(y) = C_1' e^{-y} J_\nu(\alpha M e^{-y}) + C_2' e^{-y} Y_\nu(\alpha M e^{-y}), \tag{3.35}$$

where $\nu = \sqrt{\alpha^2 + 1}$, and $J_\nu(z)$ and $Y_\nu(z)$ are Bessel functions of the first and second kind (Olver et al., 2010).

These Bessel functions admit the following asymptotic expansion when ν is fixed and for $z \to 0$, i.e. $J_\nu(z) \sim (z/2)^\nu / \Gamma(\nu+1)$ for $\nu \neq -1, -2, \ldots$ and $Y_\nu(z) \sim -\Gamma(\nu)(z/2)^{-\nu}/\pi$ for $\Re(\nu) > 0$. Substituting this into (3.35) and using the first boundary condition (2.33), we directly obtain

$$C_2' = 0. \tag{3.36}$$

Employing the second boundary condition (3.3) into (3.35), we obtain the eigenvalue problem

$$\alpha M J_{\nu+1}(\alpha M) - (\nu + 1) J_\nu(\alpha M) = 0, \tag{3.37}$$

where M is the free parameter and α is the sought eigenvalue.

For a given M, (3.37) defines the α_+ which denote the crossings (labelled with red crosses) of the $\omega = \alpha$ line with the modal lines as shown in figure 3.5(a) and figure 3.6(a). A modal line is the black solid line referring to the real parts of the eigenvalues at varying parameters. Or for spatial stability, (3.37) defines the ω_+ which stands for the crossings (labeled with red crosses) of the $\alpha = \omega$ line with the modal lines as shown in figure 3.14(a) and figure 3.15(a). Further, they mark the starting points of temporally unstable modes with $\omega_i \neq 0$ (at crosses $\omega_i = 0$) in the ω_i-α diagram as may be taken from figure 3.6(b), and the starting points of spatially unstable modes with $\alpha_i \neq 0$ (at crosses $\alpha_i = 0$) in the α_i-ω diagram as may be taken from figure 3.15(b).

In the limit of large M, (3.37) may be solved explicitly. For this we use the asymptotic expansion of the Bessel function of the first kind when ν is fixed and for $z \to \infty$, which reads $J_\nu(z) = \sqrt{2/(\pi z)}\cos(z - \nu\pi/2 - \pi/4)$ (Olver et al., 2010). Using this for the limit $M \to \infty$ and implementing it into (3.37), the first term, i.e. $\alpha M J_{\nu+1}(\alpha M)$ in (3.37), becomes the leading order term. For the cosine function to become zero, the argument of the trigonometric function in the asymptotic expansion has to satisfy

$$\alpha M = n\pi + \frac{\nu\pi}{2} + \frac{\pi}{4}, \tag{3.38}$$

which gives a dispersion relation and indicates that $n \in \mathbb{N}$ has to be large in the limit of large M, i.e. $n\pi$ is dominant on the right-hand side of (3.38). Thus, an explicit expression of infinite eigenvalues reads

$$\alpha = \frac{n\pi}{M}, \tag{3.39}$$

for large M and large $n \in \mathbb{N}$.

All the above analytical results are validated by the computations shown in §3.3 and §3.4. The number of the intersections is increasing with growing Mach numbers, as may be taken from figures 3.5(a), 3.6(a), 3.14(a) and 3.15(a). Intersections can be computed numerically through (3.37), which gives the critical wavenumber for each mode for fixed Mach number or the critical Mach number for each mode for fixed wavenumber. The neutral stability line $(\omega_i = 0)$ in figure 3.8 and the neutral stability line $(\alpha_i = 0)$ in figure 3.17 are also determined through (3.37).

3.3 Results for temporal stability

In this section, we present detailed results in the case of the eigenvalue problem (3.14) for temporal stability. For this, the key difficulty is the precise numerical evaluation of the CHF, i.e. the *H*c function and its derivative. For this purpose, we employed both `Maple 2020` and Matlab code for which we used the external CHF package by Motygin (2018). The latter package was used to validate the results obtained by `Maple 2020`. The *H*c function in `Maple 2020` circumvents the complex connection problem between different series expansions and instead applies an analytic continuation method that provides high precision numerical evaluations in the whole complex domain. From a computational point of view, this is a major advantage compared to the solutions obtained by the Frobenius method in Campos & Serrão (1998).

The root-finding algorithm for determining ω from (3.14) is based on Müller's method (Lang & Frenzel, 1994), which is an extension of the secant method using quadratic interpolation for faster convergence. An introduction to this numerical algorithm can be found in Zhang (2018). Meanwhile, a detailed description of the numerical method to obtain initial guesses for using Mueller's method is given by Baumgärtner (2020). For large values of M and α, the convergence when evaluating (3.14) became increasingly difficult. This made it necessary to increase the number of digits up to 150 for both `Maple 2020` and Matlab and to drastically reduce the termination error down to $\mathcal{O}(10^{-20})$.

Note that because α and M are real-valued, the imaginary parts of the eigenvalues, i.e. ω_i, are symmetric about the real axis (Schmid & Henningson, 2012). In the following, only the positive values of ω_i are shown. Here we recall the symmetry (3.15) or, in other words, the eigenvalue ω is complex conjugate, i.e. the stable behaviour due to $-\omega$ and produced by $-\alpha$ is not considered presently.

3.3.1 Numerical eigenvalues

Figures 3.4-3.6 display results for the frequency ω_r versus the wavenumber α and the temporal growth rate ω_i versus the wavenumber α for six fixed Mach numbers, $M = 0.2$, $M = 0.5$, $M = 0.8$, $M = 1$, $M = 1.5$ and $M = 3$. Each solid line stands for one mode. We call these lines the modal line. The first mode, i.e. the lowermost continuous line in each case, corresponds to the smallest ω_r for a given α and the second and higher modes refer to increasing ω_r.

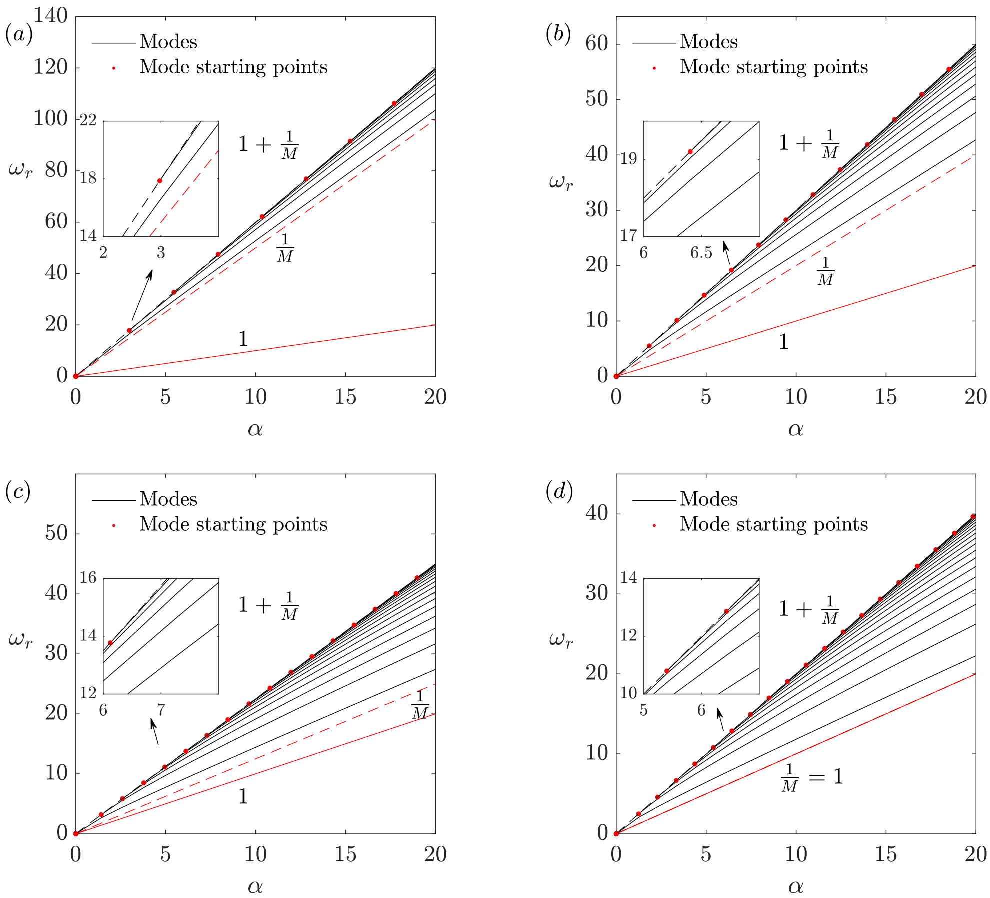

Figure 3.4: The frequency ω_r at the Mach numbers (a) $M = 0.2$, (b) $M = 0.5$, (c) $M = 0.8$ and (d) $M = 1$. Line types of bounds are defined in figure 3.2.

It should be emphasised, as mentioned in §3.1, that the lowermost line here indicates the first acoustic mode corresponding to the second (Mack) mode. Particularly, the so-called first (Mack) mode of a compressible boundary layer (or entropy/vorticity/hydrodynamic/Kelvin-Helmholtz mode in some literature) is not expected to presently appear due to the isothermal assumption associated with a constant speed of sound (Mack 1969; Candelier et al. 2012). This type of mode will be induced by introducing a temperature gradient in the equation of state or due to energy changes, such as an energy equation is supplemented to the PDE system. This does not lead to the PBE but the generalised PBE. The black dashed and red dashed lines, respectively corresponding to the slopes $\omega_r/\alpha = 1 + 1/M$ and $\omega_r/\alpha = 1/M$ represent the upper and lower bounds of the phase velocity for the acoustic modes. On the upper bound, the black dashed line, the starting point for each higher mode is designated by a red bullet. Note that values exactly on the black dashed line, subsequently named mode starting points, only produce trivial solutions because they make $\theta = 0$ in (2.35). To determine the mode starting points, we substitute the relation $\omega = (1 + 1/M)\,\alpha$ into the eigenvalue equation (3.14) and then apply the root-finding algorithm to obtain the eigenvalues. The red solid line corresponds to the transonic line, $\omega_r = \alpha$, where the phase velocity of the perturbations equals the free-stream velocity. This line designates the border below which the imaginary part of the eigenvalue becomes non-zero and thus is named the neutral-unstable mode border, which was detailed discussed in subsection §3.2.4. The blue dashed line corresponding to $\omega_r/\alpha = 1 - 1/M$ stands for the lower bound of subsonic modes, i.e. those modes with eigenvalues below it are supersonic modes. It is only shown for supersonic cases, see figure 3.5 and figure 3.6.

In figure 3.4, only the real parts of the eigenvalue for the cases $M = 0.2$, $M = 0.5$, $M = 0.8$ and $M = 1$ are plotted because the imaginary part of ω is zero. This result validates the previous conclusion by Mack (1990) that there is no acoustic instability for the subsonic and transonic cases. In figure 3.4, we can clearly observe that for the subsonic cases, all the eigenvalues are above the neutral-unstable mode border, i.e. $\omega_r/\alpha = 1$. The phase velocity of the perturbation is always greater than the free-stream velocity. This acoustic characteristic does not lead to acoustic instability. The critical case appears for the transonic case, where the lower bound $\omega_r/\alpha = 1/M$ overlaps with the red solid line with $\omega_r/\alpha = 1$. Furthermore, the subsonic results validate the asymptotic analysis in §3.2.2 that for small α, only unique and real eigenvalue exists, while multiple eigenvalues appear for large wavenumbers.

Figures 3.5 and 3.6 show the frequency ω_r in subfigure (a) and the growth rate ω_i in subfigure (b) for two supersonic cases $M = 1.5$ and $M = 3$. It is obvious that for the supersonic cases there are denser starting points leading to more acoustic modes. Due to the supersonic character of the free stream, the phase velocity of the perturbation can be smaller than the free-stream velocity, reflected in intersections of the different modes with the red solid line $\omega_r/\alpha = 1$, marked by red "$+$". Each intersection gives rise to a set of unstable modes. In figure 3.5 for $M = 1.5$, we have $\alpha_{+_1} = 3.62$ and $\alpha_{+_2} = 14.37$, which was computed from (3.37). To the right of the intersections, i.e. below the red solid line in figure 3.5(a) and 3.6(a), the phase velocity of the perturbation is smaller than the free-stream velocity, hence unstable acoustic modes, i.e. eigenvalues with imaginary parts, arise. In figure 3.5(b) for $M = 1.5$, the unstable modes appear as soon as the phase velocity of the perturbation is smaller than the free-stream velocity. With increasing α, the growth rate ω_i reaches the maximum marked with a red square in figure 3.5(b), whose real part is also marked in figure 3.5(a). The maximum ω_i has an order of magnitude of 10^{-11}, which might not be detected or cause any acoustic instability experimentally. However, this small value is verified not to be a numerical error and exists theoretically. It is important to mention that a second intersection exists in figure 3.5(a), which refers to a second unstable mode appearing from α_{+_2} on. However, their values are even much smaller than the order of magnitude of 10^{-11} and will not be shown presently. Such higher unstable modes are more clearly visible for larger Mach numbers. In figure 3.6 for $M = 3$, the locations of the maxima of the imaginary part of the first three modes are respectively indicated, by a red circle, a red rhombus and a red triangle and are shown in figure 3.6. In comparison with the first mode, the maximum growth rates of the higher modes fall off rapidly with an exponential decay rate.

Figures 3.4, 3.5 and 3.6 show that in subsonic and transonic boundary layer flows no unstable

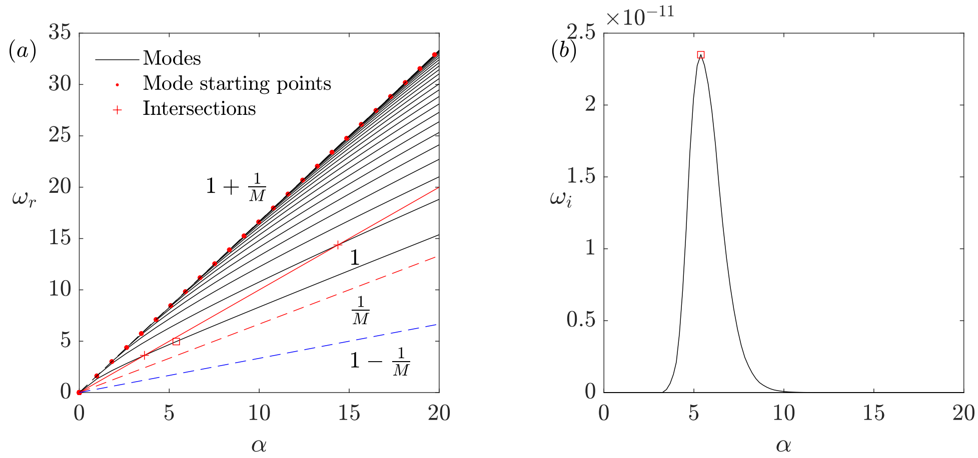

Figure 3.5: The frequency ω_r (a) and the growth rate ω_i of the first mode (b) at the Mach number $M = 1.5$. □: Maximum in ω_i. Definition of lines is according to figure 3.2.

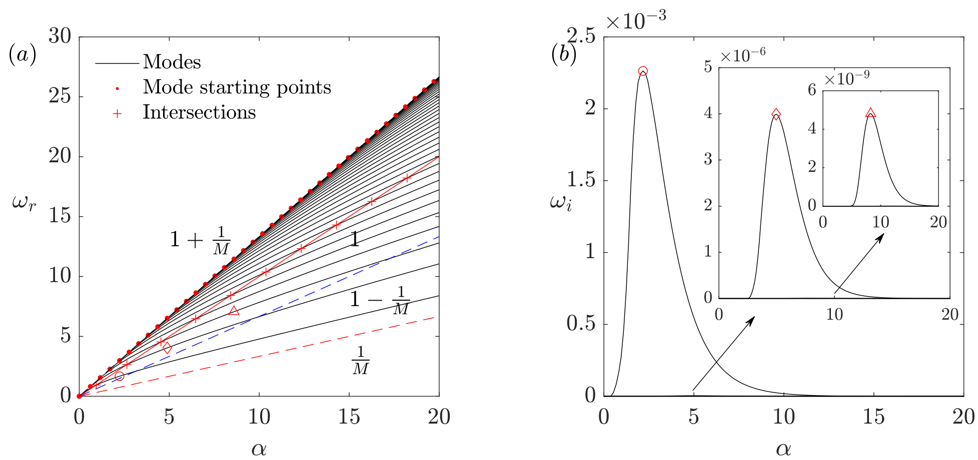

Figure 3.6: The frequency ω_r (a) and the growth rate ω_i of the first three modes (b) at the Mach number $M = 3$. ○, ◇, △: Maximum in ω_i of the first, second and third mode. Definition of lines is according to figure 3.2.

acoustic modes exist, which confirms the results of the asymptotic analysis in §3.2.3. The unstable acoustic modes exist for the supersonic exponential boundary layer, depending on whether the phase velocity of the perturbation is smaller than the free-stream velocity. The number of eigenvalues grows with the increase of both wavenumbers and Mach numbers. The higher acoustic modes have weaker unstable behaviour.

By varying the Mach numbers, figure 3.7 demonstrates the transition of the most unstable acoustic mode, i.e. the first acoustic mode, from subsonic to supersonic. For $M = 3$, the most unstable mode marked by a red triangle is a subsonic mode, i.e. lies above the $1 - 1/M$ line for $M = 3$. However, with increasing Mach numbers, here $M = 4$ and $M = 5$, the location of the maximum of ω_i shifts towards smaller α to below the corresponding sub-supersonic mode border $\omega_r/\alpha = 1 - 1/M$, i.e. the most unstable mode becomes a supersonic mode, which means $\omega_r/\alpha < 1 - 1/M$. This phenomenon is also known for other types of supersonic flows

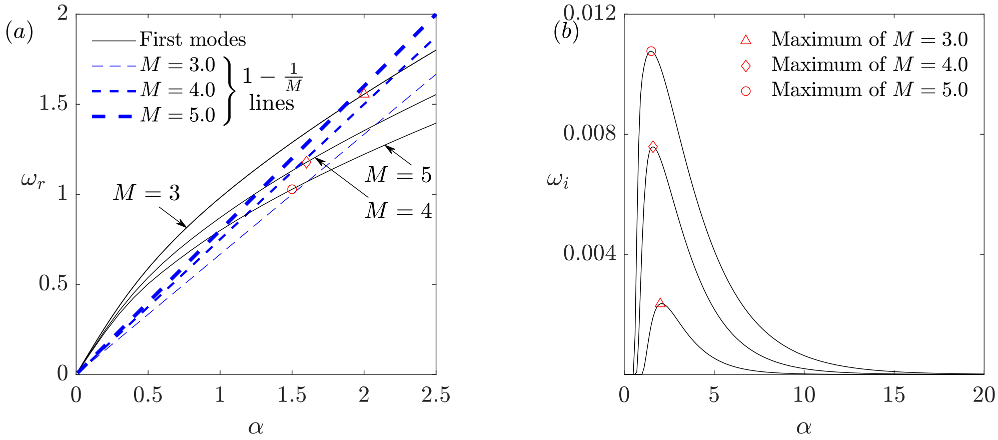

Figure 3.7: The transition of the maximum growth rate from the subsonic mode to the supersonic mode. (a) The frequency ω_r and (b) the growth rate ω_i of the first mode for Mach numbers $M = 3$, $M = 4$ and $M = 5$. Definition of blue dashed lines is according to figure 3.2.

and was also reported in a supersonic round jet flow in Parras & Le Dizès (2010) and Samanta (2016), in a supersonic cavity flow in Zhang et al. (2016), in a hypersonic boundary layer flow in Knisely (2018) and in a supersonic jet in Chen et al. (2018). Parras & Le Dizès (2010) gave precise numerical value to this type of the transition and concluded in their study for round jet flows that a supersonic mode becomes the most unstable mode when the Mach number is greater than $M \approx 5$. For the present case of an exponential boundary layer flow, this value is around $M \approx 4$, as observed in figure 3.7.

A more comprehensive overview of the stability behaviour for the present flow is obtained by means of a 3-D plot in figure 3.8, where we plot the growth rate ω_i of the first three acoustic modes as a function of M and α. Therein we give contour lines, where the thick solid line corresponds to the border between $\omega_i = 0$ and $\omega_i > 0$. This line was computed from equation (3.37), which approximates $M = 1$ for large α, and $\alpha = 0$ for large M. This is consistent with the previous conclusion that acoustic instabilities appear only for supersonic flows. In figure 3.8, the dashed line represents the maximum of ω_i for a fixed α or M.

In figures 3.8(a)-(c), we again observe that the first acoustic mode is always the most unstable one and further that the value of ω_i decreases exponentially with increasing mode number. A similar conclusion for acoustic modes was also reported by Mack (1965) for two-dimensional adiabatic flat-plate boundary layer flows and jet flows by Tam & Burton (1984b).

Mack's conclusion for boundary layer flows was that the first acoustic mode instability occurs for $M \geq 2.2$. The present critical Mach number is very close to this value, which can be observed in figure 3.8(a). Theoretically, the critical Mach number is related to the value of α and decreases with increasing wavenumbers, till $M = 1$ for $\alpha \to \infty$. Nevertheless, if we choose an effective growth rate, e.g. $\omega_i = 0.001$ to indicate the smallest detectable instability, the critical Mach number is $M_c \approx 2.7$ at $\alpha \approx 2.2$, as shown in figure 3.8(a) by the contour line for $\omega_i = 0.001$. In addition to the fact that with increasing modes the growth rates fall off exponentially, the entire contour seems to shift towards large α for higher modes.

Furthermore, through the maximum ω_i marked by a black dashed line, it is interesting to notice

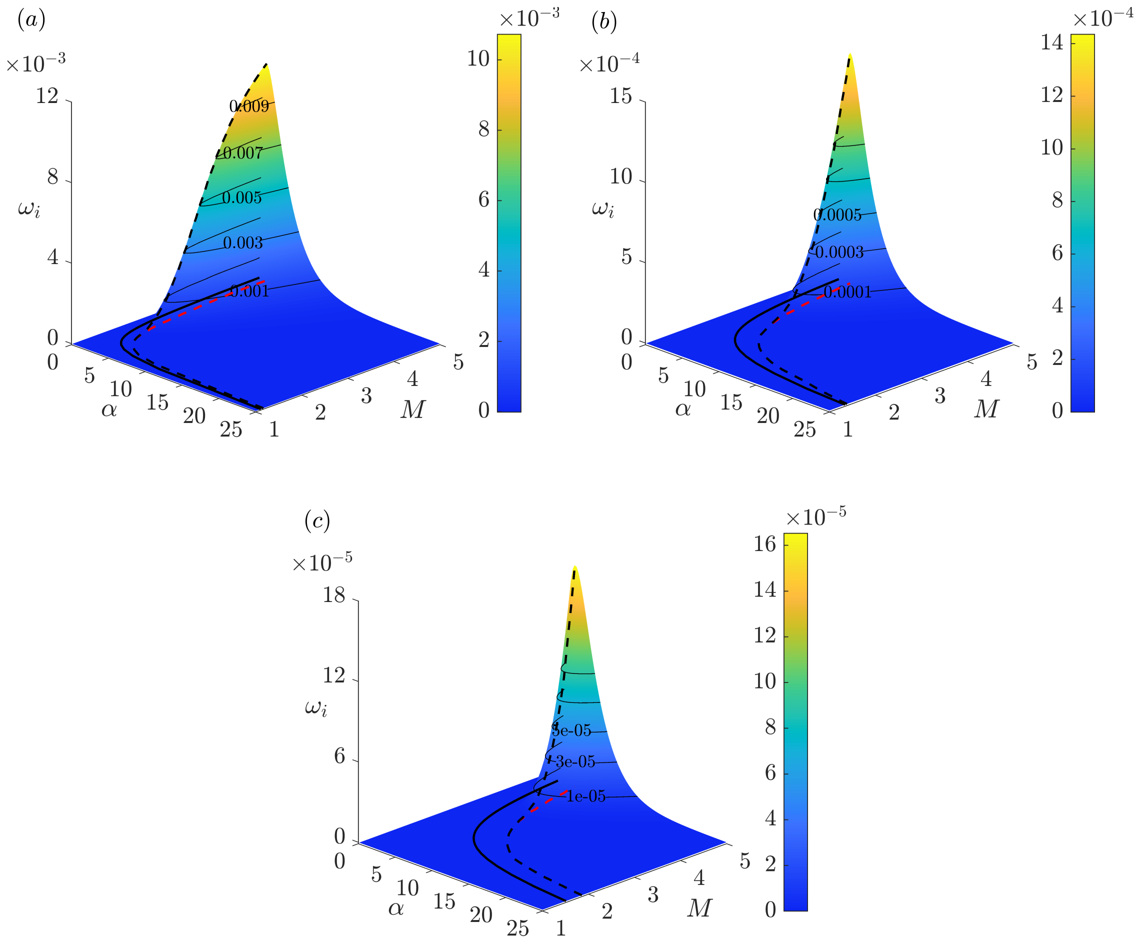

Figure 3.8: The growth rate ω_i as a function of M and α for (a) first mode, (b) second mode and (c) third mode. —— defines the neutral-unstable mode border according to (3.37). - - - defines the line of maximum growth for a given M or α and - - - defines the same line but projected onto the α-M plane.

that for every fixed Mach number there exists a maximum growth rate. The corresponding wavenumber decreases with the Mach number, and the maximum growth rate increases with the Mach number. This fact means that high Mach numbers and small wavenumbers are the most unstable cases.

3.3.2 Acoustic boundary layer

For the development of the present theory, we employed the boundary condition of a vanishing disturbance for $y \to \infty$ in (3.1). With this, however, the decay rate is not specified. From a physical and also a technical point of view, it is essential to know, which of the eigenfunctions decay very slowly, and hence, are audible far away from the boundary layer. For this, we analyse the decay rate of the eigenfunctions in the limit $y \to \infty$. For complex-valued ω, θ emerging in the density amplitude in (3.13), this can be rewritten in the form of (3.5) and $\sqrt{\theta}$ in the form of (3.12). Based on this, the density perturbation for the far-field, i.e. $y \to \infty$,

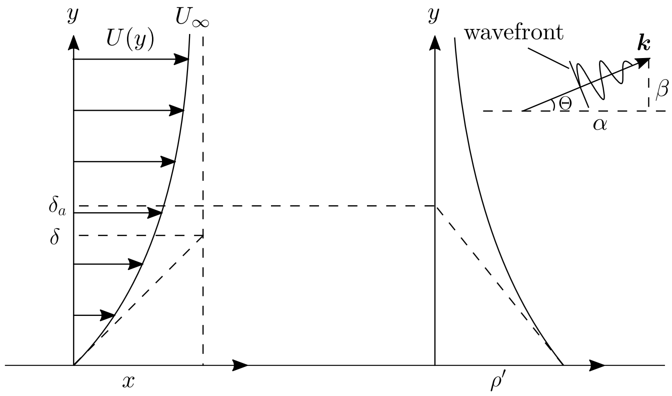

Figure 3.9: An illustration of the acoustic boundary layer δ_a and the wave angle Θ of the exponential boundary layer flows. $\boldsymbol{k}$ is the wave vector.

simplifies to

$$\rho(x, y \to \infty, t) \sim e^{-\sqrt{\theta}y} e^{i(\alpha x - \omega t)} = e^{-\beta_r y} e^{i(\alpha x + \beta_i y - \omega t)}, \tag{3.40}$$

where we have made use of the fact that e^{-y} in the exponent is negligible compared to y and $H\mathrm{c}(;0) = 1$. Further,

$$\begin{aligned}\beta_r &= \frac{\sqrt{2}}{2}\sqrt{\sqrt{{\theta_{r_t}}^2 + {\theta_{i_t}}^2} + \theta_{r_t}} \\ &= \frac{\sqrt{2}}{2}\sqrt{\sqrt{\left[\alpha^2 - M^2\left(\alpha-\omega_r\right)^2 + M^2{\omega_i}^2\right]^2 + 4M^2\left(\alpha-\omega_r\right)^2{\omega_i}^2} + \left[\alpha^2 - M^2\left(\alpha-\omega_r\right)^2 + M^2{\omega_i}^2\right]},\end{aligned} \tag{3.41}$$

represents the wall-normal exponential spatial decay and

$$\begin{aligned}\beta_i &= -\,\mathrm{sign}\left(\theta_{i_t}\right)\frac{\sqrt{2}}{2}\sqrt{\sqrt{{\theta_{r_t}}^2 + {\theta_{i_t}}^2} - \theta_{r_t}} = -\mathrm{sign}\left(\theta_{i_t}\right)\times \\ &\times\frac{\sqrt{2}}{2}\sqrt{\sqrt{\left[\alpha^2 - M^2\left(\alpha-\omega_r\right)^2 + M^2{\omega_i}^2\right]^2 + 4M^2\left(\alpha-\omega_r\right)^2{\omega_i}^2} - \left[\alpha^2 - M^2\left(\alpha-\omega_r\right)^2 + M^2{\omega_i}^2\right]},\end{aligned} \tag{3.42}$$

is the wavenumber in y-direction, where we have used (3.5).

The exponential decay with the wall distance is also true for any other fluctuating flow variable in (2.8c), (2.32) and (2.33). In order to quantify how far out an acoustic signal may be detected, an acoustic boundary layer thickness (ABLT) is defined by

$$\delta_a = \frac{1}{\beta_r}, \tag{3.43}$$

i.e. all perturbations decay as $q \sim e^{-y/\delta_a}$.

According to (2.28a) and the non-dimensionalisation of the entire system, the ABLT is a multiplier of the hydrodynamic boundary layer thickness δ. This value of δ_a quantifies the

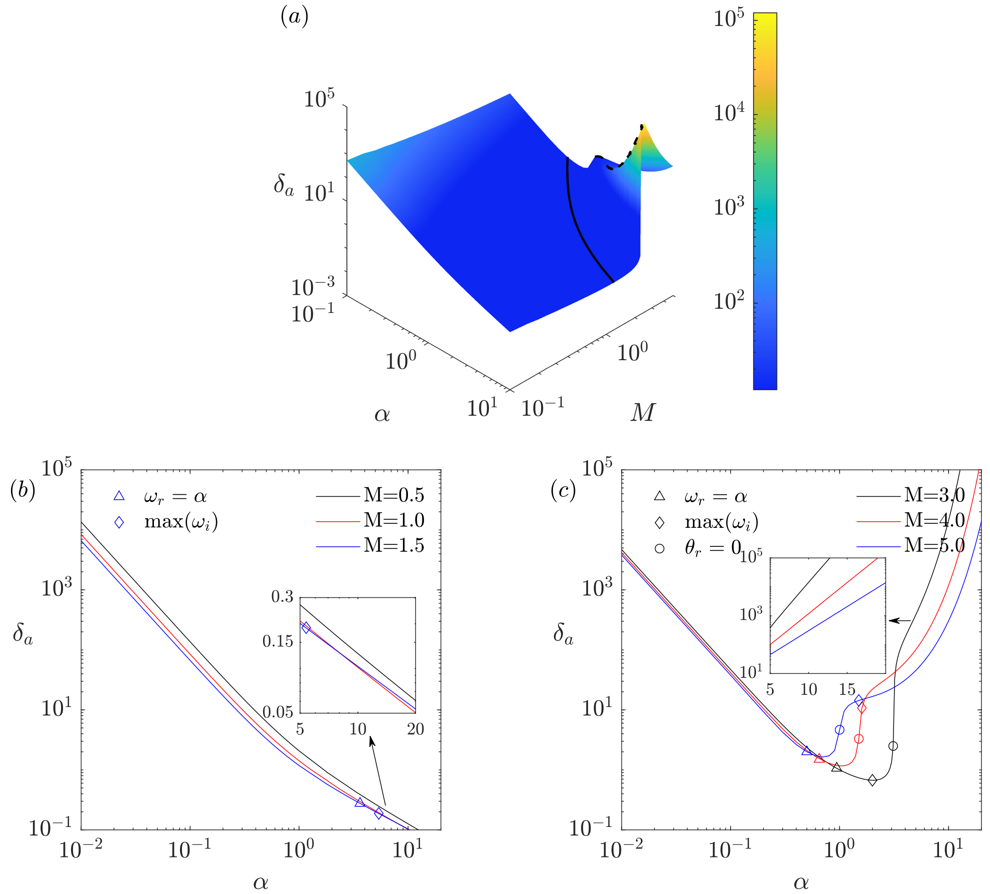

Figure 3.10: Acoustic boundary layer thickness defined by (3.43), where only the first acoustic mode is shown. (a) ABLT δ_a as a function of α and M. defines the neutral-unstable mode border according to (3.37). refers to the line of maximum δ_a for a given α. (b) and (c) δ_a for different Mach numbers $M = 0.5, 1, 1.5, 3, 4, 5$.

range of how far out the perturbation reaches, compared to the boundary layer thickness δ. Across this thickness, an acoustic signal decays to a factor $1/e$ of its original amplitude at the wall. A small β_r, or similarly a large δ_a corresponds to acoustic signals that have a far-reaching impact away from the wall. An intuitive visualisation can be found in figure 3.9.

Figure 3.10 displays the results of the ABLT defined by (3.43) for the first mode plotted on a double logarithmic scale. Figure 3.10(a) is a 3-D plot of the ABLT as a function of M and α. Its projections on the α-δ_a-plane for different fixed Mach numbers are shown in figures 3.10(b) and 3.10(c).

The 3-D plot exhibits a comprehensive picture of the ABLT. For small Mach numbers up to about 1 and small α, the ABLT behaves like an inverse power-law, i.e. $\delta_a \sim \alpha^{-n}$ with $n \approx 2$. Their large values of δ_a correspond to small or zero values of ω_i in figure 3.8. Hence the perception of noise in this parameter range does almost not exist. For large Mach numbers, the decay for small wavenumbers is similar, but with increasing α a minimum is obtained and followed by a strong increase. More detailed interpretations can be obtained from figures 3.10(b) and

3.10(c). In these two figures, we select a few representative Mach numbers to represent the three sets of cases for $M \leq 1$, $1 < M \leq 2$, and $M > 2$.

For the subsonic and transonic cases, $M = 0.5$ and $M = 1$ in figure 3.10(b), the ABLT outlines a smooth monotone power-law decay with increasing wavenumbers. However, for the supersonic cases, the behaviour becomes more complex.

For $1 < M \leq 2$, $M = 1.5$ in figure 3.10(b), the ABLT has a tendency of decay but with a slightly slower decay rate when α exceeds a value marked by a triangle indicating the appearance of $\omega_i \neq 0$. In summary, for $0 < M \leq 2$ the ABLT decays as a power-law with increasing wavenumbers. With increasing Mach numbers the ABLT generally decreases, but with the exception of the supersonic case for which the ABLT for large wavenumbers becomes greater than that in the subsonic case, see the inset in figure 3.10(b).

For $M > 2$ in figure 3.10(c), the pattern is largely different. The ABLT does not decay monotonically. Noting (3.5), (3.8) and (3.41), we observe that for $\omega_i = 0$ and $\omega_r/\alpha = 1 \pm 1/M$, there is $\beta_r = 0$, which corresponds to two singularities of the ABLT. One of the singularities, $\omega_r/\alpha = 1 + 1/M$, appears for small wavenumbers, i.e. the ABLT tends to infinity. However, the other singularity of the ABLT, i.e. $\omega_r/\alpha = 1 - 1/M$, doesn't exist due to the appearance of a non-zero ω_i. For this reason we again note (3.5), (3.8) and (3.41) in the interval, $\omega_r/\alpha \in [1 - 1/M, 1/M]$, where θ_{r_t} becomes negative. This leads to a vertical rise of the ABLT in a small interval as observed in figure 3.10(c). After a drastic growth with increasing α, the contribution of ω_i to the absolute value of θ_{r_t} in (3.41) tends to zero. At the same time, with a disappearing ω_i for large α, the ABLT increases exponentially (see the inset in figure 3.10(c) with a semi-logarithmic rescaling).

The contribution of the absolute value of ω_i for $M > 2$ is essential as it affects the location of the minimum δ_a. With increasing M, the absolute value of ω_i increases. This is the reason why the minimum does not occur exactly at the second location, where we have $\theta_{r_t} = 0$, but shifts towards slightly smaller values of α. From the preceding analysis, it is apparent that there is a certain $\alpha-$domain, where we have both $\omega_i \neq 0$ and large δ_a, such that boundary layer noise is audible from afar.

3.3.3 Wave angle

A geometrical quantity closely related to δ_a is the wave angle Θ, see figure 3.9. It is an angle between the phase velocity of the perturbation in the free stream and the streamwise direction, which reflects the pattern of the acoustic wave in the free stream. From (3.40) the wave angle Θ in the far-field may readily be define as

$$\Theta = \arctan\left(\frac{\beta_i}{\alpha}\right), \tag{3.44}$$

while according to (3.5), (3.12) and (3.42), β_i and hence Θ is apparently only non-zero for a non-zero ω_i. In other words, neutrally stable modes will always propagate along the x-axis in the free stream. Especially for subsonic boundary layer flows, the perturbation propagates along the streamwise direction parallel to the wall, regarded as evanescent waves in Campos & Serrão (1998), as can be taken from figure 3.11(a) where $\Theta = 0$ for $M \leq 1$ and all α. Note that

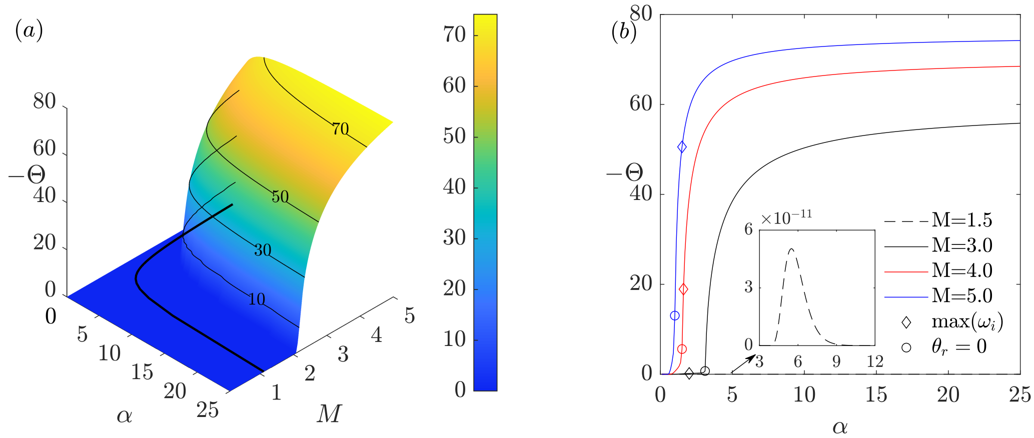

Figure 3.11: Wave angles Θ for large y defined by (3.44), where only the first acoustic mode is shown. The minus sign implies, that we only consider unstable modes. (a) Θ as a function of M and α, (b) Θ as a function of α for different Mach numbers $M = 1.5$, $M = 3$, $M = 4$ and $M = 5$. —— defines the neutral-unstable mode border according to (3.37).

for a given set of α and M, there may exist multiple eigenvalues, which may lead to multiple wave angles.

Figure 3.11(a) is a 3-D plot of the wave angle for the first mode as a function of M and α. Its projection on the α-Θ-plane for different Mach numbers is displayed in figure 3.11(b). A non-zero wave angle apparently only appears for the supersonic cases, i.e. $M > 1$, while a significant deviation from zero is only visible for $M > 2$. As noted above, for subsonic and transonic cases, acoustic waves propagate essentially parallel to the streamwise direction, i.e. no acoustic waves form in the free stream. For the supersonic cases, acoustic waves apparently propagate transversely, i.e. $\Theta \neq 0$. The rapid amplification of the wave angle observed in figure 3.11 has the same reason as explained for the ABLT in §3.3.2.

To comprehend the direction of the phase velocity of the wave for $M > 2$, note the sign of β_i in (3.44), which depends on θ_{i_t} in (3.5). From figure 3.5 and 3.6, we observe that for unstable modes, i.e. $\omega_i > 0$, $\alpha - \omega_r$ is positive. Further, it was noted above that we have the complex-conjugate eigenvalue ω, which, in turn, results in a positive θ_{i_t} for negative ω_i and a negative θ_{i_t} for positive ω_i. In concrete terms, this leads to temporally stable waves with positive Θ and unstable waves with negative Θ, respectively. Because of this sign property, we put a minus sign in front of Θ in figure 3.11, since we only want to consider wave angles for unstable modes.

We note that the described wave phenomenon is not to be confused with plane incident acoustic waves that impact a wall. By definition, these waves do not have any spatial amplitude variation in the undisturbed free stream, i.e. they are non-dispersive waves. This is different here as we note in (3.40) that the eigenfunctions decrease exponentially towards the free stream, i.e. these waves are dispersive waves. Thus, the described wave angle Θ is not to be confused with the propagation angle ψ, where the latter describes the direction in which energy travels. The propagation angle of the acoustic wave is determined by its group velocity, which is defined as

$$v_g = \frac{\partial \omega}{\partial k}, \tag{3.45}$$

where ω is the angular frequency and k is the angular wavenumber. The direction of the group velocity can be derived from the dispersion relation in the free stream given by

$$\theta = \beta^2 = -M^2 (\alpha - \omega)^2 + \alpha^2, \tag{3.46}$$

where $\beta = \beta_r + i\beta_i$ is the complex wavenumber in y-direction. Taking the implicit differentiation of (3.46), the propagation angle ψ determined by the group velocity reads

$$\psi = \arctan\left(\frac{\partial\omega/\partial\beta}{\partial\omega/\partial\alpha}\right) \approx \arctan\left(\frac{\beta_i}{\alpha - M^2(\alpha - \omega_r)}\right), \tag{3.47}$$

where ω_i, due to its relatively small value in comparison with ω_r, i.e. $\omega_i \ll \omega_r$, is neglected. Under consideration of ω_i, a detailed derivation of ψ is given in Appendix A.4. From (3.42) and (3.47), it follows that a supersonic unstable mode produces acoustic waves in the free stream with a positive direction of the group velocity, i.e. radiative waves. The instability mechanism thus generates dispersive waves that spatially decrease in amplitude towards the free stream. This radiative phenomenon generated by unstable modes has been confirmed in recent numerical simulations (Li et al. 2010; Knisely & Zhong 2019a, 2019b) and experiments (Maslov et al. 2009; Zhang et al. 2013; Zhu et al. 2020).

3.3.4 Eigenfunction

To observe the wave feature of the acoustic modes, the eigenfunctions of different modes for the parameters $\alpha = 2$ and $M = 4$ are illustrated in figure 3.12. Therein the eigenfunction of the first unstable mode for a fixed time in the x-y-plane is shown in figure 3.12(a). From figure 3.7, we know that for this parameter set the unstable mode is supersonic (compare also figure 3.2(c)). In figure 3.12(a), transversal waves can be identified in the free stream, whose amplitude grows exponentially with decreasing y towards the wall. Near the wall, we observe strong variations and at the wall itself, though not clearly visible, a zero gradient of the density amplitude $\hat{\rho}$ is present because the density fluctuations are displayed. This observation may be characterised as an accumulation of energy, which saturates near the wall, and leads to temporal instability. In contrast, in figure 3.12(b) and 3.12(c) and also for the parameter set $\alpha = 2$, $M = 4$ we have displayed the second mode, which is weakly unstable and subsonic, and the third mode, which is a neutrally stable subsonic mode. Both the first two modes exhibit a wave-type spatial variation for large y, though only visible in figure 3.12(a), while this is not the case for figure 3.12(c). Note that there is an extremely weak inviscid instability so that the waves in the far-field in figure 3.12(b) are hardly visible.

3.4 Results for spatial stability

This section focuses on the results of the eigenvalue problem for spatial stability defined by the eigenvalue equation (3.14). We adopt the same approach of precise numerical evaluation when dealing with the temporal stability problem. The relevant description is given at the beginning of §3.3. In spatial stability, as parameters, M and ω are real-valued. Under this circumstance, the imaginary parts of the eigenvalues, i.e. α_i, are always symmetric about the

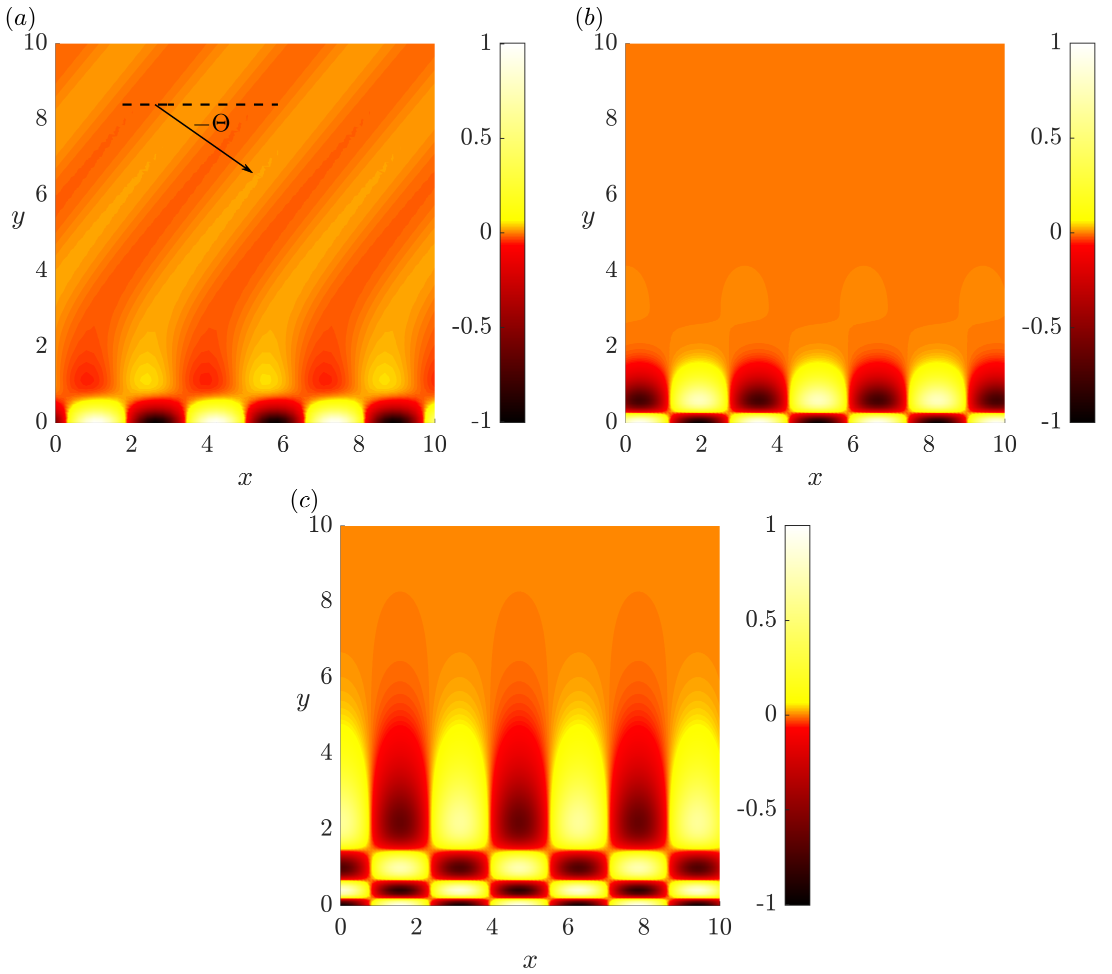

Figure 3.12: Eigenfunction plot at $\alpha = 2$ and $M = 4$. (a) Unstable supersonic mode ($\omega \approx 1.353 + i7.198 \times 10^{-3}$) with a wave-type behaviour in the far-field with the angle $\Theta \approx -39.35°$. The arrow indicates the direction of unstable waves. A weak spatial exponential decay for large y is present though on the given domain hardly visible. (b) Unstable subsonic mode ($\omega \approx 1.906 + i2.014 \times 10^{-5}$) with extremely weak unstable oscillatory behaviour in the far-field; and a wave-type behaviour almost parallel to the wall ($\Theta \approx -4.42° \times 10^{-4}$). (c) Neurally stable subsonic mode ($\omega \approx 2.403$) with no unstable wave behaviour in the far-field ($\Theta = 0°$).

real axis (Schmid & Henningson, 2012). To be concise, only the eigenvalues with negative α_i corresponding to unstable modes are displayed in this section.

3.4.1 Numerical eigenvalues

Figures 3.13-3.15 display results for the wavenumber α_r versus the frequency ω, as well as the spatial growth rate $-\alpha_i$ versus the frequency ω for four representative fixed Mach numbers $M = 0.5$, $M = 1$, $M = 1.5$ and $M = 3$. We follow the study applied in §3.3.1 and refer to the definitions of different lines in figure 3.3. Each solid line represents one mode and is named

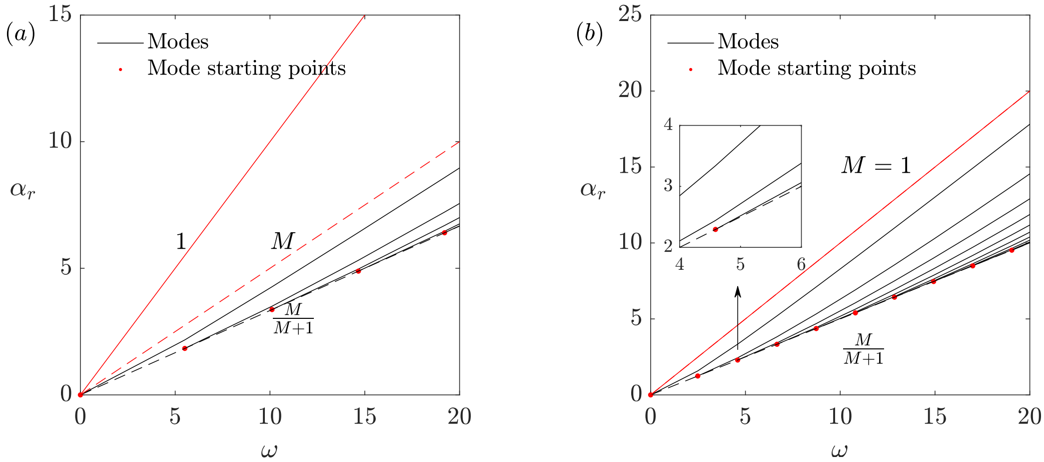

Figure 3.13: The wavenumber α_r at Mach numbers (a) $M = 0.5$ and (b) $M = 1$. Line types of bounds are defined in figure 3.3.

as the modal line. In order to be consistent with the analysis of temporal stability, the solid line consisting of the mode with the lowest frequency is still taken as the first mode. In other words, the mode that appears for the largest α_r, i.e. the uppermost continuous line in each figure, represents the first acoustic mode, i.e. the second (Mack) mode. The first (Mack) mode is still not detected due to the assumption of homentropic flows. The inverse of the phase velocity $\alpha_r/\omega = M/(M+1)$ and $\alpha_r/\omega = M$ form the lower and upper bounds of the acoustic modes and are illustrated herein by black dashed and red dashed lines. Each starting point is determined on the lower bound and marked by a red bullet. In fact, the positions of these points in both temporal and spatial stability problems are identical and fixed in the α_r-ω_r-plane. The transonic line where the phase velocity of the perturbation equals the free-stream velocity, i.e. $\alpha_r = \omega$, is represented by a red solid line. This line is also the neutral-unstable mode border for the spatial stability problem because the modes beyond this line become unstable, i.e. the imaginary part of the eigenvalue α_i becomes non-zero. This case happens only for Mach numbers beyond one in figure 3.14(a) and figure 3.15(a). The blue dashed line corresponding to $\alpha_r/\omega = M/(M-1)$ separates the subsonic mode from the supersonic mode.

Figure 3.13(a) and figure 3.13(b) are results of the eigenvalues at $M = 0.5$ and $M = 1$. Only the real part of the eigenvalues α_r is shown since the imaginary part of the eigenvalues α_i is always zero, i.e. no unstable mode exist for the subsonic flow. It can be seen that the relation α_r/ω is close to linear. In particular, when ω is close to zero, the linear relation is consistent with the asymptotic solution (3.25). With increasing Mach numbers, higher neutrally stable modes are found. In the investigated ω-domain there is no overlap between the modes and the first mode seems to have the largest gradient. For all subsonic cases, the transonic line, i.e. $\alpha_r/\omega = 1$, is not crossed and the phase velocity of the perturbation is always greater than the free-stream velocity.

Figures 3.14 and 3.15 show the wavenumber α_r and the corresponding spatial growth rate $-\alpha_i$ for the supersonic cases $M = 1.5$ and $M = 3$. For a given ω interval, the number of modes raises with increasing Mach number, i.e. more acoustic modes are detected and the starting points become denser. The phase velocity of the perturbation falls below the free-stream velocity

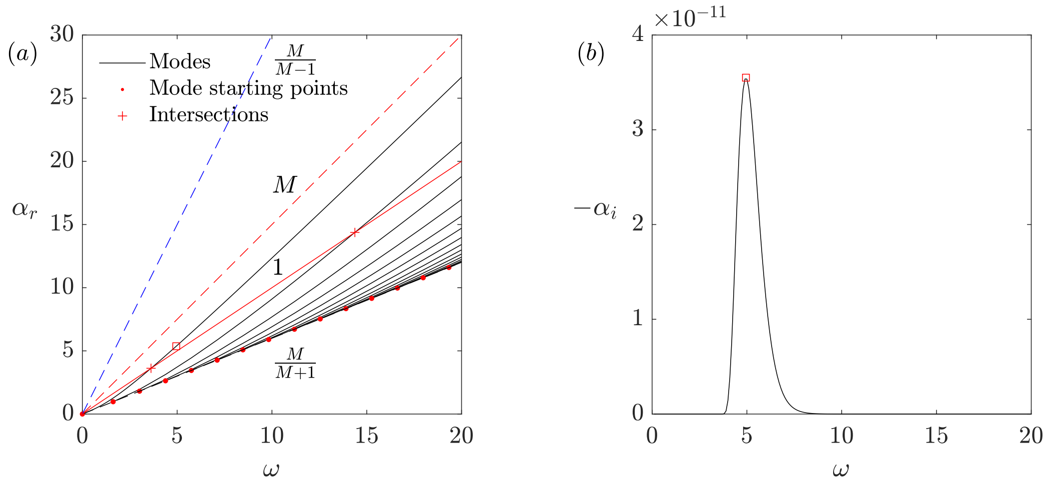

Figure 3.14: The wavenumber α_r (a) and the growth rate α_i of the first mode (b) at the Mach number $M = 1.5$. □: Maximum in α_i. Definition of lines is according to figure 3.3.

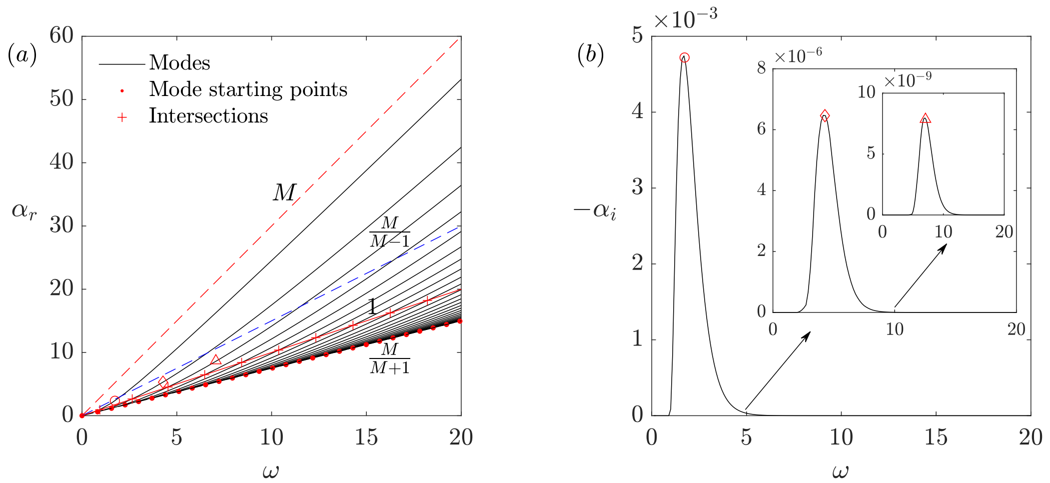

Figure 3.15: The wavenumber α_r (a) and the growth rate α_i of the first three modes (b) at the Mach number $M = 3$. ○, ◇, △: Maximum in ω_i of the first, second and third mode. Definition of lines is according to figure 3.3.

and the transonic line $\alpha_r/\omega = 1$ is crossed by the modes, where the intersections are marked by red "+". For $M = 1.5$ in figure 3.14(a), we have the same location of the intersections as shown in figure 3.5(a), i.e. $\omega_{+1} = 3.62$ and $\omega_{+2} = 14.37$. Above these intersections, i.e. above the red solid line in figures 3.14 and 3.15, the velocity of the perturbation is smaller than the free-stream velocity and unstable acoustic modes are identified. The amplification rate $-\alpha_i$ in figure 3.14(b) for $M = 1.5$ instantly rises after the modes surpass the red solid line. With increasing ω, the amplification rate $-\alpha_i$ reaches its maximum, marked by a red square, which is in the order of magnitude of 10^{-11}. This extremely small value has only a theoretical meaning. The second mode in figure 3.14 also has a part that is above the transonic line and therefore represents a set of unstable modes. However, the maximum value of $-\alpha_i$ is even much smaller than the order of magnitude to 10^{-11} and therefore it is not displayed here.

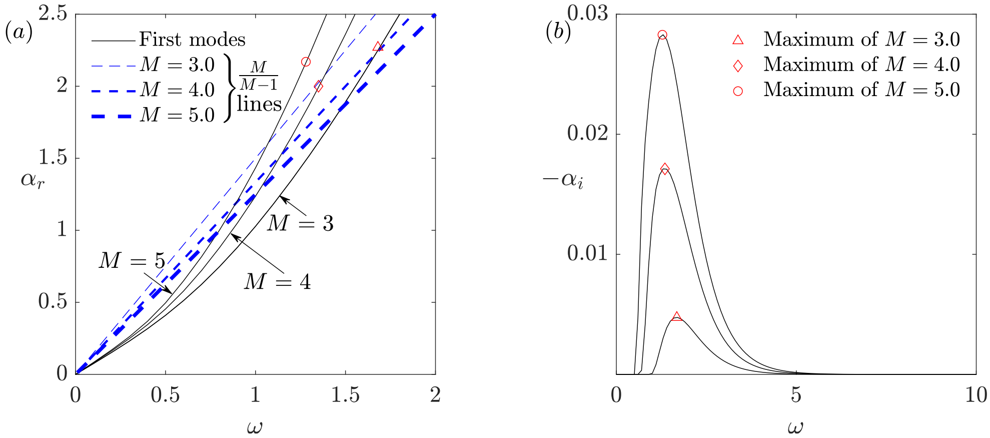

Figure 3.16: The transition of the maximum growth rate from the subsonic mode to the supersonic mode. (a) The frequency ω_r and (b) the growth rate ω_i of the first mode for Mach numbers $M = 3$, $M = 4$ and $M = 5$. Definition of blue dashed lines is according to figure 3.3.

Figure 3.15 shows the results of the eigenvalue for $M = 3$. In figure 3.15(b), the growth rates $-\alpha_i$ of the first three modes are shown. Their maxima are respectively marked by a circle, a triangle and a rhombus in red colour. It is noticeable that the maximum value of the higher modes' growth rate decays exponentially in comparison to that of the first unstable mode.

From figures 3.13-3.15, we conclude that no unstable acoustic modes but only neutrally stable acoustic modes exist in subsonic and transonic boundary layer flows.

Unstable modes only arise in supersonic exponential boundary layers when the phase velocity of the perturbation is smaller than the free-stream velocity. Among the unstable modes, the first mode is the most unstable mode. Higher modes exist for growing M and ω but have significantly smaller maximum growth rates $-\alpha_i$ compared to the first mode.

With increasing Mach numbers, a transition of the most unstable acoustic mode, i.e. the first acoustic mode, from subsonic to supersonic is again observed in figure 3.16 for the spatial case. For $M = 3$, the most unstable mode marked by a triangle is a subsonic mode, i.e lies below the $M/(M-1)$ line for $M = 3$. However, with increasing Mach numbers, here $M = 4$ and $M = 5$, the location of the maximum of α_i shifts towards smaller ω to above the corresponding sub-supersonic mode border $\alpha_r/\omega = M/(M-1)$ marked by blue dashed lines, i.e. the most unstable mode becomes a supersonic mode. This phenomenon is very similar to the result observed in figure 3.7 for the temporal stability problem. But for the present spatial case, the critical Mach number for the transition of the most unstable mode from a subsonic to a supersonic mode is around $M \approx 3.5$. This value is smaller than that in the temporal case where it is approximately $M \approx 4$.

In figure 3.17, the spatial growth rate $-\alpha_i$ of the first three acoustic modes is displayed as a function of M and ω by 3-D plots, together with contour lines for $-\alpha_i$. The thick contour line marks $\alpha_i = 0$, i.e. beyond which imaginary eigenvalues become non-zero, the black dashed line corresponds to the maximum $-\alpha_i$ values for a fixed ω or M.

Once again, it is observed that the first acoustic mode is the most unstable one and the maximum

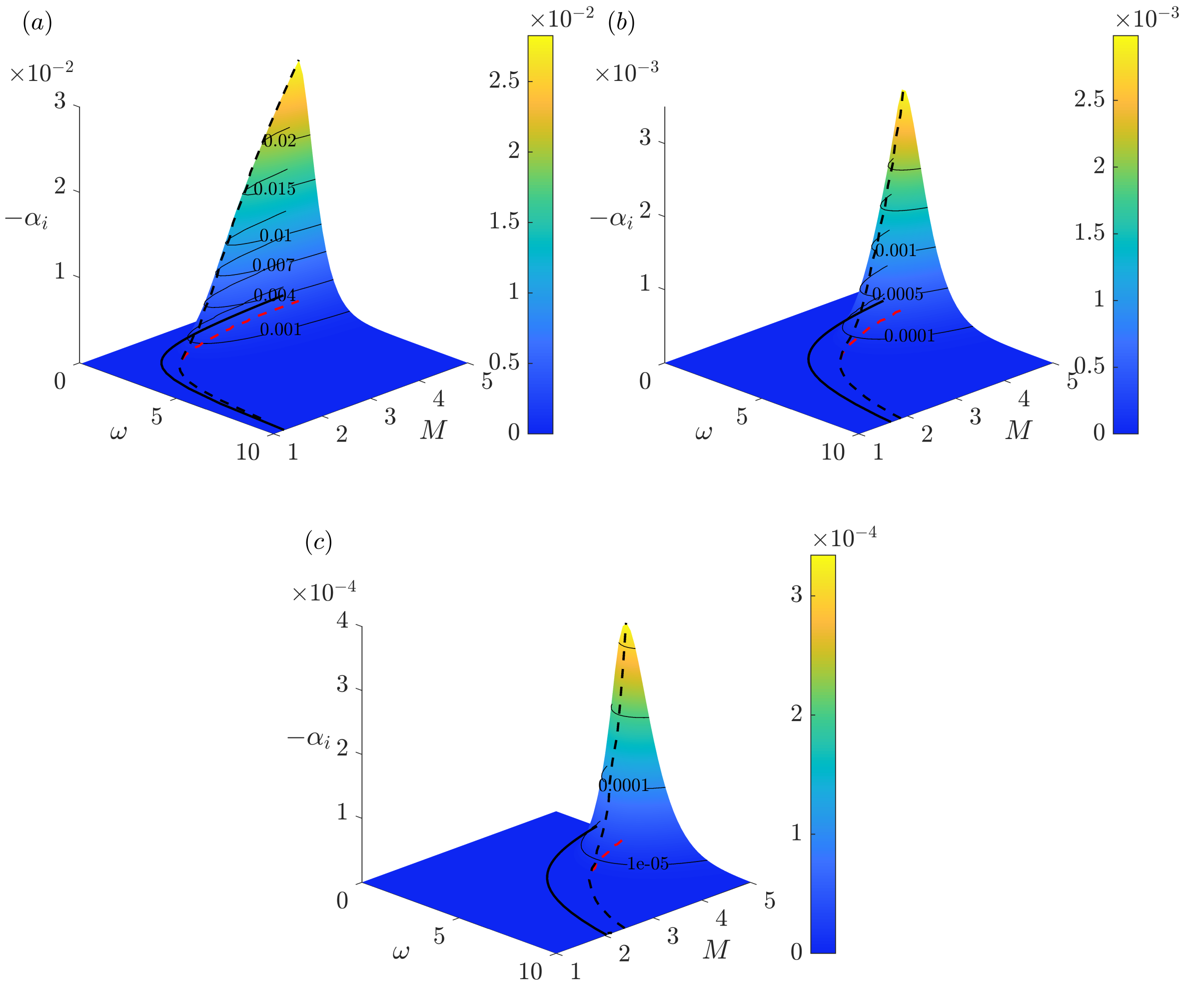

Figure 3.17: The growth rate α_i as a function of M and ω. (a) first mode, (b) second mode and (c) third mode. —— defines the neutral-unstable mode border according to (3.37). - - - defines the line of maximum growth for a given M or ω and - - - defines the same line but projected onto the ω-M plane.

values for $-\alpha_i$ decrease exponentially with increasing mode numbers. In comparison with the Mack-discovered critical Mach number $M_c \approx 2.2$ and $M_c \approx 2.7$ for temporal instability as described in §3.3.1, the critical Mach number, where exponential instability growth appears, is found to be $M_c \approx 2.5$ at $\omega \approx 2$ for spatial instability. The reference value of the growth rate is selected to 0.001 corresponding to a detectable spatial instability. This is visualized by the contour line $-\alpha_i = 0.001$ as shown in figure 3.17(a). Since instability only occurs at larger values of ω for higher-order modes, the entire contour moves towards higher frequencies ω in figure 3.17(b) and 3.17(c) compared to figure 3.17(a). By observing the dashed line for the maximum growth rate, it is clear that the most unstable case occurs under high Mach numbers and small frequencies.

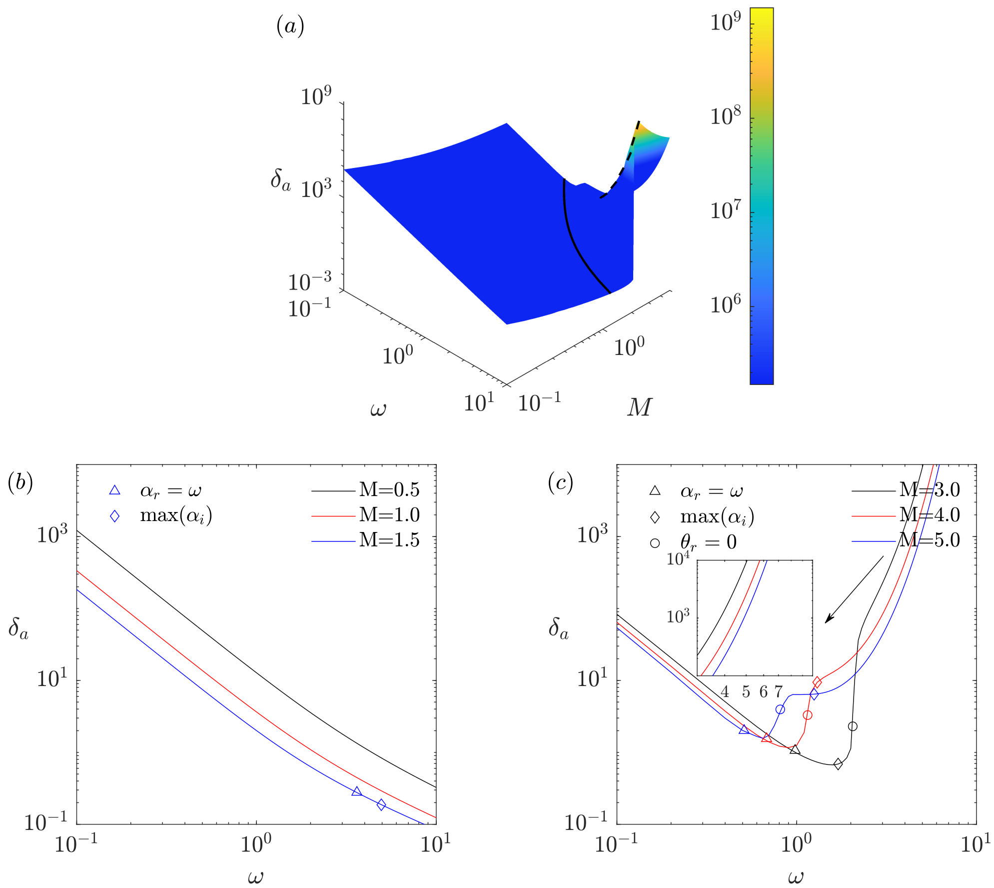

Figure 3.18: Acoustic boundary layer thickness defined by (3.43), where only the first acoustic mode is shown. (a) ABLT δ_a as a function of ω and M. —— defines the neutral-unstable mode border according to (3.37). - - - refers to the line of maximum δ_a for a given ω. (b) and (c) δ_a for different Mach numbers $M = 0.5, 1, 1.5, 3, 4, 5$.

3.4.2 Acoustic boundary layer and wave angle

In order to investigate how far from the boundary layer an acoustic signal is still audible and to consider the propagation properties of the acoustic wave for spatial instability, we show the results of the ABLT and the wave angle in this section. We recall (3.13), from which the density amplitude can be rewritten for $y \to \infty$ as

$$\rho(x, y \to \infty, t) \sim e^{-\sqrt{\theta} y} e^{i(\alpha x - \omega t)} = e^{-\beta_r y} e^{i(\alpha x + \beta_i y - \omega t)}, \tag{3.48}$$

where again $\widetilde{Hc}(;0) = 1$ according to the definition of the CHF has been used (Ronveaux & Arscott, 1995). For the spatial stability problem, the real part of the complex wavenumber β is given by

$$\beta_r = \frac{\sqrt{2}}{2} \sqrt{\sqrt{{\theta_{r_s}}^2 + {\theta_{i_s}}^2} + \theta_{r_s}}, \tag{3.49}$$

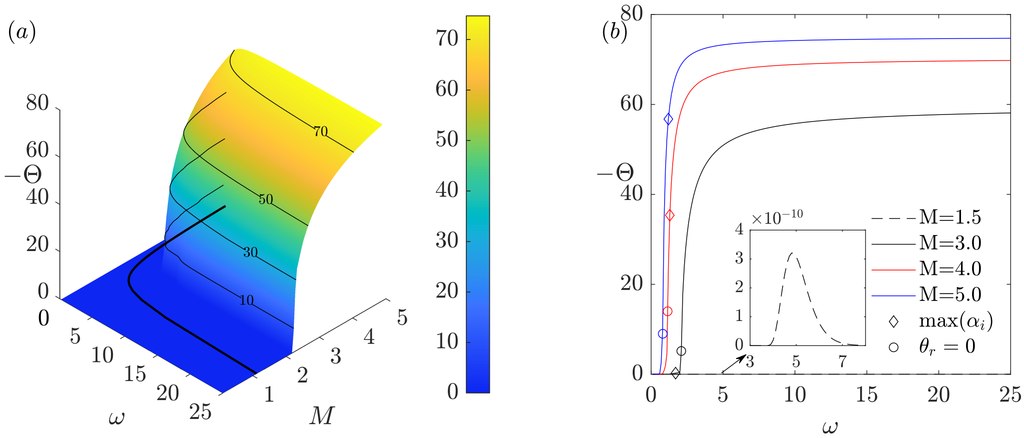

Figure 3.19: Wave angles Θ for large y defined by (3.44), where only the first acoustic mode is shown. The minus sign implies, that we only consider unstable modes. (a) Θ as a function of M and α, (b) Θ as a function of ω for different Mach numbers $M = 1.5$, $M = 3$, $M = 4$ and $M = 5$. —— defines the neutral-unstable mode border according to (3.37).

which characterises the exponential spatial decay of the disturbance in the wall-normal y-direction. The imaginary part of β reads

$$\beta_i = -\text{sign}\left(\theta_{i_s}\right) \frac{\sqrt{2}}{2} \sqrt{\sqrt{{\theta_{r_s}}^2 + {\theta_{i_s}}^2} - \theta_{r_s}}, \tag{3.50}$$

which is the wavenumber in y-direction. The expressions of θ_{r_s} and θ_{i_s} are taken from (3.11).

The ABLT δ_a defined in (3.43) is further applied in this section to quantify how far out an acoustic signal can be perceived. The previously calculated sets of eigenvalues for M, α, and ω are used to compute β_r and thereafter δ_a according to (3.43). Its result, i.e. the ABLT as a function of M and ω, is displayed as a 3-D plot in figure 3.18(a) for the first mode plotted on a double logarithmic scale. Some representative fixed Mach numbers are picked from figure 3.18(a) and their projections on the ω-δ_a-plane are shown in figures 3.18(b) and 3.18(c).

From figure 3.18(b), in the range $M \leq 2$, a divergence for δ_a is observed in the limit $\omega \to 0$ and it follows as in inverse power-law according to $\delta_a \sim \omega^{-n}$ with $n \approx 2$. In the same Mach range, $\omega \to \infty$ also yields an inverse power-law, but with an exponent of $n \approx 1$ in $\delta_a \sim \omega^{-n}$. Such results mean that acoustic signals are barely detectable away from the boundary layer. In 3.18(c) for the Mach range $M > 2$ nothing changes in the limiting case $\omega \to 0$, but for $\omega \to \infty$ an exponential behaviour according to $\delta_a \sim e^{n\omega}$ becomes visible with a scaling factor of $n \approx 0.5$. The transonic line is marked by the thick solid line in figure 3.18(a). The dashed line marks the maximum values for δ_a at fixed frequencies ω.

In figure 3.19(a), a 3-D plot of the wave angle Θ defined by (3.44) as a function of M and ω is given, therein only eigenvalues of the first modes are considered. Its projection on the α-Θ-plane for four representative Mach numbers is presented in figure 3.19(b). In the subsonic and transonic cases, waves propagate primarily in the streamwise direction and significant wave angles only occur for $M \geq 2$. In supersonic cases, transversely propagating acoustic waves with $\Theta \neq 0$ are observed. For $M \geq 2$, the values for $-\Theta$ increase rapidly with increasing ω as shown in figure 3.19(b). The angle $-\Theta$ increases for larger Mach numbers up to $75°$.

To figure out the direction of the phase velocity of the wave for $M > 2$, it is necessary to go back directly to (3.11b). The sign of θ_{i_s} decides the sign of β_i due to the negative sign-function given in (3.50) and is therefore decisive for the direction of the wave propagation. For unstable modes, i.e. for $\alpha_i < 0$, there is always $\Theta < 0$. Neutrally stable modes, i.e. $\alpha_i = 0$, lead to $\Theta = 0$. In a brief summary, a spatial unstable wave has a negative Θ and a spatial stable wave holds a positive Θ.

As the direction of the group velocity, i.e. the direction of energy propagation, the propagation angle ψ defined in (3.47) still holds and gives a positive direction of the group velocity for unstable supersonic spatial modes, i.e. radiative waves that radiate energy to the free stream. In other words, the spatial instability generates dispersive waves that spatially decrease in amplitude towards the free stream and meanwhile exhibits a spatial growth along the positive x-direction.

3.5 Comparison and association between temporal and spatial stability

In this section, we first compare the results for temporal and spatial stability problems, where similarities and differences are clearly pointed out. Then, a close connection between them is established through the real parts of the eigenvalues in their respective problems and thereby a linear relation between the growth rates, i.e. ω_i and α_i, is computed for the temporal-spatial stability problem, in which both the frequency and wavenumber are complex-valued.

We begin with the comparison of the results in §3.3 and §3.4. From figure 3.4 and figure 3.13, it can be concluded that the imaginary part of the frequency, i.e. ω_i, in the temporal stability problem and the imaginary part of the wavenumber, i.e. α_i, in the spatial stability problem are always zero for free-stream velocities in a subsonic range, i.e. $M \leq 1$. Physically, this means that neither temporal nor spatial instabilities appear for subsonic boundary layer flows. Meanwhile, for the subsonic case, neutrally stable higher-order modes are always existent.

As the Mach number exceeds one, i.e. for supersonic flows, unstable modes emerge for both temporal and spatial stability problems. Moreover, the growth rates, i.e. ω_i and α_i, become larger as the Mach number increases. Higher modes are found but the growth rate decreases exponentially with mode orders. These similarities of patterns can be obtained by comparing figure 3.6 and figure 3.15. To determine at which flow velocity instability plays a non-negligible role, a criterion of the growth rate for the existence of a noticeable instability is set by 0.001. Noticeable instabilities exist around the critical Mach number $M_c \approx 2.7$ in the temporal stability problem. This critical value is by $M_c \approx 2.5$ in the spatial stability problem.

With figure 3.8 and figure 3.17, we can overview very similar patterns of the growth rate of the first three modes in the temporal and the spatial stability problems. The first mode is confirmed to be dominant and there is always maximum growth rates that are marked by dashed lines for fixed Mach numbers.

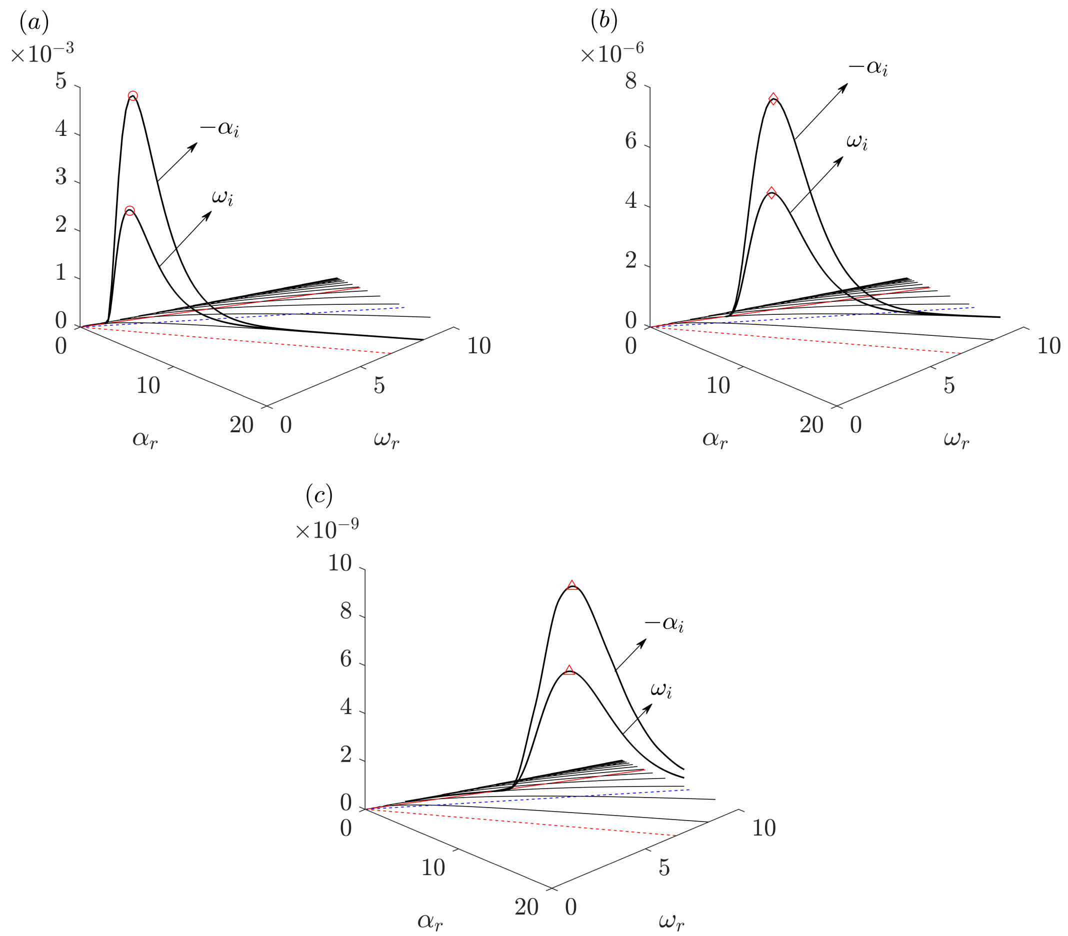

Figure 3.20: The temporal growth rate ω_i and the spatial growth rate $-\alpha_i$ as a function of resonant frequency ω_r and resonant wavenumber α_r for $M = 3$. (a) First mode, (b) second mode and (c) third mode. Definition of lines in the ω_r-α_r-plane is according to figure 3.2 and figure 3.3. ○, ◇, △ : Maximum in ω_i and α_i of the first, second and third mode.

Due to the similarity of the pattern of growth rates, the resulting quantities, the ABLT δ_a and wave angle Θ, provide overall very similar results in the temporal and spatial stability problems. A remarkable difference is noticed by comparing figure 3.10 and figure 3.18. The maximum of the ABLT in the considered spectrum for $M = 5$ is determined as $\delta_a = 10^9$. This value exceeds far greater than the ABLT in the temporal case, where $\delta_a = 10^5$. This means that the ABLT of spatially unstable modes is much larger than that of the temporal case and thus acoustic signals can be detected further away from the wall. Comparisons of the wave angle by figure 3.11 and figure 3.19 show that there are no significant differences, but only some tiny differences in values, which do not matter physically. These differences are due to the fact that the spatial growth rate α_i is in general slightly larger than the temporal growth rate ω_i. In a brief summary, for the wave angle Θ, not much physical effect is caused by the tiny difference of the growth rates. In contrast, it causes large consequences for the ABLT δ_a.

In fact, by observing figures 3.4 and 3.13 in the subsonic cases, we notice that on the ω-α-plane, the modal lines are exactly identical for the temporal and spatial stability problems.

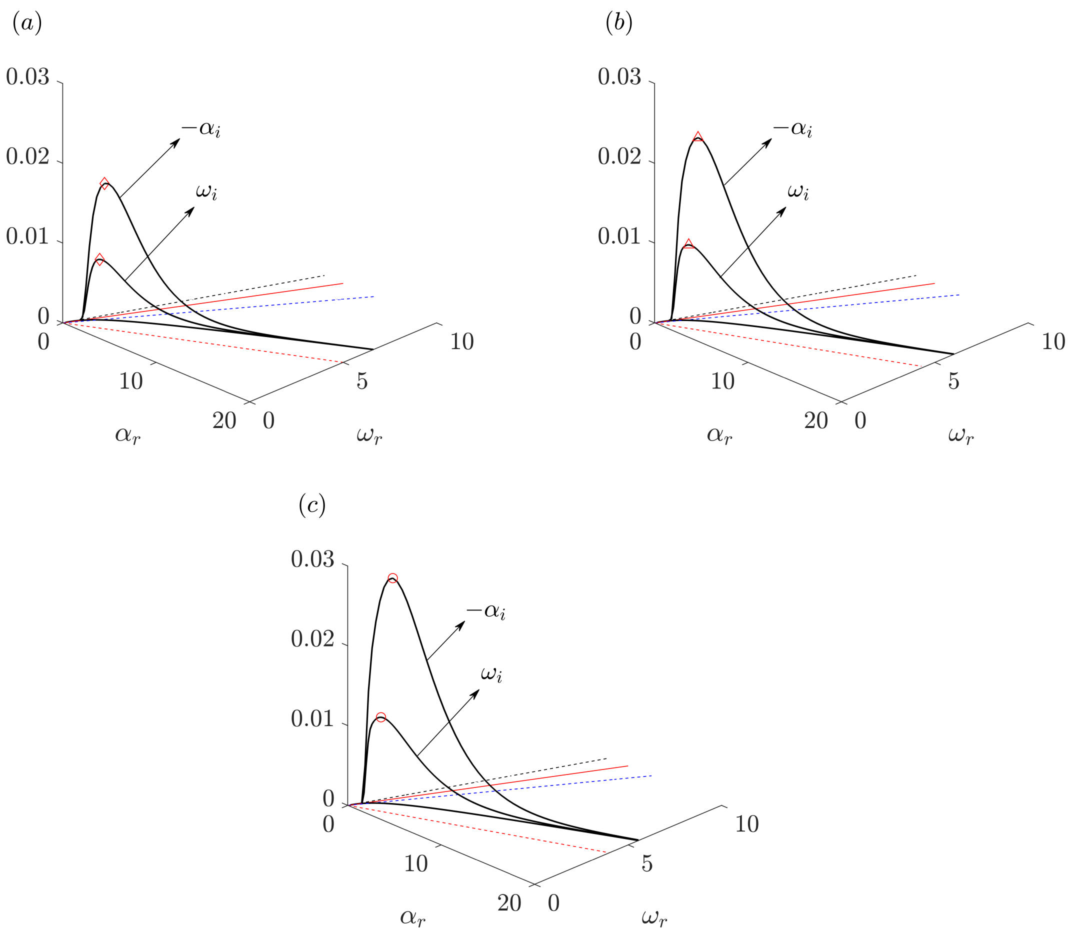

Figure 3.21: The temporal growth rate ω_i and the spatial growth rate $-\alpha_i$ as a function of resonant frequency ω_r and resonant wavenumber α_r for the first mode. (a) $M = 4$, (b) $M = 4.5$ and (c) $M = 5$. Definition of lines in the ω_r-α_r-plane is according to figure 3.2 and figure 3.3. ○, ◇, △: Maximum in ω_i and α_i.

In other words, ω and α that lay on the modal lines are the roots of the eigenvalue equation (3.14). A similar result can be drawn to the unstable modes in supersonic cases. If we observe figure 3.5(a) and figure 3.14(a), or figure 3.6(a) and figure 3.15(a), we will find that for both temporal and spatial stability problems, not only the modal lines of neutrally stable modes but also the modal lines of the unstable modes coincide exactly on the ω_r-α_r-plane. To better verify this result, we display figure 3.20, from which the temporal growth rate ω_i and spatial growth rate $-\alpha_i$ for the first three modes corresponding to the ω_r-α_r-plane for the Mach number $M = 3$ are shown. In fact, the subfigure (a)-(c) correspond to the three results in figure 3.6(b) and 3.15(b) including the inset, respectively.

The real parts of eigenvalues on the modal lines are very special because they may trigger instabilities. We subsequently refer to the frequencies corresponding to these modal lines as resonant frequencies and the corresponding wavenumbers as resonant wavenumbers. For the temporal stability problem, the resonant frequencies as eigenvalues with $\omega_i \neq 0$ trigger instability in time. For spatial stability problems, the resonant wavenumbers as eigenvalues

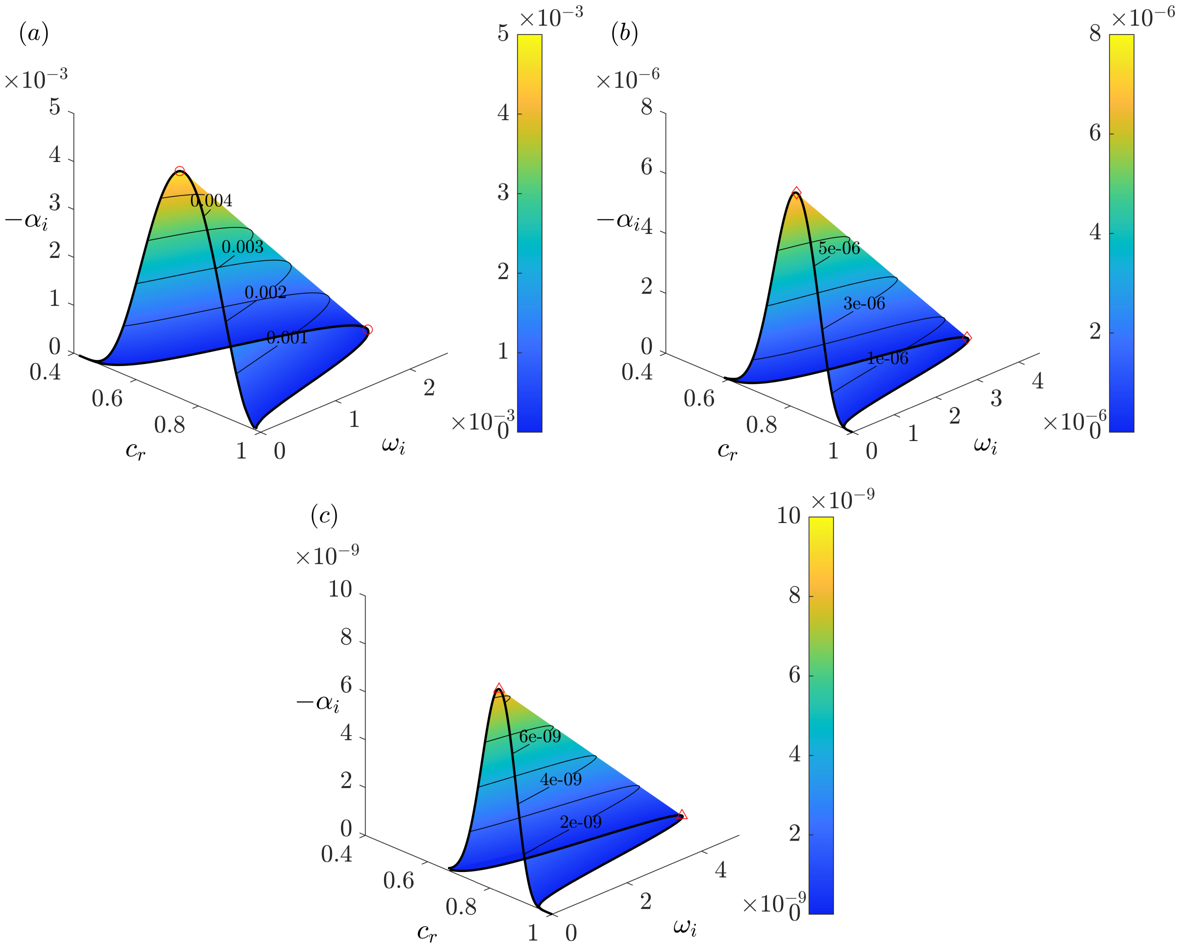

Figure 3.22: The spacial growth rate $-\alpha_i$ as a function of the spatial growth rate ω_i and the resonant phase velocity c_r for $M = 3$. (a) First mode, (b) second mode and (c) third mode. ○, ◇, △ : Maximum in ω_i and α_i. The thick solid lines —— depict the result of purely temporal or purely spatial stability.

with their imaginary parts $\alpha_i \neq 0$ trigger instability in space. For a more intuitive understanding in this section, we refer to these modal lines on the ω_r-α_r-plane as the resonance line.

Through figure 3.20 we can clearly see the exact coincidence of the projection of the growth rates in time and space on the ω_r-α_r-plane. By comparing the absolute values of ω_i and α_i we note that the absolute value of the spatial growth rate is always greater than the absolute value of the temporal growth rate, with the former being approximately twice as large as the latter. By observing the position of the maximum values on ω_r-α_r-plane we conclude that the maximum values of temporal stability and spatial stability do not coincide exactly on the modal line and that there is a small displacement.

Figure 3.21 shows the results of the growth rates of the first mode as a function of ω_r and α_r for different Mach numbers $M = 4$, $M = 4.5$ and $M = 5$. Again, we observe a complete overlap of the modal lines of the temporal growth rate and the spatial growth rate in the ω_r-α_r-plane, i.e. the resonance lines. In these results, there is a significant increase in the growth rate with

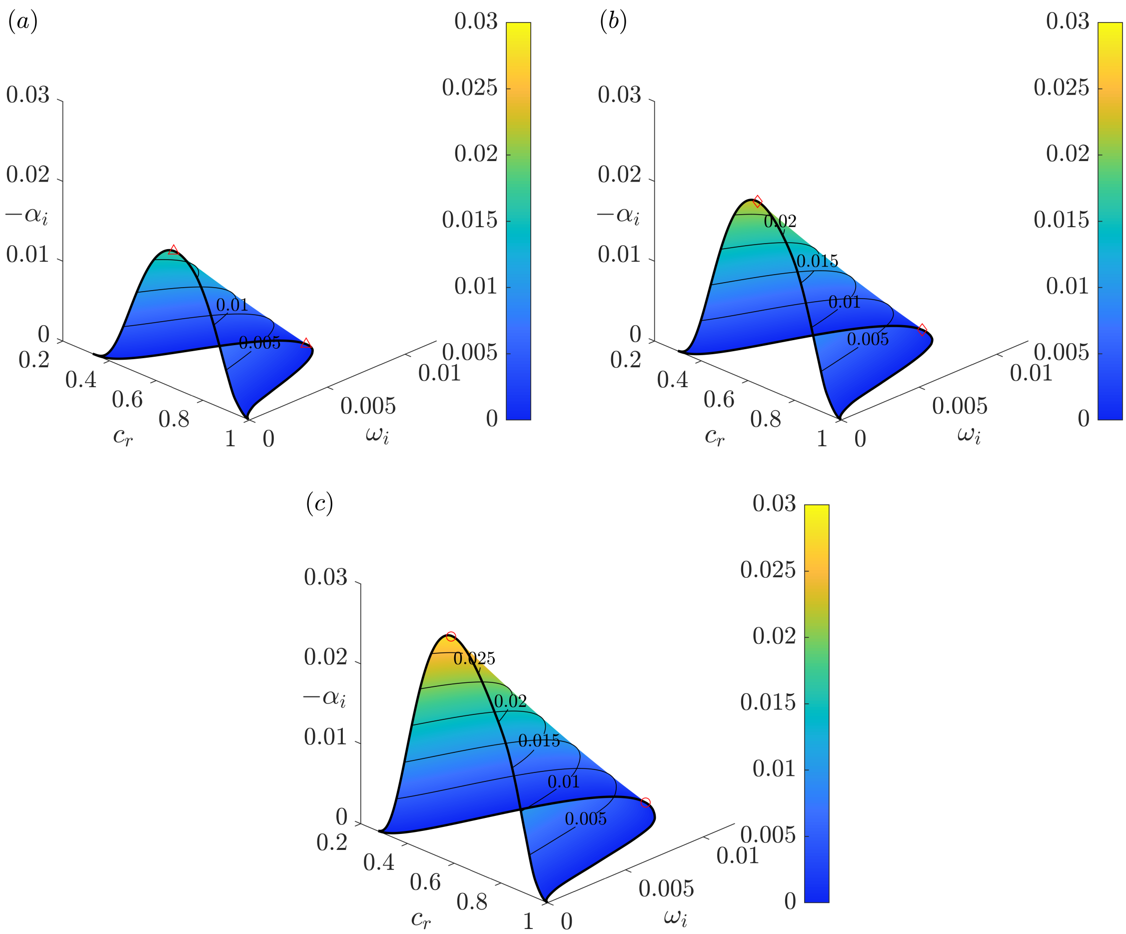

Figure 3.23: The spacial growth rate $-\alpha_i$ as a function of the spatial growth rate ω_i and the resonant phase velocity c_r for the first mode. (a) $M = 4$, (b) $M = 4.5$ and (c) $M = 5$. ○, ◇, △ : Maximum in ω_i and α_i. The thick solid lines —— depict the result of purely temporal or purely spatial stability.

Mach numbers. In addition, there is a more pronounced displacement of the position of the maximum of the growth rate on the ω_r-α_r-plane. The original datasets of two of the results for $M = 4$ and $M = 5$, i.e. figure 3.21(a) and (c), can be found in figure 3.7 and figure 3.16.

The above results show a close connection between temporal and spatial stability. They are linked in the real part of the eigenvalues by resonant lines. In the following step, we further investigate the relation between the temporal and spatial growth rates, i.e. ω_i and α_i, on the resonance lines.

We first consider the case of the first three modes with a fixed Mach number $M = 3$. Since the resonance lines are defined by specific ω_r to α_r, we newly define their ratio, i.e. $c_r = \omega_r/\alpha_r$, as a parameter in a physical sense of phase velocity, which we call it here the resonant phase velocity. Figure 3.22 shows the connection between the imaginary parts of the eigenvalues in the spatial and temporal stability eigenvalue problems through resonant phase velocities.

To obtain the results in figure 3.22, we formulate a new eigenvalue problem but using the same eigenvalue equation (3.14) as used in the temporal and spatial stability problem. This time, we consider both $\omega \in \mathbb{C}$ and $\alpha \in \mathbb{C}$. Therefore, taking $\omega = \omega_r + i\omega_i$ and $\alpha = \alpha_r + i\alpha_i$ into (3.14), we obtain

$$\begin{aligned}&\left(M\alpha_i - iM\alpha_r - \sqrt{\theta}\right)\widetilde{H\mathrm{c}}\left(;\frac{\alpha_r + i\alpha_i}{\alpha_r - \omega_r + i\left(\alpha_i - \omega_i\right)}\right) - \frac{\alpha_r + i\alpha_i}{\alpha_r - \omega_r + i\left(\alpha_i - \omega_i\right)}\times \\ &\times \widetilde{H\mathrm{c}}'\left(;\frac{\alpha_r + i\alpha_i}{\alpha_r - \omega_r + i\left(\alpha_i - \omega_i\right)}\right) = 0.\end{aligned} \tag{3.51}$$

Note that θ and the parameters of the $\widetilde{H\mathrm{c}}$ function also contain the complex-valued frequency and wavenumber, which are not shown explicitly here. In this newly formulated eigenvalue equation, we regard the resonant frequency ω_r, the resonant wavenumber α_r, the temporal growth rate ω_i, and the Mach number M as parameters and the spatial growth rate α_i as the sought eigenvalue. In the concrete process, we set the value of ω_i from the temporal stability problem as the starting point and gradually reduce it to perform the root-finding algorithm.

By computation of the eigenvalue equation (3.51) we find that decreasing the temporal growth rate ω_i on the resonance lines, i.e. at the resonant phase velocities c_r, gives a non-zero α_i as the new eigenvalue. When ω_i is reduced to zero in the final, a value of α_i obtained in a purely spatial stability problem is found. To present the results in 3-D form, we take $c_r = \omega_r/\alpha_r$ as one parameter and ω_i as the other, as shown in figure 3.22. In figure 3.22, it is noticed that the relation between α_i and ω_i is linear for a fixed c_r e.g. by observing the straight line between the maximum values marked by red triangles, rhombuses and circles. The same linear relation can be obtained through computation by regarding ω_i as the sought eigenvalue, and gradually reducing α_i to zero. In fact, the thick solid line in the c_r-ω_i plane actually corresponds to the ω_i-curve in figure 3.20. And the thick solid line in the c_r-α_i plane is actually the α_i-curve in figure 3.20. The surface in the middle part of the two thick solid lines represents the linear relation between ω_i and α_i.

Figure 3.23 shows the results for the first mode at three different Mach numbers, $M = 4$, $M = 4.5$ and $M = 5$. Basically, we get similar results of the ω_i-α_i linear relation at resonant phase velocities. In addition, from figure 3.22 and figure 3.23 we can observe that both ω_i in the temporal stability problem and α_i in the spatial stability problem become non-zero from the point where $c_r = 1$. Eventually, it gives the concrete quantities that tend to zero with c_r approaching $1/M$, which is the lower bound of acoustic modes.

The present results provide a strong basis for a kind of coupled instability in which temporal and spatial stability cooccur. We refer to this instability as temporal-spatial instability. From the physical point of view, the appearance of instability must be a smooth process. That is, when the frequency or wavenumber of the perturbation in the boundary layer reaches resonant values, there should be a growth rate starting from zero instead of a sudden appearance. This causes the occurrence of spatial-temporal instability. From a mathematical point of view, through the eigenvalue equation, we can understand that a linear relation between ω_i and α_i on the resonance lines enables the LHS of the eigenvalue equation (3.14) to be adjusted somewhat so as to keep it zero.

3.6 Conclusion and discussion

In this section, we summarise the main conclusions of this chapter and then give a discussion about potential directions of the future study.

3.6.1 Conclusion

In this chapter, we study the stability problem of an exponential boundary layer flow based on the exact solution to the PBE. With the exact solution and the boundary conditions, the eigenvalue problem is formulated. Based on this, both the temporal stability problem and the spatial stability problem are considered and thoroughly investigated. The eigenvalue equation is first solved analytically for limiting cases, i.e. for small and large wavenumbers in temporal stability, and for small and large frequencies in spatial stability, both at small Mach numbers, and then numerically for arbitrary values and Mach numbers.

The acoustic unstable modes are thoroughly discussed. For subsonic and transonic cases, only neutral modes are present. The unstable acoustic modes are proven to exist only in a supersonic exponential boundary layer flow, where the most unstable mode is always the first acoustic mode. In our study, we have observed that the most unstable mode transitions from a subsonic mode to a supersonic mode with increasing Mach numbers. Comprehensive diagrams of the unstable modes are obtained in terms of the wavenumber and the Mach number for the temporal stability problem. For the spatial stability problem, similar results are shown in terms of the frequency and the Mach number.

Based on these unstable modes, various acoustic characteristics are analysed. The study of the ABLT δ_a gave us a comprehensive insight into the extension of the region where sound is audible. Of particular interest are the cases when $M > 2$. For small α or ω, δ_a has an algebraic singularity, reaches a minimum with increasing wavenumbers or frequencies, and then starts to exponentially grow where in this exponential-growth region the instability reaches its maximum too. For even larger wavenumbers or frequencies, the instability is accompanied by a decrease of ω_i or α_i. This gives a hint to avoid the noise caused by acoustic instability by avoiding maximum values of ω_i or α_i. In other words, it is always worthy to avoid the appearance of the drastic growth region in figure 3.10(c) and figure 3.18(c) to surpress the noise perceptibility afar from the wall. One effective way to control the sound radiation is to determine the minimum of the ABLT in figure 3.10(c) and figure 3.18(c) as well as the corresponding wavenumber as a threshold for each Mach numbers. To surpress the instability, one should control the wavenumber or the frequency of the perturbation smaller than a certain threshold. This could be achieved by a wave filter, which changes the wavelength or the frequency. A device which exactly induces this effect has been applied in the inlet and outlet of the air jet engine (Henderson, 2010).

The eigenfunctions show that when $M > 1$, the amplitude of the unstable acoustic wave reaches its maximum value near the wall. Even for $M \leq 1$, there is the propagation of neutrally stable waves in the streamwise direction. Thus, another feasible way to alter the near-wall effects is to change the wall condition, i.e. the acoustic wall impedance. This initiative provides an idea for further research. Applying the acoustic impedance to the wall boundary condition will result in different eigenvalue equations. In this way, the eigenvalues can be calculated by varying the acoustic impedance to find the optimal acoustic impedance to suppress instabilities or even hinder propagation. This approach has already been applied to civil aviation. In Oppeneer (2014), porous materials are applied to the liner wall of the Auxiliary Power Unit (APU) of an aircraft, which changes the eigenvalues and hence attenuates the noise.

By comparing the results of the temporal and spatial stability problems, we define resonance lines in the ω_r-α_r-plane. The values on these lines are actually the real parts of the eigenvalues in the stability problems. They are identical in both temporal and spatial stability problems. For temporally and spatially unstable modes they give rise to their own but different valued imaginary parts of the eigenvalues, which trigger instability. Overall, the imaginary part of a spatially unstable mode's wavenumber is twice as large as the imaginary part of a temporally unstable mode's frequency. At the same time, we formulate a new stability problem where both the wavenumber and the frequency are complex numbers and thereby explore the relation between the temporal and spatial growth rates based on resonance lines. The results show an inverse proportional linear relation at a fixed resonant phase velocity c_r. It means that for the eigenvalue equation, there are maximum absolute values of ω_i and $-\alpha_i$ at the resonant phase velocity, corresponding to pure temporal instability and pure spatial instability, respectively. A decrease in one of ω_i and $-\alpha_i$ will cause an increase in the other. In between, there exists a coupled temporal-spatial instability, i.e. ω_i and α_i are simultaneously non-zero. Such a result provides a strong argument for the temporal-spatial stability problem.

The unstable mode is characterised as an energy accumulation and saturation near the wall and produces radiative waves towards the free stream. This instability mechanism indicates that inviscid perturbations can extract energy from shear flows. In geophysical fluid dynamics, a similar mechanism is related to the over-reflection of waves (Lindzen, 1988). This kind of instability is explained as waves that are trapped within a region determined by the rigid wall and the turning level, and in turn, grow by the process of multiple reflections. This was first presented in Lindzen & Rosenthal (1976) for internal gravity waves and in Takehiro & Hayashi (1992) for shallow water waves. From the instability mechanism that we observed, we further infer that over-reflection of acoustic waves in boundary layer flows exists and will be influenced by the unstable modes. To some extend this inference seems to be confirmed in Campos & Kobayashi (2013), in which a hyperbolic-tangent is used to mimic the flow in the semi-infinite domain of a boundary layer flow and where not only an over-reflection of acoustic waves is observed, but the coefficient of over-reflection has an unusual high peak at a certain resonant frequency (see the case $M = 4.5$ in figure $6(a)$ in Campos & Kobayashi (2013)). For this, no further explanation was given, but the values lie close to the eigenvalues we obtained for instability. These ambiguous results motivate us, and therefore, over-reflection of acoustic waves and its close link with unstable modes in boundary layer flows is the topic of the next chapter.

3.6.2 Discussion

In this section, we extend the discussion of possible approaches based on the engineering needs for compressible boundary layer instability and noise control. One method is to control the wall temperature, which requires the introduction of a temperature gradient into the governing equation, i.e. to study the generalised PBE (2.25). This potential study may be realised from analytical solutions based on contributions from the Heun class functions. Another method is to apply the acoustic impedance.

3.6.2.1 Non-isothermal exponential boundary layer flows

We begin with the active control of compressible boundary layer instability through wall temperature.

Typically, the instability of a supersonic boundary layer is dominated by the first (Mack) mode up to a Mach number about $M = 4$ and by the second (Mack) mode thereafter (Smith, 1989). Recent reviews about influences and contributions of the first (Mack) and second (Mack) modes to laminar-turbulent transition can be found in Reed et al. (1996), Saric et al. (2003), Fedorov (2011) and Zhong & Wang (2012). The shift of the most unstable mode between the first and second (Mack) modes is largely influenced by many factors, such as chemical reactions, thermal non-equilibrium, transverse curvature, porous walls, and gas injection, detailed reviewed by Bitter & Shepherd (2015). Among them, the linear stability of compressible boundary layers is greatly influenced by the wall temperature. Lees & Lin (1946) first found that wall cooling leads to a stabilisation of the inviscid instability, i.e. first (Mack) mode instability. Subsequently, Lees (1947) showed that the supersonic flows can be completely stabilised if the wall cooling is sufficient enough. This conclusion was improved by Van Driest (1952), who concluded that the first (Mack) mode can be stabilised for all Reynolds numbers when $1 < M < 9$. The same conclusion was extended to the three-dimensional first (Mack) mode instability by Masad et al. (1992). The wall cooling strategies to control the compressible boundary layer stability are thoroughly discussed in Mack (1975, 1993), Malik (1990), and Masad et al. (1992). Although the first (Mack) mode instability can be completely depressed by sufficient wall cooling, in the meantime second (Mack) and higher modes always persist and are even destabilised by wall cooling. These effects were validated in Lysenko & Maslov (1984), Stetson et al. (1989), and Stetson & Kimmel (1992) experimentally and in Knisely & Zhong (2019a, 2019b) by the Direct numerical simulation (DNS). In the other direction, the wall heating effect on the stability was studied by Tunney et al. (2015), which is relevant for re-entry of vehicles.

All the above studies of compressible boundary layers are based on the CRE, i.e. the generalised PBE (2.25). However, no analytical solution to (2.25) was found, even for the simplest linearly distributed velocity and temperature profiles. All stability analyses have utilised numerical methods, or given approximate solutions for asymptotically small or large wavenumber conditions. Therefore, there is an urgent need to find the analytical solution of generalised PBE. The motivation is manifold. At first, it would help to find the first (Mack) mode directly and exactly, which has a significant contribution to the laminar-turbulent transition. Secondly, effects of the temperature profile will be observed intuitively, thereby developing the theory of active control by adjusting wall temperatures, both cooling and heating wall. In view of this, we could consider the generalised PBE (2.25) with a coupled form of velocity and temperature profiles in order to obtain the general solution. For this, we introduce a temperature profile that is a quadratic function of the exponential velocity profile. The theoretical basis for this is the Crocco-Busemann relation (Busemann, 1931; Crocco, 1932) given by

$$T(y) = T_w + (T_{aw} - T_w)\, u_0(y) + (T_\infty - T_{aw})\, u_0(y)^2, \tag{3.52}$$

where T_w is the wall temperature, T_∞ stands for the free-stream temperature, and T_{aw} denotes the adiabatic wall temperature. The generalised PBE (2.25) with an exponential velocity profile and a temperature profile in the form of

$$T(y) = (\epsilon_1 - \epsilon_2 u_0(y))^2 \,, \tag{3.53}$$

where ϵ_1 and ϵ_2 are simple functions of T_w, T_∞ and T_{aw}, and $u_0(y) = 1 - e^{-y}$, allows an exact solution in terms of the general Heun function (GHF) (Ronveaux & Arscott, 1995).

Based on the exact solution, once the algebraic eigenvalue problem is successfully established and all the eigenvalues are numerically obtained, it is possible to conduct a detailed comparison of the growth rates of the first (Mack) and second (Mack) modes. From this, it is possible to particularly learn which mode is dominant in a Mach number range, and the influence of the temperature gradient on the acoustic modes. Further, the parameters of temperature profile give chances to study both wall cooling and heating effects, which may directly serve as controls of boundary layer stability.

Nonetheless, this new approach as a way to find modes using the exact solution to the CRE equation with exponential profiles contains still a variety of challenges: (i) The analysis of the GHF is difficult because of the lack of knowledge of the general Heun equation that contains four singularities. (ii) The complicated form of the solution to the CRE increases challenges, which will lead to difficulties in analysing the GHF and establishing the eigenvalue equation. (iii) Numerical computations could require an extremely high degree of precision to obtain convergent results. According to experience gathered in analysing the CHF, we determine that up to 150 digits are necessary for convergence.

It is worth mentioning that the PBE for free shear flows mimicked by a hyperbolic-tangent velocity profile is found to have the same form as the general Heun equation (GHE), whose exact solution is given by the GHF (Ronveaux & Arscott, 1995). A detailed related study can be found in Görtz (2020).

3.6.2.2 Acoustic impedance

In acoustic theory, it is common to model sound absorption of a surface by defining the acoustic impedance, which could be understood as a transfer function between an external load to the surface and its resulting dynamic behavior (Rienstra & Hirschberg, 2020). Typically the passive surface property is specified in the frequency domain as (frequency dependent) wall impedance. For this, we introduce the elastic acoustic wall impedance Z defined by

$$Z(\boldsymbol{x};\omega) = \frac{\hat{p}(\boldsymbol{x};\omega)}{\hat{\boldsymbol{v}}(\boldsymbol{x};\omega)\cdot\boldsymbol{n}}, \tag{3.54}$$

where $\boldsymbol{n}$ is the normal vector into the surface and $\boldsymbol{x}$ denotes points on the boundary. The acoustic impedance Z can be employed as a modified boundary conditions at the wall. Equation (3.54) mimics the effect of how much the motion of a fluid particle (or a surface) is impeded when a pressure wave impinges on it. The most common type is a rigid wall that indicates $Z = \infty$. By setting different wall types, such as an elastic wall, porous wall or flexible wall, the characters of the acoustic waves can be changed, which could help release or even dismiss waves.

Based on (3.54), different wall types in terms of their acoustic response may be defined, and the properties of these different wall types are formulated mathematically by the acoustic impedance. With different wall types, i.e. given values of Z, the resulting eigenvalue equation for unstable acoustic modes can be reformulated, which reads

$$\left[\left(-iM\alpha - \sqrt{\theta}\right) Z + i\omega\right] H\mathrm{c}\left(;\frac{\alpha}{\alpha-\omega}\right) - \frac{\alpha Z}{\alpha-\omega} H\mathrm{c}'\left(;\frac{\alpha}{\alpha-\omega}\right) = 0. \tag{3.55}$$

In comparison between the new eigenvalue equation (3.55) and (3.14), $Z \in \mathbb{C}$ is an additional parameter. It is critical to understand how ω_i or α_i behaves as a function of Z. The key aim is to find optimised acoustic impedance Z, which minimises the growth rate. The numerical root-finding algorithm based on Müller's method that is used in the present work can still be applied for (3.55).

The change of Z is expected to have various effects on stability: (i) Acoustic instability depending on modes might be suppressed or amplified. (ii) The occurrence of instability, usually at $M \sim 2.2$, can be delayed or advanced. (iii) The maximum of the growth rate ω_i or α_i shifts. Finally, the acoustic impedance will be optimised in order to suppress instability. The results will eventually reveal the effect of wall types on the suppression of an exponential boundary layer stability, thus providing new insights for engineering applications, e.g. acoustic liner in jet engines.

A preliminary investigation of (3.55) and acoustic impedance can be found in De Broeck (2021).

4 Boundary layer acoustics

4.1 State of the art

The propagation, reflection and refraction of acoustic waves in shear flows have been of great interest in engineering fields. Initially, investigations were triggered by an urgent need to understand and reduce noise that is induced by flows and machinery. To examine the properties of acoustics in free shear flows, a simple model is that of a plane vortex sheet (Jones & Morgan 1972; Crighton & Leppington 1974). It facilitates the solution of the governing equations but is largely simplified and neglects the effect of the shear layer thickness, the critical level (layer), and turning levels on acoustic wave propagation. Another model for mimicking free shear flows is by a linear velocity profile. As early as 1958 Pridmore-Brown (1958) derived an acoustic wave equation in plane parallel shear flows based on the LEE, known as the Pridmore-Brown equation (PBE). This wave equation was intensively employed to investigate the propagation of acoustic waves by Goldstein & Rice (1973), Jones (1977), Scott (1979), Koutsoyannis et al. (1979), Koutsoyannis (1980), Campos (1999), Hau et al. (2015) and Chagelishvili et al. (2016). Meanwhile, a more realistic non-linear velocity profile for mimicking a free shear-layer, the hyperbolic-tangent velocity profile, was investigated by Michalke (1965), Blumen et al. (1975), Tam (1978), Drazin & Reid (1979), and Michalke (1984), with the main aim to investigate the stability of this profile. The Fuchs-Frobenius series solution to the PBE for this profile was given by Campos & Kobayashi (2000), who studied the scattering effect of the free shear flow on acoustic waves. Both the linear and hyperbolic-tangent profiles have been very successful in modelling the shear layers formed in different jet regions behind modern aircraft engines. For example, in a coaxial jet exhaust of a typical turbofan (Royce-Rolls, 2015), the core region is approximated by a linear profile (Hau, 2017), and the mixing region is mimicked by a hyperbolic-tangent profile (Perrault-Joncas & Maslowe 2008; Gloor et al. 2013).

In addition to free shear flows, the propagation of acoustic waves in boundary layer flows is of increasing interest. Initially, a boundary layer was modelled by a simple linear profile extended by a constant velocity to meet a finite value in the free stream. This approximation is frequently used in the case where the thickness of the boundary layer is very small (Rienstra & Darau 2011; Brambley 2013). Its advantage is the presence of an analytical solution. However, an artificial kink inevitably caused by this model between the linear and constant parts of the velocity profile has a significant impact on the propagation of acoustic waves, resulting in them being reflected or refracted at the kink. Therefore, for boundary layer flows a non-linear smooth profile is physically more sound compared to linear ones. For this, an exponential velocity profile was introduced by Campos & Serrão (1998), as it allows for a smooth transition between the boundary layer and the free-stream flow, which is much closer to the physical reality. They gave a Fuchs-Frobenius series solution to the PBE for an exponential velocity profile and studied the propagation of acoustic waves within boundary layer flows. Of particular concern is the series solution near the critical layer, which contains a logarithmic term. Nonetheless, in the analysis of leading orders of the series solution, they proved that the amplitude of the pressure perturbation near the critical layer tends to be constant rather than an infinite value. By studying the amplitude of acoustic waves, they noticed an attenuation of the wave amplitude adjacent to the critical layer. More recent, Zhang & Oberlack (2021) gave an exact solution to the PBE for an exponential velocity profile in terms of the confluent Heun function (CHF). Based on this, they investigated the temporal stability of an exponential boundary layer flow and succeeded in giving unstable acoustic modes.

Links concerning shear layer instabilities and acoustic waves were first proposed in Gill (1965). In his study of shear layers separated by a vortex sheet, he argued that incident waves at certain resonant frequencies enhance instabilities. Based on this, Cohn (1983), Payne & Cohn (1985), Zaninetti (1986), and Zaninetti (1987) gave detailed investigations of 'reflection modes' and temporal instability. Subsequently, Tam & Hu (1989b, 1989c) extended their studies to spatial instability in finite-thickness shear layers as well as mixing layers inside a rectangular channel, in which supersonic unstable waves generated by continuous reflections were obtained. The links between instabilities and acoustic waves in previous work provided guidance for this chapter.

A unique phenomenon that arises in the acoustics of shear flows, and we will presently focus on this, is the over-reflection[5] of waves, i.e. reflected amplitudes are greater than the amplitudes of incoming waves. This phenomenon is validated to exist in many different shear systems (see e.g. Lindzen, 1988).

The phenomenon of over-reflection was first discovered simultaneously and independently by Ribner (1957) and Miles (1957) in the study of plane acoustic waves, which impinge onto a moving medium, and in the study of plane acoustic waves, which propagate in two moving media separated by a vortex sheet, respectively. After this, studies on over-reflection were mainly focused on geophysical fluid dynamics (GFD), i.e. typically gravity waves and Rossby waves. The over-reflection of internal gravity waves in stratified shear flows was discovered by Jones (1968), who extended the research of Booker & Bretherton (1967) to Richardson numbers smaller than $1/4$, thereby proposing that these waves were able to extract energy and momentum from the base flow and in turn, lead to over-reflections. Following this, Breeding (1971) explored numerically non-linear effects of the critical layer to internal gravity waves that produce over-reflections predicted from the linear theory. Analytical work also on internal gravity waves was done by Eltayeb & McKenzie (1975), in which they proved Jones' inference that the over-reflection can arise because incident waves indeed extract energy from shear flows. Analogous to the over-reflection mechanisms of gravity waves, the over-reflection of Rossby waves exists when they propagate across a jet flow. In Lindzen & Tung (1978) and Yamada & Okamura (1984) the necessary and sufficient conditions for the over-reflection of Rossby waves were derived.

The link between the over-reflection and instabilities of shear flows has been extensively explored by Lindzen and his coworkers, though focusing on the over-reflection of internal gravity waves and shear instabilities of stratified flows (Rosenthal & Lindzen 1983a, 1983b; Lindzen & Barker 1985), over-reflection of Rossby waves and barotropic instabilities (Lindzen & Tung, 1978), over-reflection of Rossby waves and baroclinic instabilities (Lindzen et al.,

[5] This terminology is written in the literature as over-reflection, overreflection, over reflection, and over-reflexion. We adopt the one that is more common in recent years.

1980), and over-reflection of Rossby waves and instabilities of viscous Poiseuille flows (Lindzen & Rambaldi, 1986). In Lindzen (1988), the growth rate of unstable modes is estimated by the over-reflection coefficient, thereby successfully linking the over-reflection and unstable modes. Furthermore, he inferred a mechanism of instability triggered by over-reflections and concluded that the instability of shear flows is caused by a combined process of the over-reflection and the 'Orr mechanism' (Boyd, 1983), which describes a transient growth process inducing instability. In Lindzen's theory, the over-reflection of waves acts like a source term, which provides a constant impetus for the 'Orr mechanism' and thereby the transfer and transformation of energy from the base flow to the perturbation. An exhaustive description of this mechanism can be found in Harnik & Heifetz (2007) from the Rossby wave perspective.

Lindzen's theory is confirmed in many areas. However, there are researchers who do not support his finding and have been opposed to the conclusions. Among them, Takehiro & Hayashi (1992) suggested that the 'Orr mechanism' does not apply to the instability and over-reflection of shallow-water waves. They proposed an alternative theory that is based on momentum conservation of reflected and transmitted waves to reveal the mechanism by which over-reflection phenomena produce instabilities. This theory well explains the instability in linear shallow-water shear flows investigated by Satomura (1981a, 1981b). A theoretical study was followed by Knessl & Keller (1995) and therein their results were well matched to the numerical results in Takehiro & Hayashi (1992). In Balmforth (1999), he extended further the study in shallow-water flows to viscous and non-linear regimes. It should be emphasised that the shallow-water wave equation is found to be the same form as the PBE employed in the present work. However, the analogous phenomenon of acoustic waves in an exponential boundary layer flow has not been investigated.

This gap triggered our interest. Applying the exact solution (2.35) to the PBE (2.31) for an exponential velocity profile, it is straightforward to obtain an explicit expression for the reflection coefficient of acoustic waves. Note that the approach to establishing a link between the over-reflection and instability in the present study differs from most previous work in GFD. Their focus was on how the over-reflection, an acoustic behaviour, triggers instability. In contrast, from an acoustic perspective, we are concerned about how over-reflections are influenced by unstable modes and how they behave.

Another very special over-reflection phenomenon is the so-called hyper-reflection, which is however less well studied. This phenomenon describes an over-reflection that is infinitely strong. Physically, this means that the reflected waves can exist without the triggering incident waves, i.e. they are spontaneously emitted by a homogeneous flow. In some publications, a resonant over-reflection is also known as hyper-reflection. The earliest description of this special over-reflection originated in the study of Helmholtz instabilities of acoustic-gravity waves at a plane vortex sheet led by McKenzie (1972). In the study of Helmholtz instabilities of vertical stratified flows, Lindzen (1974) observed this phenomenon for internal gravity waves. In addition, resonant over-reflection was also found in two classical models of GFD. Resonantly over-reflected Rossby waves were found to exist in jets on the β-plane model (Maslowe, 1991). More recently, Benilov & Lapin (2012) found that the resonant over-reflection also occurs in internal gravity waves within rotating shallow water on the f-plane model.

A similar phenomenon has also been observed in the present work of the study of the acoustic over-reflection in boundary layer flows. When the frequency of an incident acoustic wave is close to the resonant frequency, which is defined in §3 as the real part of the eigenvalues

ω_r of unstable modes, it is shown that there is an unusual but finite enhancement of the over-reflection. This phenomenon is defined by us as the resonant over-reflection. Note that, to the author's knowledge, both the terminologies 'resonant over-reflection' and 'hyper-reflection' are not well defined as well as distinguished in GFD and the acoustics communities. In view of this situation, we give them clear definitions in the context of our study, for details see §4.2.3.

This chapter is structured as follows. In §4.2, a number of concepts in boundary layer acoustics are established. To describe an incident acoustic wave, the concept of incident angle ϕ is introduced, and a relationship between the incident angle and frequency is established. According to the form of the propagation of acoustic waves in the free stream, two types of waves are distinguished. In addition, a critical angle of incidence for the existence of the critical layer is given. The above introduced physical quantities specify the computational domain for the over-reflection. Based on the exact solution to the PBE (2.31), the reflection coefficient R is derived and explicitly expressed by the CHF. In the last part of §4.2, a proof that in the case of the existence of a critical layer $|R| > 1$ always hold is given. A link between the over-reflection and a jump of a key quantity at the critical layer is further established, and it is shown how this jump causes over-reflection. In §4.3, the reflection coefficient as a function of the wavenumber α, the Mach number M, and the incident angle ϕ is displayed. Over-reflection of acoustic waves has been validated to exist in boundary layer flows and is closely related to the critical layer. The phenomenon of resonant over-reflection is observed and its close relation with unstable modes is interpreted. Eigenfunctions of acoustic waves are then displayed and thereby three patterns of the propagation of acoustic waves in boundary layer flows are identified. In §4.4, we state main conclusions of this chapter. Parts of the analysis and numerics in this chapter are aided by `Maple` (Maplesoft, 2020) and `MATLAB 2020a` (Mathworks, 2020).

Essential parts of this chapter (§4.2, §4.3 and §4.4) are based on the peer-reviewed publication Zhang et al. (2022).

4.2 Basic concepts

4.2.1 Zone of silence

Assume that the incoming acoustic wave has a unity amplitude and propagates at a constant speed of sound c_0, which is characterised by the dimensional quantities of the frequency $\tilde{\omega}$ and the horizontal wavenumber $\tilde{\alpha}$. The incident angle ϕ being a 'secondary' parameter is defined as the angle between the wavenumber vector $\tilde{\boldsymbol{k}}$ of the incident wave and the x-direction shown in figure 4.1. Here we intend to first establish a relationship between the incident angle ϕ and the frequency $\tilde{\omega}$ in order to facilitate ϕ as the main parameter to visually describe the incident acoustic wave. Using ϕ instead of $\tilde{\omega}$ reduces one parameter in analysing the critical cases that are shown in figure 4.2.

The horizontal wavenumber of an acoustic wave in a medium at rest is given by

$$\tilde{\alpha} = |\tilde{\boldsymbol{k}}| \cos(\phi) = \frac{\tilde{\omega}}{c_0} \cos(\phi). \tag{4.1}$$

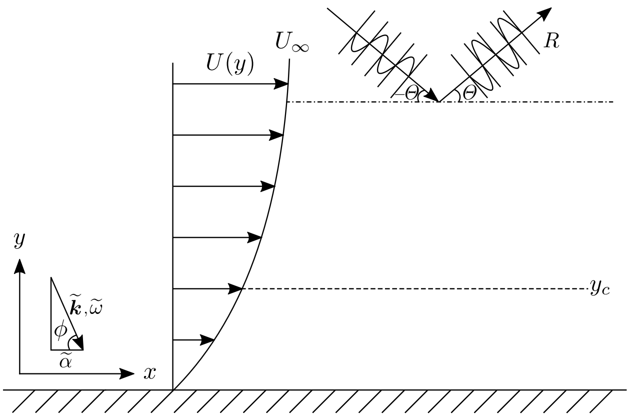

Figure 4.1: Illustration of an exponential boundary layer flow. An incident acoustic wave from the free stream gives rise to a reflected wave with angle Θ, characterised by the reflection coefficient R. The critical layer y_c is marked by a dashed line. Further, a geometric relation of an acoustic wave with frequency $\tilde{\omega}$ in a medium at rest, between wavenumber vector $\tilde{\boldsymbol{k}}$ and streamwise wavenumber $\tilde{\alpha}$ is given by their angle ϕ (incident angle).

Considering the reference values, i.e. the free-stream velocity U_∞ and the shear layer thickness δ, in non-dimensional form it gives

$$\omega = \frac{\alpha}{M\cos(\phi)}, \tag{4.2}$$

where a non-dimensional wavenumber $\alpha = \tilde{\alpha}\delta$ has been used or alternatively the wavelength $\tilde{\lambda}$ may be employed $\tilde{\alpha} = 2\pi/\tilde{\lambda}$ so that we have

$$\alpha = \frac{2\pi\delta}{\tilde{\lambda}}, \tag{4.3}$$

which implies a ratio between the shear layer thickness and the wavelength of the perturbation. This ratio indicates the range of α taken in §4.3 from 0.1 to 10 implying that the thickness of the boundary layer varies from small to large relative to the wavelength scale.

Note that the incident angle ϕ in (4.2), which is an angle between the wave number vector $\boldsymbol{k}$ and the streamwise direction, is strictly speaking for a medium at rest, i.e. $U_\infty = 0$. Hence ϕ is only an 'auxiliary' parameter used as a replacement to implicitly express the frequency, and we restrict $\phi \in [0°, 90°]$. It is not the true propagation angle of the acoustic wave in the free stream. The 'true' angle of the incident wave propagating towards the boundary layer in the free stream, due to the velocity of the free stream U_∞, is determined by the wavenumber of the acoustic wave in the y-direction. This wavenumber is given by the solution to the PBE in the free stream.

In the free stream ($y \to \infty$), where any shear is absent, the PBE (2.31) simplifies to

$$\frac{d^2\hat{\rho}}{dy^2} + \left[M^2(\omega - \alpha)^2 - \alpha^2\right]\hat{\rho} = 0, \tag{4.4}$$

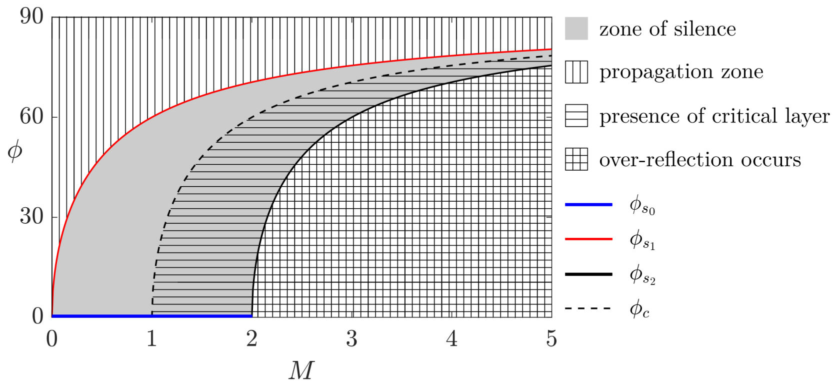

Figure 4.2: Borders of the zone of silence ϕ_{s_0} (———), ϕ_{s_1} (———), ϕ_{s_2} (———) in (4.9) and the critical value for the presence of the critical layer ϕ_c (- - -) in (4.11) as functions of the Mach number M. The grey region indicates the zone of silence. The vertical-stripe region is the propagation zone, and the horizontal-stripe region represents the presence of the critical layer.

which has oscillatory (waveform) solutions when the term in square bracket of (4.4) is greater than zero, i.e. $\theta = -M^2(\alpha-\omega)^2 + \alpha^2 < 0$. The same result can also be derived directly by setting $y \to \infty$ in the exact solution (2.35), where $H\mathrm{c}(;0) = 1$ and $\widetilde{H\mathrm{c}}(;0) = 1$, and the solution reads

$$\hat{\rho}(y) = C_1 e^{\sqrt{\theta} y} + C_2 e^{-\sqrt{\theta} y}, \tag{4.5}$$

where the principal value of $\sqrt{\theta}$ is taken and the branch cut is along the negative real axis.

For $\theta < 0$, the wavenumber in the y-direction in the free stream reads

$$\beta = \sqrt{-\theta}, \tag{4.6}$$

where the principal value of the square root is taken. It follows that the two solutions in (4.5) stand for an outgoing wave ($C_1 e^{i\beta y}$) and an incoming wave ($C_2 e^{-i\beta y}$), respectively, for $\theta < 0$ and $\theta \in \mathbb{R}$. This can be intuitively observed by the shifts of peaks and troughs of the waves in time by adding the time dependence in the normal mode (2.11). For $\theta > 0$, there would be a non-wave/exponential behaviour of the solution in (4.5).

The angle of propagation with respect to the x-axis of an acoustic wave in the free stream is therefore defined as

$$\Theta = \arctan\left(\frac{\beta}{\alpha}\right), \tag{4.7}$$

as shown in figure 4.1.

Next, two types of acoustic waves in boundary layer flows are distinguished as propagating waves and evanescent waves, for waves that can propagate in a vertical direction and waves that cannot. These two cases correspond to (2.36) $\theta < 0$ and $\theta > 0$, respectively. Considering the relation (4.2) gives the critical case, i.e.

$$-\theta = \alpha^2 \left[\left(\frac{1}{\cos(\phi)} - M\right)^2 - 1\right] = 0, \tag{4.8}$$

which gives two solutions ϕ_s indicating to 'zones of silence' given by

$$\phi_s \in \begin{cases} \left[0, \text{arccos}\left(\frac{1}{M+1}\right)\right], & M \leq 2, \\ \\ \left[\text{arccos}\left(\frac{1}{M-1}\right), \text{arccos}\left(\frac{1}{M+1}\right)\right], & M > 2. \end{cases} \tag{4.9}$$

In (4.9), the lower border for $M \leq 2$ is denoted as ϕ_{s_0}, the upper border for both cases as ϕ_{s_1} and the lower border for $M > 2$ as ϕ_{s_2}. An intuitive illustration is shown in figure 4.2, where the zone of silence is marked in grey. No propagating waves exist for the areas defined in (4.9), i.e. the grey area in figure 4.2.

The introduction of ϕ instead of ω gives the critical case (4.9), which has only one independent variable M. It is possible to avoid the introduction of ϕ, which, however, would imply that the critical case for ω involves two variables instead of one, i.e. α and M.

Equation (4.9) indicates that acoustic perturbations with ϕ_s being as the incident angle do not propagate in a waveform in the free stream because their amplitudes decay exponentially and tend to zero. Therefore, they are called evanescent waves. Whereas outside the ϕ_s region, acoustic perturbations in the free stream exist as oscillatory waves, i.e. they can propagate in the y-direction and therefore denote propagating waves. We define the region out of ϕ_s as the 'propagation zone', which is represented by vertical stripes in figure 4.2. The introduction of the concept of the incident angle instead of the frequency physically defines the range of parameter ϕ for the existence of incident and outgoing waves at different Mach numbers.

4.2.2 Critical layer

Per definition, the critical layer is a wall-parallel plane, where the phase velocity of the acoustic wave ω/α is equal to the local base flow velocity $u_0(y)$, i.e. $\omega/\alpha = 1 - e^{-y}$. Considering an incident acoustic wave in (4.2), the location of the critical layer is given by

$$y_c = -\ln\left(1 - \frac{1}{M\cos(\phi)}\right), \tag{4.10}$$

shown in figure 4.1. It follows from (4.10) that in order to ensure the existence of a critical layer, the argument of the logarithm has to be greater than zero and smaller than one, and with this, the incident angle has to be less than a critical value given by

$$\phi_c = \text{arccos}\left(\frac{1}{M}\right), \tag{4.11}$$

displayed in figure 4.2. When the incident angle is greater than ϕ_c, i.e. $\phi > \phi_c$, there is no critical layer in the shear flow. For the limiting case $\phi = \phi_c$, the critical layer is located at infinity.

Figure 4.2 shows limiting curves of the zone of silence ϕ_s as well as the corresponding critical incident angle of the critical layer ϕ_c as a function of the Mach number M. The thick red and black solid lines in the figure represent the borders ϕ_{s_1} and ϕ_{s_2} of the zone of silence according to (4.9). The grey region between them is the zone of silence. The critical incident angle for the presence of the critical layer is represented by the dashed line. These critical angles, ϕ_{s_1}, ϕ_{s_2} and ϕ_c, provide a reference for the computation domain in §4.3.

In §4.3, we focus mainly on the propagation zone ($\theta < 0$) where the critical layer is present ($\phi < \phi_c$) because these conditions ensure the presence of incident and reflected (propagating) waves in the free stream and the occurrence of over-reflection. A detailed study of the critical layer leading to over-reflection is given in §4.2.4. To satisfy these two conditions simultaneously, the checkered region, shown in figure 4.2, is concerned. Considering the transformation of ϕ corresponding to the checkered region to ω, it is equivalent to $\omega/\alpha \in [1/M, 1-1/M]$. This phase velocity range is corresponding to the supersonic mode range in the temporal stability problem, which is corresponding to the area between the red and blue dashed lines shown in figure 3.2(c).

4.2.3 Reflection coefficient

In this section, we derive the reflection coefficient R, which is the amplitude ratio of the reflected to the incident wave. This will be based on the exact solution (2.35) to the PBE (2.31), and the boundary conditions. We consider first the boundary condition at the wall, i.e. $y = 0$. There, the condition is obtained through the impermeability condition, wherein in the present work, we adopt the simplest case, i.e. a rigid (inelastic) wall. Thus, the normal component of the velocity perturbation at the wall vanishes, i.e.

$$\hat{v}(0) = 0. \tag{4.12}$$

Using the boundary condition (4.12) together with (2.33) and (2.35), where the derivative of the density perturbation reads

$$\begin{aligned}\frac{d\hat{\rho}}{dy} =& C_1 \left[\left(-iM\alpha e^{-y} + \sqrt{\theta} \right) Hc \left(; \frac{\alpha e^{-y}}{\alpha - \omega} \right) - \frac{\alpha e^{-y}}{\alpha - \omega} Hc' \left(; \frac{\alpha e^{-y}}{\alpha - \omega} \right) \right] e^{iM\alpha e^{-y} + \sqrt{\theta} y} \\ &+ C_2 \left[\left(-iM\alpha e^{-y} - \sqrt{\theta} \right) \widetilde{Hc} \left(; \frac{\alpha e^{-y}}{\alpha - \omega} \right) - \frac{\alpha e^{-y}}{\alpha - \omega} \widetilde{Hc}' \left(; \frac{\alpha e^{-y}}{\alpha - \omega} \right) \right] e^{iM\alpha e^{-y} - \sqrt{\theta} y},\end{aligned} \tag{4.13}$$

we obtain

$$\begin{aligned}\hat{v}(0) =& \frac{-ie^{iM\alpha}}{M^2\omega} \left\{ C_1 \left[\left(-iM\alpha + \sqrt{\theta} \right) Hc \left(; \frac{\alpha}{\alpha - \omega} \right) - \frac{\alpha}{\alpha - \omega} Hc' \left(; \frac{\alpha}{\alpha - \omega} \right) \right] \right. \\ &\left. + C_2 \left[\left(-iM\alpha - \sqrt{\theta} \right) \widetilde{Hc} \left(; \frac{\alpha}{\alpha - \omega} \right) - \frac{\alpha}{\alpha - \omega} \widetilde{Hc}' \left(; \frac{\alpha}{\alpha - \omega} \right) \right] \right\} = 0.\end{aligned} \tag{4.14}$$

From (4.14), a relation between C_1 and C_2 is induced and reads

$$C_1 = -C_2 \frac{\left(-iM\alpha - \sqrt{\theta} \right) \widetilde{Hc} \left(; \frac{\alpha}{\alpha - \omega} \right) - \frac{\alpha}{\alpha - \omega} \widetilde{Hc}' \left(; \frac{\alpha}{\alpha - \omega} \right)}{\left(-iM\alpha + \sqrt{\theta} \right) Hc \left(; \frac{\alpha}{\alpha - \omega} \right) - \frac{\alpha}{\alpha - \omega} Hc' \left(; \frac{\alpha}{\alpha - \omega} \right)}. \tag{4.15}$$

We assume that the amplitude of the incoming wave at $y \to \infty$, which is the second term of equation (2.35), is unity and thus, combining (2.35) with (4.15) the amplitude of the density perturbation reads

$$\hat{\rho}(y) = Re^{iM\alpha e^{-y}+\sqrt{\theta}y}Hc\left(;\frac{\alpha e^{-y}}{\alpha-\omega}\right) + e^{iM\alpha e^{-y}-\sqrt{\theta}y}\widetilde{Hc}\left(;\frac{\alpha e^{-y}}{\alpha-\omega}\right), \tag{4.16}$$

where R is the reflection coefficient defined by

$$R = -\frac{\left(-iM\alpha-\sqrt{\theta}\right)\widetilde{Hc}\left(;\frac{\alpha}{\alpha-\omega}\right) - \frac{\alpha}{\alpha-\omega}\widetilde{Hc}'\left(;\frac{\alpha}{\alpha-\omega}\right)}{\left(-iM\alpha+\sqrt{\theta}\right)Hc\left(;\frac{\alpha}{\alpha-\omega}\right) - \frac{\alpha}{\alpha-\omega}Hc'\left(;\frac{\alpha}{\alpha-\omega}\right)}. \tag{4.17}$$

In (4.17), there are three parameters, i.e. the wavenumber α, the Mach number M and the frequency ω, where ω can be replaced by the incident angle ϕ according to (4.2).

In Campos & Kobayashi (2013), a similar reflection coefficient is obtained for the PBE with a hyperbolic tangent profile, which is used to mimic a boundary layer flow. Not only an over-reflection of acoustic waves is observed but the reflection coefficient has an unusual high peak at a certain frequency (see the case $M = 4.5$ in Figure 6A in Campos & Kobayashi (2013) and note that there is a mistake in the figure, i.e. Figure 6A should be for $|R|$ but not for $|T|$). For this, no further explanation was given, but the values lie close to the eigenvalues we obtained for instability.

In the remaining part of this chapter, we will analyse the reflection coefficient R, and we will observe various effects such as over-reflection or resonant over-reflection. In §4.2.4 we give a detailed analysis that for boundary layer flows the presence of a critical layer is intimately linked to the occurrence of over-reflection. In §4.3, the analysis is validated by computations and furthermore a special enhancement of over-reflections are found.

We recall that the stability problems in §3. The eigenvalue equation derived therein was obtained from the exact solution (2.35), in combination with boundary conditions of vanishing disturbances at infinity and zero wall-normal velocity. The former condition leads to $C_1 = 0$ in (2.35), and the latter condition gives $d\hat{\rho}/dy(0) = 0$ in (4.13). The eigenvalue equation (3.14) is therefore obtained. It is interesting to notice that the eigenvalue equation (3.14) coincides with the current acoustic case, in which the numerator of (4.17) is equal to zero. Acoustically, this indicates that no reflected waves are allowed to exist. But for unstable modes $\omega_i > 0$ in the temporal stability problem or $\alpha_i < 0$ in the spatial stability problem, setting $C_1 = 0$ implies the opposite scenario, i.e. that there are no incoming waves but only outgoing waves because the 'outgoing wave' must be redefined. Since the unstable modes show dispersive waves with decreasing amplitude to zero as y tends to infinity, the group velocity (direction) is considered to be the true propagation velocity (direction) of the waves. In Appendix A.4, it is demonstrated that the unstable wave with decreasing amplitude as $y \to \infty$ has a positive group velocity with a negative phase velocity. This leads to C_1-term in the current context having an opposite physical meaning to that in the stability problem. This might give a physical insight: perturbations that acquire energy from the shear flow are not allowed to emit in the form of over-reflections, thereby manifesting themselves as an onset of a temporal or spatial instability, i.e. in a certain parameter range we obtain unstable eigenvalues $\omega \in \mathbb{C}$ for temporal instability or $\alpha \in \mathbb{C}$ for spatial instability, or even a mixed temporal-spatial instability.

To distinguish resonant over-reflection and hyper-reflection very clearly within the present work let's consider the following setting. From an acoustic point of view, in the free stream, the first term of (4.16) represents the outgoing wave, while the second term represents the incoming wave. Taking the principle value of $\sqrt{\theta}$, setting $C_2 = 0$ means that a phenomenon occurs in which the incident wave is zero at an infinite distance to the wall while the reflected wave persists with a constant amplitude for $y \to \infty$. Considering the boundary condition at the wall, an eigenvalue problem is formulated, in which the eigenvalue equation is equivalent to setting the denominator in (4.17) to zero. Thus, in this case, the sought eigenvalues lead to an infinite R. To distinguish this case from the over-reflection induced by resonant frequencies in the present work, we define the above phenomenon of the reflection coefficient R tending to infinity as the hyper-reflection.

The focus of the present chapter is to investigate the over-reflection, and the special over-reflection induced by the resonant frequencies in an instability context that we presently call resonant over-reflection. Infinitely strong over-reflection, i.e. hyper-reflection as defined above, is not considered.

4.2.4 Analysis of the critical layer

In this section, we show how the critical layer is intimately linked to the over-reflection. We further present an analytical relation between the amplitude of the density perturbation at the critical layer and the reflection coefficient R of the boundary layer flow.

For this, a transformation of the independent variable y is introduced in order to eliminate the first order derivative in the PBE (2.31) and bring it to its normal form by introducing (see Olver et al., 2010)

$$\tilde{y} = \int e^{-\int \frac{2\alpha \frac{du_0(y)}{dy}}{\omega - \alpha u_0(y)} dy} dy. \tag{4.18}$$

With (4.18), the transformed PBE (2.31) takes the form

$$\frac{d^2\hat{\rho}}{d\tilde{y}^2} + \frac{\left[M^2(\omega - \alpha u_0)^2 - \alpha^2\right]}{(\omega - \alpha u_0)^4}\hat{\rho} = 0. \tag{4.19}$$

In concrete terms and using $u_0(y)$ given by its non-dimensional form $u_0(y) = 1 - e^{-y}$, i.e. (2.28a), $\tilde{y}$ is given by

$$\tilde{y} = 2\alpha(\alpha - \omega)e^{-y} - \frac{\alpha^2}{2}e^{-2y} + y(\alpha - \omega)^2. \tag{4.20}$$

Next, (4.19) is multiplied by the conjugate solution $\hat{\rho}^*$ and integrated between the boundaries defined by $\tilde{y}_1$ and $\tilde{y}_2$. We limit to the imaginary part, to which we refer by $\Im$. This is motivated by a certain invariant of the transformed PBE, which will be explained in more detail below at equation (4.27). With the above we obtain

$$\Im\left(\frac{d\hat{\rho}}{d\tilde{y}}\hat{\rho}^*\right)\Bigg|_{\tilde{y}_1}^{\tilde{y}_2} = \int_{\tilde{y}_1}^{\tilde{y}_2} \Im\left(\frac{\alpha^2}{(\omega - \alpha u_0)^4} - \frac{M^2}{(\omega - \alpha u_0)^2}\right)|\hat{\rho}|^2 d\tilde{y}. \tag{4.21}$$

The following analysis revolves around the equation (4.21). We will discuss both sides of (4.21) thoroughly in three parts: (i) The left-hand side (LHS) of (4.21) is analysed with respect to its relation with the reflection coefficient R. (ii) The LHS of (4.21) is proven to be associated with a jump in the value of the so-called quasi-invariant at the critical layer. In the presence of a critical layer, the value of the quasi-invariant jumps directly at the critical layer, i.e. is constant above and below the critical layer. The step-like variation of this quasi-invariant is further related to the logarithmic singularity at the critical layer. These two facts will indicate that the reflection coefficient is always larger than one in the presence of a critical layer. (iii) We will discuss the right-hand side (RHS) of (4.21) and evaluate the integrals in order to obtain an analytical relation between the reflection coefficient and the perturbed quantities at the critical layer. In addition, appendices A.5, A.6, and A.7 provide supplements for the above-mentioned three parts. Appendix A.5 derives the Fuchs-Frobenius solution, establishing the jump due to the critical layer. The jump is proved to be positive in the present context by fixing the branched cut selected based on the causality in Appendix A.6. These two appendices support part (ii). A detailed derivation of the extended unitarity condition mentioned in part (iii) is given in Appendix A.7.

To begin with part (i), the evaluation of the LHS of (4.21), it reveals a close link to the reflection coefficient R. For this, we recall the principle asymptotics of the acoustic solution in the limit $y \to \infty$, which is taken from (4.5). An incident wave with unity amplitude and a reflected wave with complex amplitude R at $y \to \infty$ are assumed, which refers to $\tilde{y}_2$. At $\tilde{y}_1$, a location corresponding to the wall, i.e. $y = 0$, the rigid-wall boundary condition (4.12) leads with (2.33) to a vanishing y-derivative of the density. To sum up, the boundary conditions read

$$\hat{\rho}(y \to \infty) \sim Re^{i\beta y} + e^{-i\beta y}, \tag{4.22a}$$

$$\left.\frac{d\hat{\rho}}{d\tilde{y}}\right|_{\tilde{y}_1} = \left.\frac{dy}{d\tilde{y}}\frac{d\hat{\rho}}{dy}\right|_{y=0} = 0. \tag{4.22b}$$

Inserting (4.22a) and (4.22b) into the LHS of (4.21), it can be reshaped to

$$\Im\left(\frac{d\hat{\rho}}{d\tilde{y}}\hat{\rho}^*\right)\Bigg|_{\tilde{y}_1}^{\tilde{y}_2} = \Im\left(\frac{d\hat{\rho}}{dy}\frac{dy}{d\tilde{y}}\hat{\rho}^*\right)\Bigg|_{\tilde{y}_1}^{\tilde{y}_2} = \frac{\beta}{(\alpha-\omega)^2}\left(|R|^2 - 1\right). \tag{4.23}$$

Up to this point, we make a connection between the LHS of the equation and the reflection coefficient R through the boundary conditions.

Moving on to part (ii), we try to establish a connection between the LHS of (4.21) and a positive jump, thereby proving that the over-reflection coefficient is always greater than one. For this, we further rewrite the LHS of (4.23) below to obtain a relationship between the reflection coefficient, namely the RHS of (4.23), and the physical properties at the critical layer.

Considering the y-derivative of the LHS of (4.23), we show that it vanishes outside the critical layer, i.e.

$$\frac{d}{dy}\left(\Im\left(\frac{d\hat{\rho}}{d\tilde{y}}\hat{\rho}^*\right)\right) = \Im\left(\frac{d^2\hat{\rho}}{d\tilde{y}^2}\hat{\rho}^* + \left|\frac{d\hat{\rho}}{d\tilde{y}}\right|^2\right) = \Im\left(\frac{d^2\hat{\rho}}{d\tilde{y}^2}\hat{\rho}^*\right), \tag{4.24}$$

which is, using (4.19), rewritten as

$$\frac{d}{dy}\left(\Im\left(\frac{d\hat{\rho}}{d\tilde{y}}\hat{\rho}^*\right)\right) = \Im\left(-\frac{M^2(\omega-\alpha u_0)^2-\alpha^2}{(\omega-\alpha u_0)^4}|\hat{\rho}|^2\right) = 0\big|_{y\neq y_c} \tag{4.25}$$

The above derivation only holds outside the critical layer since at the critical layer the coefficient function in (4.19) is singular. From this, we follow that

$$I = \Im\left(\frac{d\hat{\rho}}{d\tilde{y}}\hat{\rho}^*\right), \tag{4.26}$$

is a constant which undergoes a jump at the critical layer. Therefore, we call I a quasi-invariant, since it is invariant only in limited domains. Thus, the boundaries between which the LHS of (4.23) is evaluated can also be chosen just above and below the critical layer $\tilde{y}_c$, which yields

$$I|_{\tilde{y}_1}^{\tilde{y}_2} = \Im\left(\frac{d\hat{\rho}}{d\tilde{y}}\hat{\rho}^*\right)\Bigg|_{\tilde{y}_1}^{\tilde{y}_2} = \Im\left(\frac{d\hat{\rho}}{d\tilde{y}}\hat{\rho}^*\right)\Bigg|_{\tilde{y}_c^-}^{\tilde{y}_c^+} = \frac{\beta}{(\alpha-\omega)^2}\left(|R|^2-1\right). \tag{4.27}$$

Subsequently, Appendix A.5 will be used to evaluate the jump of the quasi-invariant at the critical layer. Transforming the LHS of (4.27) to the coordinate $\xi = \omega/\alpha - u_0(y)$, which was used to derive the Frobenius solution (A.34) at the critical layer in Appendix A.5, yields

$$I|_{\tilde{y}_1}^{\tilde{y}_2} = \Im\left(\frac{d\hat{\rho}}{d\tilde{y}}\hat{\rho}^*\right)\Bigg|_{\tilde{y}_c^-}^{\tilde{y}_c^+} = \Im\left(\frac{dy}{d\tilde{y}}\frac{d\xi}{dy}\frac{d\hat{\rho}}{d\xi}\hat{\rho}^*\right)\Bigg|_{0^+}^{0^-} = -{u_0}'(y_c)\,\Im\left(\frac{1}{\xi^2}\frac{d\hat{\rho}}{d\xi}\hat{\rho}^*\right)\Bigg|_{0^+}^{0^-}. \tag{4.28}$$

Taking the Fuchs-Frobenius solution (A.34) into (4.28) leads to

$$\begin{aligned} I|_{\tilde{y}_1}^{\tilde{y}_2} = \Im\left(\frac{d\hat{\rho}}{d\tilde{y}}\hat{\rho}^*\right)\Bigg|_{\tilde{y}_c^-}^{\tilde{y}_c^+} &= -3c_*{u_0}'(y_c)|B|^2\Im\left(\ln(\xi)\right)|_{0^+}^{0^-} \\ &= -3c_*\,{u_0}'(y_c)|B|^2\ln\left(0^-\right) = -3\pi c_*\,{u_0}'(y_c)|B|^2, \end{aligned} \tag{4.29}$$

where B is a constant in the Fuchs-Frobenius series and c_* is a rational function in α and ω as defined in (A.35). The causal choice of the logarithmic branch cut as explained in Appendix A.6 is important since it leads to $\Im\left(\ln\left(0^-\right)\right) = \pi$. Note that an non-causal choice of the branch cut, i.e. a choice that does not follow the branch cut defined in Appendix A.6, would lead to the opposite sign.

Taking into account that c_* is always negative in the presence of a critical layer as shown in Appendix A.5 by analysing (A.36), we find that the RHS of equation (4.29) is always positive. Thus it can be concluded that the jump of $I = \hat{\rho}^*\,d\hat{\rho}/d\tilde{y}$ over the critical layer is also always positive and thus, in considering equation (4.27), the reflection coefficient in the presence of a critical layer is always greater than one, i.e. $R > 1$, since we obtain

$$\frac{\beta}{(\alpha-\omega)^2}\left(|R|^2-1\right) = -3\pi c_*\,{u_0}'(y_c)|B|^2. \tag{4.30}$$

In absence of a critical layer, the RHS of equation (4.21) vanishes since the coefficients are real and the integral contains no singularity that would lead to an imaginary part, following the theory of generalised functions and distributions given in Galapon (2016). Likewise, considering equation (4.23) with the knowledge that $I = \hat{\rho}^*\,d\hat{\rho}/d\tilde{y}$ is invariant over the entire physical domain in absence of a critical layer, we conclude that $R = 1$ must hold without a critical layer. This means that without a critical layer there is no mechanism of damping or amplification of the reflected wave.

Thus, in an exponential boundary layer flow with a rigid wall energy can only be transferred from the base flow to the acoustic wave, and the acoustic wave cannot be damped, since $R = 1$ in the absence of a critical layer and $R > 1$ in the presence of a critical layer.

With parts (i) and (ii), we have obtained some information through the RHS of equation (4.21), i.e. a positive jump caused by the critical layer makes the over-reflection coefficient always greater than 1. However, we do not know how much the value of this jump is. To answer this question, we proceed to part (iii), i.e. we focus on the evaluation of the RHS of (4.21). For this, we evaluate both parts of (4.21) separately using the theory of distributions, which leads to

$$\int_{\tilde{y}_1}^{\tilde{y}_2} \Im\left(\frac{\alpha^2}{(\omega-\alpha u_0)^4} - \frac{M^2}{(\omega-\alpha u_0)^2}\right)|\hat{\rho}|^2 d\tilde{y} = \pi\left(\left(\frac{M^2}{\alpha}\frac{d}{d\xi} - \frac{\alpha}{6}\frac{d^3}{d\xi^3}\right)\frac{|\hat{\rho}|^2}{\frac{du_0}{d\tilde{y}}}\right)\Bigg|_{\xi=0}, \tag{4.31}$$

where we have further introduced a coordinate based on the location of the critical layer, i.e.

$$\xi = \omega - \alpha u_0(y), \tag{4.32}$$

and therefore $\xi = 0$ is the location of the critical layer. A detailed derivation of (4.31) is given in Appendix A.7.

In a final step, we use (4.21), where the LHS was replaced by (4.23) and the RHS by (4.31). Transforming this back to the initial variable y leads to a relation between the amplitude of the reflected wave and the amplitude of density perturbation and its derivations at the critical layer, which reads

$$\frac{\beta}{(\alpha-\omega)^2}\left(|R|^2 - 1\right) = \pi\alpha^2(\alpha-\omega)^5\left(\frac{d}{dy}\left(\frac{|\hat{\rho}|^2}{\frac{du_0}{dy}}\right) - 2\frac{|\hat{\rho}|^2}{\frac{du_0}{dy}}\right)\Bigg|_{y=y_c}. \tag{4.33}$$

There is only information on the amount of the reflection coefficient here, the phase shift of the reflected wave compared to the incident one does not result from (4.33). Since R is complex, the phase shift of the reflected wave is included in the argument of R.

Equation (4.33) is similar to the 'unitarity condition', introduced by Lapin (2011) in the context of waves interacting with a jet, thus we call it 'extended unitarity condition' in terms of the current context of acoustics.

With the key results (4.30) and (4.33), we show that the over-reflection is directly caused by the critical layer. The critical layer causes a jump of the quasi-invariant I, which leads to the amplitude of the reflected wave being larger than that of the incident wave. An analytical relation between the reflection coefficient and the amplitude of density perturbation is given by the extended unitarity condition.

4.3 Over-reflection analysis depending on α, M and ϕ

In this section, we present detailed results of the reflection coefficient R given by (4.17), which depends on three non-dimensional parameters, i.e. wavenumber α, Mach number M, and frequency ω. Subsequently, the frequency ω is always rewritten as a function of the incident angle ϕ according to (4.2). Here we are only concerned with the reflection coefficients within the range of parameters in which propagating waves and the critical layer exist simultaneously, i.e. the checkered region in figure 4.2. In this parameter range, incident acoustic waves are always over-reflected, i.e. $R > 1$, due to the jump of the quasi-invariant demonstrated in §4.2.4. Therefore, in the following, we refer to the reflection coefficient directly as the over-reflection coefficient.

The key results of the over-reflection coefficient R are presented in five groups. Mach numbers are all within the range $[2, 5]$. Firstly, results of the over-reflection coefficient are shown as a function of the Mach number M and incident angle ϕ for a small representative set of wavenumbers below one, i.e. $\alpha \leq 1$. In this α range, the over-reflection coefficient is not influenced by resonant frequencies, which are the unstable eigenvalues ω emerging due to acoustic instabilities of the exponential boundary layer profile. This can be concluded by figure 3.7 in §3. In figure 3.7, for $\alpha \leq 1$ the eigenvalues are all above the blue dashed line, which indicates that the modes are subsonic modes but not supersonic modes. In other words, for $\alpha \leq 1$ and $M \leq 5$, there are no unstable supersonic modes and their corresponding resonant frequencies that affect over-reflection. We refer to those over-reflections that are not affected by the resonant frequencies as non-resonant over-reflections. Secondly, we display the reflection coefficient in the wavenumber range $1 < \alpha < 2$, in which the resonant frequencies begin to appear in the propagation region and trigger the resonant over-reflection. In the third group, in order to disclose the connection between the resonant over-reflection and unstable modes, the results of the reflection coefficient are displayed as a function of the wavenumber α and the incident angle ϕ, for different fixed Mach numbers. The close connection is revealed by the resonance lines, and the synchronisation of peaks of the over-reflection coefficient and growth rate of unstable modes in the α-ϕ plane. Resonance lines are those in §3.5 defined modal lines consisting of real parts of eigenvalues in the ω_r-α_r-plane. In the fourth group, a set of larger wavenumbers is chosen up to $\alpha = 10$ to show the results of the over-reflection coefficient as a function of the Mach number M and the incident angle ϕ, while revealing a result that higher unstable modes in addition to the first unstable mode can also lead to resonant over-reflections. In the last group, we exhibit a series of eigenfunctions and identify three patterns of acoustic waves propagating in an exponential boundary layer flow.

All numerical evaluations of the CHF were computed with `Maple` (Maplesoft, 2020) and verified by the open-source code by Motygin (2018) based on `MATLAB` (Mathworks, 2020).

4.3.1 Non-resonant over-reflection

Figure 4.3 displays the numerical results for the over-reflection coefficient as a function of the Mach number M and the incident angle ϕ, where the wavenumber α is chosen in the range between 0.1 and 1. Therein we have included also contour lines, where the thick solid line corresponds to the border ϕ_{s_2} between the propagation zone and the zone of silence, which is shown in figure 4.2. The reflection coefficient in the latter region is either equal to one or has no real physical significance due to exponential non-oscillatory decay of the amplitude into the free stream.

Observing figures 4.3(a)-4.3(f), we note first that the over-reflection coefficient decreases with increasing wavenumbers. For small wavenumbers, as in figures 4.3(a)-4.3(c), there are rather large values of the over-reflection coefficient. Particular for $\alpha = 0.1$, the maximum value even reaches approximately $R = 3$. While the values of the over-reflection coefficient shown

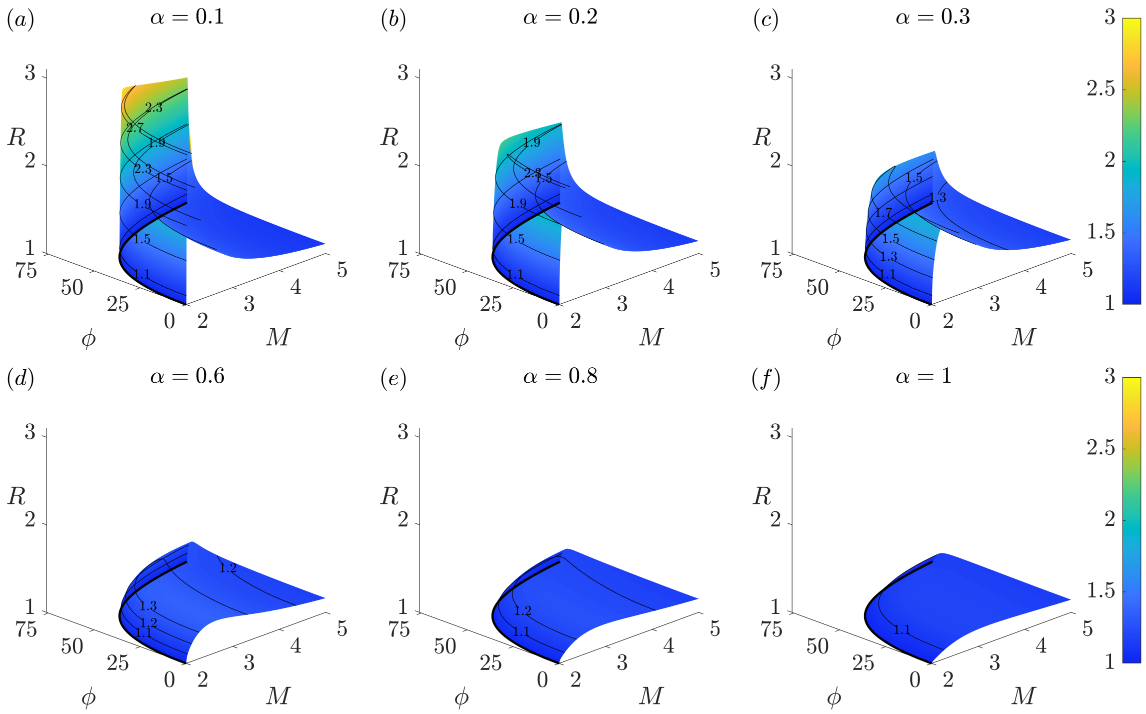

Figure 4.3: Over-reflection coefficient R defined by (4.17) as a function of M and ϕ. (a)-(f) for α in a range from 0.1 to 1. ——— defines the over-reflection border ϕ_{s_2} according to figure 4.2.

in figures 4.3(d)-4.3(f) are relatively small. This result means that for small wavenumbers, relatively strong over-reflections occur.

In addition, the large values of the over-reflection coefficient gather around the line of silence ϕ_{s_2} and go along with large gradients nearby. Particularly visible is that at $\alpha = 0.1$, a large gradient of variation in the over-reflection coefficient near the over-reflection border ϕ_{s_2} can be detected by observing the contours from $R = 1.9$ to $R = 2.7$ that become progressively narrower. And as the wavenumber α increases, in figure 4.3(b) and figure 4.3(c), the peak gradually moves away from the line of silence ϕ_{s_2}. Meanwhile, the contours become sparse, which indicates that the drastic variation becomes flatter as α increases as in figures 4.3(d)-4.3(f). This result suggests that over-reflections generated by small wavenumbers are more sensitive to variations in the Mach number than over-reflections generated by moderate wavenumbers.

4.3.2 Coincidence of resonantly over-reflected waves and unstable acoustic modes

In this section, we focus on the resonant over-reflection and its connection to unstable acoustic modes. We first depict a phenomenon in which an unusual peak of the over-reflection coefficient appears with increasing wavenumbers in figure 4.4. Subsequently, through figure 4.5 and figure 4.6, we establish links between the resonant frequencies and the peaks, i.e. links between unstable modes and resonant over-reflection. In figure 4.7, the synchronisation of the growth rate of unstable modes and the over-reflection coefficient on the resonance line is shown.

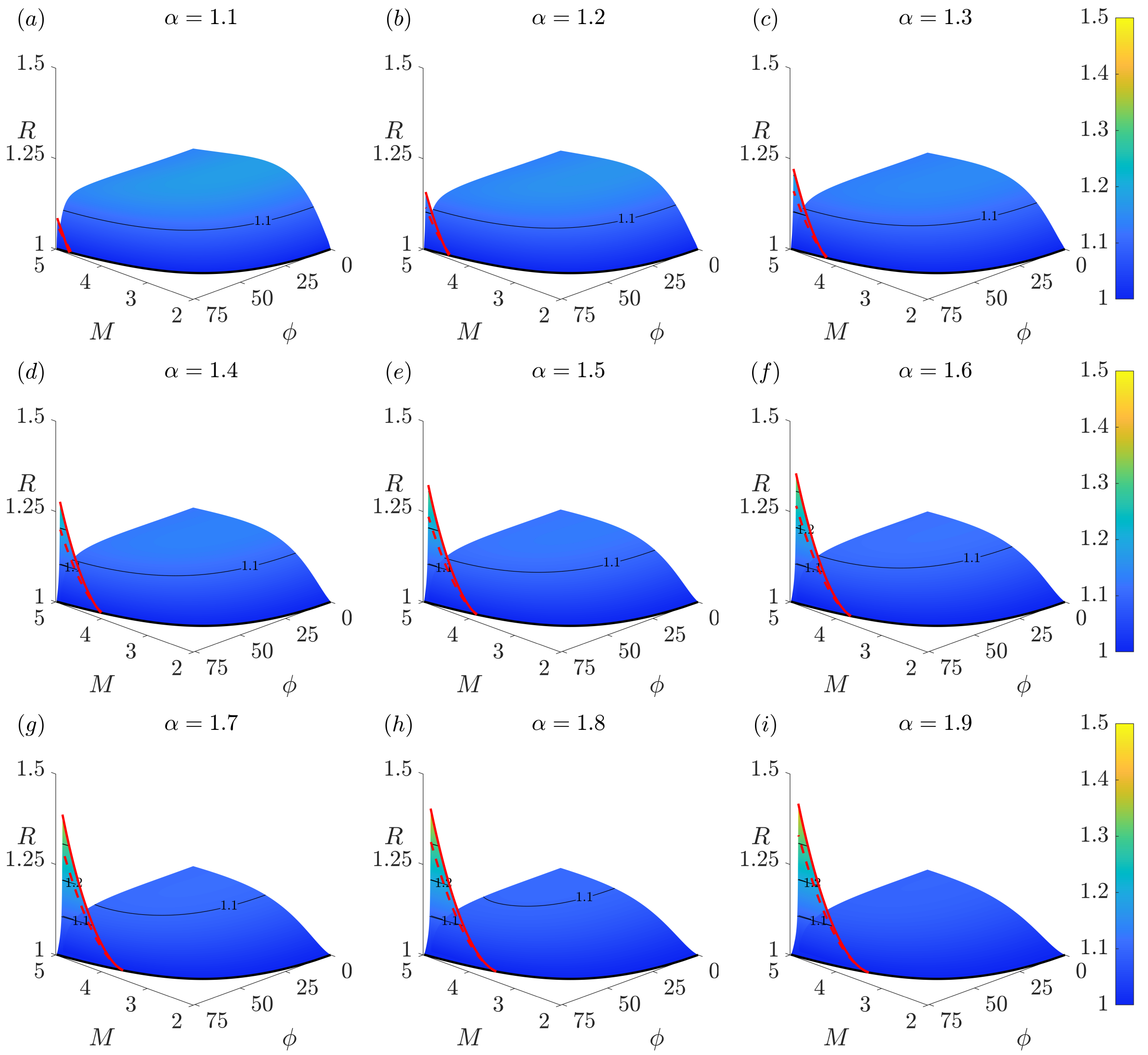

Figure 4.4: Over-reflection coefficient R defined by (4.17) as a function of M and ϕ. (a)-(f) for α in a range from 1.1 to 1.9. —— defines the over-reflection border ϕ_{s_2} according to figure (4.2). —— defines the local/global maximum R. - - - defines R at resonant frequencies.

Figure 4.4 depicts the variation of the over-reflection coefficient in a range of wavenumbers between $\alpha = 1.1$ and $\alpha = 1.9$, where the range of Mach numbers is still chosen to be between $M = 2$ and $M = 5$. Note that in figure 4.4 we have now swapped the coordinates M and ϕ to better observe the key effect in this subsection, i.e. that at a wavenumber $\alpha = 1.1$, an unusual local peak appears near the incident angle $\phi \approx 75$ and Mach number $M \approx 4.5$. This local peak grows as the wavenumber increases and becomes a global peak finally at $\alpha \approx 1.3$. Thereafter, the peak continues to increase with wavenumber until $\alpha \approx 2$ in figure 4.8(a) and then starts decreasing again. These peaks occur within a very small range of the parameter ϕ. The variation of the over-reflection coefficient in the remaining part is not affected by the peak and remains largely smooth. As the wavenumber increases, the remaining part slowly decreases.

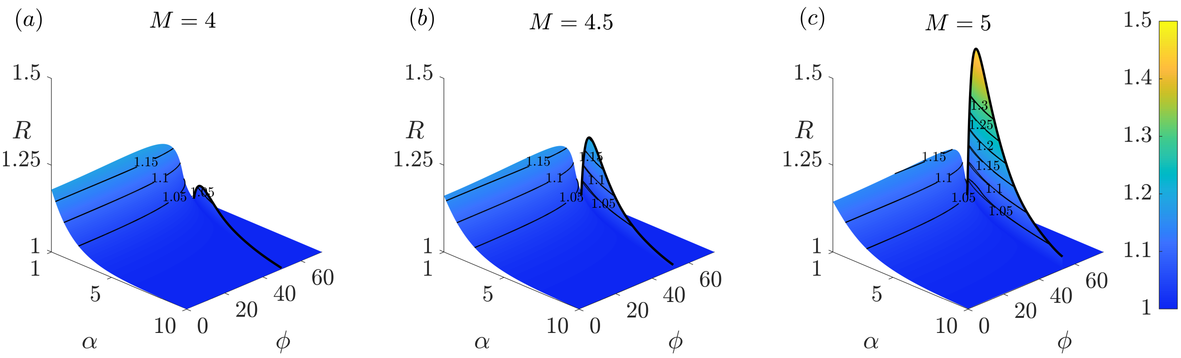

Figure 4.5: Over-reflection coefficient R as a function of α and ϕ for different Mach numbers. In this parameter domain, only the first unstable mode induced resonant over-reflections and their peaks are shown and marked by thick solid lines.

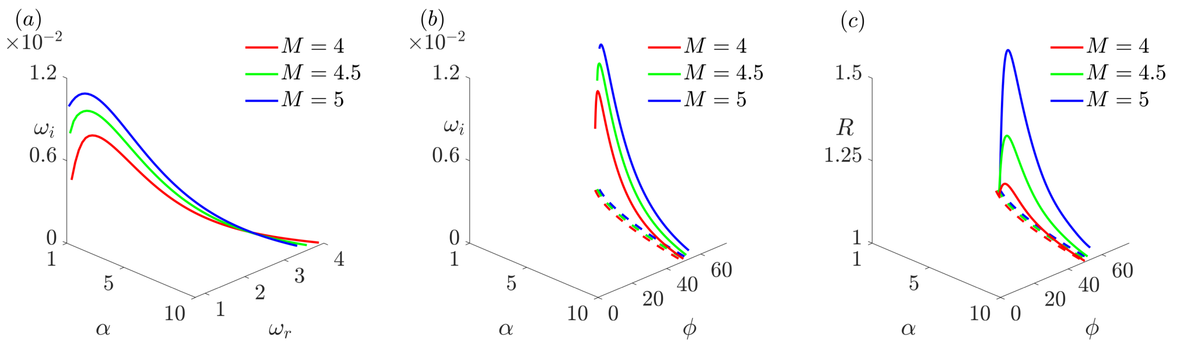

Figure 4.6: Coincidence of unstable modes and resonant over-reflection. (a) The first unstable acoustic mode of temporal instability for different Mach numbers, where the eigenvalue $\omega \in \mathbb{C}$ as a function of α, ω_r is the resonant frequency and ω_i is the growth rate. (b) The α-ω_r-plane in (a) is converted to α-ϕ-plane according to (4.2). (c) Local maximum value of the resonant over-reflection in figure 4.5 and their projections on α-ϕ-plane. The dashed lines in (b) and (c) represent the projection of the solid lines on the α-ϕ-plane.

In the following, the goal is to unravel a connection between resonant over-reflections and unstable modes. To achieve this, in the figure 4.5(a), 4.5(b) and 4.5(c) we show the results of the over-reflection coefficient as a function of the wavenumber α and the incident angle ϕ, where the wavenumber ranges from 1 to 10 and the Mach numbers are fixed to $M = 4$, $M = 4.5$ and $M = 5$. From figure 4.5, we note that the resonant over-reflection peaks appear as the wavenumber increases. To explain the peaks, we next establish the relationship between the resonant frequencies and the resonant over-reflections.

In §3, we deduce the eigenvalue problem for stability of the exponential boundary layer profile and this is essentially based on the exact solution (2.35). The imaginary part of the eigenvalue derived there off, i.e. the growth rate ω_i, is a function of the Mach number M and the wavenumber α is of key importance here. Since we have shown in §3.5 that both temporal instability and spatial instability occur on resonance lines in the α_r-ω_r-plane, we show in figure 4.6 only one of the temporal growth rates of unstable modes, i.e. the temporal growth rate. The case of resonant wavenumbers on the resonance line is discussed additionally

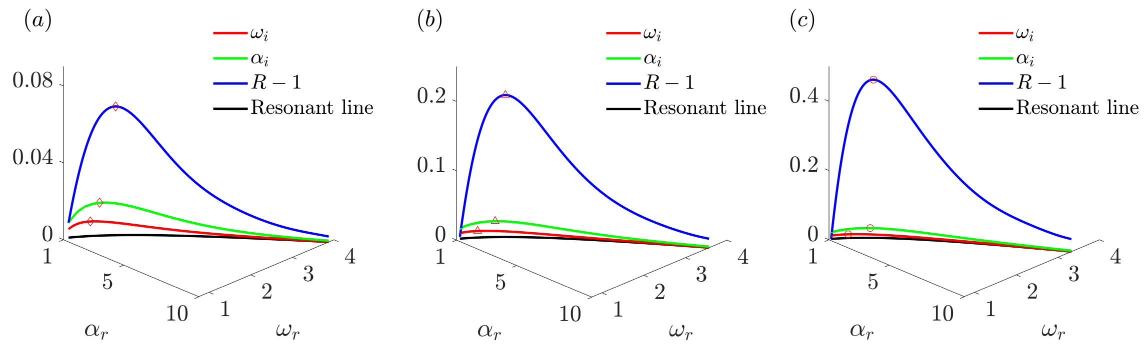

Figure 4.7: Temporal growth rate ω_i, spatial growth rate α_i and over-reflection coefficient R on resonance lines. (a) $M = 4$, (b) $M = 4.5$ and (c) $M = 5$, where maximum values of each curve are marked by ◇, △ and ○, respectively. The black thick lines are resonance lines in the α_r-ω_r-plane, which are given in figure 3.21.

in figure 4.7. With figure 4.6, we will first show that unusual peaks arise on the resonance line in the α_r-ω_r-plane. In other words, resonant over-reflection occurs when the frequency and wavenumber of the acoustic wave are both values on the resonance line.

In figure 4.6(a), we apply this result and show the curves of the growth rate ω_i and the resonant frequency ω_r, i.e. the imaginary and real part of the eigenvalue of temporal unstable modes, of the first temporal unstable modes as functions of the wavenumber α for fixed Mach numbers $M = 4$, $M = 4.5$ and $M = 5$. In fact, these results can be found in figure 3.21 in §3.5. But it is to be noted that figure 3.21 contains the parameter range for the silent zone as shown in figure 4.2. Figure 4.6(a) does not show that part. In order to relate the unstable modes, i.e. the resonant frequencies ω_r and the growth rate ω_i, to the corresponding over-reflection coefficient, we convert ω_r to the incident angle ϕ according to (4.2) in figure 4.6(b). At the same time, we extract the projection to the α-ϕ plane of the maximum curve of the resonant peak, the black thick line, from figure 4.5 and place it in figure 4.6(c). Also, the dashed lines in figure 4.6(b) are projections of the main curves onto the α-ϕ plane. By comparing figure 4.6(b) with figure 4.6(c), we find that the corresponding dashed lines highly coincide and the trend of the peaks are largely synchronised. This means that resonant lines can not only trigger temporal and spatial instability in the stability problems, but it can also cause a rapid increase in over-reflections in acoustic problems, i.e. resonant over-reflections. We therefore conclude that the resonant frequency (resonant wavenumber) of unstable modes triggers the peak of the over-reflection coefficient. This suggests that an unusual over-reflection enhancement occurs when the frequency (wavenumber) of the incident wave is close to the resonant frequency (wavenumber).

Next, we try to find the correlation between the variation of the over-reflection coefficient on the resonance line and the variation of the growth rate of the unstable modes. With figure 4.7, we observe a synchronisation of the growth rate in the stability problem with the over-reflection coefficient more clearly. We can first observe that those marked maximum values are clustered together, although the position of the maximum values on the resonance line does not coincide exactly with each other. In §3.5 we mentioned that the positions on the resonance line where the maxima of ω_i and α_i are located do not coincide either. Secondly, from figure 4.7 we can

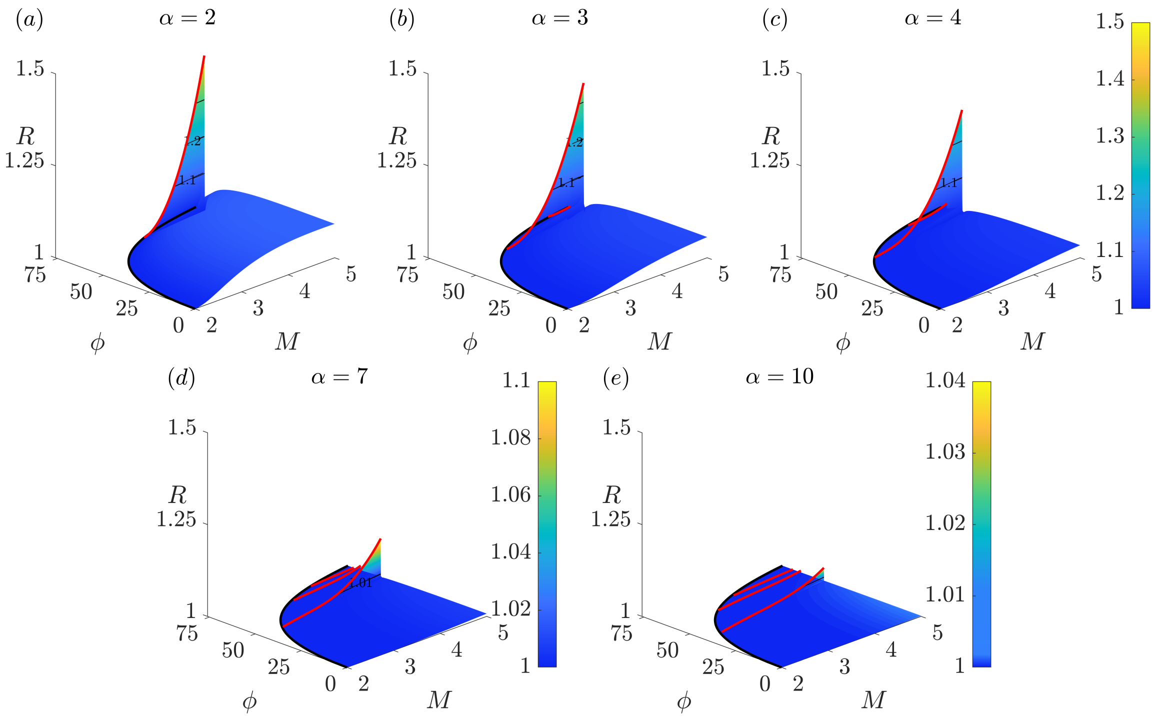

Figure 4.8: Over-reflection coefficient R defined by (4.17) as a function of M and ϕ. (a)-(e) for α in a range from 2 to 10. —— defines the over-reflection border ϕ_{s_2} according to figure 4.2. - - - defines the resonant over-reflection induced by unstable modes.

identify that the rise and fall of these curves are roughly synchronised. From $\alpha \approx 1$ to $\alpha \approx 2$, they all have a relatively rapid rise, then a slow fall.

The above conclusion is first verified by the results in figure 4.4 and explains well the appearance of the local and global peaks. If converted to the frequency, then the incident angles corresponding to peaks are approximately equal to the real part of the resonant frequencies in the first unstable modes. Here we have to further indicate that the local/global maximum value of the over-reflection coefficient, i.e. the red solid line, and the over-reflection coefficient corresponding to the resonant frequency, i.e. the red dashed line, do not exactly coincide, however, they differ by at most two decimal digits of accuracy. This minor difference reaches its maximum around $\alpha \approx 1.7$ and then continuously decreases with increasing α. As $\alpha \geq 2$, the difference becomes almost unrecognizable and therefore is not shown in figure 4.8. This small difference is likely to be caused by the growth rate of the unstable modes, i.e. the imaginary part of the eigenvalue. If we observe figure 3.20(a) and figure 3.21, α_r always has the largest growth rate in $\alpha \approx 1.7$ to $\alpha \approx 2$. In figure 4.4, the deviation between the red dashed line and red solid line also happens to reach a maximum value in $\alpha \approx 1.7$ to $\alpha \approx 2$. In other words, the maximum value of the resonant over-reflection does not occur exactly at the resonant frequencies (on the resonance line). The deviation from the resonant frequencies is affected by the imaginary part of the eigenvalue, i.e. the larger the imaginary part of unstable modes, the more the corresponding frequency of the local/global maximum values deviates from the resonant frequencies (the resonance lines).

Next, we apply our conclusion to higher unstable modes. In the stability analysis as presented in §3, the higher modes gradually appear as the wavenumber increases. However, the first mode always remains the most unstable mode, i.e. the largest ω_i. This feature is also observed in resonant over-reflections induced by unstable modes. Figure 4.8 illustrates the variation of the over-reflection coefficient for wavenumbers in a range from $\alpha = 2$ to $\alpha = 10$ and Mach number from $M = 2$ to $M = 5$. We find that at $\alpha = 3$, the second mode appears and induces a new local peak. At $\alpha = 7$, the third mode appears. Although the third unstable mode is rather weak, it still induces a local peak. At the same time, the first mode always maintains its maximum peak.

With increasing wavenumber α, i.e. figure 4.8(d) and 4.8(e), the effect of resonant frequencies on over-reflections causes a steep increase of $(R-1)$ of tens of times compared to the surrounding $(R-1)$ of non-resonant over-reflections. In regions where non-resonant over-reflections occur, the over-reflection coefficient is very close to one. Once the resonance frequency intervenes, extremely steep peaks appear. Another character that can be obtained by observing figure 4.8 is that the maximum value of the non-resonant over-reflection continues to move away from the ϕ_{s_2} line relative to the over-reflection of small and moderate wavenumbers. In figures 4.8(b)-4.8(e), the over-reflection coefficient even forms a monotonic rise with Mach numbers. Meanwhile, R in non-resonant over-reflection regions is very insensitive to variations in Mach numbers.

More specific data about resonant frequencies of higher unstable modes are given in Appendix A.8.

4.3.3 Eigenfunction

In this section, we will present and discuss the eigenfunction (4.16), which is intuitively separated into the first and the second term. The first term represents the eigenfunction for reflected waves and the second term stands for the eigenfunction for unitary incident waves from the free stream.

Figure 4.9 illustrates three representative patterns. Of these, the first group of figures 4.9(a)-4.9(c) corresponds to the case where there is no critical layer and hence, no over-reflection occurs ($R = 1$). It can be observed that the amplitudes of the incident wave in figure 4.9(a) and the reflected wave in figure 4.9(b) are equal. Meanwhile, we observe from this group of figures the effect of shear layers on the direction of acoustic wave propagation. This effect is caused by the significant velocity gradient close to the wall. In addition, a slight increase in the amplitude of the acoustic wave near the wall is detected.

The second group of figures 4.9(d)-4.9(f) and the third group of figures 4.9(g)-4.9(i) correspond to the case of over-reflections. The third group of figures coincides with the occurrence of the resonant over-reflection, but the over-reflection coefficient only produces local peaks in R. Thus, the over-reflection coefficient for the third group of figures 4.9(g)-4.9(i) is less than the non-resonant over-reflection coefficient for the second group of figures 4.9(d)-4.9(f). Observing the second and third groups, different patterns of over-reflection are detected. In the second group, particularly visible in figure 4.9(f), the amplitude of the acoustic wave near the wall is less than the amplitude of the acoustic wave in the free stream. In contrast, in the third group, i.e. figures 4.9(g)-4.9(i), the amplitude of the acoustic wave near the wall is much greater than the amplitude of the acoustic wave in the free stream.

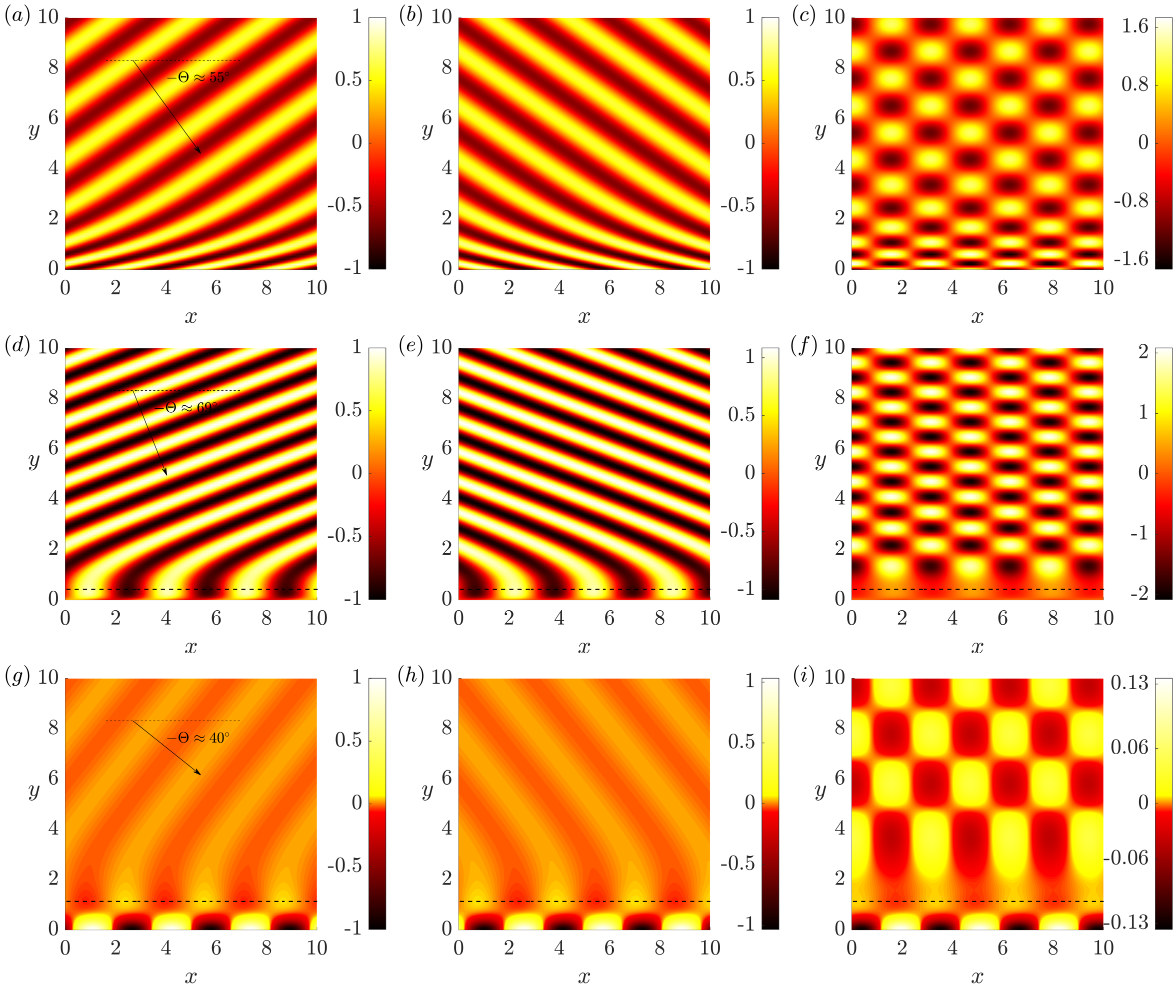

Figure 4.9: Eigenfunctions of incident (the left column), reflected acoustic waves (the middle column) and (4.16) (the right column) for Mach number $M = 4$ and wavenumebr $\alpha = 2$. (a), (b) and (c) for the frequency $\omega = 2.88$ ($\phi \approx 80^\circ$) and $R = 1$. (d), (e) and (f) for the frequency $\omega = 0.58$ ($\phi \approx 30^\circ$) and $R = 1.08$. (g), (h) and (i) for the frequency $\omega = 1.35$ ($\phi \approx 68^\circ$) and $R = 1.04$. The dashed line - - - stands for the location of the critical layer y_c. The angle of of propagation in the free stream Θ according to (4.7) is shown for incident waves.

In addition, from figure 4.9(f) and figure 4.9(i), we find that the amplitude of acoustic waves is relatively small near the critical layer. This suggests that the critical layer has an attenuating effect on acoustic waves, in agreement with the conclusion proposed in Campos & Serrão (1998). It is important to point out that the transformation between the second and third patterns occurs continuously and smoothly with variations of ω, i.e. their difference is not due to the resonant over-reflection. In the vicinity of $\omega = 1.35$, i.e. the region where non-resonant over-reflections occur, e.g. $\omega = 1.32$, the pattern of the eigenfunction remains similar to the third group. Conversely, the pattern of the eigenfunction of the resonant over-reflection always keeps the third one, i.e. the amplitude near the wall is much greater than that in the free stream. This suggests, from another point of view, that resonant over-reflection (instability) is a special case of over-reflections.

In the third group of figures 4.9(g)-4.9(i), we note a pattern of the eigenfunction similar to that

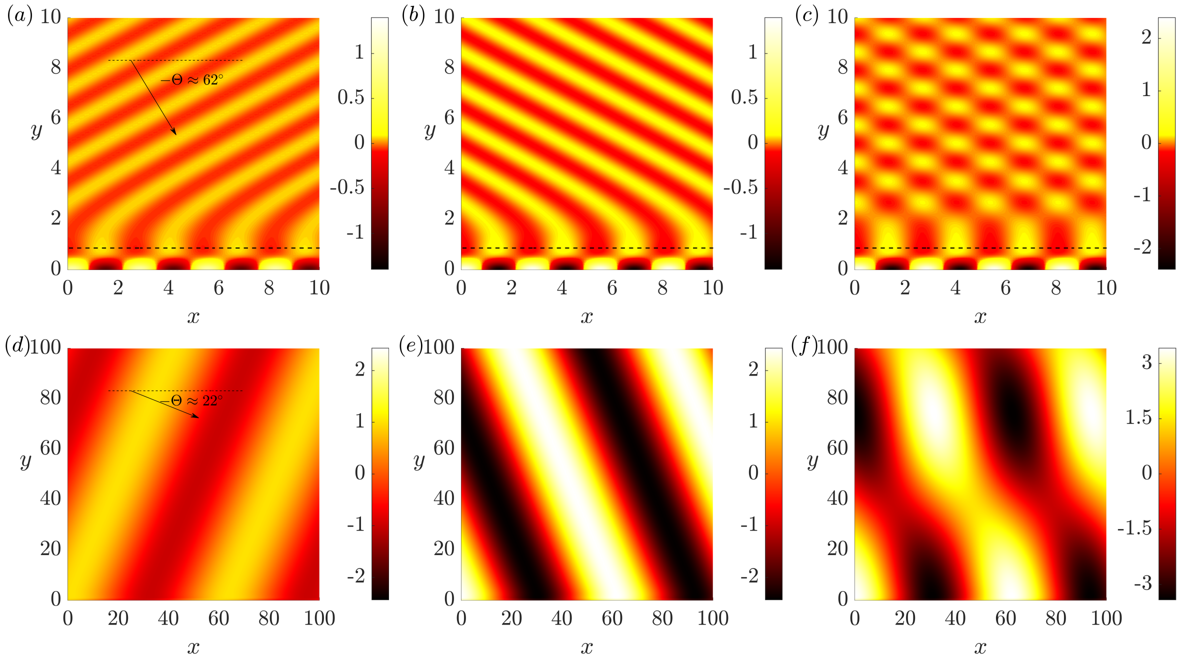

Figure 4.10: Eigenfunctions of incident (the left column), reflected acoustic waves (the middle column) and (4.16) (the right column) for Mach number $M = 5$. (a), (b) and (c) for the wavenumebr $\alpha = 2.33$, the frequency $\omega = 1.34$ ($\phi \approx 70^\circ$) and $R = 1.46$ corresponding to the global maximum value in figure 4.5(c). (d), (e) and (f) for the wavenumebr $\alpha = 0.1$, the frequency $\omega = 0.078$ ($\phi \approx 75^\circ$) and $R = 2.42$. The dashed line - - - stands for the location of the critical layer y_c. The angle of of propagation in the free stream Θ according to (4.7) is shown for incident waves.

of the unstable modes in §3.12. Through figures 4.9(g)-4.9(i) we clearly observe the acoustic waves trapped between the first relative sonic line and the wall (For a detailed definition of the relative sonic line see e.g. Knisely 2018. Here it means that the relative Mach number equals minus one), similar to the surface wave (mode) (see e.g. Rienstra & Hirschberg, 2020). This indicates that complex reflections and refractions occur near the wall. In contrast to the non-resonant over-reflection in figures 4.9(d)-4.9(f), on the one hand, the distance between the first sonic line and the wall is not sufficient to generate strong complex reflections and refractions, and on the other hand, the attenuating effect of the critical layer covers this distance. Thus, as read from the pattern in the second group of figure 4.9, no related instability may exist. As the critical layer moves away from the wall, the surface wave (mode) becomes apparent, where complex reflections and refractions occur near the wall, which is an infallible sign for a related unstable mode at a particular frequency.

The above inference is confirmed by figure 4.10. Similar to the setting in figure 4.9, figure 4.10 shows the eigenfunction of acoustic waves but at the Mach number $M = 5$, where figure 4.10(a)-(c) for $\alpha = 2.2$ is corresponding to the maximum value of the peak in figure 4.5(c). The enhancement of the reflected waves can be clearly observed by the colour gradient. Meanwhile, the amplitudes near the wall are much greater than in the remaining domain, where complex reflection and refraction occurs. This region is necessary to induce instability as was shown in figure 4.9. From 4.10(d)-(f) for $\alpha = 0.1$, we observe similar acoustic wave propagation to the second pattern in figure 4.9. Small wavenumbers α do not allow for complex reflections and refractions that increase the amplitude near the wall. Therefore, despite the large over-reflection coefficient $R = 2.42$, no resonant over-reflections could occur with the near-wall pattern in figure 4.10(d)- 4.10(f), i.e. no unstable modes exist related to these parameters.

4.4 Conclusion

In this chapter, we investigate the over-reflection of acoustic waves in boundary layer flows based on the exact solution to the PBE for an exponential velocity profile. The over-reflection coefficient is shown in detail as a function of problem parameters Mach number M, wavenumber α and incident angle ϕ. Over-reflection exhibits very different patterns depending on small, moderate and large wavenumbers α. In comparison with small α, moderate α lead to smaller over-reflection coefficients, while at the same time a reduced sensitivity to the Mach number is observed. However, an increase in α, leads to the occurrence of resonant over-reflections. The resonant over-reflection coefficient initially induces a local peak, which increases with α and becomes a global maximum value around $\alpha = 1.3$. Thereafter, the peak continues to increase, reaches a maximum value around $\alpha = 2$ before it gradually decreases. Although the resonant over-reflection attenuates as $\alpha > 2$, the resonant over-reflection is more noticeable relative to the non-resonant over-reflection. In other words, for large α, over-reflection is hard to be detected. At specific resonant frequencies, however, resonant over-reflections may be observed.

Both over-reflection and instability reflect the extraction of energy of acoustic waves/modes from shear flows. The phenomenon of over-reflection is obtained from a purely acoustic point of view. The inviscid instability, in contrast, is obtained from a stability point of view. For acoustic waves disturbances that gain energy from shear flows, this will manifest itself in the form of an over-reflection. Stability analysis, from the point of view of boundary conditions, is based on two strict boundary conditions, resulting in an eigenvalue problem. For acoustics, in contrast, only a rigid wall boundary condition is inferred and the relatively weak boundary condition of the presence of acoustic waves at infinity is brought in. Thus, instability can also be seen as a special form of over-reflection. This is evident from the fact that the eigenvalue equation of the temporal and spatial stability problem coincides with the special case in (4.17).

In this chapter, the investigation is carried out mainly from an acoustic point of view. From the results, we confirm that the resonant frequencies generated by unstable modes are not just the first unstable mode but also higher unstable modes lead to an enhancement of the over-reflection, i.e. the resonant over-reflection. This is demonstrated by comparing the eigenvalues of the unstable modes with the unusually high over-reflection coefficients. The eigenvalues obtained in the stability analysis represent the resonant frequencies, which are properties of the boundary layer flow. Around these frequencies, acoustic waves or disturbances can absorb more energy from the base flow. By comparing the eigenfunctions of acoustic waves, we identify the mechanism by which resonant over-reflection occurs. The acoustic waves gain energy from the base flow at the critical layer, accumulate energy in the area close to the wall and form an area with complex reflections and refractions, and subsequently induce the resonant over-reflection. The relevant mechanism is also concluded in the study on stability in §3.3.4.

In the present analysis, we show that the critical layer plays an important role in the energy exchange between waves and shear flows. The critical layer is the most effective location for energy exchange to occur, this is due to the phase velocity of the disturbance or wave being equal to the velocity of the base flow there. Thus the critical layer is the most likely location to have interaction. We further proof that in supersonic boundary layer flows with a critical layer over a rigid wall, the jump of the quasi-invariant at the critical layer always causes an amplification of the reflected waves, i.e. reflected waves extract energy from the base flow. The presence or absence of a critical layer therefore determines whether an over-reflection or instability occurs, which is validated by our results.

We further establish an extended unitarity condition between the over-reflection coefficient and the jump of the quasi-invariant at the critical layer. This condition shows that the over reflection coefficient is closely linked to the acoustic perturbation at the critical layer.

The three patterns in figure 4.9 give insight into practical noise control. Avoiding noise from boundary layer flows requires countermeasures that are based on the physical properties pointed out above. Specifically, measures of the noise reduction are based on the actual location where the noise reduction is required, e.g. civil aviation cabin noise reduction or emission noise reduction. Considering the emission noise reduction, i.e. to the free stream out of the boundary layer, then over-reflection should be avoided. If only the near-wall noise reduction is considered, e.g. noise into the cabin, the second pattern in figure 4.9 has advantages due to a weakened amplitude (loudness) of acoustic waves near the wall. In some specific parametric intervals, however, the third pattern in figure 4.9 would occur. This pattern should be avoided in noise control, as the amplitude (loudness) of acoustic waves is amplified both near the wall and in the free stream, and may induce instability.

To achieve this, one possible way is to control the wavenumber in terms of the results in §4.3.1 and §4.3.2 and keep the frequency smaller than certain thresholds according to (4.2) and figure 4.2. This could be achieved by a wave filter, which changes the wavelength and the frequency. A device that exactly achieves these effects has been applied in the inlet and outlet of the jet engine (Henderson, 2010).

Another feasible way to control the noise is to change the wall condition, i.e. the acoustic wall impedance. The investigation of the propagation of acoustic waves in boundary layer flows with acoustic impedance conditions is a popular topic in recent years, which stems from an interest in noise regulation by using acoustic liners in aircraft engines. Representative work includes Brambley (2011b) and Rienstra & Darau (2011), who proposed modified Myers conditions with a finite boundary layer thickness, thus avoiding the ill-posed problem in the time domain. Based on these, Gabard (2013) gave the reflection coefficient of acoustic waves in half-space flows in terms of the Myers (1980) condition and the modified Myers conditions and investigates the effect of acoustic impedance and boundary layer thickness on it. In addition, he gave a comparison of the effect of sound absorption between results using the Myers condition and other impedance conditions, one of which is derived based on the exact solution to the PBE for a special case, i.e. a linear velocity profile. In our context, applying the acoustic impedance to replace the current rigid-wall boundary condition will result in a different equation of the reflection coefficient. In this way, the reflection coefficient can be regulated by varying the acoustic impedance to find the optimal acoustic impedance to suppress or even hinder over-reflection. A related work in a preliminary stage was done by Albert (2022).

In the next chapter, we will verify the phenomena of over-reflection and the resonant over-reflection of acoustic waves in exponential boundary layer flows by means of direct numerical simulations (DNS). One of the conceivable difficulties lies in the construction of acoustic waves close to the real situation. At the same time, the resonant over-reflections that we find only occur in a very narrow parameter interval, i.e. near the resonance lines, and therefore this requires a high accuracy on the wavelength and frequency of the acoustic waves as well as the simulations.

5 Numerical simulation of acoustic wave propagation in a boundary layer flow

5.1 State of the art

Shear flows are a widespread type of flow model. A velocity gradient causes this type of flow to be different from a normal uniform flow. Therefore, it is well imaginable that wave propagation in a shear flow would be very different. A better-known example is the effect of the Kelvin-Helmholtz instability present in shear flows on internal gravity waves in a linear (Lindzen & Rosenthal, 1976) and a non-linear way (Fritts, 1979). We recommend the book by Bühler (2014) for a deeper insight into the propagation of (acoustic) waves in shear flows.

Acoustics in shear flows is an essential topic in engineering applications, e.g. the propagation of sound in inlets or outlets of jet engines, in which shear flows lead to fundamentally new phenomena (Rienstra & Hirschberg, 2020). In shear flows, the propagation of acoustic waves dramatically differs from those in uniform flows due to interactions between acoustic waves and shear layers (Delfs, 2016). In addition to this, the instability present in shear flows has a non-negligible effect on acoustic waves (Fedorov & Tumin, 2003).

A remarkable phenomenon that could arise in shear flows is over-reflection, which means that the reflected wave is stronger than the incident wave. Ribner (1957) and Miles (1957) were simultaneously the first to investigate the amplification effect of acoustic waves in flows. In their studies of plane acoustic waves, which impinge onto a moving medium separated by a vortex sheet, over-reflection was possible if the moving medium was at high enough speeds. Blumen et al. (1975) explained the amplification of acoustic waves during their reflection as a resonant effect. In their study, they increased the vortex sheet smoothly to some finite width, in which a thin critical layer appears inside the vortex sheet, and thereby speculated that the energy of the acoustic wave increases from this layer.

Much of the research on the reflection of acoustic waves in the subsonic regime focused on a particular model of shear flows, the boundary layer flow. The study of the boundary layer flow is caused by an urgent need to control noise through the acoustic wall impedance. In Brand & Nagel (1982), the reflection coefficient of a boundary layer flow constructed by a uniform flow together with a linear velocity profile was studied in limiting parameter cases. In Gabard (2013) and Saverna et al. (2019) they derived the reflection coefficient for subsonic boundary layer flows using the modified Myers condition (Rienstra & Darau 2011; Brambley 2011b; Brambley et al. 2012) and compared them with results derived by using the exact solution of the linear velocity profile. It was verified in these studies that no over-reflection appears. This is mainly because acoustic waves always travel faster than the flow velocity within subsonic flows, making it difficult for them to extract energy from the flow. In addition to this, there are no over-reflections that are triggered or amplified by unstable modes. This is due to the fact that in a subsonic boundary layer flow, the T-S mode (see e.g. §3.1) dominates the instability, which cannot be correlated with acoustic waves in the same way as acoustic modes. In Wu (2014), he gave a further explanation that the characteristic wavelength of the T-S mode is normally much smaller than that of acoustic waves, which means that the matching of the wavenumbers is not satisfied unless a scale-conversion mechanism, e.g. surface roughness, is present. For the supersonic case, the picture becomes quite different. Similar over-reflection phenomena were found in Campos & Kobayashi (2013) in studying a hyperbolic-tangent boundary layer flow, in Zhang et al. (2022) in studying an exponential boundary layer flow, and in Hernández & Wu (2019) and Liu et al. (2020) in studying the receptivity of a flat-plate boundary layer to impinging acoustic waves.

Another important topic in boundary layer flows that largely influences the behaviour of acoustic waves is instability. Mack (1965) was the pioneer of the stability problem for compressible boundary layers. He discovered the higher-order modes that can dominate instability in the supersonic condition. In recent studies, Chuvakhov & Fedorov (2016) carried out direct numerical simulations (DNS) to study the radiation effects arising from the instability of supersonic boundary layer flows at the Mach number $M = 6$. Outwardly radiative acoustic waves were observed through actuator-generated wave trains and wave packets propagating over a flat plate. In addition, the radiative acoustic waves caused the elongation and modulation of the wave packet. Knisely & Zhong (2019a, 2019b) verified the similar phenomenon of sound radiation by the instability of hypersonic blunt cone boundary layers through DNS. These acoustic wave structures of radiation caused by unstable acoustic modes were also observed in experiments on a hypersonic boundary layer of a flared cone (Zhang et al., 2013; Zhu et al., 2020).

In recent work in Zhang et al. (2022), the authors focused on the propagation of acoustic waves in two-dimensional (2-D) compressible boundary layer flows and the resulting over-reflection phenomena. At the theoretical level, their study was developed based on how acoustic waves extract their energy from the base flow. According to linear theory, there is a critical layer in boundary layer flows where the phase velocity of the acoustic wave is equal to the base flow velocity, and the acoustic wave indeed acquires energy from the shear layers and is thereby over-reflected. In addition to this, a stronger over-reflection occurs when the acoustic wave frequency approaches the resonant frequency of the unstable modes, called resonant over-reflection. The interval of resonant frequencies in which the resonant over-reflection occurs was a very narrow parameter range and was therefore difficult to detect. A related work about unstable modes and instability of exponential boundary layer flows can be found in Zhang & Oberlack (2021). Based on these studies from linear theory, we conduct DNS using the in-house BoSSS code (Kummer et al., 2009) to validate further the over-reflection of acoustic waves in an exponential boundary layer flow in a supersonic regime. For this, we give incident acoustic waves in the form of a wave packet in the free stream that is more closely matching the reality. These waves propagate into an inviscid compressible exponential boundary layer flow and are eventually reflected by the wall. Through DNS, we record the amplitude of reflected waves and compare it with that of the incident wave. Finally, it is verified that over-reflection occurs, and there is a highly narrow frequency interval that allows the over-reflection to become strong, i.e. corresponding to a resonant over-reflection.

This chapter is structured as follows. In §5.2, we introduce the BoSSS framework based on the DG method. In §5.3, we give the numerical setup, including the computation domain, initial condition, and boundary conditions. A model of the superimposed wave packet is constructed for the present study. In §5.4, we show the simulation results for the Mach number $M = 5$, the wavenumber $\alpha = 4$, and different frequencies. These results show good agreement with theoretical results in §4. The ver-reflection of acoustic waves exists, and the resonant over-reflection is observed when the frequency is close to the resonant frequency. In §5.5, we state the main conclusions of this chapter and discuss some limitations.

5.2 The generic discontinuous Galerkin software framework BoSSS

As the present work depends highly on the accurate numerical simulation of acoustic phenomena, the need for a valid code is obvious. In particular, ensuring low numerical dissipation and small dispersion errors is the key to such high-accuracy simulations. As we mentioned in §1.2.2, even small orders of disturbances can significantly influence acoustic waves. For this reason, higher-order methods, such as DG methods, are often favoured in the acoustic community. Compared with traditional numerical methods, such as the Finite Difference Method (FDM), the Finite Volume Method (FVM), and the Finite Element Method (FEM), the advantages of the high-order DG method in acoustics are manifold. It avoids problems associated with the FDM, e.g. spurious waves appearing in the numerical solutions, which might contaminate the physical results in spite of being numerical in nature (Trefethen 1982; Colonius & Lele 2004; Tam 2004). Compared to the FVM, which can accomplish a higher-order discretisation only by increasing the stencil, the DG method achieves an arbitrarily high-order discretisation by representing the solution in cell-local polynomials (De Grazia et al., 2014). In addition, it allows for hanging nodes. However, FVM is sensitive to the meshes produced in this way. The advantage of the DG method concerning the Finite Element Method (FEM) is that it is not limited to a global continuous basis function but is locally conservative, i.e. numerical errors do not violate conservation laws. Both high accuracy and low costs associated with the DG method are advantageous in the field of aeroacoustics (Tam, 2004).

Within the past few years, the BoSSS (Bounded Support Spectral Solver) code has been developed and refined by the group at the Chair of Fluid Dynamics (FDY), TU Darmstadt. It is based on the DG method with arbitrarily small and pre-definable discretisation error. In fact, the BoSSS code is a library designed in a couple of layers rather than a monolithic CFD code. This library was coded in *C#* and is thus based on the *.NET/Mono* framework (Kummer et al., 2020). To date, BoSSS is developed to be able to solve arbitrary PDE systems, including elliptic, parabolic, hyperbolic and mixed type problems. At this point, solvers for several related issues have been implemented in BoSSS. For the unsteady incompressible Navier-Stokes equations, two variants of the so-called projection method was implemented (Kummer 2011; Emamy et al. 2017). Furthermore, the well-known SIMPLE algorithm was adapted to DG for the case of steady and unsteady, incompressible flows (Klein et al., 2013; Klein et al., 2015).

In the compressible flow regime, a solver for both inviscid and viscid compressible flows based on the HLLC Riemann solver (Toro, 2013) was implemented and tested by Müller (2011). Based on BoSSS, the scheme relies on the HLLC Riemann solver, which was improved to provide excellent approximations of the exact solution to the Riemann problem with reasonable effort. In addition, it is designed to support generic time-stepping schemes, e.g. explicit Runge-Kutta (RK) methods up to fourth order, and generic boundary conditions, which is particularly useful for the implementation of the required non-reflecting boundary conditions (NRBCs)

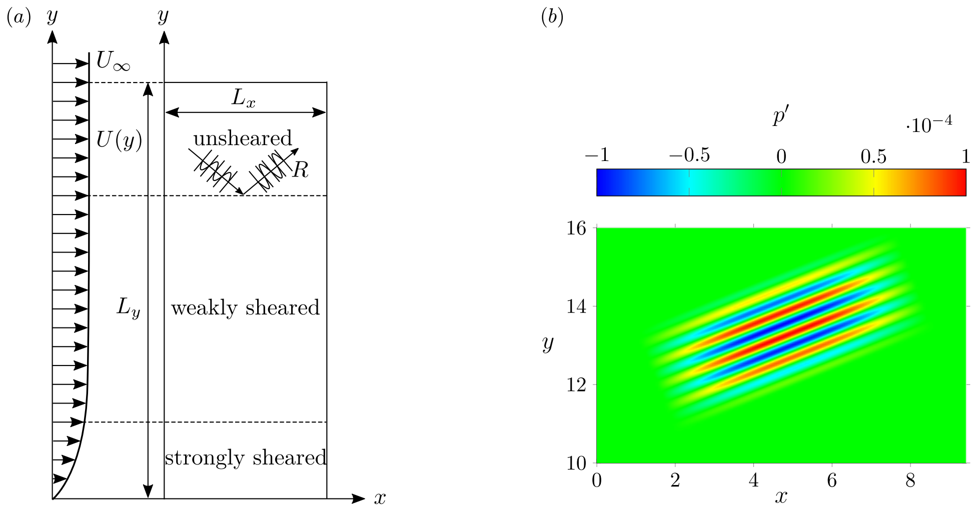

Figure 5.1: (a) Sketch of a two-dimensional (2-D) exponential boundary layer flow and the computational domain, where L_x and L_y are the size of the computational box in the x- and y-direction. Dashed lines divide the field into three sub-regions, i.e. strongly sheared, weakly sheared and unsheared regions. An incident acoustic wave from the free stream gives rise to a reflected wave, characterised by the reflection coefficient R. (b) Wave packet superimposed in the free stream. The colour scale varies from blue to red with an increasing value of p'. The wave packet is constructed by the exact solution (4.16) and the described model in §5.3.3. The centre of the wave packet contains a part of the plane acoustic waves with constant wavelength and amplitude, which has a wavenumber $\alpha = 4$ and a frequency $\omega = 1.85$. In the part of the wave packet where the amplitude decreases, the acoustic wave described by the exact solution is distorted.

(Müller et al., 2017). To date, BoSSS contains a compressible Navier-Stokes (CNS) solver, which has a robust and efficient high-order numerical scheme for the simulation based on a discontinuous Galerkin immersed boundary method (DG IBM) (Krämer-Eis, 2017) and an extended discontinuous Galerkin (XDG) method (Geisenhofer, 2021). Based on this, we apply the CNS solver to compute the compressible Euler Equations in the present work, i.e. the inviscid case.

5.3 Numerical setup

In this section, we describe the setup of the numerical simulation. Firstly, the computational domain, including a flow configuration, is illustrated. Secondly, the boundary conditions, as well as the initial conditions, are introduced. Meanwhile, the model of wave packets that mimics plane waves in linear theory is constructed. Finally, the numerical discretisation is presented.

5.3.1 Computation domain

In figure 5.1(a), we present a sketch of the simulated two-dimensional (2-D) boundary layer flow (left) and the computational domain (right). The base flow is defined by $(p, u, v, \rho)^T =$

$(p_0, u_0, 0, \rho_0)^T$, where the base pressure p_0 and density ρ_0 are constant. The exponential boundary layer flow is mimicked by

$$u_0(y) = U_\infty \left(1 - e^{-\frac{y}{\delta}}\right), \tag{5.1}$$

an exponential function, i.e. (2.28a).

To re-produce the over-reflection of acoustic waves in inviscid compressible boundary layer flows, we perform the DNS using the full non-linear Euler equations for an ideal gas ($\gamma = 1.4$), which are more accurate than the linearised Euler equations (LEEs). The reference quantities used for the non-dimensional Euler equations are p_0, U_∞, ρ_0, and δ. For simplicity, we choose $p_0 = 1$ and $\rho_0 = 1$, which according to (2.21) leads to the constant speed of sound $c_0 = \sqrt{\gamma}$. The Mach number is thereby defined as

$$M = \frac{U_\infty}{c_0}, \tag{5.2}$$

which indicates the velocity of the flow in the free stream $U_\infty = Mc_0$.

The complete base flow is contained in a 2-D computational box, whose size is denoted by L_x and L_y in horizontal (x-) and vertical (y-) directions. The coordinate axes are non-dimensionalised with the shear layer thickness by setting $\delta = 1$ for simplicity. The length of L_x for the computational box is chosen based on the size of the inserted wave packet in the x-direction, i.e. chosen large enough to accommodate at least one complete wave packet. In the vertical direction, L_y of the computational box is divided into three regions, where the region closest to the wall contains the strongly sheared flows, i.e. the large velocity gradient. The weakly sheared region is in the middle, and the top region is regarded as the free stream without shear. The distinction between regions with and without shear is to exclude the influence of shear effects on acoustic waves. The difference between strongly and weakly sheared regions is made for a computational purpose to apply a more refined grid in the strongly sheared region near the wall, where the large velocity gradient may cause significant numerical errors and even divergence. In the numerical simulations, we insert the complete incident wave packet in the unsheared region to avoid the shear effects on the propagation of the acoustic waves.

In the present work, we define the strongly sheared region as $y \in [0, 2)$ and apply a finer grid there. In the region $y \geq 10$, we consider that the effect of shear is already minimal and can be approximated as an unsheared region, i.e. free stream. In the region $y \in [2, 10)$, the grid is medium-sized.

5.3.2 Boundary conditions

Periodic boundary conditions are applied in the x-direction. We choose $L_x = n\lambda$, $n \in \mathbb{Z}$ and $n \geq 4$, rather than only one wavelength such that the horizontal extent is large enough to minimise aliasing phenomena due to periodicity. The use of periodic conditions along the base flow direction offers an advantage in computational costs. Further, this avoids the uncertainty associated with the inflow and outflow boundary conditions. In particular, within the boundary layer, as the velocity decreases close to the wall, there always exists a location where the velocity of the flow is exactly equal to the speed of sound, thus dividing the computational domain into two sub-regions i.e. subsonic and supersonic regions. The use of periodic boundary conditions avoids the necessity to set separate supersonic and subsonic boundary conditions for the two sub-regions. Note that in the present work, we are modelling a boundary layer flow where the exponential profile remains unchanged, rather than a flat-plate type boundary layer that develops gradually with distance. A periodic boundary condition is therefore feasible. The bottom of the computational domain is set as an adiabatic slip wall, which enforces a zero normal velocity and non-zero horizontal velocity in the current context of the Euler equations. The top of the computational domain is a supersonic outlet, where no considerable reflections from the outlet are observed because, in current work, the flow is always supersonic. These two boundary conditions have already been inserted in BoSSS and can be selected to use. For details see e.g. Krämer-Eis (2017) and Geisenhofer (2021).

5.3.3 Initial condition and wave packet

At $t=0$, we superimpose a wave packet in the form of small perturbations in the unsheared region of figure 5.1(a), similar to the superposition in (2.7). We construct such incident waves through the exact solution (4.16) to the PBE (2.31) in linear theory and the normal-mode ansatz (2.11). The eigenfunction of the density perturbation reads

$$\rho'(x,y,t) = e^{iM\alpha e^{-y}-\sqrt{\theta}y}\widetilde{H\mathrm{c}}\left(;\frac{\alpha e^{-y}}{\alpha-\omega}\right)e^{i(\alpha x-\omega t)}, \tag{5.3}$$

where the paremeters of the Hc function is given in (2.38). Considering (2.32) and (2.33), the small perturbation of velocities reads

$$\begin{aligned} u'(x,y,t) = e^{iM\alpha e^{-y}-\sqrt{\theta}y}\Bigg[&\widetilde{H\mathrm{c}}\left(;\frac{\alpha e^{-y}}{\alpha-\omega}\right)\frac{\alpha\left(\omega-\alpha+\alpha e^{-y}\right)+iM\alpha e^{-2y}+\sqrt{\theta}e^{-y}}{M^2\left(\omega-\alpha+\alpha e^{-y}\right)^2} \\ &+\widetilde{H\mathrm{c}}'\left(;\frac{\alpha e^{-y}}{\alpha-\omega}\right)\frac{\alpha e^{-2y}}{\left(\alpha-\omega\right)M^2\left(\omega-\alpha+\alpha e^{-y}\right)^2}\Bigg]e^{i(\alpha x-\omega t)}, \end{aligned} \tag{5.4}$$

$$\begin{aligned} v'(x,y,t) = e^{iM\alpha e^{-y}-\sqrt{\theta}y}&\left[\widetilde{H\mathrm{c}}\left(;\frac{\alpha e^{-y}}{\alpha-\omega}\right)\left(-iM\alpha e^{-2y}-\sqrt{\theta}e^{-y}\right)-\widetilde{H\mathrm{c}}'\left(;\frac{\alpha e^{-y}}{\alpha-\omega}\right)\frac{\alpha e^{-y}}{\alpha-\omega}\right]\times \\ &\times\frac{e^{i(\alpha x-\omega t)}}{iM^2\left(\omega-\alpha+\alpha e^{-y}\right)}. \end{aligned} \tag{5.5}$$

Applying the constant speed of sound c_0 and the relation between the density and pressure perturbation (2.27), the pressure perturbation reads

$$p'(x,y,t) = \gamma\rho'. \tag{5.6}$$

It is notable that (5.3)-(5.6) are non-dimensional forms, in which the time t is non-dimensionlised by U_∞ and δ. Since the free flow velocity is newly defined by $U_\infty = Mc_0$, in order to keep the parameter settings in the simulation consistent with the results in §4, we need to rescale t with multiplying a factor Mc_0 in the simulation.

To keep the perturbation small enough, we further introduce a factor ϵ and multiply (5.3) with this factor. As a result, the incident acoustic wave has an amplitude of the order of ϵ in the far-field. The factor $\epsilon = 10^{-4}$ is chosen in the current work to avoid non-linear effects. Smaller

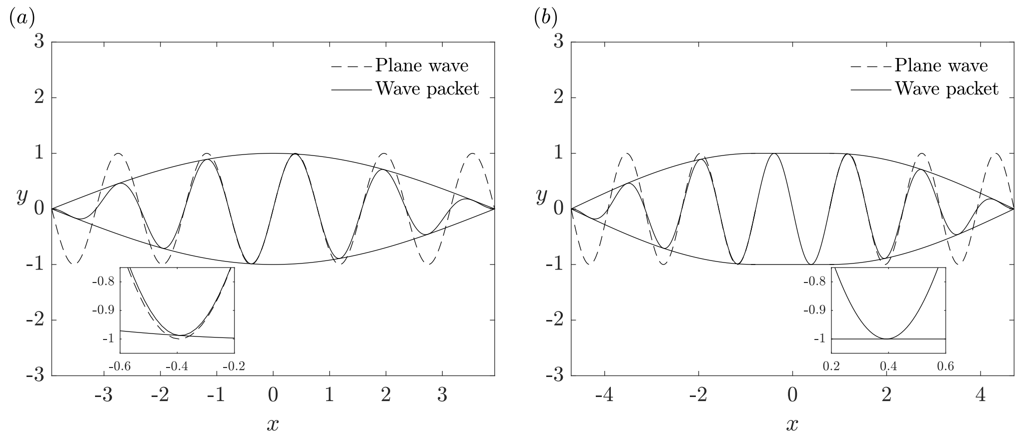

Figure 5.2: Wave packet models (a) with distorted wavelengths (b) with implemented segment including plane waves with constant wavelength and amplitude.

ϵ is validated by test computations that it does not produce significantly better results but requires much higher costs and hence is not used. Note that the superimposed wave packet propagates simultaneously in both positive and negative y-axis directions in the simulation. Here we only consider the wave packet propagating in the negative y-direction as incident waves. The upward (positive y-direction) and downward (negative y-direction) propagating waves cause a separation of the wave packet so that the maximum amplitude of the incident wave is not equal to the initial value set by ϵ. This requires a record of the amplitude of the incident wave amplitude, which is described later through figure 5.6 and related descriptions.

For the incident wave to be inserted smoothly into the initial condition, we apply a trigonometric cos-function multiplied by the wave function (5.3) and choose a length of $n\lambda$, $n \in \mathbb{Z}$ with $n \geq 2$ as the length of the wave packet. In this way, a wave packet can be created in the free stream, containing several wavelets, as shown in figure 5.2(a) as an example for 1-D waves. This wave packet model is close to the reality of acoustic wave propagation but gives rise to new problems. Firstly, the trigonometric function that describes the envelope of the wave packet distorts the exact solution (5.3), e.g. the wavelength in the x- and y-direction in the exact solution is changed due to the multiplied trigonometric function of the wave packet as shown in 5.2(a). Since the reflection coefficient is very sensitive to the wavenumber α (Zhang et al., 2022), a slight variation in the wavelength in the x-direction leads to unpredictable changes in the reflection coefficient. Secondly, due to the geometric dispersion relation of the acoustic waves, a wave packet generated in this way will disperse in the free stream. The dispersion relation of an acoustic wave in the free stream can be found in (4.6), which describes the effect of changes in the wavenumber in the x-direction on the wavenumber in the y-direction. In other words, inconsistencies in wavelengths on the wave packet shown in 5.2(a) can lead to a dispersion of the wave packet[6]. To avoid and minimise the model problems described above, we apply the present work's wave packet model depicted in figure 5.2(b). Based on the superimposed wave packet in figure 5.2(a), we further apply a segmentation function to insert a straight line of factor one into a wave packet described by the trigonometric function. This is to ensure that the centre part of the wave packet is close to plane acoustic waves with constant wavelength and amplitude. In this way, the eigenfunction of the incident wave (5.3)

[6] Dispersion of a wave packet is a phenomenon where the shape of the wave packet becomes flattened due to the different phase velocities of the individual wavelets in the wave packet.

obtained in linear theory is implanted into the wave packet model without distortion, thereby avoiding errors induced by inaccurate wavelength on both sides of the wave packet. Figure 5.2(b) illustrates such a wave packet with a part consisting of plane waves with a constant amplitude. In comparison to the wave packet model in figure 5.2(a), where a deviation of the wavelength in the wave packet is always present, the centre part of the wave packet in figure 5.2(b) contains waves with a constant wavelength and amplitude. In this way, it minimises the influence caused by dispersion because a plane wave with constant wavelength does not give rise to the dispersion.

Figure 5.1(b) shows an example of an inserted wave packet in the free stream. The colour scale changes from blue to red to indicate a change in pressure perturbation from low to high. The amplitude at the centre of the wave packet is the area where the maximum amplitude of the acoustic wave is tracked and recorded. We regard the acoustic wave as a plane wave with constant wavelength and amplitude in the centre region. It should be emphasised that the length of the central section is chosen to be at least half a wavelength, i.e. to ensure that the maximum and minimum amplitudes described by the exact solution are included. The rest of the green domain is free of any perturbations.

5.3.4 Numerical discretisation

Numerical simulations of the proposed acoustic wave propagation are challenging because the amplitude of the acoustic wave perturbation is extremely small, and the acoustic wave propagation requires to be simulated for a long enough time to obtain the complete reflected waves in the free stream. For this, we need to adopt a numerical discretisation scheme that guarantees small dissipation and dispersion errors and ensures that the simulation results are not affected by the numerical discretisation. We, therefore, solve the full (non-linear) Euler equations in a conservative form using a higher-order Runge-Kutta DG discretisation within the BoSSS framework.

To avoid numerical errors when cells are skewed (Schäfer, 2013), our numerical discretisation only uses equidistant quadratic cells, and 6-th order polynomials are applied. In the region far away from the wall, i.e. the unsheared region, we apply a simple equidistant quadratic cells grid. As the shear effect increases approaching the wall, the accuracy of the grid is increased by adding more equidistant quadratic cells. In the region close to the wall, i.e. the strongly sheared region, where the grid needs to be resolved more accurately, we, therefore, use a finer grid. Transitions between different regions of the grid are made with hanging nodes. The length of the cell in the strongly sheared region is chosen to be $\Delta x = \Delta y = 1.5 \times 10^{-2}$, and therefore, the number of grids can be calculated with $N_x \times N_y = L_x/\Delta x \times L_y/\Delta y$. The cell lengths for the weakly shear region and the unsheared region are $\Delta x = \Delta y = 3 \times 10^{-2}$ and $\Delta x = \Delta y = 6 \times 10^{-2}$, respectively.

In time, we choose a standard third-order Runge-Kutta scheme. To fulfil the Courant-Friedrichs-Lewy (CFL) stability criterion of the fully discrete Runge-Kutta DG discretisation, a time step size of $\Delta t = 2 \times 10^{-5}$ is required, and the CFL number is set to 0.5. It is verified that the numerical solution does not change when further decreasing the time step size.

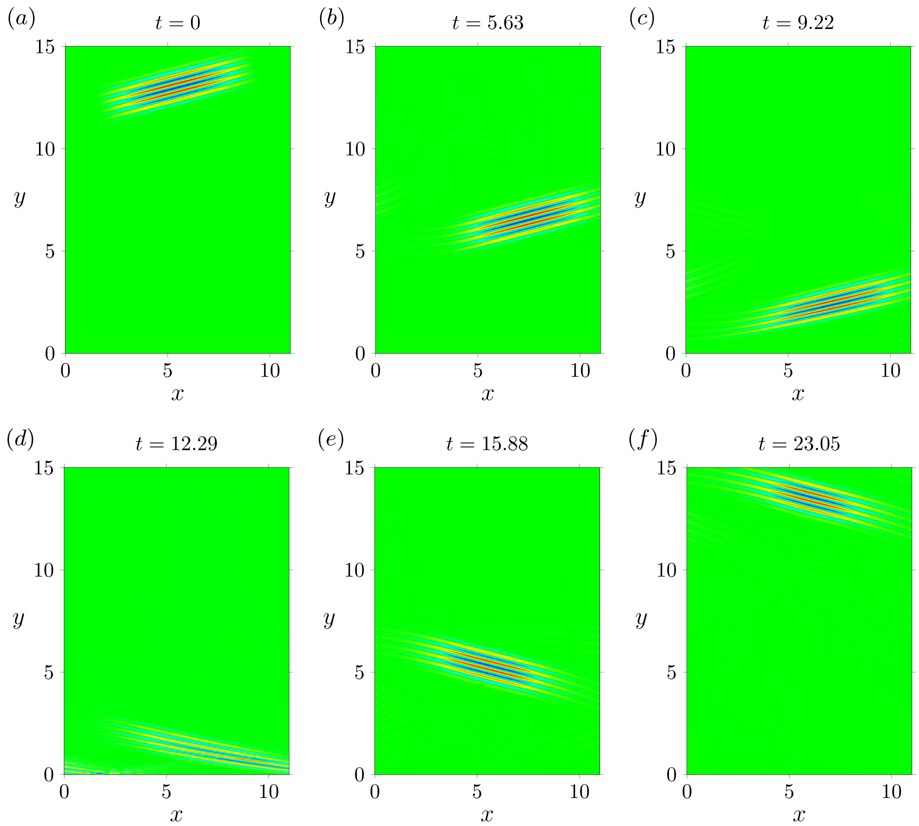

Figure 5.3: DNS results of the acoustic waves for the Mach number $M = 5$, the wavenumber $\alpha = 4$, and the frequency $\omega = 0.8$. At non-dimensional time (a) $t = 0$, (b) $t = 5.63$, (c) $t = 9.22$, (d) $t = 12.29$, (e) $t = 15.88$, (f) $t = 23.05$. The color scale varies from blue to red with increasing p' referring to figure 5.1(b).

5.4 Simulation results

This section shows DNS results of the propagation of wave packets containing plane waves with constant wavelength and amplitude in exponential boundary layer flows. These results consist of seven different sets of frequencies ω for the fixed Mach number $M = 5$ and the wavenumber $\alpha = 4$. The results for the reflection coefficients corresponding to the selected parameters are representative, including the over-reflection and the resonant over-reflection.

Figure 5.3 shows the simulation results of the acoustic waves for the Mach number $M = 5$, the wavenumber $\alpha = 4$, and the frequency $\omega = 0.8$. Figures 5.3(a)-5.3(c) present the incidence of the acoustic waves into the boundary layer. Figures 5.3(d)-5.3(f) depict the process of acoustic waves leaving the boundary layer. It can be observed that as the acoustic wave approaches the wall, the wave packet undergoes a deformation, which is mainly caused by the continuous variation of the boundary layer flow velocity in the y-direction. This deformation is essentially symmetrical for the case depicted in figure 5.3, i.e. the wave packet regains its original shape after leaving the boundary layer. The reflection coefficient of the simulation is calculated to be $R \approx 1.031$, which indicates that the acoustic wave extracts little energy from the shear flow. Figure 5.4 shows the temporal evolution of the acoustic waves at the resonant frequency $\omega = 1.85$. A comparison of figure 5.4(a) with figure 5.4(f) reveals that the shape of the

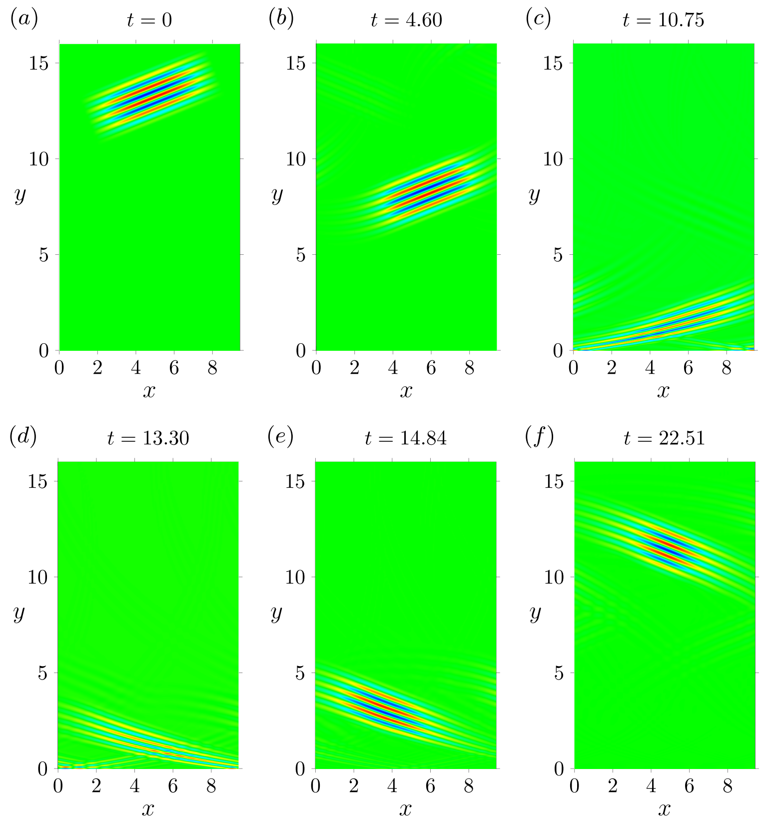

Figure 5.4: DNS results of the acoustic waves for the Mach number $M = 5$, the wavenumber $\alpha = 4$ and the frequency $\omega = 1.85$. At non-dimensional time (a) $t = 0$, (b) $t = 4.60$, (c) $t = 10.75$, (d) $t = 13.30$, (e) $t = 14.84$, (f) $t = 22.51$. The color scale varies from blue to red with increasing p' referring to figure 5.1(b).

wave packet is changed. The wave packet contracts towards the central part, which suggests more increases in the amplitude. The reflection coefficient finally obtained by calculation is $R \approx 1.145$, which indicates that the acoustic waves draw more energy from the boundary layer flow.

It is difficult to distinguish the increase in reflected wave amplitude by the change in colour in figure 5.3 and figure 5.4. Therefore, an accurate record of the maximum value of the wave packet amplitude in the computational domain is required to provide the results of the over-reflection. Figure 5.5 shows the results of the maximum value of the wave amplitude $|p'|_{max}$ as a function of non-dimensional time for different frequencies, 5.5(a) for $\omega = 0.8,\ 1.0,\ 1.5$ and 5.5(b) for $\omega = 1.82,\ 1.85,\ 2.0$. Using the wave packet model described in §5.3.3, we keep that the maximum amplitude occurs at the centre of the wave packet. The centre part always contains a complete acoustic wave with constant wavelength and amplitude.

We set up the simulation to record the maximum amplitude value for the domain $y \leq 10$. Thus, as the wave packet gradually moves from a position where $y > 10$ to $y \leq 10$, the maximum value of the amplitude gradually rises and remains constant as the central part enters. As the shear effect increases, the wave packet begins to scatter and deform, creating a peak at the wall due to the overlap of the incident and reflected waves. Eventually, as the acoustic wave travels away from the wall, it returns to the level of the amplitude of the incident wave.

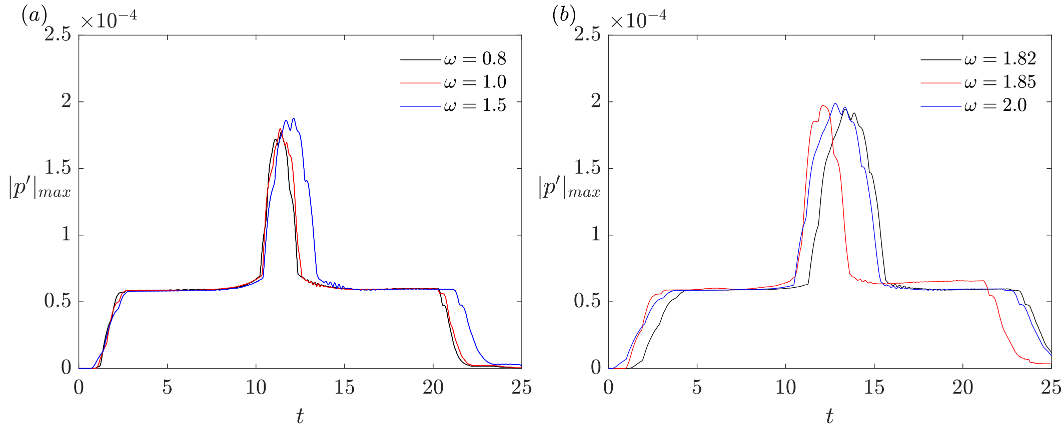

Figure 5.5: Simulation results for the maximum value $|p'|_{max}$ for different frequencies (a) $\omega = 0.8,\ 1.0,\ 1.5$ and (b) $\omega = 1.82,\ 1.85,\ 2.0$.

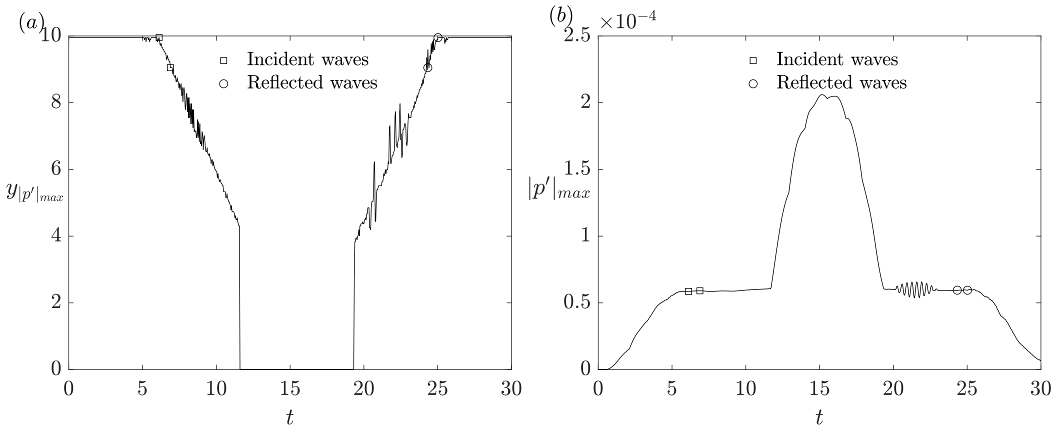

Figure 5.6: Simulation results for (a) locations of the maximum value $|p'|_{max}$ and (b) the maximum value $|p'|_{max}$ for $\omega = 2.4$. Square □ marks the start and end sampling points for the incident wave amplitude. Circle ○ marks the start and end sampling points for the reflected wave amplitude.

Of particular note is the significant increase in the amplitude of the reflected waves at the resonant frequency $\omega = 1.85$. In the stability theory, the temporal instability of the boundary layer manifests itself as an acoustic wave radiating outwards. For the resonant over-reflection shown in figure 5.4 and figure 5.5(b), a significant increase in the amplitude of the reflected waves is associated with this instability mechanism.

Next, we take figure 5.6 as an example to illustrate how the reflection coefficient in the DNS results is calculated. Figure 5.6(a) shows the y-location in the domain $y \in [0, 10]$ of the maximum amplitude for the Mach number $M = 5$, the wavenumber $\alpha = 4$, and the frequency $\omega = 2.4$ as a function of non-dimensional time t. Figure 5.6(b) is the corresponding maximum amplitude in the same domain as a function of t. The maximum value starts to be recorded when the acoustic wave enters the domain $y \in [0, 10]$. This value remains at $y_{|p'|_{max}} = 10$ until the centre part of the acoustic wave passes through $y = 10$, after which $y_{|p'|_{max}}$ starts to decrease. After being completely reflected, the maximum value of the amplitude $|p'|_{max}$ at the centre of the wave packet moves in the positive y-direction and finally passes through the

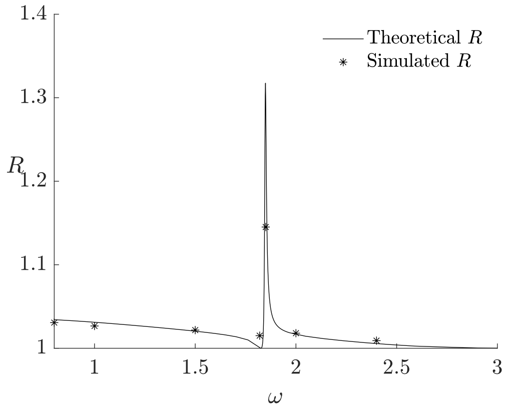

Figure 5.7: Comparison between theoretical reflection coefficients and simulated results for Mach number $M = 5$ and wavenumber $\alpha = 4$ and different frequencies $\omega = 0.8,\ 1.0,\ 1.5,\ 1.82,\ 1.85,\ 2.0,\ 2.4$.

recording boundary at $y = 10$.

Since the maximum amplitude $|p'|_{max}$ of the acoustic wave in the numerical simulation fluctuates within a range, we take the mean value of $|p'|_{max}$ for y falling into the interval $y \in [9, 10]$ as the amplitude of the incident and reflected waves, which increases the reliability of the results. The box in figure 5.6 marks the range selected for the mean value of the incident wave amplitudes, and the circle indicates the range chosen for the mean value of the reflected wave amplitudes. The mean value of the maximum amplitude in these two ranges is used to calculate the reflection coefficient.

It should be noted that a noticeable oscillation in figure 5.6 is observed. It is caused by the artificial effect of the inserted wave packet edges. Artificial waves appear at the beginning from the wave packet edges and are reflected by the wall, which slightly affect the records of $|p'|_{max}$, see e.g. small oscillations around $t = 15$ in figure 5.5. However, these artificial effects only superimpose an interference effect and are either small or local, i.e. no influence on the reflected wave amplitude in the free stream is found.

A comparison of the numerical simulations with the theoretical over-reflection coefficients is given in figure 5.7. The reflection coefficients for the seven simulations are calculated by the method described in figure 5.6 and are marked with an asterisk in figure 5.7. The solid line is the theoretical result and computed by (4.17) in linear theory for the Mach number $M = 5$, the wavenumber $\alpha = 4$, and different frequencies.

Overall, the results of the numerical simulations match the theoretical predictions well in most cases. In particular, there is an exceptionally large value of the reflection coefficient at the resonant frequency $\omega = 1.85$, while at $\omega = 1.82$ and $\omega = 2$, the reflection coefficient remains relatively small level. The exceptionally large over-reflection coefficient around the resonant frequency points to an occurrence of the resonant over-reflection. Nevertheless, it is also near the resonant frequency $\omega = 1.85$ as shown in figure 5.7 that relatively large discrepancies between the simulation and theoretical results arise. The reason is that the reflection coefficients caused by the resonant frequencies increase promptly in a small frequency interval. A slight deviation of the frequency can lead to a significant difference in the results.

Therefore, the accuracy of the incident wave parameters inserted is critical. The accuracy of the incident wave parameters is determined on the one hand by the accuracy of the grid. It costs high to give such incident waves in the simulation accurately. On the other hand, the shear flow influences the incident wave. Although the shear effect is extremely weak in the defined 'free stream', it may still cause the parameters of the inserted incident wave to deviate from the set value.

5.5 Conclusion and discussion

5.5.1 Conclusion

By means of DNS, we simulate the entire process of acoustic waves incident from a free stream to an exponential boundary flow. For this purpose, we first build a wave packet model. In the wave packet model, plane waves with constant wavelength and amplitude are inserted into the packet so that the simulated acoustic waves have the same parameters corresponding to that in linear theory, i.e. the wavelength and the frequency. Through the initial condition, the wave packet model is superimposed with the base flow in the form of small perturbations, thereby creating acoustic waves that are incident from the free stream into the boundary layer. As the acoustic waves enter the sheared region, dispersive effects of the wave packets are observed. This is mainly due to the velocity changes of the base flow in the y-direction. The elongation of the wave packet reaches its maximum as it approaches the wall. Eventually, the acoustic waves are reflected at the wall and return to the free stream. In the process, the elongated wave packet is largely restored to its original form as the y-direction distances and the base flow velocity increase. The ratio of the maximum amplitude of the reflected wave in the free stream to the maximum amplitude of the incident wave is recorded as the reflection coefficient in the simulations. Seven sets of simulations for different frequencies for the Mach number $M = 5$ and the wavenumber $\alpha = 2$ are conducted, and the simulated results were obtained. The reflection coefficient in simulations were compared with that obtained from linear theory, which are in good agreement. In particular, there is an unusual peak in the simulated over-reflection coefficient with a frequency $\omega = 1.85$. This is consistent with the resonant over-reflection phenomenon in the theoretical results.

5.5.2 Discussion

It should be noted that the wave packet model still has some limitations in the present numerical simulations. These limitations are reflected in the following two aspects.

The first limitation is the insertion of plane waves with constant wavelength and amplitude into the wave packet. This model does not exist under real conditions and is only an approximation. Since the over-reflection phenomenon and the over-reflection coefficient obtained in linear theory are based on the plane wave with constant wavelength and amplitude, a realistic wave packet, e.g. the model in figure 5.2(a), cannot reproduce the corresponding over-reflection well due to imprecise parameters of the incident waves. Therefore, we regard the employed model more as an idealised one.

The second limitation is the dispersion effect of a wave packet on the amplitude of reflected waves. Even using the model in figure 5.6(b), there is still a slight dispersion in the wave packet where the wavelength and amplitude change, i.e. the parts in 5.6(b) other than the constant central part. The reason is due to the dispersion relationship of the wave packet in the shear flow. Going back to figure 5.2(a), we can determine that the wave packet is composed of wavelets with different wavelengths, i.e. they have different wavenumbers. These components of wavelets with different wavelengths are still present in the wave packet model in figure 5.2(b) and thus will affect the plane waves with constant wavelength and amplitude in the central part. By the dispersion relation (4.6) we know that this causes the wavelets on the wave packet to have different phase velocities and thus dispersion. By numerical simulations, we find that the wave packet of the incident wave does not have significant dispersion in the region of $y \geq 10$. This means that the dispersion effect of the wave packet due to the free-stream dispersion relation is relatively small and thus can be neglected. However, the reflected wave packet could be affected by the dispersion effect in the region of $y \geq 10$. Especially for acoustic waves with a resonant frequency, the reflected acoustic waves absorb more energy from shear flows, which may lead to an unpredictable change in the shape of the wave packet, thereby leading to a more obvious dispersion effect of the reflected wave packet in the free stream.

The dispersion effect is very pronounced for the wave packet model in figure 5.2(a) and may even cause the effect of over-reflection to be completely suppressed. Therefore, a study of the dispersion effects on a wave packet could provide a more realistic picture of the over-reflection effects of acoustic waves.

6 Conclusion and outlook

This chapter consists of two parts. In §6.1, we give a summary of key results in this thesis and focus on novel contributions of the present work to the stability and acoustic research community. In §6.2, we state valuable topics and potential further work that are based on new findings of the present work.

6.1 Summary and contributions

In the present work, we focus on a detailed investigation of the stability problems and the over-reflection of acoustic waves of a compressible inviscid boundary layer flow. These studies are based on the PBE with constant temperature and an exponential base flow velocity profile and its new exact solution.

The PBE is common in both stability and acoustic problems but appears to be mixed in the literature due to different fields of study, various names, distinct non-dimensional approaches, etc. We give derivations of several forms of the PBE, including the most common form, the generalised PBE with a velocity and a temperature profile. In the process of the derivation of the equations, we identify their applications in different fields of research. By a further homentropic assumption, we then derive the key equation in this thesis, the PBE with an exponential velocity profile. We show the different non-dimensional approaches for this equation and the ways how they can be transformed into each other. The PBE with an exponential velocity profile is found to have a similar form as the confluent Heun equation (CHE) in the Heun class equations, thereby leading to the derivation of an exact solution to the PBE in terms of the confluent Heun function (CHF). This exact solution is both a cornerstone of the present work and a significant contribution that can be extended for use in other studies, see §6.2.

In the present study of the stability problem, we investigate temporal and spatial stability separately. For this, we first convert the boundary value problem into an eigenvalue problem by proposing appropriate boundary conditions, which lead to the eigenvalue equation. To find eigenvalues, we first solve the eigenvalue equation analytically in limiting cases by the method of asymptotic analysis. In the temporal stability problem, we get analytical solutions for the small and large wavenumbers at small Mach numbers. In the spatial stability problem, we obtain analytical solutions for small and large frequencies at small Mach numbers. These solutions point out that the eigenvalue for small wavenumbers or frequencies is unique as well as real-valued. For large wavenumbers or frequencies in the context of small Mach numbers, the eigenvalues are still real but multiple-valued. Despite the restriction that the CHF lacks a general series expansion, which causes the analytical solutions to be restricted to small Mach numbers, the resulting analytical solutions still provide a valuable theoretical basis and guide for subsequent numerical calculations. In particular, they make essential contributions to the setting of initial guesses in the numerical root-finding algorithm for solving the eigenvalue equation. They further provide an explanation for the existence of multiple eigenvalues. As the next step, we solve the eigenvalue equation by numerical calculation for arbitrary wavenumbers (frequencies) and Mach numbers. For this, we apply a root-finding algorithm to the eigenvalue equation. It is worth mentioning that we employ the CHF-based exact solution to find eigenvalues. The advantages of using this exact solution compared to traditional numerical methods are clear. Compared with purely numerical methods, e.g. spectral method or shooting method, the method employed in the present work avoids the appearance of spurious modes, which do not have any physical meaning and are difficult to be screened out numerically. In addition, due to the singularities present in the PBE, uniform convergence is not guaranteed for these high-precision numerical methods. Last but not least, even the most accurate methods, such as the collocation method, have a decisive disadvantage that only the first modes can be calculated to high precision. The present method does not have this disadvantage. Modes of a desired high order can be calculated with arbitrarily required accuracy without especially additional effort.

Next, having calculated the eigenvalues, we analyse the modes quantitatively and qualitatively. A series of work and novel results are summarised as follows: (i) We qualitatively summarise the classification of the discrete acoustic modes for an exponential boundary layer flow, and these modes are acoustic modes corresponding to the second (Mack) and higher modes. (ii) We conclude that with growing wavenumbers or frequencies, the number of eigenvalues increases discretely. (iii) Only for $M > 1$ unstable modes exist. (iv) We define the boundary between neutrally stable and unstable modes by the transonic line $\omega = \alpha$, where the onset of the unstable modes is determined from the degenerated eigenvalue equation. (v) We display that at the Mach number $M \approx 4$ and $M \approx 3.5$, the supersonic modes become the most unstable mode regarding temporal and spatial stability, respectively. (vi) We calculate the imaginary part of the first three modes and mark their corresponding maximum values for different Mach numbers and the neutral-unstable mode border. (vii) The acoustic boundary layer thickness (ABLT) and the wave angle that reflect the acoustic properties of the perturbation are studied. For $M > 1$ and large wavenumbers α or frequencies ω, the ABLT δ_a grows exponentially, i.e. in this parameter range, sound is perceptible even far from the boundary layer. A particularly steep rise of δ_a is observed when $M > 2$, which means that there is a parameter range in which the growth rate and δ_a are both large and thus generate a powerful noise impact. (viii) Through the eigenfunctions, we illustrate the properties of perturbations in exponential boundary layers. The eigenfunctions describe how the perturbations propagate in waveform and how they change behaviour when the Mach number varies. (ivv) We explain the instability mechanism and its acoustic properties. Instability is characterised as a resonance phenomenon and associated with the radiation of acoustic waves. A strong increase in the amplitude of acoustic waves can be identified in the vicinity of the wall, which indicates an accumulation and saturation of energy, thereafter leading to instability and sound radiation in the free stream.

In the last part of the stability considerations, we compare temporal and spatial stability and find similarities in growth rates and acoustic behaviour of the unstable modes. In addition, we define the concept of resonance lines by the coincidence of the real parts of the eigenvalues of both problems and thereby link temporal and spatial stability. Based on this, we calculate the eigenvalues on the resonance line for frequencies and wavenumbers that are simultaneously complex-valued by formulating a new eigenvalue problem. A linear relation between the temporal and spatial growth rates is eventually determined. On this basis, we propose temporal-spatial instability of a boundary layer flow.

In the study of acoustic problems, we explore in detail the propagation and over-reflection of acoustic waves in an exponential boundary layer flow. We first examine boundary layer acoustics by classifying acoustic waves into propagating and attenuating waves, thereby providing a summary of the parameter range for acoustic waves that can and can not propagate in the free stream. We then make full use of the exact solution to the PBE again to give the reflection coefficient in an explicit form containing the CHF. Based on this explicit form of the reflection coefficient, the phenomenon of over-reflection of acoustic waves is investigated in depth. We start with a theoretical analysis of the critical layer and find that a logarithmic term arises in the Fuchs-Frobenius series solution at the critical layer. This logarithmic term leads to a jump in the value of a quasi-invariant while passing the critical layer. We relate this jump to the over-reflection coefficient through the boundary conditions, thereby showing that it is this jump as an input that directly causes the over-reflection coefficient to be greater than one. This result provides proof that acoustic waves extract energy from the base flow. In addition to this, a specific mathematical expression to connect the over-reflection coefficient and the amplitude of the density fluctuation at the critical layer is derived to evaluate the over-reflection coefficient analytically.

Subsequently, by means of the explicit expression for the reflection coefficient, including the CHF, we compute the over-reflection coefficient in a wide range of parameters and investigate the over-reflections of acoustic waves. The following novel results are found: (i) We validate the theoretical analysis showing that over-reflection occurs in boundary layer flows. (ii) For small wavenumbers there are relatively large over-reflection coefficients, but they are unaffected by the resonant frequency. (iii) Through computations of the over-reflection coefficient, we discover a special over-reflection, the resonant over-reflection. At resonant frequencies of the first temporally unstable mode, the over-reflection coefficient exhibits an unusual peak in an extremely narrow frequency interval. (iv) The maximum values of the unusual peaks are largely synchronised with the variation of the growth rate of the unstable modes. From this, we associate the resonant over-reflections with the unstable modes. (iv) The resonant over-reflection also appears at resonant frequencies of other higher unstable modes in the stability problem, but the peaks of the over-reflection coefficient are always smaller than that induced by the first unstable mode. (vi) By analysing the eigenfunctions of acoustic waves, an effect of attenuating the amplitude of acoustic waves near the critical layer is observed. (vii) Three patterns of acoustic wave propagation in boundary layer flows are identified, where one of them exhibits a similar pattern to the supersonic unstable mode. (viii) By comparison with the other two patterns, the mechanism by which the instability or resonant over-reflection occurs is revealed. The acoustic perturbations first gain energy from the base flow at the critical layer. Then, they accumulate energy in the area close to the wall and form complex reflections and refractions, thereby inducing instability or resonant over-reflection.

The study of boundary layer stability and acoustic over-reflections reveals an important fact. Small perturbations or acoustic waves present in an exponential boundary layer have resonant behaviours for certain combinations of frequencies and wavenumbers. In the present work, we find these frequencies and wavenumbers, which are named resonant frequencies and resonant wavenumbers. They are the real part of the eigenvalues of the unstable modes in the stability problems and are a function of the Mach number. The determination of these resonant frequencies and resonant wavenumbers provides a theoretical value reference for applications in engineering, especially in order to avoid instability and noise amplification in boundary layers.

To validate the phenomenon of the over-reflection of acoustic waves in boundary layer flows, direct numerical simulations (DNS) are carried out by using the in-house BoSSS code. For this purpose, the full non-linear Euler equations are computed. To achieve the incidence of acoustic waves from outside the boundary layer, the wave packets containing the plane acoustic waves with a constant wavelength and amplitude are predefined in the free stream through the initial condition. Through numerical simulations, we simulate the entire process of acoustic waves entering from the free stream into an exponential boundary layer flow. There, the waves are reflected by the wall and eventually return to the free stream. The ratio of the amplitude of the reflected wave in the free stream to the amplitude of the incident wave is recorded and used to calculate the reflection coefficient. This reflection coefficient is compared with the over-reflection coefficient obtained from linear theory. The results are in good agreement. In particular, there is a significant enhancement of the over-reflection around the resonant frequency, which indicates the occurrence of resonant over-reflection.

6.2 Outlook

Based on the work in this thesis, a few potential topics can be foreseen as directions for future research. The first noteworthy aspect is the further study of boundary layer flows for walls with acoustic impedances based on the exact solution in terms of the CHF. As can be seen from the results of the present work, the exact solution in terms of the CHF is reliable in dealing with the eigenvalue problem. Changes in wall conditions will give rise to many topics worthy of further investigation, e.g. the influence of acoustic impedances on stability problems and on over-reflections. The study in this thesis employs the simplest wall condition, a rigid wall, and its corresponding results can be used as a reference to compare with other results obtained by more realistic wall conditions. This will be of great interest for applications in engineering. An example is the study of acoustic liners. In addition, the Myers condition can be improved by the exact solution to the PBE for the exponential boundary layer flow. The Myers condition integrates the boundary layer flow and the acoustic impedance as a single boundary condition. In this way, a base flow, e.g. a duct flow, can be reduced to a Myers condition superimposed with a uniform flow, thus greatly simplifying the model. The idea of improving the Myers condition originates from the work of Rienstra & Darau (2011). They gave a modified Myers condition by taking the linear velocity profile as a boundary layer and using the exact solution to the PBE for the linear velocity profile. Thus, based on the exact solution to the PBE for a more realistic exponential velocity profile, a more improved result is highly expected.

Through the present work, we are introduced to the Heun class equations. Although these equations were given by Heun (1888) more than a hundred years ago, they have been not well developed. However, in recent years the Heun class functions have been made possible to be evaluated in numeric computing software represented by `Maple`. Since 2020, `Mathematica` has offered packages for evaluations of the Heun class functions too. Therefore, for some equations with the form of the Heun class equations, it is worthwhile to find their analytical solutions based on the Heun class functions to enable further numerical calculations. For example, for the generalised PBE with an additional temperature profile, it is expected that this equation will be solved analytically for the first time in terms of the general Heun function (GHF), and a number of valuable studies will be extended.

In terms of DNS, the high-precision resonant frequencies obtained from linear theory provide reference values for subsequent numerical simulation studies. Especially for acoustic waves in the form of small perturbations that are sensitive to numerical errors, an accurate resonant frequency as well as wavelength is crucial to simulations of both over-reflections and instabilities. In linear theory, we artificially separate the stability problem from the acoustic problem. In real situations, instability and acoustic over-reflections may occur simultaneously and interact with each other. It is still not clear how this process looks like. In particular, the non-linear effects of instability can further lead to laminar-turbulent transition. Regarding this, a preliminary work of the investigation of non-linear effects of exponential boundary layer instability is done by Putz (2021). These points are not observed in the simulations of the present work due to the limitations of simulation time and computational domain. In geophysical fluid dynamics (GFD), the over-reflection of internal gravity waves and Rossby waves is able to induce instability of shear flows. Therefore, in future work, a direct numerical simulation (DNS) study of interactions between unstable modes and over-reflections is valuable.

Bibliography

Airbus. (2020). *Airbus Annual Report 2020* (tech. rep.).

Albert, J. (2022). *On over-reflection in boundary layer flows of acoustic wall impedance* (Bachelor's thesis). TU Darmstadt.

Almgren, M. (1986). Acoustic boundary layer influence on scale model simulation of sound propagation: Theory and numerical examples. *Journal of sound and vibration*, *105*(2), 321–337.

Altmann, C., & Beck, A. D., & Hindenlang, F., & Staudenmaier, M., & Gassner, G. J., & Munz, C. (2013). An efficient high performance parallelization of a discontinuous Galerkin spectral element method. In *Facing the Multicore-Challenge III* (pp. 37–47). Springer.

Avital, E. J., & Sandham, N., & Luo, K. H. (1998a). Mach wave radiation by mixing layers. Part I: Analysis of the sound field. *Theoretical and Computational Fluid Dynamics*, *12*(2), 73–90.

Avital, E. J., & Sandham, N., & Luo, K. H. (1998b). Mach wave radiation by mixing layers. Part II: Analysis of the source field. *Theoretical and computational fluid dynamics*, *12*(2), 91–108.

Bakas, N. A. (2009). Mechanisms underlying transient growth of planar perturbations in unbounded compressible shear flow. *Journal of fluid mechanics*, *639*, 479.

Balsa, T. F. (1976). The far field of high frequency convected singularities in sheared flows, with an application to jet-noise prediction. *Journal of Fluid Mechanics*, *74*(2), 193–208.

Balmforth, N. J. (1999). Shear instability in shallow water. *Journal of Fluid Mechanics*, *387*, 97–127.

Baumgärtner, J. (2020). *Spatially developing acoustic instability modes in boundary layer flows* (Bachelor's thesis). TU Darmstadt.

Benilov, E., & Lapin, V. N. (2012). On resonant over-reflection of waves by jets. *Geophysical And Astrophysical Fluid Dynamics*, *107*, 1–24.

Bender, C., & Orszag, S. (1999). *Advanced mathematical methods for scientists and engineers I: Asymptotic methods and perturbation theory* (Vol. 1). Springer Science & Business Media.

Bergmann, P. G. (1946). The wave equation in a medium with a variable index of refraction. *The Journal of the Acoustical Society of America*, *17*(4), 329–333.

Bitter, N. P., & Shepherd, J. E. (2015). Stability of highly cooled hypervelocity boundary layers. *Journal of Fluid Mechanics*, *778*, 586–620.

Blumen, W., & Drazin, P. G., & Billings, D. F. (1975). Shear layer instability of an inviscid compressible fluid. Part 2. *Journal of Fluid Mechanics*, *71*(2), 305–316.

Booker, J. R., & Bretherton, F. P. (1967). The critical layer for internal gravity waves in a shear flow. *Journal of Fluid Mechanics*, *27*(3), 513–539.

Borissov, R. S., & Fiziev, P. P. (2010). Exact solutions of Teukolsky master equation with continuous spectrum. *Bulgarian Journal of Physics*, *37*, 65–89.

Boyd, J. P. (1983). The continuous spectrum of linear couette flow with the beta effect. *Journal of the atmospheric sciences*, *40*(9), 2304–2308.

Brambley, E. J., & Darau, M., & Rienstra, S. W. (2012). The critical layer in linear-shear boundary layers over acoustic linings. *Journal of Fluid Mechanics*, *710*, 545–568.

Brand, R. S., & Nagel, R. T. (1982). Reflection of sound by a boundary layer. *Journal of Sound and Vibration*, *85*(1), 31–38.

Brambley, E. J. (2011a). Acoustic implications of a thin viscous boundary layer over a compliant surface or permeable liner. *Journal of Fluid Mechanics*, *678*, 348–378.

Brambley, E. J. (2011b). Well-posed boundary condition for acoustic liners in straight ducts with flow. *AIAA Journal*, *49*(6), 1272–1282.

Brambley, E. J. (2013). Surface modes in sheared boundary layers over impedance linings. *Journal of Sound and Vibration*, *332*(16), 3750–3767.

Breeding, R. J. (1971). A non-linear investigation of critical levels for internal atmospheric gravity waves. *Journal of Fluid Mechanics*, *50*(3), 545–563.

Brown, W. B., & Sayre, P. H., & Pfenninger, W. (1954). *An exact solution of the Orr-Sommerfeld stability equation for low Reynolds numbers*. Northrop Aircraft.

Brun, C., & Juve, D., & Manhart, M., & Munz, C. (2008). *Numerical Simulation of Turbulent Flows and Noise Generation*. Springer.

Bühler, O. (2014). *Waves and mean flows*. Cambridge University Press.

Busemann, A. (1931). *Gasdynamik Handbuch der Experimental Physik* (Vol. 4). Akademische Verlagsgesellschaft.

Campos, L. M. B. C., & Kobayashi, M. H. (2000). On the reflection and transmission of sound in a thick shear layer. *Journal of Fluid Mechanics*, *424*, 303–326.

Campos, L. M. B. C., & Kobayashi, M. H. (2009). On the propagation of sound in a high-speed non-isothermal shear flow. *International Journal of Aeroacoustics*, *8*(3), 199–230.

Campos, L. M. B. C., & Oliveira, J. M. G. S. (2011). On the acoustic modes in a duct containing a parabolic shear flow. *Journal of Sound and Vibration*, *330*(6), 1166–1195.

Campos, L. M. B. C., & Kobayashi, M. H. (2013). On an acoustic oscillation energy for shear flows. *International Journal of Aeroacoustics*, *12*(1-2), 123–167.

Campos, L., & Legendre, C., & Sambuc, C. (2014). On the acoustics of an impedance liner with shear and cross flow. *Proceedings of the Royal Society A: Mathematical, Physical and Engineering Sciences*, *470*(2163), 20130732.

Campos, L. M. B. C., & Serrão, P. G. T. A. (1998). On the acoustics of an exponential boundary layer. *Philosophical Transactions of the Royal Society of London*, *356*(1746), 2335–2378.

Campos, L. M. B. C. (2007). On 36 forms of the acoustic wave equation in potential flows and inhomogeneous media. *Applied Mechanics Reviews*, *60*, 149–171.

Campos, L. M. B. C. (1999). On sound propagation in a linear shear flow. *Journal of Sound and Vibration*, *219*(5), 739–770.

Candelier, J., & Le Dizès, S., & Millet, C. (2012). Inviscid instability of a stably stratified compressible boundary layer on an inclined surface. *Journal of Fluid Mechanics*, *694*, 524–539.

Chagelishvili, G., & Hau, J., & Khujadze, G., & Oberlack, M. (2016). Mechanical picture of the linear transient growth of vortical perturbations in incompressible smooth shear flows. *Physical Review Fluids*, *1*(4), 043603.

Chagelishvili, G. D., & Khujadze, G. R., & Lominadze, J. G., & Rogava, A. D. (1997a). Acoustic waves in unbounded shear flows. *Physics of Fluids*, *9*(7), 1955–1962.

Chagelishvili, G. D., & Tevzadze, A. G., & Bodo, G., & Moiseev, S. S. (1997b). Linear mechanism of wave emergence from vortices in smooth shear flows. *Physical review letters*, *79*(17), 3178.

Chen, Z., & Wu, J., & Ren, A., & Chen, X. (2018). Mode-switching and nonlinear effects in supersonic jet noise. *AIP Advances*, *8*(1), 015126.

Chuvakhov, P. V., & Fedorov, A. V. (2016). Spontaneous radiation of sound by instability of a highly cooled hypersonic boundary layer. *Journal of Fluid Mechanics*, *805*, 188–206.

Cline, D. (2017). *Variational principles in classical mechanics*. University of Rochester River Campus Librarie.

Cockburn, B., & Karniadakis, G. E., & Shu, C. W. (2000). The development of discontinuous Galerkin methods. In *Discontinuous Galerkin Methods* (pp. 3–50). Springer.

Cohn, H. (1983). The stability of a magnetically confined radio jet. *The Astrophysical Journal*, *269*, 500–512.

Colonius, T., & Lele, S. K. (2004). Computational aeroacoustics: Progress on nonlinear problems of sound generation. *Progress in Aerospace sciences*, *40*(6), 345–416.

Colonius, T., & Lele, S. K., & Moin, P. (1997). Sound generation in a mixing layer. *Journal of Fluid Mechanics*, *330*, 375–409.

Crighton, D. G., & Leppington, F. G. (1974). Radiation properties of the semi-infinite vortex sheet: The initial-value problem. *Journal of Fluid Mechanics*, *64*(2), 393–414.

Crighton, D. G., & Gaster, M. (1976). Stability of slowly diverging jet flow. *Journal of Fluid Mechanics*, *77*(2), 397–413.

Criminale, W. O., & Drazin, P. G. (1990). The evolution of linearized perturbations of parallel flows. *Studies in Applied Mathematics*, *83*(2), 123–157.

Crocco, L. (1932). *Transmission of heat from a flat plate to a fluid flowing at a high velocity* (Vol. 12). National Advisory Committee for Aeronautics.

Curle, N. (1955). The influence of solid boundaries upon aerodynamic sound. *Proceedings of the Royal Society of London. Series A. Mathematical and Physical Sciences*, *231*(1187), 505–514.

De Grazia, D., & Mengaldo, G., & Moxey, D., & Vincent, P. E., & Sherwin, S. J. (2014). Connections between the discontinuous Galerkin method and high-order flux reconstruction schemes. *International journal for numerical methods in fluids*, *75*(12), 860–877.

De Broeck, L. (2021). *Noise suppression in boundary layer flows through optimized acoustic wall impedance* (Master's thesis). TU Darmstadt.

Delorme, P., & Mazet, P., & Peyret, C., & Ventribout, Y. (2005). Computational aeroacoustics applications based on a discontinuous Galerkin method. *Comptes Rendus Mécanique*, *333*(9), 676–682.

Delfs, J. (2016). *Basics of Aeroacoustics*. TU Braunschweig.

Demetriades, A. (1974). Hypersonic viscous flow over a slender cone. III-Laminar instability and transition. *7th Fluid and Plasma Dynamics Conference*, 535.

Dethe, T., & Gill, H., & Green, D. (2019). Causality and dispersion relations. *American Journal of Physics*, *87*, 279–290.

Doak, P. E. (1972). Analysis of internally generated sound in continuous materials: 2. A critical review of the conceptual adequacy and physical scope of existing theories of aerodynamic noise, with special reference to supersonic jet noise. *Journal of Sound and Vibration*, *25*(2), 263–335.

Drazin, P. G., & Reid, W. H. (1979). *Hydrodynamic stability*. Cambridge University Press.

Dryden, H. L. (1947). *Some recent contributions to the study of transition and turbulent boundary layers* (No. 1168). National Advisory Committee for Aeronautics.

Dunn, D. W. (1955). On the stability of the laminar boundary layer in a compressible fluid. *Journal of the Aeronautical Sciences*, *22*(7), 455–477.

Eltayeb, I. A., & McKenzie, J. F. (1975). Critical-level behaviour and wave amplification of a gravity wave incident upon a shear layer. *Journal of Fluid Mechanics*, *72*(4), 661–671.

Emamy, N., & Kummer, F., & Mrosek, M., & Karcher, M., & Oberlack, M. (2017). Implicit-explicit and explicit projection schemes for the unsteady incompressible Navier–Stokes equations using a high-order DG method. *Computers & Fluids*, *154*, 285–295.

Fabre, D., & Jacquin, L. (2004). Viscous instabilities in trailing vortices at large swirl numbers. *Journal of Fluid Mechanics*, *500*, 239–262.

Farrell, B. F., & Ioannou, P. J. (2000). Transient and asymptotic growth of two-dimensional perturbations in viscous compressible shear flow. *Physics of Fluids*, *12*(11), 3021–3028.

Fedorov, A., & Tumin, A. (2003). Initial-value problem for hypersonic boundary-layer flows. *AIAA Journal*, *41*(3), 379–389.

Fedorov, A., & Tumin, A. (2011). High-speed boundary-layer instability: Old terminology and a new framework. *AIAA Journal*, *49*(8), 1647–1657.

Fedorov, A. (2011). Transition and stability of high-speed boundary layers. *Annual Review of Fluid Mechanics*, *43*, 79–95.

Ffowcs Williams, J. E., & Hawkings, D. L. (1969). Sound generation by turbulence and surfaces in arbitrary motion. *Philosophical Transactions of the Royal Society of London*, *264*(1151), 321–342.

Filippone, A. (2014). Aircraft noise prediction. *Progress in Aerospace Sciences*, *68*, 27–63.

Fraport-AG. (2019). *Frankfurt Airport Air Traffic Statistics 2019* (tech. rep.).

Fritts, D. C. (1979). The excitation of radiating waves and Kelvin-Helmholtz instabilities by the gravity wave-critical level interaction. *Journal of Atmospheric Sciences*, *36*(1), 12–23.

Gabard, G. (2013). A comparison of impedance boundary conditions for flow acoustics. *Journal of Sound and Vibration*, *332*(4), 714–724.

Gallagher, A. P., & Mercer, A. M. (1965). On the behaviour of small disturbances in plane couette flow with a temperature gradient. *Proceedings of the Royal Society of London. Series A, Mathematical and Physical Sciences*, *286*(1404), 117–128.

Galapon, E. A. (2016). The Cauchy principal value and the hadamard finite part integral as values of absolutely convergent integrals. *Journal of Mathematical Physics*, *57*(3), 033502.

Geisenhofer, M. (2021). *From shock-capturing to high-order shock-fitting using an unfitted discontinuous Galerkin method*. Technische Universität Darmstadt.

Gill, A. E. (1965). Instabilities of ”top-hat” jets and wakes in compressible fluids. *The Physics of Fluids*, *8*(8), 1428–1430.

Gloor, M., & Obrist, D., & Kleiser, L. (2013). Linear stability and acoustic characteristics of compressible, viscous, subsonic coaxial jet flow. *Physics of Fluids*, *25*(8), 084102.

Goldstein, M., & Rice, E. (1973). Effect of shear on duct wall impedance. *Journal of Sound and Vibration*, *30*(1), 79–84.

Goldstein, M. E. (2003). A generalized acoustic analogy. *Journal of Fluid Mechanics*, *488*, 315–333.

Goldstein, M. E. (2005). On identifying the true sources of aerodynamic sound. *Journal of Fluid Mechanics*, *526*, 337.

Goldstein, M. E. (1982). High frequency sound emission from moving point multipole sources embedded in arbitrary transversely sheared mean flows. *Journal of Sound and Vibration*, *80*(4), 499–522.

Goldstein, M. E. (1984). Aeroacoustics of turbulent shear flows. *Annual Review Fluid Mechanics*, *16*, 263–285.

Görtz, S. (2020). *Theory of sound generation in free shear flows* (Master’s thesis). TU Darmstadt.

Gottlieb, D., & Orszag, S. A. (1977). *Numerical analysis of spectral methods: Theory and applications*. Society for Industrial; Applied Mathematics.

Gutmark, E. J., & Schadow, K. C., & Yu, K. H. (1995). Mixing enhancement in supersonic free shear flows. *Annual Review of Fluid Mechanics*, *27*(1), 375–417.

Harnik, N., & Heifetz, E. (2007). Relating overreflection and wave geometry to the counter-propagating rossby wave perspective: Toward a deeper mechanistic understanding of shear instability. *Journal of the atmospheric sciences*, *64*(7), 2238–2261.

Hau, J., & Chagelishvili, G., & Khujadze, G., & Oberlack, M., & Tevzadze, A. (2015). A comparative numerical analysis of linear and nonlinear aerodynamic sound generation by vortex disturbances in homentropic constant shear flows. *Physics of Fluids*, *27*(12), 126101.

Hau, J., & Oberlack, M., & Chagelishvili, G. (2017). On the optimal systems of subalgebras for the equations of hydrodynamic stability analysis of smooth shear flows and their group-invariant solutions. *Journal of Mathematical Physics*, *58*(4), 043101.

Hau, J. (2017). *On the basic phenomena of acoustic wave generation and dynamics in compressible shear flows*. Cuvillier Verlag.

Haurwitz, B. (1931). *Zur Theorie der Wellenbewegungen in Luft und Wasser*. Geophysikalischen Institut der Universität Leipzig.

Heathrow-Airport. (2014). *Noise data for the first 17 months of Boeing 787 operations at Heathrow airport* (tech. rep.).

Henderson, B. (2010). Fifty years of fluidic injection for jet noise reduction. *International Journal of Aeroacoustics*, *9*(1-2), 91–122.

Hernández, C. G., & Wu, X. (2019). Receptivity of supersonic boundary layers over smooth and wavy surfaces to impinging slow acoustic waves. *Journal of Fluid Mechanics*, *872*, 849–888.

Heun, K. (1888). Zur Theorie der Riemann'schen Functionen zweiter Ordnung mit vier Verzweigungspunkten. *Mathematische Annalen*, *33*(2), 161–179.

Hortaçsu, M. (2018). Heun functions and some of their applications in physics. *Advances in High Energy Physics*, *2018*.

Howe, M. S. (1975). Contributions to the theory of aerodynamic sound, with application to excess jet noise and the theory of the flute. *Journal of Fluid Mechanics*, *71*(4), 625–673.

Howe, M. S. (1978). A review of the theory of trailing edge noise. *Journal of sound and vibration*, *61*(3), 437–465.

Ishii, S., & Kakutani, T. (1987). Acoustic waves in parallel shear flows in a duct. *Journal of sound and vibration*, *113*(1), 127–139.

Jones, D. S., & Morgan, J. P. (1972). The instability of a vortex sheet on a subsonic stream under acoustic radiation. *Mathematical Proceedings of the Cambridge Philosophical Society*, *72*(3), 465–488.

Jones, W. L. (1968). Reflexion and stability of waves in stably stratified fluids with shear flow: A numerical study. *Journal of Fluid Mechanics*, *34*(3), 609–624.

Jones, D. S. (1977). The scattering of sound by a simple shear layer. *Philosophical Transactions of the Royal Society of London*, *284*(1323), 287–328.

Karabasov, S. A. (2010). Understanding jet noise. *Philosophical Transactions of the Royal Society of London*, *368*(1924), 3593–3608.

Khamis, D., & Brambley, E. J. (2016). Acoustic boundary conditions at an impedance lining in inviscid shear flow. *Journal of Fluid Mechanics*, *796*, 386–416.

Klein, B., & Kummer, F., & Oberlack, M. (2013). A SIMPLE based discontinuous Galerkin solver for steady incompressible flows. *Journal of Computational Physics*, *237*, 235–250.

Klein, B., & Kummer, F., & Keil, M., & Oberlack, M. (2015). An extension of the SIMPLE based discontinuous Galerkin solver to unsteady incompressible flows. *International Journal for Numerical Methods in Fluids*, *77*(10), 571–589.

Knessl, C., & Keller, J. B. (1995). Stability of linear shear flows in shallow water. *Journal of Fluid Mechanics*, *303*, 203–214.

Knisely, C. P., & Zhong, X. (2019a). Sound radiation by supersonic unstable modes in hypersonic blunt cone boundary layers. I. Linear stability theory. *Physics of Fluids*, *31*(2), 024103.

Knisely, C. P., & Zhong, X. (2019b). Sound radiation by supersonic unstable modes in hypersonic blunt cone boundary layers. II. Direct numerical simulation. *Physics of Fluids*, *31*(2), 024104.

Knisely, C. P. (2018). *Supersonic unstable modes in hypersonic boundary layers with thermo-chemical nonequilibrium effects* (Doctoral dissertation). University of California, Los Angeles.

Koutsoyannis, S. P., & Karamcheti, K., & Galant, D. C. (1979). Acoustic resonances and sound scattering by a shear layer. *AIAA Journal*, *18*(12), 1446–1454.

Koutsoyannis, S. P. (1980). Characterization of acoustic disturbances in linearly sheared flows. *Journal of Sound and Vibration*, *68*(2), 187–202.

Krämer-Eis, S. (2017). *A high-order discontinuous Galerkin method for unsteady compressible flows with immersed boundaries* (Doctoral dissertation). TU Darmstadt.

Küchemann, D. (1938). Störungsbewegungen in einer Gasströmung mit Grenzschicht. *ZAMM-Journal of Applied Mathematics and Mechanics/Zeitschrift für Angewandte Mathematik und Mechanik*, *18*(4), 207–222.

Kummer, F., & Emamy, N., & Teymouri, R. M. B., & Oberlack, M. (2009). Report on the development of a generic discontinuous Galerkin framework in .NET. *ParCFD 2009, 21st International Conference on Parallel Computational Fluid Dynamics*, 383–397.

Kummer, F., & Müller, B., & Geisenhofer, M., & Kahle, J., & Krause, D., & Smuda, M., & Utz, T., & Krämer-Eis, S., & Dierkes, D., & Kikker, A., & Keil, M. (2020). *BoSSS-Handbook*. TU Darmstadt.

Kummer, F. (2011). *The extended DG discretization of discontinuous PDE's and the BoSSS software framework* (Doctoral dissertation). TU Darmstadt.

Kuttruff, H. (2007). *Acoustics: An introduction*. CRC Press.

Landau, L. D., & Lifshitz, E. M. (2013). *Fluid mechanics: Landau and Lifshitz: Course of theoretical physics* (Vol. 6). Elsevier.

Landau, L., & Lifshitz, E. M. (1987). Fluid mechanics. *Journal of Fluid Mechanics*, *205*, 593–594.

Lang, M., & Frenzel, B. C. (1994). Polynomial root finding. *IEEE Signal Processing Letters*, *1*(10), 141–143.

Lapin, V. N. (2011). *Resonant over-reflection of waves by jets* (Doctoral dissertation). University of Limerick, Limerick.

Lees, L., & Lin, C. C. (1946). *Investigation of the stability of the laminar boundary layer in a compressible fluid* (No. 1115). National Advisory Committee for Aeronautics.

Lees, L., & Reshotko, E. (1962). Stability of the compressible laminar boundary layer. *Journal of Fluid Mechanics*, *12*(4), 555–590.

Lees, L. (1947). The stability of the laminar boundary layer in a compressible fluid. *National Advisory Committee for Aeronautics*.

Li, X., & Fu, D., & Ma, Y. (2010). Direct numerical simulation of hypersonic boundary layer transition over a blunt cone with a small angle of attack. *Physics of Fluids*, *22*(2), 025105.

Lighthill, M. J. (1952). On sound generated aerodynamically I. General theory. *Proceedings of the Royal Society of London. Series A. Mathematical and Physical Sciences*, *211*(1107), 564–587.

Lighthill, M. J. (1954). On sound generated aerodynamically II. Turbulence as a source of sound. *Proceedings of the Royal Society of London. Series A. Mathematical and Physical Sciences*, *222*(1148), 1–32.

Lighthill, M. J. (1958). *An introduction to fourier analysis and generalised functions*. Cambridge University Press.

Lilley, G. M. (1974). *On the noise from jets* (No. 131). Advisory Group for Aerospace Research and Development.

Lindgren, B., & Österlund, J. M., & Johansson, A. V. (2004). Evaluation of scaling laws derived from Lie group symmetry methods in zero-pressure-gradient turbulent boundary layers. *Journal of Fluid Mechanics*, *502*, 127–152.

Lindzen, R. S., & Rosenthal, A. J. (1976). On the instability of Helmholtz velocity profiles in stably stratified fluids when a lower boundary is present. *Journal of Geophysical Research*, *81*(9), 1561–1571.

Lindzen, R. S., & Tung, K. K. (1978). Wave overreflection and shear instability. *Journal of Atmospheric Sciences*, *35*(9), 1626–1632.

Lindzen, R. S., & Farrell, B., & Tung, K. (1980). The concept of wave overreflection and its application to baroclinic instability. *Journal of Atmospheric Sciences*, *37*(1), 44–63.

Lindzen, R. S., & Barker, J. W. (1985). Instability and wave over-reflection in stably stratified shear flow. *Journal of Fluid Mechanics*, *151*, 189–217.

Lindzen, R. S., & Rambaldi, S. (1986). A study of over-reflection in viscous Poiseuille flow. *Journal of Fluid Mechanics*, *165*, 355–372.

Lindzen, R. S. (1974). Stability of a Helmholtz velocity profile in a continuously stratified, infinite Boussinesq fluid—applications to clear air turbulence. *Journal of Atmospheric Sciences*, *31*(6), 1507–1514.

Lindzen, R. S. (1988). Instability of plane parallel shear flow (toward a mechanistic picture of how it works). *Pure and Applied Geophysics*, *126*(1), 103–121.

Liu, Y., & Dong, M., & Wu, X. (2020). Generation of first mack modes in supersonic boundary layers by slow acoustic waves interacting with streamwise isolated wall roughness. *Journal of Fluid Mechanics*, *888*, A10.

Liu, B. (2008). Noise radiation of aircraft panels subjected to boundary layer pressure fluctuations. *Journal of Sound and Vibration*, *314*(3-5), 693–711.

Luo, K. H., & Sandham, N. D. (1997). Instability of vortical and acoustic modes in supersonic round jets. *Physics of Fluids*, *9*(4), 1003–1013.

Lysenko, V. I., & Maslov, A. A. (1984). The effect of cooling on supersonic boundary-layer stability. *Journal of Fluid Mechanics*, *147*, 39–52.

Macaraeg, M. G., & Streett, C. L., & Hussaini, M. Y. (1988). *A spectral collocation solution to the compressible stability eigenvalue problem* (No. 2858). National Aeronautics and Space Administration.

Mack, L. M. (1965). The stability of the compressible laminar boundary layer according to a direct numerical solution. In *AGARDograph 97: Recent Developments in Boundry Layer Research Part I* (pp. 329–362). North Atlantic Treaty Organization.

Mack, L. M. (1969). *Boundary layer stability theory* (No. 900–277). Jet Propulsion Laboratory, California Institute of Technology.

Mack, L. M. (1975). Linear stability theory and the problem of supersonic boundary-layer transition. *AIAA Journal*, *13*(3), 278–289.

Mack, L. M. (1984). *Boundary-layer linear stability theory* (No. 709). Jet Propulsion Laboratory, California Institute of Technology.

Mack, L. M. (1990). On the inviscid acoustic-mode instability of supersonic shear flows. *Theoretical and Computational Fluid Dynamics*, *2*(2), 97–123.

Mack, L. M. (1993). Effect of cooling on boundary-layer stability at Mach number 3. In *Instabilities and turbulence in engineering flows* (pp. 175–188). Springer.

Malik, M. R. (1990). Numerical methods for hypersonic boundary layer stability. *Journal of computational physics*, *86*(2), 376–413.

Mancinelli, M., & Pagliaroli, T., & Camussi, R., & Castelain, T. (2018). On the hydrodynamic and acoustic nature of pressure proper orthogonal decomposition modes in the near field of a compressible jet. *Journal of Fluid Mechanics*, *836*, 998–1008.

Mani, R. (1976). The influence of jet flow on jet noise. Part 1. The noise of unheated jets. *Journal of Fluid Mechanics*, *73*(4), 753–778.

Maplesoft. (2020). *Maple User Manual*. Waterloo, Ontario.

Marcus, P. S., & Press, W. H. (1977). On Green's functions for small disturbances of plane couette flow. *Journal of Fluid Mechanics*, *79*(3), 525–534.

Mariano, S. (1971). Effect of wall shear layers on the sound attenuation in acoustically lined rectangular ducts. *Journal of Sound and Vibration*, *19*(3), 261–275.

Maslov, A., & Bountin, D., & Shiplyuk, A., & Sidorenko, A., & Shen, Q., & Bi, Z. (2009). Experimental study of compressible boundary layer on a cone at angles of attack. *Acta Mechanica Sinica*, *25*(3), 325–333.

Masad, J. A., & Nayfeh, A. H., & Al-Maaitah, A. A. (1992). Effect of heat transfer on the stability of compressible boundary layers. *Computers & fluids*, *21*(1), 43–61.

Maslowe, S. A. (1991). Barotropic instability of the Bickley jet. *Journal of Fluid Mechanics*, *229*, 417–426.

Mathworks. (2020). *MATLAB User Manual*. Natick, Massachusetts, The MathWorks, Inc.

McKenzie, J. F. (1972). Reflection and amplification of acoustic-gravity waves at a density and velocity discontinuity. *Journal of Geophysical Research*, *77*(16), 2915–2926.

Michalke, A., & Fuchs, H. V. (1975). On turbulence and noise of an axisymmetric shear flow. *Journal of Fluid Mechanics*, *70*(1), 179–205.

Michalke, A. (1965). On spatially growing disturbances in an inviscid shear layer. *Journal of Fluid Mechanics*, *23*(3), 521–544.

Michalke, A. (1977). On the effect of spatial source coherence on the radiation of jet noise. *Journal of Sound and Vibration*, *55*(3), 377–394.

Michalke, A. (1984). Survey on jet instability theory. *Progress in Aerospace Sciences*, *21*, 159–199.

Miles, J. W. (1957). On the reflection of sound at an interface of relative motion. *The Journal of the Acoustical Society of America*, *29*(2), 226–228.

Möhring, W., & Müller, E., & Obermeier, F. (1983). Problems in flow acoustics. *Reviews of modern physics*, *55*(3), 707–724.

Morkovin, M. V., & Reshotko, E., & Herbert, T. (1994). Transition in open flow systems-a reassessment. *Bulletin of the American Physical Society*, *39*, 1–31.

Morkovin, M. V. (1969). On the many faces of transition. In *Viscous drag reduction* (pp. 1–31). Springer.

Morkovin, M. V. (1985). Bypass transition to turbulence and research desiderata. In *Transition in Turbines* (pp. 161–204). National Aeronautics; Space Administration.

Mostowski, A., & Stark, M. (2014). *Introduction to higher algebra*. Elsevier.

Motygin, O. V. (2018). On evaluation of the confluent Heun functions. *2018 Days on Diffraction (DD)*, 223–229.

Müller, G., & Möser, M. (2012). *Handbook of engineering acoustics*. Springer Science & Business Media.

Müller, B., & Krämer-Eis, S., & Kummer, F., & Oberlack, M. (2017). A high-order discontinuous Galerkin method for compressible flows with immersed boundaries. *International Journal for Numerical Methods in Engineering*, *110*(1), 3–30.

Müller, B. (2011). *Implementation of an inviscid flow solver based on the discontinuous Galerkin library BoSSS* (Master's thesis). TU Darmstadt.

Myers, M. K., & Chuang, S. L. (1984). Uniform asymptotic approximations for duct acoustic modes in a thin boundary-layer flow. *AIAA Journal*, *22*(9), 1234–1241.

Myers, M. K. (1980). On the acoustic boundary condition in the presence of flow. *Journal of Sound and Vibration*, *71*(3), 429–434.

Nash, E. C., & Lowson, M. V., & McAlpine, A. (1999). Boundary-layer instability noise on aerofoils. *Journal of Fluid Mechanics*, *382*, 27–61.

Nayfeh, A. H. (1973). Effect of the acoustic boundary layer on the wave propagation in ducts. *The Journal of the Acoustical Society of America*, *54*(6), 1737–1742.

Nold, A., & Oberlack, M. (2013). Symmetry analysis in linear hydrodynamic stability theory: Classical and new modes in linear shear. *Physics of Fluids*, *25*(10), 104101.

Oberlack, M. (2001). A unified approach for symmetries in plane parallel turbulent shear flows. *Journal of Fluid Mechanics*, *427*, 299–328.

Olver, F. W., & Lozier, D. W., & Boisvert, R. F., & Clark, C. W. (2010). *NIST Handbook of Mathematical Functions* (1st). Cambridge University Press.

Oppeneer, M., & Lazeroms, W., & Rienstra, S., & Sijtsma, P., & Mattheij, B. (2011). Acoustic modes in a duct with slowly varying impedance and non-uniform mean flow and temperature. *17th AIAA/CEAS Aeroacoustics Conference (32nd AIAA Aeroacoustics Conference)*, 2871.

Oppeneer, M. (2014). *Sound propagation in lined ducts with parallel flow* (Doctoral dissertation). TU Eindhoven.

Pagneux, V., & Froelich, B. (2001). Influence of low Mach number shear flow on acoustic propagation in ducts. *Journal of Sound and vibration*, *246*(1), 137–155.

Parras, L., & Le Dizès, S. (2010). Temporal instability modes of supersonic round jets. *Journal of Fluid Mechanics*, *662*, 173–196.

Payne, D. G., & Cohn, H. (1985). The stability of confined radio jets - the role of reflection modes. *The Astrophysical Journal*, *291*, 655–667.

Perrault-Joncas, D., & Maslowe, S. A. (2008). Linear stability of a compressible coaxial jet with continuous velocity and temperature profiles. *Physics of Fluids*, *20*(7), 074102.

Phillips, O. M. (1960). On the generation of sound by supersonic turbulent shear layers. *Journal of Fluid Mechanics*, *9*(1), 1–28.

Powell, A. (1964). Theory of vortex sound. *The journal of the acoustical society of America*, *36*(1), 177–195.

Pridmore-Brown, D. C. (1958). Sound propagation in a fluid flowing through an attenuating duct. *Journal of Fluid Mechanics*, *4*(4), 393–406.

Putz, F. (2021). *Direct numerical simulation of linear and non-linear acoustic instabilities in boundary layer flow* (Master's thesis). TU Darmstadt.

Rayleigh, R. (1887). On the stability or instability of certain fluid motions, II. *Proceedings of the London Mathematical Society*, *1*(1), 67–75.

Reddy, S. C., & Henningson, D. S. (1993). Energy growth in viscous channel flows. *Journal of Fluid Mechanics*, *252*, 209–238.

Reed, H. L., & Saric, W. S., & Arnal, D. (1996). Linear stability theory applied to boundary layers. *Annual Review of Fluid Mechanics*, *28*(1), 389–428.

Research, W. (2020). *Mathematica User Manual*. Wolfram Centre, United Kingdom.

Ribner, H. S. (1957). Reflection, transmission, and amplification of sound by a moving medium. *The Journal of the Acoustical Society of America*, *29*(4), 435–441.

Rienstra, S. W., & Darau, M. (2011). Boundary-layer thickness effects of the hydrodynamic instability along an impedance wall. *Journal of Fluid Mechanics*, *671*, 559–573.

Rienstra, S. W., & Hirschberg, A. (2020). *An Introduction to Acoustics*. TU Eindhoven.

Rienstra, S. W. (2020). Numerical and asymptotic solutions of the Pridmore-Brown equation. *AIAA Journal*, *58*(7), 3001–3018.

Ronveaux, A., & Arscott, F. M. (1995). *Heun's Differential Equations*. Clarendon Press.

Rosenthal, A. J., & Lindzen, R. S. (1983a). Instabilities in a stratified fluid having one critical level. part ii: Explanation of gravity wave instabilities using the concept of overreflection. *Journal of the Atmospheric Sciences*, *40*(3), 521–529.

Rosenthal, A. J., & Lindzen, R. S. (1983b). Instabilities in a stratified fluid having one critical level. Part III: Kelvin-Helmholtz instabilities as overreflected waves. *Journal of the Atmospheric Sciences*, *40*(3), 521–529.

Royce-Rolls. (2015). *The jet engine*. John Wiley & Sons.

Saddoughi, S. G., & Veeravalli, S. V. (1994). Local isotropy in turbulent boundary layers at high reynolds number. *Journal of Fluid Mechanics*, *268*, 333–372.

Samanta, A. (2016). On the axisymmetric stability of heated supersonic round jets. *Proceedings of the Royal Society A: Mathematical, Physical and Engineering Sciences*, *472*(2188), 20150817.

Saric, W. S., & Reed, H. L., & White, E. B. (2003). Stability and transition of three-dimensional boundary layers. *Annual Review of Fluid Mechanics*, *35*(1), 413–440.

Satomura, T. (1981a). An investigation of shear instability in a shallow water. *Journal of the Meteorological Society of Japan*, *59*(1), 148–167.

Satomura, T. (1981b). Supplementary note on shear instability in a shallow water. *Journal of the Meteorological Society of Japan*, *59*(1), 168–171.

Saverna, C., & Auregan, Y., & Pagneux, V. (2019). Assymetric improvement by a shear flow of the absorption of an acoustic wall. *25th AIAA/CEAS Aeroacoustics Conference*, 2504.

Schmid, P. J., & Henningson, D. S. (2001). Transition to turbulence. In *Stability and Transition in Shear Flows* (pp. 401–475). Springer.

Schmid, P. J., & Henningson, D. S. (2012). *Stability and transition in shear flows*. Springer Science & Business Media.

Schubauer, G. B., & Skramstad, H. K. (1947). Laminar boundary-layer oscillations and transition on a flat plate. *Journal of the Aeronautical Sciences*, *38*(251), 92.

Schmid, P. J. (2007). Nonmodal stability theory. *Annual Review Fluid Mechanics*, *39*, 129–162.

Schäfer, M. (2013). *Numerik im Maschinenbau*. Springer Verlag.

Schlichting, V. H. (1933). Laminare Strahlausbreitung. *Zeitschrift für Angewandte Mathematik und Mechanik*, *13*(4), 260–263.

Scott, J. N. (1979). Propagation of sound waves through a linear shear layer. *AIAA Journal*, *17*(3), 237–244.

Sinayoko, S., & Agarwal, A., & Hu, Z. (2011). Flow decomposition and aerodynamic sound generation. *Journal of Fluid Mechanics*, *668*, 335.

Smith, F. T. (1989). On the first-mode instability in subsonic, supersonic or hypersonic boundary layers. *Journal of Fluid Mechanics*, *198*, 127–153.

Spurk, J., & Aksel, N. (2007). *Fluid mechanics*. Springer Science & Business Media.

Stetson, K., & Thompson, E., & Donaldson, J., & Siler, L. (1989). Laminar boundary layer stability experiments on a cone at Mach 8. V-tests with a cooled model. *20th Fluid Dynamics, Plasma Dynamics and Lasers Conference*, 1895.

Stetson, K., & Kimmel, R. (1992). On hypersonic boundary-layer stability. *30th Aerospace Sciences Meeting and Exhibit*, 737.

Tack, D. H., & Lambert, R. F. (1965). Influence of shear flow on sound attenuation in a lined duct. *The Journal of the Acoustical Society of America*, *38*(4), 655–666.

Takehiro, S. I., & Hayashi, Y. Y. (1992). Over-reflection and shear instability in a shallow-water model. *Journal of Fluid Mechanics*, *236*, 259–279.

Tam, C. K. W., & Viswanathan, K., & Ahuja, K. K., & Panda, J. (2008). The sources of jet noise: Experimental evidence. *Journal of Fluid Mechanics*, *615*, 253–292.

Tam, C. K., & Morris, P. J. (1980). The radiation of sound by the instability waves of a compressible plane turbulent shear layer. *Journal of Fluid Mechanics*, *98*(2), 349–381.

Tam, C. K., & Burton, D. E. (1984a). Sound generated by instability waves of supersonic flows. Part 1. two-dimensional mixing layers. *Journal of Fluid Mechanics*, *138*, 249–271.

Tam, C. K., & Burton, D. E. (1984b). Sound generated by instability waves of supersonic flows. Part 2. Axisymmetric jets. *Journal of Fluid Mechanics*, *138*, 273–295.

Tam, C. K., & Hu, F. (1989a). The instability and acoustic wave modes of supersonic mixing layers inside a rectangular channel. *Journal of Fluid Mechanics*, *203*, 51–76.

Tam, C. K. W., & Hu, F. Q. (1989b). The instability and acoustic wave modes of supersonic mixing layers inside a rectangular channel. *Journal of Fluid Mechanics*, *203*, 51–76.

Tam, C. K. W., & Hu, F. Q. (1989c). On the three families of instability waves of high-speed jets. *Journal of Fluid Mechanics*, *201*, 447–483.

Tam, C. K. W. (2004). Computational aeroacoustics: An overview of computational challenges and applications. *International Journal of Computational Fluid Dynamics*, *18*(6), 547–567.

Tam, C. K. W. (1978). Excitation of instability waves in a two-dimensional shear layer by sound. *Journal of Fluid Mechanics*, *89*(2), 357–371.

Tam, C. K. W. (1995a). Computational aeroacoustics: Issues and methods. *AIAA Journal*, *33*(10), 1788–1796.

Tam, C. K. W. (1995b). Supersonic jet noise. *Annual Review of Fluid Mechanics*, *27*(1), 17–43.

Tietjens, O. (1925). Beiträge zur Entstehung der Turbulenz. *ZAMM-Journal of Applied Mathematics and Mechanics/Zeitschrift für Angewandte Mathematik und Mechanik*, *5*(3), 200–217.

Tollmien, W. (1930). Über die Entstehung der Turbulenz. In *Vorträge aus dem Gebiete der Aerodynamik und verwandter Gebiete* (pp. 18–21). Springer.

Toro, E. F. (2013). *Riemann solvers and numerical methods for fluid dynamics: A practical introduction*. Springer Science & Business Media.

Trefethen, L. N. (1982). Group velocity in finite difference schemes. *SIAM review*, *24*(2), 113–136.

Tumin, A. (2011). The biorthogonal eigenfunction system of linear stability equations: A survey of applications to receptivity problems and to analysis of experimental and computational results. *41st AIAA Fluid Dynamics Conference and Exhibit*, 3244.

Tunney, A. P., & Denier, J. P., & Mattner, T. W., & Cater, J. E. (2015). A new inviscid mode of instability in compressible boundary-layer flows. *Journal of Fluid Mechanics*, *785*, 301–323.

Van Driest, E. R. (1952). Calculation of the stability of the laminar boundary layer in a compressible fluid on a flat plate with heat transfer. *Journal of the Aeronautical Sciences*, *19*(12), 801–812.

Vilenski, G. G., & Rienstra, S. W. (2007). On hydrodynamic and acoustic modes in a ducted shear flow with wall lining. *Journal of Fluid Mechanics*, *583*, 45–70.

Wagnild, R. M. (2012). *High enthalpy effects on two boundary layer disturbances in supersonic and hypersonic flow* (tech. rep.). University of Minnesota.

Wang, M., & Freund, J. B., & Lele, S. K. (2006). Computational prediction of flow-generated sound. *Annual Review Fluid Mechanics*, *38*, 483–512.

Wu, X. (2005). Mach wave radiation of nonlinearly evolving supersonic instability modes in shear layers. *Journal of Fluid Mechanics*, *523*, 121.

Wu, X. (2014). On the role of acoustic feedback in boundary-layer instability. *Philosophical Transactions of the Royal Society of London*, *372*(2020), 20130347.

Yamada, M., & Okamura, M. (1984). Overreflection and overtransmission of rossby waves. *Journal of the atmospheric sciences*, *41*(16), 2531–2535.

Zaninetti, L. (1986). Numerical results on instabilities of ”top hat” jets. *The Physics of fluids*, *29*(1), 332–333.

Zaninetti, L. (1987). Maximum instabilities of compressible jets. *The Physics of fluids*, *30*(2), 612–614.

Zhang, C., & Tang, Q., & Lee, C. (2013). Hypersonic boundary-layer transition on a flared cone. *Acta Mechanica Sinica*, *29*(1), 48–54.

Zhang, C., & Wan, Z., & Sun, D. (2016). Mode transition and oscillation suppression in supersonic cavity flow. *Applied Mathematics and Mechanics*, *37*(7), 941–956.

Zhang, Y., & Oberlack, M. (2021). Inviscid instability of compressible exponential boundary layer flows. *AIP Advances*, *11*(10), 105308.

Zhang, Y., & Görtz, S., & Oberlack, M. (2022). Over-reflection of acoustic waves by compressible boundary layer flows. *Journal of Fluid Mechanics*, *945*.

Zhang, Y. (2018). *Sound generation in an exponential boundary layer* (Master’s thesis). TU Darmstadt.

Zhong, X., & Wang, X. (2012). Direct numerical simulation on the receptivity, instability, and transition of hypersonic boundary layers. *Annual Review of Fluid Mechanics*, *44*, 527–561.

Zhong, S., & Huang, X. (2018). A review of aeroacoustics and flow-induced noise for beginners. *Acta Aerodynamica Sinica*, *36*(3), 363–371.

Zhu, W., & Shi, M., & Zhu, Y., & Lee, C. (2020). Experimental study of hypersonic boundary layer transition on a permeable wall of a flared cone. *Physics of Fluids*, *32*(1), 011701.

A Appendix

A.1 Derivation of the solution to the PBE

In this appendix, we derive the general solution to the PBE (2.31) given in terms of the solution to the CHE. The PBE reads

$$\frac{d^2\hat{\rho}}{dy^2} + \frac{2\alpha e^{-y}}{\omega - \alpha + \alpha e^{-y}}\frac{d\hat{\rho}}{dy} + \left[M^2\left(\omega - \alpha + \alpha e^{-y}\right)^2 - \alpha^2\right]\hat{\rho} = 0. \tag{A.1}$$

We first transform (A.1) by changing the independent variable to

$$y = -\ln(\chi(\alpha - \omega)/\alpha), \tag{A.2}$$

and the dependent variable to

$$\hat{\rho}(y) = w(\chi)e^{iM(\alpha-\omega)\chi}\chi^{-\sqrt{\theta}}, \tag{A.3}$$

where $\theta = -M^2(\alpha - \omega)^2 + \alpha^2$, which gives

$$w''(\chi) + \left[2iM(\alpha-\omega) + \frac{1-2\sqrt{\theta}}{\chi} - \frac{2}{\chi - 1}\right]w'(\chi) + \left\{\frac{2iM(\alpha-\omega)\left[iM(\alpha-\omega) - \frac{1}{2} - \sqrt{\theta}\right]}{(\chi-1)} - \frac{iM(\alpha-\omega) - 2M^2(\alpha-\omega)^2 - 2\sqrt{\theta}\left[iM(\alpha-\omega)+1\right]}{\chi(\chi-1)}\right\}w(\chi) = 0. \tag{A.4}$$

(A.4) is structurally identical to the non-symmetrical canonical form of the CHE (Ronveaux & Arscott, 1995), which is defined by

$$w''(z) + \left(4p_* + \frac{\gamma_*}{z} + \frac{\delta_*}{z-1}\right)w'(z) + \frac{4\alpha_* p_* z - \sigma_*}{z(z-1)}w(z) = 0, \tag{A.5}$$

and has two regular singularities at $z = 0$ and $z = 1$, and an irregular singularity at infinity. The CHE in (A.5) has local (Frobenius) solutions denoted by

$$Hc\left(p_*, \alpha_*, \gamma_*, \delta_*, \sigma_*; z\right), \tag{A.6}$$

with five arbitrary complex values of the parameters. Note that we use α_* and γ_* to distinguish the parameters of the solution to the CHE and non-dimensional wavenumbers. Besides, we denote p_* to distinguish the parameter of the solution to the CHE and the pressure p, and we denote δ_* to distinguish the parameter of the solution to the CHE and the boundary layer thickness δ. A second linear independent solution to (A.5) reads (Ronveaux & Arscott, 1995)

$$z^{1-\gamma_*} H\mathrm{c}\left(p_*, \alpha_* - \gamma_* + 1, 2 - \gamma_*, \delta_*, \sigma_* + (-4p_* + \delta_*)(\gamma_* - 1); z\right). \tag{A.7}$$

The general solution to the CHE (A.5) can be expressed by

$$\begin{aligned} w(z) &= C_{1*} H\mathrm{c}\left(p_*, \alpha_*, \gamma_*, \delta_*, \sigma_*; z\right) \\ &\quad + C_{2*} z^{1-\gamma_*} H\mathrm{c}\left(p_*, \alpha_* - \gamma_* + 1, 2 - \gamma_*, \delta_*, \sigma_* + (-4p_* + \delta_*)(\gamma_* - 1); z\right), \end{aligned} \tag{A.8}$$

where the above two $H\mathrm{c}$ functions are linearly independent solutions to the CHE when $1 - \gamma_*$ is not an integer. Due to the resembling form of (A.4) and (A.5), the parameters to the $H\mathrm{c}$ function of (A.4) immediate read

$$\begin{gathered} p_* = \frac{iM(\alpha - \omega)}{2}, \quad \alpha_* = iM(\alpha - \omega) - \frac{1}{2} - \sqrt{\theta}, \\ \gamma_* = 1 - 2\sqrt{\theta}, \quad \delta_* = -2, \\ \sigma_* = iM(\alpha - \omega) - 2M^2(\alpha - \omega)^2 - 2\sqrt{\theta}\left[iM(\alpha - \omega) + 1\right]. \end{gathered} \tag{A.9}$$

Employing the general solution to the CHE, and considering $\hat{\rho}(y) = w(\chi) e^{iM(\alpha-\omega)\chi} \chi^{-\sqrt{\theta}}$ and the inverse transformation $\chi = \alpha e^{-y}/(\alpha - \omega)$, we obtain the general solution to the PBE (2.31), i.e.

$$\begin{aligned} \hat{\rho}(y) &= C_1 e^{iM\alpha e^{-y} + \sqrt{\theta} y} H\mathrm{c}\left(p_*, \alpha_*, \gamma_*, \delta_*, \sigma_*; \frac{\alpha e^{-y}}{\alpha - \omega}\right) + C_2 e^{iM\alpha e^{-y} - \sqrt{\theta} y} \times \\ &\quad \times H\mathrm{c}\left(p_*, \alpha_* - \gamma_* + 1, 2 - \gamma_*, \delta_*, \sigma_* + (-4p_* + \delta_*)(\gamma_* - 1); \frac{\alpha e^{-y}}{\alpha - \omega}\right). \end{aligned} \tag{A.10}$$

This solution is validated in the `Maple 2020` (Maplesoft, 2020) symbolic computing platform. However, in `Maple`, there are different notations of the CHE. Details about the transformation between notations can be found in Borissov & Fiziev (2010).

The nomenclature of the CHF is not well standardised. This is due to the fact that the theory of the Heun class functions is so far not well developed compared to other special functions (Hortaçsu, 2018). We recommend the book by (Ronveaux & Arscott, 1995) , which is by far the most detailed and complete one in the study of Heun functions. This book contains different forms of the CHE, which are classified in terms of the location of the regular singularities, and the nomenclature. The non-symmetrical canonical form of the CHE we adopt is employed in `Maple`, `Mathematica`, and many other papers in recent ten years. This form of the CHE means that two regular singularities locate at 0 and 1, and one irregular singularity at $+\infty$. The nomenclatures in `Maple` and `Mathematica` have no difference in nature. `Mathematica` and the open code in Motygin (2018) basically followed the notations in Ronveaux & Arscott (1995) directly. It is worth noting that Maple uses a different form of the parameters because in this way the form of the second independent solution of the confluent Heun equation can be written in a concise form, so that its coefficients of the series expansion, which are obtained from a three terms recurrence-relation, are easily obtained from the first independent solution.

The form and notations of the CHE in Olver et al. (2010), Motygin (2018) and `Mathematica`

12.1 (2020) are the same and read

$$w''(z) + \left(\epsilon_{**} + \frac{\gamma_{**}}{z} + \frac{\delta_{**}}{z-1}\right) w'(z) + \frac{\alpha_{**} z - q_{**}}{z(z-1)} w(z) = 0, \tag{A.11}$$

with the five independent parameters q_{**}, α_{**}, γ_{**}, δ_{**} and ϵ_{**}. (A.11) is slightly different to (A.5). The transformation between notations is give by

$$\begin{gathered} q_{**} = \sigma_*, \quad \alpha_{**} = 4p_*\alpha_*, \quad \gamma_{**} = \gamma_*, \\ \delta_{**} = \delta_*, \quad \epsilon_{**} = 4p_*. \end{gathered} \tag{A.12}$$

A.2 ω in the asymptotic limit for small and large α

In this appendix, we show the details of the asymptotic expansion of (3.18) and (3.21). The Taylor-series expansion of the Hc function (see e.g. Ronveaux & Arscott (1995)) for $|z| < 1$ is given by

$$\begin{aligned} H\mathrm{c}\left(p_*, \alpha_*, \gamma_*, \delta_*, \sigma_*; z\right) &= \sum_{k=0}^{\infty} c_k z^k \\ &= 1 - \frac{\sigma_*}{\gamma_*} z + \frac{\gamma_*\left(4p_*\alpha_* - \sigma_*\right) + \sigma_*\left(4p_* + \sigma_* - \delta_*\right)}{2\gamma_*\left(\gamma_* + 1\right)} z^2 + \mathcal{O}(z^3), \end{aligned} \tag{A.13}$$

Substituting the first three terms of the expansion into (3.14) to replace the Hc function and its derivative and then, according to (3.16), expanding ω into a Taylor-series about $\alpha = 0$, we obtain $a_1(k_1; M)\alpha + a_2(k_1, k_2; M)\alpha^2 + a_3(k_1, k_2, k_3; M)\alpha^3 + O(\alpha^4) = 0$. As each coefficient has to vanish, we have

$$a_1(k_1; M) = -\frac{{k_1}^2 \sqrt{1 - M^2 \left(k_1 - 1\right)^2}}{(k_1 - 1)^2} = 0, \tag{A.14}$$

which gives

$$k_1 = \frac{M+1}{M}\alpha. \tag{A.15}$$

Next, the coefficient of α^2, i.e. the second leading order term in (3.18), reads

$$
\begin{aligned}
a_2(k_1, k_2; M) = \frac{1}{(k_1-1)^2} \Bigg\{ & \left(i{k_1}^2 M - iM - 2k_1 k_2\right) \sqrt{1 - M^2 (k_1 - 1)^2} \\
& + \frac{2{k_1}^2 k_2 \sqrt{1 - M^2 (k_1-1)^2}}{k_1 - 1} + \frac{{k_1}^2 k_2 M^2 (k_1 - 1)}{\sqrt{1 - M^2 (k_1-1)^2}} \\
& - (k_1 - 1) \left[M^2 (k_1 - 1) \left(\frac{1}{2} - 3{k_1}^2 \right) + 3k_1 + 1 \right] \\
& + 4{k_1}^2 \left[1 - M^2 (k_1 - 1)^2 \right] \Bigg\} = 0,
\end{aligned}
\tag{A.16}
$$

where k_1 from (A.15) implemented into (A.16) leads to zero in the denominator and thus a regular singularity to (A.16) is obtained, which indicates that k_2 should be zero. Employing the value of k_1 from (A.15) and $k_2 = 0$ into the power-series expansion above we obtain

$$
a_3(k_1, k_2; M) = -\sqrt{2k_3 M}\,(M+1)^2 + \frac{M^3}{3} + \frac{5M^2}{2} + 2M = 0, \tag{A.17}
$$

which gives the value of k_3

$$
k_3 = -\frac{M\left(2M^2 + 15M + 12\right)^2}{72(M+1)^4}. \tag{A.18}
$$

For the limit $\alpha \to \infty$, it turned out that ω may be expanded in terms of a Laurant series according to (3.19). Further, using the expansion of Hc function and its derivativ in (A.13) in (3.14) and collecting the leading order terms to obtain $b_1(l_1; M)\alpha^2 + b_2(l_1, l_2; M)\alpha^1 + b_3(l_1, l_2, l_3; M)\alpha^0 + O(\alpha^{-1}) = 0$. Each of the coefficients has to vanish separately, i.e.

$$
b_1(l_1; M) = \frac{\left[(l_1 - 1)M + \sqrt{(l_1-1)^2 M^2 - 1}\right]\left(M^2 {l_1}^2 - M^2 l_1 - 1\right) M}{(l_1 - 1)^2 M^2 - 1} = 0, \tag{A.19}
$$

and

$$
\begin{aligned}
b_2(l_1, l_2; M) = & \frac{1}{(l_1 - 1)\left[1 - (l_1-1)^2 M^2\right]^2} \Bigg\{ \Bigg[iM + l_2 (l_1 - 1)^5 M^6 + \frac{i}{2}(l_1 - 1)^4 M^5 \\
& -2 l_1 l_2 (l_1 - 1)^2 M^4 - \frac{3i}{2}(l_1 - 1)^2 M^3 + l_2 (l_1 - 1) M^2 \Bigg] \\
& + \sqrt{1 - (l_1 - 1)^2 M^2} \Bigg[i(l_1 - 1)^4 l_2 M^5 - \left({l_1}^2 - \frac{1}{2} l_1 + \frac{1}{2} \right)(l_1 - 1)^3 M^4 \\
& - i l_1 (l_1 - 1) l_2 M^3 + \left(2{l_1}^3 - \frac{7}{2}{l_1}^2 + \frac{7}{2} l_1 - 2 \right) M^2 - l_1 \Bigg] \Bigg\} = 0,
\end{aligned}
\tag{A.20}
$$

which gives the value of l_1, l_2 in (3.21) and (3.22). The multiple values of l_2 comes from the branch of square root in l_1.

It should be noted that according to (A.14) two values of k_1 were obtained, i.e. $(M \pm 1)/M$. They correspond to the classical branches of acoustic waves propagating upstream and downstream in a uniform flow. However, we only keep (A.15) and exclude the other one because of its corresponding next higher-order term, which is always negative and real, similar to (A.18). This would result in eigenvalues below the lower bound as defined in section 3.2.3 with a slope of $1 - 1/M$. Dating back to (2.35), as a result, $\sqrt{\theta}$ would become purely imaginary, i.e. an oscillatory solution at infinity, and therefore cannot satisfy the boundary condition (3.1). This case does not happen for (A.15). Implementing (A.15) into (3.16) we can determine that the eigenvalues will be below the upper bound with a slope $1 + 1/M$.

The same interpretation is valid for the asymptotic analysis in the limit $\alpha \to \infty$, where $l_1 = \left(M - \sqrt{M^2+4}\right)/2M$ as a solution of (A.19) has been excluded. The above analysis is verified in our numerical results. In figure 3.4-3.6, for both small and large wavenumbers, no eigenvalues are found around the lower bound, which is different e.g. from the results in duct flows (Vilenski & Rienstra, 2007).

A.3 α in the asymptotic limit for small and large ω

In this appendix, we show the details of the asymptotic expansion of (3.25) and (3.28). Substituting the first three terms of the Taylor-series expansion of the *H*c function (A.13) into (3.14) to replace the *H*c function and its derivative and then, according to (3.23), expanding α into a Taylor-series about $\alpha = 0$, we obtain $c_1(m_1; M)\omega + c_2(m_1, m_2; M)\omega^2 + c_3(m_1, m_2, m_3; M)\omega^3 + O(\omega^4) = 0$. As each coefficient has to vanish, we have

$$c_1(m_1; M) = -\frac{\sqrt{{m_1}^2 - (m_1 - 1)^2 M^2}}{(m_1 - 1)^2} = 0, \tag{A.21}$$

which gives

$$m_1 = \frac{M}{M+1}\omega. \tag{A.22}$$

Next, without giving details, we find that implementing m_1 (A.22) into $c_2(m_1, m_2; M)$ and $c_3(m_1, m_2, m_3; M)$ leads to zero in the denominator, i.e. singularities appear, which indicates that both m_2 and m_3 should be zero. Therefore, taking the value of m_1 from (A.22) and $m_2 = m_3 = 0$ into the power-series expansion we obtain (3.25).

For the limit $\omega \to \infty$, it turned out that α may be expanded in terms of a Laurant series according to (3.26). Further, substituting the expansion of *H*c function in (A.13) and its derivativ into (3.14) and collecting the leading order terms to obtain $d_1(n_1; M)\omega^2 + d_2(n_1, n_2; M)\omega^1 + d_3(n_1, n_2, n_3; M)\omega^0 + O(\omega^{-1}) = 0$. Each of the coefficients has to vanish separately, i.e.

$$d_1(l_1; M) = -\frac{\left(M^2 n_1 - M^2 + {n_1}^2\right)}{\sqrt{{n_1}^2 - (n_1 - 1)^2 M^2}} = 0, \tag{A.23}$$

and

$$d_2(n_1, n_2; M) = \frac{n_1}{2\,(n_1-1)\,[(M+1)\,n_1-M]^2\,[(M-1)\,n_1-M]^2}\times$$
$$\times\left\{2\,(n_1-1)\left[\left(M^2-1\right)n_1{}^2-3\,M^2 n_1+M^2\right]n_2\sqrt{n_1{}^2-(n_1-1)^2\,M^2}\right. \tag{A.24}$$
$$\left.+\left[\left(M^2-2\right)n_1{}^2-2\,M^2 n_1+M^2\right][(M+1)\,n_1-M]\,[(M-1)\,n_1-M]\right\}=0,$$

which gives the value of n_1, n_2 in (3.28) and (3.29). The multiple values of n_2 comes from the branch of square root in n_1.

Noted that according to (A.21) two values of m_1 are obtained, i.e. $M/(M\pm 1)$. For the same argument discussed in §A.2 we only keep (A.22) and exclude the other one. The same argument also holds true for the asymptotic analysis in the limit $\omega\to\infty$, where $n_1 = 2M/\left(M-\sqrt{M^2+4}\right)$ as a solution of (A.23) has been excluded. The above analysis is verified by the numerical results in figure 3.13-3.15.

A.4 Propagation direction of acoustic waves in the free stream

In this appendix, we derive the exact propagation angle ψ through the dispersion relation (3.42). The propagation angle is defined by the group velocity of acoustic waves in the free stream given by

$$\psi = \arctan\left(\frac{\partial\omega_r/\partial\beta_i}{\partial\omega_r/\partial\alpha}\right) = \arctan\left(-\frac{\partial\alpha}{\partial\beta_i}\right), \tag{A.25}$$

where the minus sign comes from the implicit differentiation. Substituting (3.5) into (3.42) and taking square value, we obtain a dispersion relation in α, β_i and ω, which reads

$$\beta_i{}^2 = \frac{1}{2}\left\{\sqrt{4M^2\,(\alpha-\omega_r)^2\,\omega_i{}^2+\left[\alpha^2-M^2\,(\alpha-\omega_r)^2+M^2\omega_i{}^2\right]^2}-\alpha^2+M^2\,(\alpha-\omega_r)^2-M^2\omega_i{}^2\right\}. \tag{A.26}$$

Differentiating of (A.26) with respect to β_i gives

$$2\beta_i = \frac{1}{2}\left\{\frac{8M^2\,(\alpha-\omega_r)\,\omega_i{}^2+\left[2\alpha^2-2M^2\,(\alpha-\omega_r)^2+2M^2\omega_i{}^2\right]\left(2\alpha-2M^2\alpha+2M^2\omega_r\right)}{2\sqrt{4M^2\,(\alpha-\omega_r)^2\,\omega_i{}^2+\left[\alpha^2-M^2\,(\alpha-\omega_r)^2+M^2\omega_i{}^2\right]^2}}\right.$$
$$\left.-2\alpha+2M^2\,(\alpha-\omega_r)\right\}\frac{\partial\alpha}{\partial\beta_i}. \tag{A.27}$$

Collecting $\partial\alpha/\partial\beta_i$ in (A.27) and taking it into (A.25), the propagation angle reads

$$\psi = \arctan\left(\frac{-2\beta_i}{\frac{4M^2(\alpha-\omega_r)\omega_i{}^2+2\left[\alpha^2-M^2(\alpha-\omega_r)^2+M^2\omega_i{}^2\right](\alpha-M^2\alpha+M^2\omega_r)}{2\sqrt{4M^2(\alpha-\omega_r)^2\omega_i{}^2+\left[\alpha^2-M^2(\alpha-\omega_r)^2+M^2\omega_i{}^2\right]^2}}-\alpha+M^2\left(\alpha-\omega_r\right)}\right). \tag{A.28}$$

Considering the limiting case for $\omega_i \to 0$, (A.28) is identified with (3.47).

A.5 Critical layer

As already shown, the PBE reaches a singularity if the phase velocity in the x-direction coincides with the base flow velocity, which means $\omega = \alpha\, u_0(y_c)$. This horizontal layer is called the critical layer. We will first examine the behaviour of the solution at the critical layer by using an asymptotic method, the Fuchs-Frobenius method. For this, we first employ a change of the independent variable to ξ, defined by

$$\xi = \frac{\omega}{\alpha} - u_0(y) = \frac{\omega}{\alpha} - \left(1 - e^{-y}\right), \tag{A.29}$$

such that y_c refers to $\xi = 0$, which converts the the PBE (2.31) to

$$\frac{d^2\hat{\rho}}{d\xi^2} - \frac{((\xi+2)\alpha - 2\omega)}{\xi\left((\xi+1)\alpha-\omega\right)}\frac{d\hat{\rho}}{d\xi} + \frac{\left(M^2\xi^2-1\right)\alpha^4}{\left((\xi+1)\alpha-\omega\right)^2}\hat{\rho} = 0. \tag{A.30}$$

A solution of (A.30) in the vicinity of $\xi = 0$ can be derived as a power series using the Fuchs-Frobenius method. Inserting the power series approach, given by

$$\hat{\rho}(\xi) = \xi^r \sum_{k=0}^{\infty} a_k \xi^k, \tag{A.31}$$

into the differential equation (A.30) and sorting by powers of ξ yields the indicial equation for r. It has two roots, which read $r_1 = 3$ and $r_2 = 0$ and indicate that their difference $r_1 - r_2 = 3$ is a positive integer. Following Olver et al. (2010), a regular implementation of the method of Frobenius in this case fails to yield two independent solutions. Hence, a second independent solution contains a logarithmic term and can be constructed by

$$\hat{\rho}_2(\xi) = c\,\hat{\rho}_1(\xi)\ln(\xi) + \xi^{r_2}\sum_{k=0}^{\infty} b_k \xi^k, \tag{A.32}$$

where the constant c can be derived by re-inserting into (A.30), starting with $b_0 = a_0 = 1$. The first independent solution is given by

$$\hat{\rho}_1(\xi) = \xi^{r_1} \sum_{k=0}^{\infty} a_k \xi^k. \tag{A.33}$$

Near the critical layer, i.e. $\xi \to 0$, the solution given by a linear combination of (A.32) and (A.33) is considered to the leading order and we obtain

$$\hat{\rho}(\xi) = A\left(\xi^3 + \mathcal{O}\left(\xi^4\right)\right) + B\left(c_*\left(\xi^3 + \mathcal{O}\left(\xi^4\right)\right)\ln(\xi) + 1 + \mathcal{O}\left(\xi^1\right)\right), \tag{A.34}$$

where A and B are two constants. Re-inserting (A.34) into (A.30) yields, after some algebra:

$$c_* = -\frac{4\alpha(\alpha-\omega) + \frac{3\alpha^5}{\alpha-\omega}}{3(\alpha-\omega)^2}, \tag{A.35}$$

From (A.34) it can be concluded that the solution tends to be a constant near the critical layer. Furthermore, c can be rewritten as

$$c_* = -\frac{4\alpha^2\left(1-\frac{\omega}{\alpha}\right) + \frac{3\alpha^4}{1-\frac{\omega}{\alpha}}}{3(\alpha-\omega)^2}. \tag{A.36}$$

This shows that the constant c_* is, in the presence of a critical layer, always negative, since the necessary condition for the occurance of a critical layer is $\omega/\alpha \in [0,1]$. We will use this knowledge in section 4.2.4 to show that $R > 1$ in this case.

A.6 Causality and the choice of branch cuts

As recognized by Brambley et al. (2012), the choice of branch cuts is crucial for the investigation of the critical layer. Thus, the question arises, which criterion allows us to choose the correct branch cut. We assume a causal signal. Following Dethe et al. (2019), "causality states that the cause precedes the effects". This means nothing else than that an effect can only be affected by the temporally previous effects, but not by the future. The causality condition can be formulated by regarding the response function in the Fourier space: As shown by Dethe et al. (2019), a causal solution mapped by a Fourier transformation to $\hat{\rho}(\omega)$ requires analyticity of the Fourier response function in the upper complex ω half-plane. Since $\xi = \omega/\alpha - u_0$, we require analyticity of the solution in the upper complex ξ half-plane (For simplicity, we restrict the consideration to positive values of α. For negative α, the consideration would be reversed, but the outcome $|R| > 1$ stays the same since the RHS of (4.23) would then also change its sign).

As shown in Appendix A.5, the solution $\hat{\rho}$ contains a logarithmic term, thus we have to define the branch cut of the complex logarithm in the complex ξ plane.

The logarithm of a complex number ξ is defined by $\ln(\xi) = |\ln(\xi)| + i\arg(\xi)$. Since $\arg(\xi)$ is 2π-periodic, we have to introduce a branch cut that ensures that for every point ξ in the complex plane there is only one solution for $\ln(\xi)$. The branch cut is chosen to be a straight line starting from the branch point $\xi = 0$, which is a singularity of $\ln(\xi)$.

If we choose the branch cut to be a straight line in the upper complex ξ half-plane, there would be a discontinuity of $\ln(\xi)$, since $\arg(\xi)$ undergoes a jump at the branch cut. However, this would contradict the causality condition, i.e. analyticity in the upper complex ω half-plane. Therefore, the only possible choice for the branch cut of $\ln(\xi)$ is the red straight line in the lower complex half-plane, as shown in figure A.1.

A.7 Derivation of the extended unitarity condition

In this section, an extended unitarity condition given by (4.33) is derived. It gives a relation between the amplitude of density perturbation, its derivatives at the critical layer and the reflection coefficient R. For this purpose, we first multiply (4.19) by $\hat{\rho}^*$, the complex conjugate of $\hat{\rho}$, take the imaginary part of the equation (which allows us to identify the reflection coefficient on the LHS), integrate it and split up the resulting integrals, which yields

$$\Im\left(\frac{d\hat{\rho}}{d\tilde{y}}\hat{\rho}^*\right)\Bigg|_{\tilde{y}_1}^{\tilde{y}_2} = -\int_{\tilde{y}_1}^{\tilde{y}_2} \Im\left(\frac{M^2}{(\omega-\alpha u_0)^2}\right)|\hat{\rho}|^2 d\tilde{y} + \int_{\tilde{y}_1}^{\tilde{y}_2} \Im\left(\frac{\alpha^2}{(\omega-\alpha u_0)^4}\right)|\hat{\rho}|^2 d\tilde{y}. \tag{A.37}$$

In order to deal with the occurring integrals in (A.37), which have a singularity at the critical layer y_c, the transformation of the independent variable to ξ, as given by (A.29), is used again and yields

$$\Im\left(\frac{d\hat{\rho}}{d\tilde{y}}\hat{\rho}^*\right)\Bigg|_{\tilde{y}_1}^{\tilde{y}_2} = \Im\left(\int_{\xi_1}^{\xi_2} \frac{1}{\xi^2}\cdot\frac{\alpha^2 M^2|\hat{\rho}|^2}{\frac{du_0}{d\tilde{y}}} d\xi\right) - \Im\left(\int_{\xi_1}^{\xi_2} \frac{1}{\xi^4}\cdot\frac{\alpha^6|\hat{\rho}|^2}{\frac{du_0}{d\tilde{y}}} d\xi\right). \tag{A.38}$$

Both integrals in equation (A.38) have a singularity at $\xi = 0$, which corresponds to the localization of the critical layer. Provided that the parameter set induces a critical layer, the value of the imaginary part of these integrals is nonzero due to the singularity, even if the integrals contain only real values. For the treatment of integrals containing singular functions, we would like to refer to the theory of distributions in the context of generalized functions. For further literature, please see Galapon (2016). The main outcome can be summarized in the Sokhotskij-Plemelj-Fox theorem, given by formula (A.40). Since we have to treat the singularity occurring in (A.38) in a distributional context, even an integral containing only real quantities must be split up into real and imaginary parts due to the regularization process. If there is no critical layer, then there is no singularity in the integrands, the integrals are real and the imaginary parts of these integrals vanish. Further information can be found for example in the book of Lighthill (1958).

In order to evaluate the singular integrals, i.e. regularize the singularity, a small imaginary frequency $i\epsilon$ is added to the singularity, i.e. $\omega \to \omega + i\epsilon$. Thus, weak temporal growth of the solution is allowed, consistent with the causality theory. The regularization and the chosen branch cut for the logarithmic term in the solution is shown in Figure A.1. It can be easily seen that a regularization of the path of integration (blue) by $\omega - i\epsilon$ would intersect with the branch cut and would thus cause another discontinuity in the integral. Therefore, the given choice $\omega + i\epsilon$ is the one that is consistent with the causality theory.

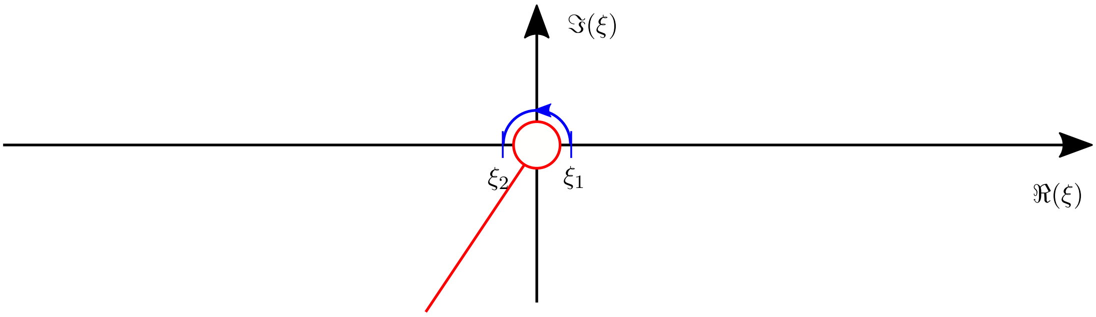

Figure A.1: Regularized path of integration and choice of the branch cut.

In the next step, the limit $\epsilon \to 0$ is taken, which represents the purely acoustic case, i.e.

$$\Im\left(\frac{d\hat{\rho}}{d\tilde{y}}\hat{\rho}^*\right)\Bigg|_{\tilde{y}_1}^{\tilde{y}_2} = \lim_{\epsilon\to 0}\left(\Im\int_{\xi_1}^{\xi_2}\frac{1}{(\xi+i\epsilon)^2}\cdot\frac{\alpha^2M^2|\hat{\rho}|^2}{\frac{du_0}{d\tilde{y}}}d\xi\right.$$
$$\left. - \Im\int_{\xi_1}^{\xi_2}\frac{1}{(\xi+i\epsilon)^4}\cdot\frac{\alpha^6|\hat{\rho}|^2}{\frac{du_0}{d\tilde{y}}}d\xi\right). \tag{A.39}$$

In order to deal with the higher-order singular integrals, the Sokhotski-Plemelj-Fox Theorem described in Galapon (2016) is applied, which includes the idea of separating the finite part from the divergent integral. The theorem reads as follows

$$\lim_{\epsilon\to 0}\int_a^b\frac{f(x)}{(x+i\epsilon)^{n+1}}dx = \text{PV}\int_a^b\frac{f(x)}{x^{n+1}}dx - i\pi\frac{f^{(n)}(0)}{n!}, \tag{A.40}$$

if $a < 0 < b$ holds. Therein, PV refers to Cauchy's principal value. To fulfill this condition in (A.39), the behaviour in ξ is investigated. The limits of integration, i.e. $y = 0$ and $y \to \infty$, change using (A.29) to $\xi_1 = \omega$ and $\xi_2 = \omega - \alpha$. Since the following derivation is intended to consider specifically the case of a critical layer at position $\xi = 0$ lying within the physical area, it has to be assumed in the following that $\omega < \alpha$, which is the condition for the existence of a critical layer. To apply the Sokhotski-Plemelj-Fox theorem (A.40), the limits of integration in (A.39) are swapped, which leads to

$$\Im\left(\frac{d\hat{\rho}}{d\tilde{y}}\hat{\rho}^*\right)\Bigg|_{\tilde{y}_1}^{\tilde{y}_2} = -\lim_{\epsilon\to 0}\left(\Im\int_{\xi_2}^{\xi_1}\frac{1}{(\xi+i\epsilon)^2}\cdot\frac{\alpha^2M^2|\hat{\rho}|^2}{\frac{du_0}{d\tilde{y}}}d\xi\right.$$
$$\left. -\Im\int_{\xi_2}^{\xi_1}\frac{1}{(\xi+i\epsilon)^4}\cdot\frac{\alpha^6|\hat{\rho}|^2}{\frac{du_0}{d\tilde{y}}}d\xi\right), \tag{A.41}$$

where $\xi_2 < 0 < \xi_1$.

Since the Cauchy principal value in (A.40) represents the finite part of the integral it is, if $f(x)$ is a real function, a real value. Since we limit to the imaginary parts of the integrals in (A.41), the principal value vanishes in the application of (A.40) on the RHS of (A.41) which yields

$$\Im\left(\frac{d\hat{\rho}}{d\tilde{y}}\hat{\rho}^*\right)\Bigg|_{\tilde{y}_1}^{\tilde{y}_2} = \pi\left(\left(M^2\alpha^2\frac{d}{d\xi} - \frac{\alpha^6}{6}\frac{d^3}{d\xi^3}\right)\frac{|\hat{\rho}|^2}{\frac{du_0}{d\tilde{y}}}\right)\Bigg|_{\xi=0}. \tag{A.42}$$

With this, the derivation of (4.31) is completed and it has been used in (4.23) to obtain (4.33). Transforming (A.42) back to the initial independent variable y and simplifying yields (4.33).

A.8 Data for higher unstable modes

In this section, data on the resonant frequencies for higher unstable modes are shown in the form of tables. Table A.1 and table A.2 show the data regarding the second and third unstable modes. Specific wavenumbers and Mach numbers are selected in order to correspond to the cases in figure 4.8. With these parameters, the resonant frequency ω_r, the incident angle ϕ and the over-reflection coefficient R are given.

$\omega_r/\phi/R$	$\alpha = 4$	$\alpha = 7$	$\alpha = 10$
$M = 4$	- / - / -	4.35/66.3/1.00011	5.52/63.1/1.00005
$M = 4.5$	2.84/71.8/1.00116	4.07/67.5/1.00233	5.14/64.4/1.00084
$M = 5$	2.69/72.7/1.01477	3.83/68.6/1.01282	4.82/65.5/1.00491

Table A.1: Values of the resonant frequency ω_r, incident angle ϕ and over-reflection coefficient R at which second unstable modes occur for different α and M.

$\omega_r/\phi/R$	$\alpha = 7$	$\alpha = 10$
$M = 4$	5.21/70.4/1.00000000000283	6.60/67.8/1.00000006739935
$M = 4.5$	4.89/71.5/1.00001182456871	6.17/68.9/1.00002458761766
$M = 5$	4.62/72.4/1.00064208260075	5.81/69.9/1.00049307847717

Table A.2: Values of the resonant frequency ω_r, incident angle ϕ and over-reflection coefficient R at which third unstable modes occur for different α and M.